

The evaluation and application of tourmaline crystal chemistry as an indicator of porphyry-style
Cu-Mo-Au mineralization

by

Christopher Edward Beckett-Brown

A thesis submitted in partial fulfillment of the requirements
for the degree of Doctor of Philosophy (PhD)
in Mineral Deposits and Precambrian Geology

The Faculty of Graduate Studies
Laurentian University
Sudbury, Ontario, Canada

© Christopher Edward Beckett-Brown, 2022

THESIS DEFENCE COMMITTEE/COMITÉ DE SOUTENANCE DE THÈSE

Laurentian University/Université Laurentienne
Office of Graduate Studies/Bureau des études supérieures

Title of Thesis Titre de la thèse	The evaluation and application of tourmaline crystal chemistry as an indicator of porphyry-style Cu-Mo-Au mineralization		
Name of Candidate Nom du candidat	Beckett-Brown, Christopher		
Degree Diplôme	Doctor of Philosophy		
Department/Program Département/Programme	Mineral Deposits and Precambrian Geology	Date of Defence Date de la soutenance	December 15, 2021

APPROVED/APPROUVÉ

Thesis Examiners/Examineurs de thèse:

Dr. Andrew W. McDonald
(Supervisor/Directeur(trice) de thèse)

Dr. Alessandro Ielpi
(Committee member/Membre du comité)

Dr. Beth McClenaghan
(Committee member/Membre du comité)

Dr. Karen Kelley
(External Examiner/Examineur externe)

Dr. Beth McLenaghan
(External Examiner/Examineur externe)

Approved for the Office of Graduate Studies
Approuvé pour le Bureau des études supérieures
Tammy Eger, PhD
Vice-President Research (Office of Graduate Studies)
Vice-rectrice à la recherche (Bureau des études supérieures)
Laurentian University / Université Laurentienne

ACCESSIBILITY CLAUSE AND PERMISSION TO USE

I, **Christopher Beckett-Brown**, hereby grant to Laurentian University and/or its agents the non-exclusive license to archive and make accessible my thesis, dissertation, or project report in whole or in part in all forms of media, now or for the duration of my copyright ownership. I retain all other ownership rights to the copyright of the thesis, dissertation or project report. I also reserve the right to use in future works (such as articles or books) all or part of this thesis, dissertation, or project report. I further agree that permission for copying of this thesis in any manner, in whole or in part, for scholarly purposes may be granted by the professor or professors who supervised my thesis work or, in their absence, by the Head of the Department in which my thesis work was done. It is understood that any copying or publication or use of this thesis or parts thereof for financial gain shall not be allowed without my written permission. It is also understood that this copy is being made available in this form by the authority of the copyright owner solely for the purpose of private study and research and may not be copied or reproduced except as permitted by the copyright laws without written authority from the copyright owner.

Abstract

As the exploration for porphyry Cu-Mo-Au deposits becomes increasingly challenging, there exists a need for exploration techniques that can detect buried deposits. Tourmaline supergroup minerals (TSM), a chemically and physically robust phase in the surficial environment, is investigated for its indicator mineral potential to identify porphyry Cu-Mo-Au systems. Samples of TSM from mineralized porphyry systems (Cu, \pm Au, \pm Mo) including Casino (Yukon Territory, Canada), Coxheath (Nova Scotia, Canada), Donoso Breccia-Los Bronces (Chile), Highland Valley Copper (British Columbia, Canada), New Afton (British Columbia, Canada), Schaft Creek (British Columbia, Canada), and Woodjam (British Columbia, Canada) were examined. Results show that TSM are generally an early hydrothermal mineral predating both mineralization and alteration assemblages. They form sub- to euhedral crystals that are exclusively black (in hand sample) and can be found throughout a porphyry system across all zones of alteration. Major-element chemistry of the TSM is unremarkable, with most having Na-Mg-Al (dravite) compositions (\sim 80 % of grains) with lesser amounts of schorl (Fe). They exhibit consistent concentrations of \sim 2.0 *apfu* Mg with most plotting along the oxy-dravite – povondraite trend reflecting the dominance of $\text{Al}^{3+} \leftrightarrow \text{Fe}^{3+}$ substitution. An investigation of TSM trace-elements (LA-ICP-MS) revealed key elements (Sr, Pb, Zn, Cu, and Ga) and select element ratios (Sr/Pb and Zn/Cu) that can be used as discriminators of its environment of formation. Utilizing an understanding of both intrinsic and extrinsic controls on TSM chemistry is an effective approach to distinguish TSM forming in porphyry bedrock samples. A decision tree was developed and applied to TSM grains recovered surrounding two known porphyry deposits including Casino-YT and Woodjam-BC to assess its effectiveness. Using both textural and chemical features of TSM from mineralized porphyry systems highlighted above, porphyry-

related grains were identified down ice and downstream of both deposits respectively, highlighting the potential for this method to be used in exploration. The crystal chemistry of TSM has been demonstrated to be sensitive to its environment of formation allowing for the discrimination and identification of TSM forming in porphyries from that forming in other geologic environments and ore systems.

Keywords: tourmaline, tourmaline supergroup minerals, indicator mineral, LA-ICP-MS, mineral chemistry, discrimination diagram, porphyry deposits, mineral exploration, crystal chemistry, trace-elements,

Co-Authorship Statement

This thesis is comprised of four separate manuscripts prepared for publication in peer-reviewed journals. Chapters two, three, four, and five have been written by the candidate with support from additional collaborators. Chapter four has been published through the Geological Survey of Canada: Beckett-Brown, C.E., McDonald, A.M., McClenaghan, M.B., Plouffe, A., and Ferbey, T., 2021. Investigation of tourmaline characteristics in bedrock and surficial sediment samples from two Canadian porphyry copper systems. In: E. Schestelaar and A. Plouffe (Editors), Targeted Geoscience Initiative 5: contributions to the understanding and exploration of porphyry deposits, Geological Survey of Canada, Bulletin 616, pp. 109-135.

<https://doi.org/10.4095/327989>.

The thesis was originally designed by Dr. John Chapman, Beth McClenaghan, Dr. Andrew McDonald, and Dr. Matthew Leybourne. Bedrock samples from Schaft Creek and Woodjam were collected by Dr. John Chapman in 2015 and 2013, respectively. Till samples surrounding Woodjam were collected by Alain Plouffe and Travis Ferbey in 2013. Casino bedrock and surficial samples were collected by the candidate with assistance from Martin McCurdy in 2017. Samples from New Afton were provided by Devin Wade. Samples from the Donoso Breccia (Rio Blanco-Los Bronces district) were provided by Dr. Stephen Cook which were collected in 2008. Samples from Coxheath and Highland Valley Copper were obtained from the Geological Survey of Canada's collection at Tunney's Pasture. Coxheath samples were collected by Dr. Art Soregaroli in 1975 and the Highland Valley Copper samples were collected by Dr. Rod Kirkham in 1982. Surficial samples from Woodjam and Casino were processed for heavy mineral concentrates by Overburden Drilling Management. All subsequent work on bedrock and surficial samples were completed by the candidate.

The four manuscripts are co-authored by Dr. Andrew McDonald and Beth McClenaghan.

Chapter 4 was additionally co-authored by Alain Plouffe and Travis Ferbey who collected the Woodjam surficial samples and provided significant background on the glacial history of the area.

Acknowledgments

This project would not have been possible without the support and expertise of many people. I am thankful for the supervision of my thesis supervisor Dr. Andy McDonald who always challenged me to be a better scientist and has devoted a decade of his career to writing me reference letters, providing both personal and academic guidance, countless rounds of edits, and endless scientific discussions (some might call them arguments). I would also like to thank Beth McClenaghan from the Geological Survey of Canada for her mentorship and guidance throughout the entire project. I would also like to acknowledge the thesis committee, the HES graduate coordinator Dr. Stephane Perrouty, the internal examiner Dr. Jeffrey Shepherd, external examiner Dr. Karen Duttweiler Kelley, and finally committee member Dr. Alessandro Ielpi for his constructive contributions to the research and also for being an excellent canoeing partner.

The Harquail School of Earth Sciences has been my home for the last decade, during which I have made some incredible friends and colleagues, guidance from numerous professors, and endless help from the support staff (Roxane, Edda, and Tobias). I am also thankful for work colleagues and friends Lindsay Cooper (former HES promotions and Communication Manager) and Lynn Bulloch (current HES promotions and Communication Manager) for allowing me to assist in promotion as well as outreach activities and being my go-to coffee break colleagues.

I have been fortunate to have some incredible laboratory assistance and training from Willard Desjardins (petrography and lapidary methods), Dr. William Zhe (SEM-EDS/EBSD), Dr. Joseph Petrus and Dr. Jeffrey Marsh (LA-ICP-MS), Dave Crabtree and Sandra Clarke (EMPA), and finally the team at Overburden Drilling Management (Stuart Averil, Michael Crawford, Donald Holmes) for the processing of the heavy mineral concentrates and working with us through our numerous requests to re-pick samples.

Support from colleagues at the Geological Survey of Canada: John Chapman (former), Dave Sinclair, Eric Grunsky, Alain Plouffe, Deborah Lemkow, Steve Irwin, Marty McCurdy, and Jan Peter.

I am thankful for the Western Copper and Gold team at Casino including Heather Brown for her geological knowledge and Mary Mioska for her logistical support. The Yukon Geological Survey staff for their expertise in the region and aiding in collaboration with Casino Scott Casselman, Craig Nicholson, and Jeff Bond.

Additionally, I have met some incredible industry professionals who have either shared samples or knowledge on porphyry systems including Steve Cook, Kevin Byrne, Leif Bailey, Devin Wade, Dave Kelley, Steve Smith, Bruce Ballantyne, and Brock Riedell.

Throughout my studies I have made many friends and had endless science discussions with including office mates Remy Poulin, Monika Haring, Thomas Gore, and Derek Leung, fellow graduate students Evan Hastie, Robbie Meek, Christoph Schaub, and Carol-Anne Genereux as well as the many other graduate students and undergraduate students I have met along the way.

Support from my Sudbury crew Tristan, Real, Tyler, and my brother Nick.

Forever grateful for the support of my close and extended family. Both my grandfathers, Harry Brown and Norman Beckett who were both science teachers inspired and supported my studies. To my parents Tom Brown and Claire Beckett for their love and support. To my Dad especially for letting me live at home for so long... I am thankful for the support of the Gauthier family over the past year and for their genuine interest in my research. Finally, my girlfriend Maxine Gauthier for her love and support and unwavering patience with my commitment to my research. I love all of you.

Research Funding

This research project was financially supported by the Geological Survey of Canada Targeted Geoscience Initiative 5 as part of the “Mineral Markers for Polymetallic Porphyry Deposits Activity” supervised by Beth McClenaghan. I was additionally funded by the Research Affiliate Program (RAP) (MSc - 2 years, Ph.D. – 3 years) which is funded by Natural Resources Canada through the Geological Survey of Canada. Additional financial support was provided by the Society of Economic Geology Canada Foundation Research Grant (2018-2019). Travel grants were supported through the Mineralogical Association of Canada (2018) and the Laurentian University graduate studies bursaries (2018).

I was additionally supported by several scholarships and awards including the Ontario Graduate Scholarship (2016-2017), the Society of Economic Geology Graduate Student Fellowship, sponsored by Anglo American (2017), the Natural Sciences and Engineering Research Council of Canada, Graduate Scholarship-Masters (2017-2018), the Peacock Medal sponsored by the Walker Mineralogical Club (2018), the Mineralogical Association of Canada Foundation Ph.D. Scholarship (2019), and finally the Natural Sciences and Engineering Research Council of Canada Alexander Graham Bell Canada Graduate Scholarship – Doctoral (2018-2021).

Table of Contents

Thesis Defence Committee /Comité de soutenance de thèse	ii
Abstract	iii
Co-Authorship Statement	v
Acknowledgments	vii
Research Funding	ix
Table of Contents	x
List of Tables	xvi
List of Figures	xviii
List of Appendices	xx
List of Short Forms	xxi
Chapter 1	22
1 Introduction to thesis	22
1.1 Background.....	22
1.2 Current Knowledge of Porphyry Indicator Minerals	22
1.3 Tourmaline Nomenclature.....	25
1.4 Tourmaline in Porphyry Deposits.....	26
1.5 Thesis Objectives	27
1.6 Structure of the Thesis	28
1.7 References	30

Chapter 2	41
2 Recognizing tourmaline in mineralized porphyry systems Part I: textures and major-element chemistry	41
2.1 Abstract	41
2.2 Introduction	42
2.3 Tourmaline in Porphyry Systems: Background.....	44
2.3.1 Occurrences and Textures	44
2.3.2 TSM Species and Major-Element Variations.....	45
2.4 Tourmaline Systems Examined in This Study	47
2.4.1 Specific Systems Examined	48
2.5 Methods.....	54
2.5.1 Major and Minor Element Chemistry	54
2.6 Results	54
2.6.1 Tourmaline physical and optical characteristics.....	54
2.6.2 Mineral Chemistry	60
2.7 Discussion.....	62
2.8 Conclusions	69
2.9 Figures.....	72
2.10 Tables.....	83
2.11 References for TSM at the deposits displayed in Fig. 2-1.....	87

2.12	References.....	88
Chapter 3		116
3	Recognizing tourmaline in mineralized porphyry systems Part II: trace-element characteristics of tourmaline: development and application to discrimination among source regions	116
3.1	Abstract	116
3.2	Introduction	117
3.3	Trace-elements in tourmaline from porphyry deposits: A review.....	119
3.3.1	Metals and Semi-Metals.....	119
3.3.2	Discrimination	120
3.4	Tourmaline Systems Examined.....	120
3.5	Analytical Conditions.....	123
3.5.1	Laser-Ablation Inductively Coupled-Plasma Mass-Spectrometry	123
3.6	Results	124
3.6.1	General Overview	124
3.6.2	Inter-deposit Variations.....	125
3.6.3	Intra-grain variations.....	127
3.7	Discussion.....	128
3.8	Conclusions	140
3.9	Figures.....	142

3.10	Tables.....	150
3.11	References.....	152
Chapter 4		171
4	Investigation of tourmaline characteristics in bedrock and surficial sediment samples from two Canadian porphyry copper systems.....	171
4.1	Abstract	171
4.2	Introduction	172
4.3	Geological Background.....	174
4.3.1	Bedrock Samples	174
4.3.2	Surficial Samples	175
4.4	Methods.....	176
4.4.1	Sample Processing	176
4.4.2	Major- and minor-element chemistry	177
4.4.3	Trace-element chemistry.....	178
4.5	Results	179
4.5.1	Tourmaline textures	179
4.5.2	Mineral chemistry.....	182
4.5.3	Major- and minor-element chemistry (SEM-EDS)	183
4.5.4	Trace-element chemistry.....	185
4.6	Discussion.....	186

4.7	Conclusions	192
4.8	Figures.....	194
4.9	Tables	208
4.10	Appendix.....	216
4.10.1	Appendix 1:	216
4.11	References.....	217
Chapter 5		230
5	The missing link between biotite and tourmaline in porphyry systems	230
5.1	Abstract	230
5.2	Introduction	231
5.3	The Casino Deposit.....	233
5.3.1	Background Geology	233
5.3.2	Sample Material and Mineralogy	233
5.3.3	Chemical Zonation.....	235
5.4	Methods: Major and Minor Element Chemistry.....	236
5.5	Results	237
5.5.1	Biotite.....	237
5.5.2	Muscovite	237
5.5.3	Tourmaline	238
5.6	Discussion.....	239

5.7	Conclusions	244
5.8	Figures.....	246
5.9	Tables	257
5.10	References.....	260

List of Tables

Table 2-1: Mineralized porphyry systems examined.....	83
Table 2-2: Tourmaline physical and optical characteristics	84
Table 2-3: Major and minor element analyses of tourmaline from the deposits examined.	85
Table 3-1: Summary of tourmaline trace-element concentrations determined by LA-ICP-MS for the seven deposits examined.....	150
Table 4-1: Select major element compositions of tourmaline from bedrock, till, and stream sediment samples collected at the Woodjam and Casino deposits.	208
Table 4-2: Summary of trace-element analyses in TSM from bedrock samples at Woodjam and Casino.....	209
Table 4-3: Summary of trace-element analyses of tourmaline from surficial sediments at the Woodjam and Casino porphyry deposits.....	210
Table 4-4: Mineral inclusions identified in detrital tourmaline grains in selected till samples at the Woodjam deposit.....	211
Table 4-5: Mineral inclusions identified in detrital tourmaline grains collected from stream sediments surrounding the Casino deposit.	212
Table 4-6: Generalizations of trace-element compositions for tourmaline from different geological settings.....	213
Table 4-7a: Number of surficial porphyry derived tourmaline grains in the 2.8 to 3.2 SG fraction of till samples from the Woodjam deposit	214
Table 4-7b: Number of surficial porphyry derived tourmaline grains in the 2.8 to 3.2 SG fraction of stream sediment samples from the Casino deposit.....	215
Table 5-1: Major and minor element chemistry for biotite grains from CEBB-012	257

Table 5-2: Major and minor element chemistry for muscovite grains.....258

Table 5-3: Summary of the major and minor element chemistry of tourmaline259

List of Figures

Figure 2-1: World map showing the distribution of porphyry deposits that contain TSM.....	72
Figure 2-2: Porphyry alteration zonation schematic overlain with TSM distribution.....	73
Figure 2-3: Tourmaline paragenesis.....	74
Figure 2-4: Hand sample photographs highlighting the textural styles of TSM.....	75
Figure 2-5: Backscattered electron images of internal TSM textures.....	77
Figure 2-6: Examples of mineral inclusions in TSM.....	78
Figure 2-7: Major element diagrams of TSM chemistry.....	79
Figure 2-8: Major element tukey box plots of TSM deposit chemistry.....	80
Figure 2-9: TSM major element chemistry and alteration.....	81
Figure 2-10: Binary plots of deposit tonnage vs. Cu grade and age of the deposit.....	82
Figure 3-1: Tukey box plots of porphyry tourmaline trace-element data.....	142
Figure 3-2: Tourmaline trace-element map.....	143
Figure 3-3: Percentile box plots of tourmaline trace-elements.....	144
Figure 3-4: Size and valence substitution constraints for trace-elements.....	147
Figure 3-5: Tourmaline trace-element discrimination diagram.....	148
Figure 3-6: Discrimination diagram trace-element concentration overlays.....	149
Figure 4-1: Location of surficial sediment samples (Woodjam-BC and Casino-YT).....	194
Figure 4-2: Tourmaline from the surficial environment.....	195
Figure 4-3: Hand sample images of tourmaline textures in bedrock.....	196
Figure 4-4: Paragenetic position of tourmaline.....	197
Figure 4-5: Internal zonation textures of tourmaline.....	198
Figure 4-6: Comparison of internal textures (Bedrock-till: Woodjam-BC).....	199

Figure 4-7: Major element trends of bedrock and surficial tourmaline	200
Figure 4-8: Trace-element grain map of tourmaline.....	201
Figure 4-9: Percentile box plots of tourmaline trace-element data for common environments of formation	202
Figure 4-10: Decision Tree: porphyry tourmaline.....	204
Figure 4-11: Ternary trace-element discrimination of surficial tourmaline grains.	206
Figure 4-12: Porphyry tourmaline dispersion maps (Woodjam and Casino).....	207
Figure 5-1: Sample locations.....	247
Figure 5-2: Hand sample photos.....	248
Figure 5-3: Photomicrographs of biotite-tourmaline textures.	249
Figure 5-4: Photomicrographs of tourmaline forming after biotite.	250
Figure 5-5: Backscattered electron images of biotite and tourmaline	251
Figure 5-6: Backscatter image montage showing tourmaline that has replaced biotite.....	253
Figure 5-7: Major and minor element chemistry for biotite and tourmaline analyses.....	254
Figure 5-8: Idealized diagram of biotite-tourmaline transition	256

List of Appendices

Chapter 2 Appendix 1 USGS Porphyry database with tourmaline occurrences and references

Chapter 4 Appendix 1 Woodjam till sample tourmaline recount data

List of Short Forms

Mineral short forms are after Whitney and Evans (2010).

apfu: atoms per formula unit

avg: average

BSEI: Backscattered Electron Image

LA-ICP-MS: Laser Ablation Inductively Coupled Plasma Mass Spectrometry

LOD: limit of detection

Mg#: $Mg/(Mg+Fe)$

PIM's: Porphyry Indicator Minerals

SEM-EDS: Scanning Electron Microscope Energy Dispersive Spectroscopy

TSM: tourmaline supergroup mineral

tot: total

vs: versus

□: Vacancy

Chapter 1

1 Introduction to thesis

1.1 Background

Porphyry indicator minerals (PIMs) are phases identified in rocks and surficial materials that indicate the presence of, or potential for, porphyry-style mineralization based on their chemistry (Averill 2011; Cooke *et al.* 2020). Recent studies have investigated using the chemistry of certain indicator minerals to vector towards high grade mineralized zones (Cooke *et al.* 2020). Primary and secondary ore minerals make up the bulk of the current PIMs in surficial materials (Averill 2011). Problems arise with some PIMs as their resistivity to physical and chemical weathering in the surficial environment is generally poor, resulting in a small or no dispersal anomaly in local sediments derived from the porphyry deposit. The effective use of indicator minerals has been carried out in diamond exploration for more than 50 years, where identifying minerals such as “G10” garnets are used to guide diamond exploration (Muggeridge, 1995; McClenaghan and Kjarsgaard, 2007; Nowicki *et al.* 2007). The goal for the application of PIMs such as TSM (tourmaline supergroup minerals), is to test its efficacy as tools in the discrimination between mineralized porphyry systems and TSM forming in other geologic environments.

1.2 Current Knowledge of Porphyry Indicator Minerals

Porphyry indicator minerals (PIMs) that are regularly observed in surficial sediment sampling programs in glaciated and weathered terrains by exploration companies include chalcopyrite, pyrite, gold, molybdenite, jarosite, alunite, pyrolusite, goethite, barite, epidote, apatite, rutile,

zircon, magnetite, and tourmaline (Averill 2011). These minerals have been classified as PIMs based on their observed presence in known porphyry systems or in sediments derived from known deposits (Averill 2011). Some of the minerals listed above are not robust indicators due to their inability to withstand both chemical and physical weathering processes, preventing their widespread dispersal or recovery in some surficial environments. Other mineral phases such as pyrite and gold are not specific to porphyry mineralization and need to be integrated with data for other PIMs to identify the presence of porphyry mineralization. The chemistry of some PIMs has been subject to recent investigations, some of which are summarized below.

It has been shown that magmatic magnetite versus magnetite of hydrothermal origin can be distinguished based on major element ratios (Al/Ti vs. V/Ti) (Cross 2000). Major element chemistry has been further used to discriminate magnetite arising from a variety of deposit types based on Ti + V vs. Ca + Al + Mn binary diagrams (Dupuis and Beaudoin 2011). Recently there have been significant studies further developing magnetite as an indicator mineral (Dare *et al.* 2014; Nadoll *et al.* 2014; Canil *et al.* 2016; Sievwright 2018). Issues such as diffusional resetting and exsolution lamellae can hinder the use of magnetite as an effective indicator.

Apatite has also been a mineral of interest in porphyry deposits (Bouzari *et al.* 2016; Mao *et al.* 2016). Recent statistical analyses, cathodoluminescence, and mineral chemistry studies on apatite have demonstrated potential in the discrimination of apatite from a variety of magmatic and hydrothermal environments in addition to porphyry sub-types (*i.e.*, Cu-Mo-Au, Mo, and alkalic Cu-Au). The challenge with apatite is that it is not as chemically resistant as other proven indicator minerals (*e.g.*, garnet). Further work at other deposits will be needed to assess the validity of these results.

Epidote is a common hydrothermal alteration phase in porphyry deposits forming in the propylitic zone and is chemically distinct from that forming in other environments (Cooke *et al.* 2014; Xiao *et al.* 2018). For example, it has been shown that trace element concentrations can be used to determine proximity to mineralized porphyry systems, with elevated concentrations of Cu and Sn being indicators of proximal mineralization (Cooke *et al.* 2014, 2017).

Based on the research presented above, there are no physically or chemically robust mineral species that have yet been proven to effectively identify porphyry mineralization, and thus there is a clear need for a robust indicator for mineralized porphyry systems. One mineral group that has been largely overlooked in porphyry systems is TSM. The TSM have characteristics that make them ideal long-term recorder of petrogenetic conditions, including 1) an ability to accommodate a wide range of major-, minor-, and trace-elements, and 2) stable across a range of temperature and pressure conditions, collectively mean that TSM are strong recorders of fluid evolution (including magmatic, magmatic-hydrothermal, and hydrothermal ore-forming fluids).

Its physical characteristics make it a useful indicator mineral in clastic sediments that are routinely collected in mineral exploration programs. Its high hardness (7 on Mohs' scale) and a lack of cleavage indicate its physical ruggedness and ability to withstand glacial erosion and glacial and fluvial transport. Its high degree of stability under most terrestrial geochemical conditions indicates that it can survive pre- and post-glacial weathering. Its moderate to high density (2.8 to max of 3.3) allows it to be readily recovered from sediment samples using common gravity concentration methods and finally is visually distinct from other mid-density indicator minerals. It is therefore essential that the characteristics of the TSM from porphyry mineralization be identified to serve as potential discriminators for TSM found anywhere, including the surficial environment.

1.3 Tourmaline Nomenclature

Tourmaline supergroup minerals have been the focus of research since their earliest description in 1707 (Dietrich 1985). The tourmaline-supergroup (consisting of 38 distinct species) is most well known as a gemstone and is the main reservoir for boron in the Earth's crust (Dutrow and Henry 2011). Hawthorne and Henry (1999) provided a systematic classification of the tourmaline group based on modern-day analytical techniques which were later redefined by Henry *et al.* (2011). This nomenclature is based on the structural formula:

$XY_3Z_6T_6O_{18}(BO_3)_3V_3W$, with $X = Na^+, K^+, Ca^{2+}, \square$ (vacancy); $Y = Al^{3+}, Cr^{3+}, V^{3+}, Fe^{2+/3+}, Mg^{2+}, Mn^{2+}, Li^+, Ti^{4+}$; $Z = Al^{3+}, Cr^{3+}, V^{3+}, Fe^{2+/3+}, Mg^{2+}$; $T = Si^{4+}, Al^{3+}, B^{3+}$; $B = B^{3+}$, $V = (OH)^-, O^{2-}$; $W = (OH)^-, F^-, O^{2-}$ are the common major constituents. The characters in the general formula represent groups of cations including $^{[9]}X$, $^{[6]}Y$, $^{[6]}Z$, $^{[4]}T$, and $^{[3]}B$. The characters V and W represent groups of anions $^{[3]}O3$ and $^{[3]}O1$ sites (Bosi 2018). Tourmaline forms in the trigonal crystal system, lacks a center of symmetry, and is polar which contributes to its piezoelectric and pyroelectric properties (Hawthorne and Dirlam 2011).

There have been numerous studies on the petrogenetic applications of TSM (Kyrynine 1964; Henry and Guidotti 1985; Henry and Dutrow 1992; Henry and Dutrow 1996; van Hinsberg and Schumacher 2006). Early work on sedimentary rocks used TSM morphology and color to identify source rock regions (Kyrynine 1964). The most notable petrogenetic contribution is the Al-Fe_(tot)-Mg ternary to distinguish TSM from different rock types (Henry and Guidotti 1985). More recent work on TSM has been on its occurrence in ore systems (*e.g.*, Slack 1996; Smith and Yardley 1996; Slack 1999; Garofalo *et al.* 2002; Jiang *et al.* 2002; Mlynarczyk and Williams-Jones 2006; Marschall and Jiang 2011; Slack and Trumbull 2011; Codeço *et al.* 2017; Kalliomäki *et al.* 2017; Launay *et al.* 2018; Harlaux *et al.* 2019; Hong *et al.* 2019; Beckett-

Brown *et al.* 2021; Li *et al.* 2021; Sciuba *et al.* 2021). Tourmaline has been reported in numerous ore deposit types (*e.g.*, porphyry Cu-Mo-Au, W-Sn-Cu polymetallic deposits, orogenic gold, VMS, SEDEX, IOCG, uranium deposits, and rare-element pegmatites) and in many cases are directly associated with ore minerals (Slack and Trumbull 2011).

1.4 Tourmaline in Porphyry Deposits

Tourmaline is commonly encountered in mineralized porphyry systems (*e.g.*, Rio Blanco-Los Bronces district - Chile, El Teniente - Chile, and Highland Valley Copper – British Columbia) but is not ubiquitous in its distribution amongst porphyry deposits as it is absent in other significant systems (*e.g.*, Bingham Canyon-United States, Grasberg-Indonesia). Tourmaline is commonly observed in hydrothermal breccias of select porphyry deposits (Sillitoe 2010), and as vein fill and disseminations in more distal regions of deposits (Beckett-Brown *et al.* 2019).

Several studies have directly focused on TSM in porphyry systems (Warnaars *et al.* 1985; Koval *et al.* 1991; Lynch and Ortega 1997; Yavuz *et al.* 1999; Skewes *et al.* 2003; Baksheev *et al.* 2010; Baksheev *et al.* 2012; Dill *et al.* 2012; Bačik *et al.* 2016; Rasekh 2016; Qiao *et al.* 2019; Li *et al.* 2021). Most of this research is deposit-specific, *i.e.*, focused on the TSM from a single deposit, meaning larger inter-deposit studies are lacking. Tourmaline is commonly observed in porphyry breccias, the breccias can additionally be dominated by other minerals such as biotite and quartz (Sillitoe 2010). In the Donoso breccia, Skewes *et al.* (2003) observed that breccias dominated by biotite cement tend to be older and/or occur in deeper portions of the porphyry system than those where TSM forms the cement. Skewes *et al.* (2003) went further and stated that in some cases, biotite and TSM coexist in the matrix with no obvious replacement relationships between these two minerals. Dill *et al.* (2012) investigated depth-related variations of TSM Fe/Mg values in the San Jorge (Argentina) porphyry Cu breccia pipe and concluded that

the overall major-element composition of TSM is rather homogeneous with changes in depth but further suggested that Fe/Mg values could be used to separate barren from mineralized TSM breccias. An investigation of TSM at the Coxheath deposit (Nova Scotia, Canada) indicated that TSM precipitation is strongly influenced by cooling and the activity of $B(OH)_3$, which becomes concentrated during boiling and further suggested that TSM could mark a boiling front in porphyry deposits (Lynch and Ortega 1997). Baksheev *et al.* (2012) outlined five general features of TSM from ten porphyry deposits in Russia and Mongolia including 1) zoning (sector and oscillatory), 2) multiple generations of growth, 3) Fe-Al (oxy-dravite – povondraite solid solution), 4) trend of Fe-rich to Mg-rich which is suggested to reflect sulfide precipitation and 5) low Li concentrations <30 ppm. Additional findings from their study included the ability to differentiate porphyry metal association (*i.e.*, Cu, Au, and Sn) using TSM major element chemistry. For example, TSM from porphyry Cu systems contains ~ 2 apfu Mg, TSM from porphyry gold deposits contains 1-2 apfu Mg, and finally, TSM from porphyry Sn contains 0-1 apfu Mg. Baksheev *et al.* (2012) study thus provides the most significant contribution to understanding the major-element chemistry of TSM from a variety of mineralized porphyry systems.

1.5 Thesis Objectives

The objectives of this thesis were to assess the indicator mineral potential of TSM in porphyry systems. This assessment was completed through the following major research activities:

- 1) Document the spatial distribution of TSM within porphyry systems, ranging from the deposit scale to that on a worldwide basis.

- 2) Constrain the temporal links between TSM, porphyry ore minerals, and alteration assemblages.
- 3) Document the external and internal textures that exist, their variations including color, morphology, grain size, inclusions populations, and chemical zonation.
- 4) Characterize the major, minor, and trace-element chemistry of TSM forming in porphyry systems.
- 5) Investigate TSM from different media including that derived from bedrock as well as recovered from the surficial environment surrounding known porphyry deposits.
- 6) Evaluate the potential for discrimination of TSM in porphyry systems compared to that forming in other environments and ore systems.

1.6 Structure of the Thesis

This thesis is organized into five chapters. Chapters two to five are written as stand-alone manuscripts which will be submitted for peer-reviewed publication. Thus, repetition may exist between chapters in certain areas.

Chapter two is a manuscript entitled “Recognizing tourmaline in mineralized porphyry systems: Part I: textures and major-element chemistry”. This manuscript has been submitted to *The Canadian Mineralogist*. This manuscript provides a holistic description of tourmaline forming in seven separate mineralized porphyry systems. This description has been accomplished through 1) qualifying the spatial distribution of TSM in porphyry systems, ranging from the deposit scale to that in deposits on a worldwide basis, 2) quantifying the temporal links between TSM, porphyry ore minerals and alteration assemblages, 3) documentation of the external and internal textures

that exist, their variations (*i.e.*, morphology, grain size, inclusions populations) and how these potentially correlate with mineralized vs. barren systems, and 4) the major and minor element variations (including chemical zonation).

Chapter three is a manuscript entitled “Recognizing tourmaline in mineralized porphyry systems: Part II: Trace-element characteristics of tourmaline: development and application of discrimination”. This manuscript has been submitted to *Economic Geology*. This manuscript investigates and evaluates the applicability and efficacy of tourmaline trace-element chemistry to identify porphyry Cu (\pm Au, \pm Mo) related tourmaline. Several key elements of porphyry tourmaline trace-elements will be addressed, including 1) elements present, 2) concentrations, 3) their relationship with texture development (internal and external texture, spatial distribution *etc.*), 4) inter/intra deposit variations, and 5) determination of those important trace-element concentrations or ratios having the highest efficacy of distinguishing tourmaline arising in mineralized porphyries from other geologic environments.

Chapter four is a manuscript entitled “Investigation of tourmaline characteristics in bedrock and surficial sediment samples from two Canadian porphyry copper systems”. This manuscript has been published in the Targeted Geoscience Initiative 5: contributions to the understanding and exploration of porphyry deposits, Geological Survey of Canada, Bulletin 616, pp. 109-135.

<https://doi.org/10.4095/327989>. This manuscript investigates and evaluates the applicability and usefulness of tourmaline as an indicator of porphyry copper systems at two sites, Woodjam in British Columbia and Casino in Yukon Territory. These studies examined tourmaline in bedrock as well as in local surficial sediments (stream sediments or till) and provides detailed documentation and comparisons of several key elements in tourmaline. These key factors include 1) chemical zonation and textural features, 2) major- and minor-element chemistry, and 3) trace-

element chemistry. The comparison of tourmaline derived from the different sample media (*i.e.*, surficial and bedrock) is crucial to the evaluation of the effectiveness of tourmaline as an indicator for porphyry deposits.

Chapter five is a manuscript entitled “The missing link between biotite and tourmaline in porphyry systems”. This manuscript is intended for submission to *Canadian Mineralogist*. This manuscript investigates the nature of the relationship between biotite and tourmaline intergrowths in a mineralized porphyry deposit. This has been accomplished through 1) documenting the relationship between biotite and tourmaline, 2) interpretation of internal and external textural relationships of these minerals (including morphology, grain size, inclusions, and internal zonation), and 3) integrating the major and minor element variation between coexisting biotite and tourmaline.

1.7 References

- Averill, S.A., 2011. Viable indicator minerals in surficial sediments for two major base metal deposit types: Ni-Cu-PGE and porphyry Cu. *Geochemistry: Exploration, Environment, Analysis*, 11(4): 279-291. <http://doi.org/10.1144/1467-7873/10-im-022>
- Bačík, P., Koděra, P., Uher, P., Ozdín, D. and Jánošík, M., 2016. Chlorine-Enriched Tourmalines In Hydrothermally Altered Diorite Porphyry From the Biely Vrch Porphyry Gold Deposit (Slovakia). *The Canadian Mineralogist*, 53(4): 673-691. <http://doi.org/10.3749/canmin.1500013>
- Baksheev, I.A., Chitalin, A.F., Yapaskurt, V.O., Vigasina, M.F., Bryzgalov, I.A. and Ustinov, V.I., 2010. Tourmaline in the Vetka porphyry copper-molybdenum deposit of the

Chukchi Peninsula of Russia. *Moscow University Geology Bulletin*, 65(1): 27-38.

<http://doi.org/10.3103/s0145875210010035>

Baksheev, I.A., Yu Prokofev, V., Zاراisky, G.P., Chitalin, A.F., Yapaskurt, V.O., Nikolaev, Y.N., Tikhomirov, P.L., Nagornaya, E.V., Rogacheva, L.I., Gorelikova, N.V. and Kononov, O.V., 2012. Tourmaline as a prospecting guide for the porphyry-style deposits.

European Journal of Mineralogy, 24(6): 957-979. <http://doi.org/10.1127/0935->

[1221/2012/0024-2241](http://doi.org/10.1127/0935-1221/2012/0024-2241)

Beckett-Brown, C.E., McDonald, A.M. and McClenaghan, M.B., 2019. Unravelling tourmaline in mineralized porphyry systems: assessment as a valid indicator mineral, Geological Survey of Canada, Targeted Geoscience Initiative: 2018 report of activities, Open File 8549.

Beckett-Brown, C.E., McDonald, A.M., McClenaghan, M.B., Plouffe, A. and Ferbey, T., 2021. Investigation of tourmaline characteristics in bedrock and surficial sediment samples from two Canadian porphyry copper systems. In: E. Schestelaar and A. Plouffe (Editors), Targeted Geoscience Initiative 5: contributions to the understanding and exploration of porphyry deposits, Geological Survey of Canada, pp. 109-135.

<http://doi.org/10.4095/327989>

Bosi, F., 2018. Tourmaline crystal chemistry. *American Mineralogist*, 103(2): 298-306.

<http://doi.org/10.2138/am-2018-6289>

Bouzari, F., Hart, C.J.R., Bissig, T. and Barker, S., 2016. Hydrothermal Alteration Revealed by Apatite Luminescence and Chemistry: A Potential Indicator Mineral for Exploring

Covered Porphyry Copper Deposits. *Economic Geology*, 111(6): 1397-1410.

<http://doi.org/10.2113/econgeo.111.6.1397>

Canil, D., Grondahl, C., Lacourse, T. and Pisiak, L.K., 2016. Trace elements in magnetite from porphyry Cu–Mo–Au deposits in British Columbia, Canada. *Ore Geology Reviews*, 72: 1116-1128. <http://doi.org/10.1016/j.oregeorev.2015.10.007>

Codeço, M.S., Weis, P., Trumbull, R.B., Pinto, F., Lecumberri-Sanchez, P. and Wilke, F.D.H., 2017. Chemical and boron isotopic composition of hydrothermal tourmaline from the Panasqueira W-Sn-Cu deposit, Portugal. *Chemical Geology*, 468: 1-16.

<http://doi.org/10.1016/j.chemgeo.2017.07.011>

Cooke, D.R., Baker, M., Hollings, P., Sweet, G., Chang, Z.S., Danyushevsky, L., Gilbert, S., Zhou, T., White, N.C., Gemmell, J.B. and Inglis, S., 2014. New Advances in Detecting the Distal Geochemical Footprints of Porphyry Systems—Epidote Mineral Chemistry as a Tool for Vectoring and Fertility Assessments. In: K.D. Kelley and H.C. Golden (Editors), *Building Exploration Capability for the 21st Century*. Society of Economic Geologists, Littleton, Colorado, pp. 127-152.

Cooke, D.R., Agnew, P., Hollings, P., Baker, M., Chang, Z., Wilkinson, J.J., Ahmed, A., White, N.C., Zhang, L., Thompson, J. and Gemmell, J.B., 2020. Recent advances in the application of mineral chemistry to exploration for porphyry copper–gold–molybdenum deposits: detecting the geochemical fingerprints and footprints of hypogene mineralization and alteration. *Geochemistry: Exploration, Environment, Analysis*, 20(2), pp.176-188. <http://doi.org/10.1144/geochem2019-039>

- Cooke, D.R., Agnew, P., Hollings, P., Baker, M., Chang, Z., Wilkinson, J.J., White, N.C., Zhang, L., Thompson, J., Gemmell, J.B., Fox, N., Chen, H., and Wilkinson, C.C., 2017. Porphyry indicator minerals (PIMS) and porphyry vectoring and fertility tools (PVFTS) – indicators of mineralization styles and recorders of hypogene geochemical dispersion haloes, in Tschirhart, V. and Thomas, M.D., ed., Proceedings of Exploration 17: Sixth Decennial International Conference on Mineral Exploration, p. 457–470.
- Cross, A.J., 2000. An investigation of the minor and trace element chemistry of hydrothermal porphyry and skarn-related magnetite, University of Canberra.
- Dare, S.A.S., Barnes, S.-J., Beaudoin, G., Méric, J., Boutroy, E. and Potvin-Doucet, C., 2014. Trace elements in magnetite as petrogenetic indicators. *Mineralium Deposita*, 49(7): 785-796. <http://doi.org/10.1007/s00126-014-0529-0>
- Dietrich, R.V., 1985. The Tourmaline Group. Van Nostrand Reinhold Company, New York. <http://doi.org/10.1007/978-1-4684-8085-6>
- Dill, H.G., Garrido, M.M., Melcher, F., Gomez, M.C. and Luna, L.I., 2012. Depth-related variation of tourmaline in the breccia pipe of the San Jorge porphyry copper deposit, Mendoza, Argentina. *Ore Geology Reviews*, 48: 271-277. <http://doi.org/10.1016/j.oregeorev.2012.04.006>
- Dupuis, C. and Beaudoin, G., 2011. Discriminant diagrams for iron oxide trace element fingerprinting of mineral deposit types. *Mineralium Deposita*, 46.
- Dutrow, B.L. and Henry, D.J., 2011. Tourmaline: A Geologic DVD. *Elements*, 7(5): 301-306. <http://doi.org/10.2113/gselements.7.5.301>

- Garofalo, P., Matthai, S.K. and Heinrich, C.A., 2002. Three-dimensional geometry, ore distribution and time-integrated mass transfer through the quartz-tourmaline-gold vein network of the Sigma deposit (Abitibi belt, Canada). *Geofluids*, 2.
- Harlaux, M., Mercadier, J., Marignac, C., Villeneuve, J., Mouthier, B. and Cuney, M., 2019. Origin of the atypical Puy-les-Vignes W breccia pipe (Massif Central, France) constrained by trace element and boron isotopic composition of tourmaline. *Ore Geology Reviews*, 114. <http://doi.org/10.1016/j.oregeorev.2019.103132>
- Hawthorne, F.C. and Dirlam, D.M., 2011. Tourmaline the Indicator Mineral: From Atomic Arrangement to Viking Navigation. *Elements*, 7(5): 307-312. <http://doi.org/10.2113/gselements.7.5.307>
- Hawthorne, F.C. and Henry, D.J., 1999. Classification of the minerals of the tourmaline group. *European Journal of Mineralogy*, 11.
- Henry, D.J. and Dutrow, B.L., 1992. Tourmaline in a Low-Grade Clastic Metasedimentary Rock - an Example of the Petrogenetic Potential of Tourmaline. *Contributions to Mineralogy and Petrology*, 112(2-3): 203-218. <http://doi.org/10.1007/Bf00310455>
- Henry, D.J. and Dutrow, B.L., 1996. Metamorphic Tourmaline and its petrologic applications. In: L.M. Anovitz and E.S. Grew (Editors), Boron, *Reviews in Mineralogy and Geochemistry*, 33(1), 503-557.
- Henry, D.J. and Guidotti, C.V., 1985. Tourmaline as a petrogenetic indicator mineral an example from the staurolite-grade metapelites of NW Maine. *American Mineralogist*, 70: 1-15.

- Henry, D.J., Novak, M., Hawthorne, F.C., Ertl, A., Dutrow, B.L., Uher, P. and Pezzotta, F., 2011. Nomenclature of the tourmaline-supergroup minerals. *American Mineralogist*, 96(5-6): 895-913. <http://doi.org/10.2138/am.2011.3636>
- Hong, W., Fox, N., Cooke, D.R., Zhang, L. and Fayek, M., 2019. B- and O-isotopic compositions of tourmaline constrain late-stage magmatic volatile exsolution in Tasmanian tin-related granite systems. *Mineralium Deposita*, 55(1): 63-78. <http://doi.org/10.1007/s00126-019-00885-5>
- Jiang, S.Y., Palmer, M.R. and Yeats, C.J., 2002. Chemical and boron isotopic compositions of tourmaline from the Archean Big Bell and Mount Gibson gold deposits, Murchison Province, Yilgarn Craton, Western Australia. *Chemical Geology*, 188(3-4): 229-247. [http://doi.org/10.1016/S0009-2541\(02\)00107-9](http://doi.org/10.1016/S0009-2541(02)00107-9)
- Kalliomäki, H., Wagner, T., Fusswinkel, T. and Sakellaris, G., 2017. Major and trace element geochemistry of tourmalines from Archean orogenic gold deposits: Proxies for the origin of gold mineralizing fluids? *Ore Geology Reviews*, 91: 906-927. <http://doi.org/10.1016/j.oregeorev.2017.08.014>
- Kelley, K.D., Eppinger, R.G., Lang, J., Smith, S.M. and Fey, D.L., 2011. Porphyry Cu indicator minerals in till as an exploration tool: example from the giant Pebble porphyry Cu-Au-Mo deposit, Alaska, USA. *Geochemistry: Exploration, Environment, Analysis*, 11(4): 321-334. <http://doi.org/10.1144/1467-7873/10-im-041>
- Koval, P.V., Zorina, L.D., Kitajev, N.A., Spiridonov, A.M. and Ariunbileg, S., 1991. The Use of Tourmaline in Geochemical Prospecting for Gold and Copper Mineralization. *Journal of*

- Geochemical Exploration*, 40(1-3): 349-360. [http://doi.org/10.1016/0375-6742\(91\)90047-X](http://doi.org/10.1016/0375-6742(91)90047-X)
- Kyrynine, P.D., 1964. The Tourmaline Group in Sediments. *The Journal of Geology*, 54(2), 65-87.
- Launay, G., Sizaret, S., Guillou-Frottier, L., Gloaguen, E. and Pinto, F., 2018. Deciphering fluid flow at the magmatic-hydrothermal transition: A case study from the world-class Panasqueira W–Sn–(Cu) ore deposit (Portugal). *Earth and Planetary Science Letters*, 499: 1-12. <http://doi.org/10.1016/j.epsl.2018.07.012>
- Li, W., Qiao, X., Zhang, F. and Zhang, L., 2021. Tourmaline as a potential mineral for exploring porphyry deposits: a case study of the Bilihe gold deposit in Inner Mongolia, China. *Mineralium Deposita*: 1-22. <http://doi.org/10.1007/s00126-021-01051-6>
- Lynch, G. and Ortega, S., 1997. Hydrothermal alteration and tourmaline-albite equilibria at the Coxheath porphyry Cu-Mo-Au deposit, Nova Scotia. *Canadian Mineralogist*, 35(1): 79-94.
- Mao, M., Rukhlov, A.S., Rowins, S.M., Spence, J. and Coogan, L.A., 2016. Apatite Trace Element Compositions: A Robust New Tool for Mineral Exploration. *Economic Geology*, 111(5): 1187-1222. <http://doi.org/10.2113/econgeo.111.5.1187>
- Marschall, H.R. and Jiang, S.Y., 2011. Tourmaline Isotopes: No Element Left Behind. *Elements*, 7(5): 313-319. <http://doi.org/10.2113/gselements.7.5.313>
- McClenaghan, M.B., 2005. Indicator mineral methods in mineral exploration. *Geochemistry-Exploration Environment Analysis*, 5: 233-245. <http://doi.org/10.1144/1467-7873/03-066>

- McClenaghan, M.B., and Kjarsgaard, B.A. 2007. Indicator mineral and surficial geochemical exploration methods for kimberlite in glaciated terrain: Examples from Canada. In: W.D. Goodfellow (Ed.), *Mineral Deposits of Canada: A Synthesis of Major Deposit-Types, District Metallogeny, the Evolution of Geological Provinces, and Exploration Methods*. Geological Association of Canada, Mineral Deposits Division, Special Publication No. 5, pp. 983-1006.
- Mlynarczyk, M.S.J. and Williams-Jones, A.E., 2006. Zoned tourmaline associated with cassiterite Implications for fluid evolution and tin mineralization. *The Canadian Mineralogist*, 44: 347-365.
- Muggeridge, M.T. 1995. Pathfinder sampling techniques for location primary sources of diamond: recovery of indicator minerals, diamonds and geochemical signatures. *Journal of Geochemical Exploration*, 53: 183-204.
- Nadoll, P., Angerer, T., Mauk, J.L., French, D. and Walshe, J., 2014. The chemistry of hydrothermal magnetite: A review. *Ore Geology Reviews*, 61: 1-32.
<http://doi.org/10.1016/j.oregeorev.2013.12.013>
- Nowicki, T.E., Moore, R.O., Gurney, J.J. and Baumgartner, M.C. 2007. Diamonds and associated heavy minerals in kimberlite: a review of key concepts and applications. *Developments in Sedimentology*, 58: 1235-1267. [https://doi.org/10.1016/s0070-4571\(07\)58046-5](https://doi.org/10.1016/s0070-4571(07)58046-5)
- Qiao, X., Li, W., Zhang, L., White, N.C., Zhang, F. and Yao, Z., 2019. Chemical and boron isotope compositions of tourmaline in the Hadamiao porphyry gold deposit, Inner

- Mongolia, China. *Chemical Geology*, 519: 39-55.
<http://doi.org/10.1016/j.chemgeo.2019.04.029>
- Rasekh, P.M., M. and Esfahani, M.M, 2016. Origin and Chemical Characteristics of Tourmaline in Kahang Porphyry Copper Deposit, NE Isfahan, Central Province of Iran. *Iran Conference*.
- Sciuba, M., Beaudoin, G. and Makvandi, S., 2021. Chemical composition of tourmaline in orogenic gold deposits. *Mineralium Deposita*, 56(3): 537-560.
<http://doi.org/10.1007/s00126-020-00981-x>
- Siewwright, R., 2018. Developing magnetite chemistry as an exploration tool for porphyry copper deposits; Ph.D. thesis, Imperial College London, 340 p.
- Sillitoe, R.H., 2010. Porphyry copper systems. *Economic Geology*, 105(1): 3-41.
<http://doi.org/0.2113/gsecongeo.105.1.3>
- Sinclair, W.D., 2007. Porphyry deposits. In: W.D. Goodfellow (Editor), *Mineral Deposits of Canada: A Synthesis of Major Deposit-Types, District Metallogeny, the Evolution of Geological Provinces, and Exploration Methods*: Geological Association of Canada, Mineral Deposits Division, Special Publication, 5: 223-243.
- Skewes, M.A., Holmgren, C. and Stern, C.R., 2003. The Donoso copper-rich, tourmaline-bearing breccia pipe in central Chile: petrologic, fluid inclusion and stable isotope evidence for an origin from magmatic fluids. *Mineralium Deposita*, 38(1): 2-21.
<http://doi.org/10.1007/s00126-002-0264-9>
- Slack, J.F., 1996. Tourmaline Associations with Hydrothermal Ore Deposits. In: L.M. Anovitz and E.S. Grew (Editors), *Boron. Reviews in Mineralogy and Geochemistry*.

Mineralogical Society of America, Oak Ridge, Tennessee, USA, pp. 559-644.

<http://doi.org/10.1515/9781501509223-013>

Slack, J.F. and Trumbull, R.B., 2011. Tourmaline as a Recorder of Ore-Forming Processes.

Elements, 7(5): 321-326. <http://doi.org/10.2113/gselements.7.5.321>

Slack, J.F.R., A.R.; Griffin, W.L.; Win, T. T.; French D. H.; Ryan, C. G., 1999. Trace Elements in Tourmaline from the Kidd Creek Massive Sulfide Deposit and Vicinity, Timmins, Ontario A Proton Microprobe Study, The Giant Kidd Creek Volcanogenic Massive Sulfide Deposit, Western Abitibi Subprovince, Canada. *Economic Geology Monograph*, pp. 415-429. <http://doi.org/10.5382/mono.10.16>

Smith, M.P. and Yardley, W.D., 1996. The boron isotopic composition of tourmaline as a guide to fluid processes in the southwestern England orefield: An ion microprobe study.

Geochemica et Cosmochimica Acta, 8, 1415-1427. [https://doi.org/10.1016/0016-7037\(96\)00007-5](https://doi.org/10.1016/0016-7037(96)00007-5)

van Hinsberg, V.J. and Schumacher, J.C., 2006. Intersector element partitioning in tourmaline: a potentially powerful single crystal thermometer. *Contributions to Mineralogy and Petrology*, 153(3): 289-301. <http://doi.org/10.1007/s00410-006-0147-7>

Warnaars, F.W., Holmgren, C. and Barassi, S., 1985. Porphyry Copper and Tourmaline Breccias at Los-Bronces-Rio-Blanco, Chile. *Economic Geology*, 80(6): 1544-1565.

<http://doi.org/10.2113/gsecongeo.80.6.1544>

Xiao, B., Chen, H., Wang, Y., Han, J., Xu, C. and Yang, J., 2018. Chlorite and epidote chemistry of the Yandong Cu deposit, NW China: Metallogenic and exploration implications for

Paleozoic porphyry Cu systems in the Eastern Tianshan. *Ore Geology Reviews*, 100: 168-182. <http://doi.org/10.1016/j.oregeorev.2017.03.004>

Yavuz, F., Iskenderoglu, A. and Jiang, S.Y., 1999. Tourmaline compositions from the Salikvan porphyry Cu-Mo deposit and vicinity, northeastern Turkey. *Canadian Mineralogist*, 37: 1007-1023.

Chapter 2

2 Recognizing tourmaline in mineralized porphyry systems Part I: textures and major-element chemistry

2.1 Abstract

Samples of tourmaline supergroup minerals (TSM) from seven mineralized porphyry systems (Cu, ±Au, ±Mo) including Casino (Yukon Territory, Canada), Coxheath (Nova Scotia, Canada), Donoso Breccia-Los Bronces (Chile), Highland Valley Copper (British Columbia, Canada), New Afton (British Columbia, Canada), Schaft Creek (British Columbia, Canada), and Woodjam (British Columbia, Canada) were examined at a variety of scales to evaluate their relationships with mineralization. Data from paragenetic observations show that TSM are generally an early hydrothermal mineral that predates both mineralization and alteration (*e.g.*, overgrown and crosscut by). In general, TSM occur as sub- to euhedral crystals that are black in hand sample and can be found in a variety of mineralized settings (including breccias, veins, and disseminations) and alteration assemblages (including potassic, sodic-calcic, phyllic, propylitic, and argillic). As TSM are resilient and occur throughout a given porphyry system they are comprehensive recorders of the type and extent of various geochemical processes that exist during the complex genesis of these systems. Data from BSE imaging shows two primary zonation types, concentric, and sector. These are interpreted to reflect conditions of rapid crystallization and disequilibrium. Results from SEM-EDS analyses show that most TSM are dravite (~80 % of grains), with the remainder being primarily classified as schorl. Porphyry TSM exhibits remarkably consistent ~2.0 *apfu* Mg values (range: 0.69 – 2.89) with the majority of TSM plotting along the oxy-dravite – povondraite trend, reflecting the predominance of the

$\text{Al}^{3+} \leftrightarrow \text{Fe}^{3+}$ substitution at constant Mg values. This pattern starts from the povondraite side (reflecting the oxidizing nature of early porphyry mineralizing fluids) and trends towards oxydravite as a porphyry system evolves, a feature that can, in turn, be interpreted to reflect relative emplacement depths. In mineralized porphyry systems, TSM exhibit remarkably similar physical and chemical characteristics among the systems examined suggesting the source and geological processes must be extraordinarily similar. Unfortunately, these characteristics are not solely unique to porphyry systems and such observations should be integrated with additional data such as trace-element mineral chemistry to effectively discriminate TSM that have formed in porphyry systems.

2.2 Introduction

Tourmaline supergroup minerals (TSM) are common accessories in many geological environments and deposit types (Henry and Guidotti 1985; Slack 1996; Slack and Trumbull 2011). The major, minor, trace, and isotopic features of TSM have been widely used as indicators of the primary environments of TSM formation, primarily owing to the wide variation in elements that may be accommodated (Henry and Guidotti 1985; Bosi and Lucchesi 2004; Bosi and Lucchesi 2007; Marschall and Jiang 2011). In general, TSM occur in many hydrothermal deposits worldwide including volcanogenic massive sulfide (VMS), sediment-hosted base metal, orogenic gold, Sn-W, porphyry Cu-Mo-Au, and emerald mineralization (Clarke *et al.* 1989; Slack and Coad 1989; Slack 1993; Griffin *et al.* 1996; Jiang *et al.* 1996; Slack 1996; Yavuz *et al.* 1999; Frikken *et al.* 2005; Galbraith *et al.* 2009; Baksheev *et al.* 2010; Baksheev *et al.* 2011; Slack and Trumbull 2011; Baksheev *et al.* 2012; Baksheev *et al.* 2017; Kalliomäki *et al.* 2017; Launay *et al.* 2018; Manéglija *et al.* 2018; Codeço *et al.* 2019; Byrne *et al.* 2020; Codeço *et al.* 2020; Sciuba *et al.* 2021). Although several mineral groups have been evaluated as potential

indicators of mineralized porphyry systems (e.g., apatite, epidote, and chlorite group minerals; Ahmed *et al.* 2020; Baker *et al.* 2020; Cooke *et al.* 2020a; Cooke *et al.* 2020c; Pacey *et al.* 2020; Wilkinson *et al.* 2020), holistic studies of TSM in a similar manner have not been conducted to date. The study described herein is focused on mineralized porphyry-type settings, and builds upon the approaches, data sets, and interpretations made through allied studies, while also comparing and contrasting the features of porphyry TSM to that forming in other deposits as well as in unmineralized environments.

The TSM are a common but not entirely ubiquitous accessory phase in both barren and mineralized porphyry systems, although their origin and genetic significance in these systems are not entirely understood. Importantly, TSM form in some of the world's most prolific and notable porphyry deposits including Los Bronces – Rio Blanco district-Chile, El Teniente-Chile, Highland Valley Copper-Canada, Cadia District-Australia, and Yerington District-United States. Detailed understanding and documentation of the occurrence of TSM in mineralized porphyry systems are thus key to evaluating their roles in the formation of mineralized porphyry systems as well as to document and evaluate those features and variations that may exist. The purpose of the current study is to investigate and evaluate the applicability and efficacy of TSM as indicators for porphyry-style mineralization. This has been accomplished through: 1) qualifying the spatial distribution of TSM in porphyry systems, ranging from the deposit scale to that in deposits on a worldwide basis, 2) quantifying the temporal links between TSM, porphyry ore minerals and alteration assemblages, 3) documentation of the external and internal textures that exist, their variations (*i.e.*, morphology, grain size, inclusions populations), and 4) the major and minor element variations (including chemical zonation). The trace-element concentrations of TSM and their relevance is presented in a companion study (Chapter 3). The integration of these

data from the numerous deposits considered in this study will provide a baseline as well as a reference for TSM found in porphyry systems but also aid in guiding indicator mineral exploration studies.

2.3 Tourmaline in Porphyry Systems: Background

Studies of TSM from mineralized porphyry systems have been to-date, deposit-specific, sporadic, and have generally lacked a comprehensive overview of how these minerals integrate into the genesis and evolution of these systems. A detailed review of TSM in porphyry systems is absent in the literature and as such, is summarized here.

2.3.1 Occurrences and Textures

Of roughly 550 porphyry systems worldwide (using the USGS porphyry Cu database; Singer *et al.* 2008), nearly 30% are reported to contain TSM (Figure 2-1). Notable deposits that contain significant concentrations of TSM include the Los Bronces-Rio Blanco district and El Teniente. Importantly, TSM breccias at the Los Bronces-Rio Blanco deposit have been empirically considered to be the most favorable host for mineralization due to the porosity and open space created by radiating TSM crystals (Warnaars *et al.* 1985). Paragenetically, TSM were identified as the first hydrothermal mineral to crystallize in the breccia matrix (Skewes *et al.* 2003) and a transition from a biotite cement upward into a TSM cement and finally into a quartz-sericite-TSM cement has been noted at the Sur-Sur breccia Rio Blanco – Los Bronces, Chile (Frikken *et al.* 2005). At El Teniente, TSM-cemented breccias are observed, having been generated by the exsolution of magmatic fluids and TSM are also found in later veins (Skewes *et al.* 2002). At this locality, TSM occur as black fracture coatings and veinlets with sharp borders, while in the breccias, they occur as replacements of wall rock fragments (also black), or in some cases,

replacing plagioclase feldspars (Skewes *et al.* 2002). At El Teniente, TSM are found in variable amounts throughout the numerous breccias but are most abundant in the “tourmaline-breccia” (Vry *et al.* 2010). Veins of TSM commonly cut early *A*-veins (defined as early sinuous quartz \pm bornite or chalcopyrite following the nomenclature of Sillitoe (2010); and references therein) but definitive relationships with later vein types are unclear (Gustafson and Hunt 1975). Some *B*-type veins are also reported to commonly contain TSM (Gustafson and Hunt 1975). Molybdenite rarely occurs in close proximity to TSM and most TSM veins do not exhibit sulfide or alteration halos nor is TSM present in late pyritic veins (Gustafson and Hunt 1975). Little is known about the vertical zonation of TSM in a given porphyry. At the El Salvador deposit (Chile) vertical zoning of TSM is strong with rare TSM veins on the 2400 ft level and an increase in abundance of both TSM-veins and disseminations towards the surface where TSM are abundant and widespread as well as reportedly contemporaneous with sulfides (Gustafson and Hunt 1975).

2.3.2 TSM Species and Major-Element Variations

Major and minor element variations of TSM are dependent on a myriad of factors including (but not limited to) fluid/melt composition (Trumbull *et al.* 2011), nature of co-crystallizing minerals (Taylor 1984; Taylor 1999), *P-T* conditions (van Hinsberg *et al.* 2011), oxygen fugacity (van Hinsberg *et al.* 2011), and crystal structure constraints (Bosi 2018). Therefore, the only way to completely understand the variation in the overall elemental composition of TSM is to holistically understand the interplay amongst the inter- and intra-variables that are in operation during (in the simplest case) crystallization. However, it must also be appreciated that recognizing the most important factors influencing the chemical composition of a TSM may be recognized, as these are in effect, encapsulated within said TSM. For example, processes including oxidation (*i.e.*, through examination of the redox-sensitive elements, *e.g.*, $\text{Fe}^{2+}/\text{Fe}^{3+}$),

fractionation (variations in $Mg\#$), alteration (changes in alkali content), *etc.*, can all be investigated through examination of the variations in the chemical composition of TSM. Further, the potential use of such chemical variations to discriminate between TSM arising in differing environments of formation becomes an important, feasible outcome and it is this latter aspect, specifically with respect to those characteristics of TSM from mineralized porphyry systems, that serve as the locus of this present study.

The most comprehensive study of major-element chemistry of TSM is from seven mineralized porphyry Cu systems in Russia (Baksheev *et al.* 2012). Results from their study demonstrated that TSM from porphyry systems generally follows a Fe-Mg trend, initially being Fe-rich. They also noted the common occurrence of $Fe^{3+} \leftrightarrow Al^{3+}$ coupled substitution, leading to the development of an oxy-dravite $[Na(MgAl_2)MgAl_5(Si_6O_{18})(BO_3)_3(OH)_3O]$ to povondraite $[NaFe^{3+}_3(Mg_2Fe^{3+}_4)(Si_6O_{18})(BO_3)_3(OH)_3O]$ trend (here in referred to as “O-P trend”) which suggests the presence of Fe^{3+} (also identified by $Fe^{3+}_{(calc)}$ and confirmed by Mössbauer). This chemical trend is directly relevant to understanding the evolving chemistry of TSM, in that it points towards the role of oxidation in the evolving chemistry of TSM. The calculated Mg contents were found to be variable amongst the differing types of mineralized porphyry systems: in those strictly considered as being Cu-dominant, the TSM have ~ 2 Mg *apfu*, while those that are considered to be Au-porphyrines have a lesser amount (1-2 Mg *apfu*) and those that are Sn-porphyrines have even lesser amounts (0-1 Mg *apfu*) (Baksheev *et al.* 2012). Tourmaline from the Coxheath porphyry deposit (NS-Canada) is restricted to regions of sodic alteration that overprints potassic alteration and conforms to the O-P trend (Lynch and Ortega 1997). It has also been suggested that the TSM demarcate the boiling front in that system (Lynch and Ortega 1997). Variations in TSM major-element chemistry as a function of depth was investigated at the

San Jorge porphyry Cu deposit, Argentina (Dill *et al.* 2012). It was determined that the overall composition of TSM was homogeneous over a 100 m interval but with TSM from so-called fertile breccias showing stronger Fe-Mg correlations ($R^2 > 0.8$) than those from barren breccias (Dill *et al.* 2012). Results from an examination of TSM from the Hadamio porphyry Au deposit (China) showed the existence of two broad groups of TSM, which were proposed to be related to magmatic and hydrothermal processes (Qiao *et al.* 2019). Those TSM associated with the magmatic stage of formation occur in the matrix of granite porphyry dikes as disseminated dark brown anhedral grains whereas those associated with the hydrothermal stage TSM form veins of euhedral radiating aggregates (Qiao *et al.* 2019). In terms of major element chemistry, both TSM types classify as schorl-dravite with the hydrothermal grains having lower Ca and higher Vac components (0.094 and 0.206 *avg. apfu* respectively) than the magmatic (0.089 and 0.245 *avg. apfu* respectively) TSM (Qiao *et al.* 2019).

2.4 Tourmaline Systems Examined in This Study

This study examined TSM from seven mineralized porphyry systems: Casino (Yukon Territory, Canada), Coxheath (Nova Scotia, Canada), Donoso Breccia (Rio-Blanco – Los Bronces, Chile), Highland Valley Copper (British Columbia, Canada), New Afton (British Columbia, Canada), Schaft Creek (British Columbia, Canada), and Woodjam (British Columbia, Canada). These deposits were selected to cover a diverse range in mineralization type (Cu, Cu-Au, Cu-Au-Mo) as well as varying age, host lithology, porphyry classification (calc-alkalic and alkalic), associated alteration, and tectonic setting (Table 2-1). Host rocks of calc-alkaline affinity vary from diorite (Coxheath) to granodiorite (Highland Valley Copper), with one deposit of alkaline affinity hosted in a monzonite (New Afton). Ages range from Miocene to Triassic, with one deposit from the Precambrian being included (Coxheath). As TSM are found to occur in a variety

of alteration environments, samples were selected to include potassic (*e.g.*, biotite, K-feldspar), phyllic (*e.g.*, quartz, sericite), sodic-calcic (*e.g.*, albite, actinolite, magnetite), propylitic (*e.g.*, chlorite, epidote, albite, carbonate), and argillic (*e.g.*, quartz, alunite, clays) (Figure 2-2). Unfortunately, TSM are not observed in all alteration styles at a single porphyry deposit. Samples of TSM are investigated from ore zones as well as zones of alteration, barren of mineralization.

2.4.1 Specific Systems Examined

2.4.1.1 *Casino (Yukon Territory, Canada)*

The Casino deposit located ~300 km NW of Whitehorse, Yukon Territory, Canada is a calc-alkaline porphyry hosted in Late Cretaceous quartz monzonite and associated breccias (Casselman and Brown 2017). It is unique among Canadian deposits in having a relatively well-preserved leached cap and supergene oxide zone which overlie hypogene mineralization (Casselman and Brown 2017). Tourmaline at the Casino deposit is relatively widespread and was first noted at Casino by Godwin (1975) who observed it in potassic and phyllic alteration zones. Godwin (1975) also produced a contour diagram based on the observed modal mineralogy which empirically demonstrated a correlation between TSM and Fe-oxides (magnetite/hematite), with the highest concentration of TSM in the core of the deposit and decreasing away from the core (their fig. 3.10; Godwin 1975). Breccias with TSM cement are also observed at Casino. These are found at the contact between the older Dawson Range Batholith and the Casino Suite rocks that are the primary ore host and are interpreted to be products of late-stage hydrothermal activity (Bower *et al.* 1995; Casselman and Brown 2017). The Casino Suite rocks consist of the Patton Porphyry (porphyritic plagioclase intrusive of rhyodacite composition) and associated

breccias (Bower *et al.* 1995; Casselman and Brown 2017). The most common historic report of TSM is in *D*-veins (late quartz-pyrite \pm chalcopyrite veins with feldspar-destructive alteration selvages), followed by disseminated TSM in zones of phyllic alteration (Bower *et al.* 1995). A review of drill logs, conducted in this study, shows that TSM is noted throughout the current deposit outline (including in the leached cap, oxide supergene, and hypogene zones), but is also present in areas distal to the deposit, where mineralization is absent. In hand sample, TSM form as small mm-scale black radiating prismatic grains as disseminations, in veins, and as a breccia cement. Under transmitted light, grains show a range in colors from blue-green to brown and in some cases colorless. Grains commonly occur in clusters or aggregates, more rarely as individual grains.

2.4.1.2 Coxheath (Nova Scotia, Canada)

The Coxheath deposit is located in Nova Scotia, Canada (Kontak *et al.* 2001). This deposit of calc-alkaline affinity is hosted in a hornblende diorite of Precambrian age (621 Ma) and is characterized by Cu-Mo-Au mineralization (Lynch and Ortega 1997). Results from previous studies show that TSM are largely restricted to the diorite host and occur in veins that create a stockwork associated with albite, which defines a zone of sodic alteration that overlaps the central potassic alteration (Lynch and Ortega 1997; Kontak *et al.* 2001). In these zones of sodic alteration, quartz, TSM, and albite occur with accessory muscovite, chlorite, and epidote. Rarely, TSM are also found as a replacement mineral in samples of wall rock (Kontak *et al.* 2001). The TSM is spatially associated with sulfide minerals and is thought to have formed synchronously with them (Lynch and Ortega 1997; Kontak *et al.* 2001). The TSM are massive in hand sample and black in color and can be found as a breccia cement or vein infillings within sodic alteration zones that overlap with potassic alteration. Some late propylitic alteration crosscuts TSM, which

supports the early paragenesis of TSM. Under transmitted light TSM are sub to euhedral and form clots of interlocking crystals that are strongly pleochroic from light brown to green with some grains also being blueish under plain polarized light.

2.4.1.3 Donoso Breccia – Rio Blanco-Los Bronces District (Chile)

The Donoso breccia is found within the Rio Blanco-Los Bronces copper district that is located in the Andes of central Chile and represents one of the world's most prolific porphyry districts (Warnaars *et al.* 1985). Both barren and mineralized breccias are found in the district (Skewes *et al.* 2003), but those containing TSM or biotite are empirically observed to be associated with most of the copper mineralization. Tourmaline is observed to paragenetically be the earliest mineral to crystallize in the breccias (Skewes *et al.* 2003). Other significant matrix minerals include quartz, chalcopyrite, bornite, hematite *var.* specularite, and minor anhydrite (Skewes *et al.* 2003). The Donoso breccia pipe (late Miocene to early Pliocene age) is the youngest of the more than 15 mineralized breccias in the region (Warnaars *et al.* 1985; Skewes *et al.* 2003). The TSM are dark brown acicular crystals with Fe/Mg ratios between 1.2 and 2.4 (Skewes *et al.* 2003). In some cases, there is also evidence for TSM replacing primary mafic minerals (*e.g.*, biotite and hornblende; Skewes *et al.* 2003). The TSM from the Donoso breccia, examined in this study, forms as a black (not brown as previous authors have stated) fine-grained breccia cement along with quartz and sulfides. The breccias occur within phyllic alteration zones of the deposit with TSM grains forming as euhedral radiating clots and are overgrown by sulfides.

2.4.1.4 Highland Valley Copper (British Columbia, Canada)

The Highland Valley Copper (HVC) district is located 65 km southwest of Kamloops, British Columbia (Byrne *et al.* 2020). It consists of five major deposits, hosted in the Late Triassic calc-

alkaline Guichon Creek batholith: Bethlehem, Highmont, J.A., Lornex, and Valley, all of which have been reported to contain TSM (McMillan and Panteleyev 1988). In the HVC district, TSM generally occur in mineralized (chalcopyrite) and unmineralized veins (with K-feldspar, white mica, chlorite, and sometimes epidote, surrounded by albite alteration halos), as well as TSM cemented breccias with albite-altered clasts (Byrne 2019). The TSM are found primarily associated with Na-Ca alteration and more rarely in phyllic alteration zones. Associated minerals include quartz, hematite *var.* specularite, epidote, calcite, and copper sulfides (McMillan and Panteleyev 1988). The TSM in these deposits are considered to be genetically syn- to post-ore formation, based on the occurrence of TSM breccias containing mineralized clasts (McMillan and Panteleyev 1988). The highest concentrations of TSM have been noted at the Bethlehem and Highmont deposits, where they occur in and around breccia bodies, replacing clasts and as breccia cements (McMillan and Panteleyev 1988). At Bethlehem, TSM are widespread but erratic in distribution (Briskey and Bellamy 1976). They are present within and adjacent to all the ore zones including quartz-rich breccias (Briskey and Bellamy 1976). Two samples are investigated, one from the Highmont pit and the other from the Bethlehem pit. In the hydrothermal breccia at the Highmont deposit, TSM forms as a black breccia cement with quartz and hematite. This breccia overprints and is crosscut by sulfide mineralization (Reed and Jambor 1976). Sodic alteration, in the form of albite, is prevalent. Grains of TSM are small (~50 x 500 μm) sub- to euhedral and form radiating masses of pleochroic blue-green to brown grains. The material from the Iona pit (a subset of the Bethlehem pit) contains TSM that are small (~50 x 200 μm), sub- to euhedral and form radiating masses of pleochroic green to brown grains.

2.4.1.5 New Afton (British Columbia, Canada)

The New Afton Cu-Au deposit is located 13 km west of Kamloops, British Columbia (Kwong 1981). It is a silica-saturated alkalic deposit hosted by the Late Triassic Iron Mask batholith. The TSM have been reported in the historic Afton pit (613-640 m level) in association with siderite, prehnite, and magnetite (Kwong 1981). Kwong (1981) stated that TSM only occur in areas adjacent to intense carbonate alteration. While TSM are generally considered accessory minerals, little detail has been paid to the presence of TSM here and it may be more common than what is currently reported (D. Wade, *pers comm* 2019). In this current study, samples of TSM were obtained from both the center of the phyllic zone, and the inner phyllic zone, located near the boundary with the potassic zone. At New Afton, TSM are massive black grains in hand sample that form vein fill and as a breccia cement. In transmitted light, subhedral grains are green to light brown and weakly pleochroic. In some TSM samples, grains are broken while others appear dissolved and replaced by carbonate (dolomite). Grains are overgrown by pyrite, suggesting the TSM are paragenetically earlier.

2.4.1.6 Schaft Creek (British Columbia, Canada)

The Schaft Creek deposit is located in northwestern British Columbia (Scott *et al.* 2008). It is a calc-alkaline porphyry Cu-Mo-(Au) deposit hosted by late Triassic volcanics (Stuhini Group-Stikine Terrane) and is associated with the Hickman batholith and associated porphyritic granodiorite dikes. The abundance of TSM is minor in the Main and Paramount zones but it is slightly more abundant in the West Breccia zone (Scott *et al.* 2008). In the Main zone TSM are observed as discrete disseminated grains, while the West zone mineralization comprises sericite-chlorite altered brecciated volcanics cemented by TSM-quartz-carbonate \pm sulfate \pm chalcopryrite \pm pyrite. The TSM are associated with several alteration styles including potassic,

sericite/chlorite, and propylitic. Samples of TSM are investigated from the central Paramount zone where they occur as massive black grains in hand sample as disseminations, vein fill, and breccia cement. In transmitted light, grains are prismatic and sub- to euhedral and pleochroic showing a range of colors including brown, green, and blue.

2.4.1.7 Woodjam (British Columbia, Canada)

The Woodjam deposits are a cluster of porphyries located ~50 km east-northeast of Williams Lake (del Real *et al.* 2017). They include five Mesozoic-aged, high K monzonite porphyries with calc-alkaline affinities: the Southeast Zone, Deerhorn (DH), Megabuck, Takom (TK), and Three Firs. Deerhorn (Au-Cu) and Takom (Cu-Au) have characteristics of high K calc-alkalic intrusions (del Real *et al.* 2017). The only deposits that contain TSM are DH and TK, and samples from both were examined. At Deerhorn, TSM are observed in syn- to post-ore Py-Qz-Chl±Hem±TSM veins with distinctive white halos dominated by illite (del Real *et al.* 2017). At Deerhorn, TSM are found intergrown and overprinting potassic alteration associated with minor chalcopyrite mineralization. In the Nicola Group volcanic rocks, which overly the Takom deposit, a texturally destructive TSM-albite-epidote alteration is present. Tourmaline-cemented breccias occur in the mineralized upper portion of the Takom porphyry forming in quartz-TSM-pyrite veins with albite alteration halos. In hand sample, TSM are black whereas in transmitted light they are pleochroic green-brown and more rarely blue in color. Grains are sub- to euhedral radiating prismatic crystals, sometimes replacing (occasionally, pseudomorphously) primary magmatic feldspars. Paragenetically, TSM are early, as evidenced by crosscutting relationships with alteration assemblages and their presence as inclusions within sulfides (*i.e.*, pyrite and chalcopyrite).

2.5 Methods

2.5.1 Major and Minor Element Chemistry

Chemical analyses (major and minor elements) of 2896 points from ~750 individual TSM grains in 29 different bedrock samples were conducted by scanning electron microscopy energy-dispersive spectroscopy (SEM-EDS) on a JEOL 6400 in the MicroAnalytical Centre at Laurentian University. Operating conditions include an accelerating voltage of 20 kV, a beam current of 1.0 nA, and count times of 30 seconds. Data were processed using Aztec software. The primary standards used included well-characterized materials: diopside ($MgK\alpha$, $CaK\alpha$, $SiK\alpha$), albite ($AlK\alpha$, $NaK\alpha$), chalcopyrite ($FeK\alpha$), and $CaTiO_3$ *syn* ($TiK\alpha$). Elements commonly occurring in low concentrations in TSM, including K, Mn, V, Zn, F (unreliable due to $FeL\alpha$ - $FK\alpha$ overlap), and Cl were rarely observed above the limit of detection (<0.1 wt. %) and are not reported here. Chemical data were reduced to *apfu* based on 15 cations using the program *WinTcac* (Yavuz *et al.* 2014). Values of Fe^{2+}/Fe^{3+} were calculated using the same software using a charge balance approach. Analyses were conducted on TSM grains oriented parallel to the *c*-axis, given the propensity of the mineral to develop complex chemical zonation about this axis.

2.6 Results

2.6.1 Tourmaline physical and optical characteristics

The TSM from the porphyries in this study exhibit a wide range of colors, sizes, morphology, textures, zonation, mineral associations, and inclusions. A summary of these features is presented in Table 2-2. Constraining the timing of TSM in relation to sulfides and alteration assemblages is critical in unravelling the significance of TSM physical and chemical characteristics in

mineralized porphyry systems. Sulfides are commonly found overgrowing prismatic to acicular sub- to euhedral TSM crystals suggesting sulfides are post TSM formation (Figure 2-3). In all porphyry deposits examined in this study, TSM in general forms paragenetically earlier than the associated mineralization and alteration. Development of later generations of TSM has been observed in some deposits, it is rare and is generally the result of recrystallization/dissolution-reprecipitation of pre-existing TSM.

2.6.1.1 Color (hand sample and optical microscopy)

Macroscopically, TSM ubiquitously occur as black masses in hand sample. In rare cases, TSM can be colorless, but only when viewed perpendicular to the *c*-axis using a binocular microscope. While TSM color can show a wide-range in hand sample (blue, green, red, pink, yellow, *etc.*), those examined in this study do not show any of these other colors, a situation quite different for many TSM developing in felsic pegmatite environments (Hawthorne and Dirlam 2011). The strong coloration (black) of TSM from porphyry systems reflects the predominance of Fe and Mg. Under plane-polarized light, the TSM are pleochroic and exhibit a range of colors, most commonly green to brown and blue although more rarely, they can be colorless and non-pleochroic. Grains also exhibit core-rim zonation that is most dominantly defined (looking at a cross-section perpendicular to the *c*-axis) by shades of green and more rarely brown, blue, and colorless. A range of zonation types exist with general abundance decreasing in the order concentric > sector > patchy/irregular > overgrowth/replacement, with these features best observed under backscattered electron imaging (BSEI). The concentric zonation exhibits sharp boundaries between distinct color zones and very rarely shows gradational boundaries between zones. No identifiable patterns amongst samples and deposits of core-rim zonation from transmitted light color could be discerned. Grains are observed forming with light green to

colorless cores which sharply transition to green zones and back to lighter green rims, while other grains (in some cases in the same sample) exhibit dark green to brownish cores and sharply transition to green rims.

2.6.1.2 Individual grains: Size, morphology, and occurrence

In hand sample, TGM typically occur as radiating aggregates of fine-grained sub- to euhedral crystals (μm scale), and more rarely as coarse grains (mm scale). The TSM develop in three, distinct textural styles within a porphyry system, including breccias, veins, and disseminations (Figure 2-4). In breccias, TSM develop in the matrix, cementing wall-rock breccia fragments (Figure 2-4a-e). It is also quite common to observe both quartz and sulfides (*i.e.*, chalcopyrite and pyrite) in the matrix, but these post-date the TSM. The TSM in vein-style TSM (Figure 2-4f-j) are the smallest, typically $\sim 20 \mu\text{m}$ in diameter and rarely $>100 \mu\text{m}$. The veins are mineralogically simple, containing TSM with quartz and sulfides (*i.e.*, pyrite and chalcopyrite), although other minerals (*e.g.*, epidote, apatite, and calcite) may also be present in minor proportions. The TSM commonly nucleate on the wall rock and project into the vein, more rarely nucleating within the vein matrix but not exhibiting any preferential growth orientation. The veins (mm to cm in vein thickness) also contain paragenetically later quartz and sulfide. In hand sample, the veins can exhibit bleached-white selvages, consisting of primarily alkali feldspar and quartz, although this is not universal (Figure 2-4f). Some TSM-veins form with sharp wall-rock boundaries whereas others exhibit irregular contacts. The presence of TSM in veins is not useful in determining porphyry vein style classification, as they can form in multiple types, including *B* and *D* veins (Gustafson and Hunt 1975; Sillitoe 2010). Disseminated-style TSM are recognized by their occurrence as isolated clots/patches or in rare cases as individual grains (Figure 2-4k-o). The crystals of TSM are the coarsest observed, with grains up to several cm in length.

Texturally, disseminated TSM closely resemble those of breccias (*i.e.*, as acicular to prismatic radiating masses, the interstices of which are commonly infilled by quartz), but with TSM developing in discrete individual subhedral clots/patches, rather than large radiating interlocking masses as in TSM breccias. Here, TSM forms clots/patches/masses of radiating sub- to euhedral prismatic interlocking grains (in rare cases acicular). Rarely, TSM are observed as isolated individual grains. Clusters of TSM have been observed pseudomorphically replacing or (infilling) primary porphyritic feldspars and mafic minerals (mainly biotite, and more rarely amphibole). Owing to their chemical resilience, TSM are unaffected by subsequent alteration; only in cases where earlier-formed TSM have been brecciated do we observe the modification of primary grains that are broken/dissolved (or possibly melted, akin to the textures observed by; van Hinsberg 2011) and recrystallized (*e.g.*, Schaft Creek: Figure 2-5d).

2.6.1.3 Mineral Association and Relationship of TSM to Alteration Style

The types of minerals forming in association with TSM in porphyry deposits, in this study, is highly variable and in part, dependent on the host rock composition, as well as the style of alteration in which the TSM are present. Important associated minerals include (but are not limited to): quartz, feldspars (alkali-feldspars and K-feldspar), rutile, epidote, apatite, ilmenite, hematite, biotite, chlorite carbonate, and sulfides (mainly chalcopyrite and pyrite) (Table 2-2).

Tourmaline can be observed throughout the typical alteration profile of a porphyry deposit but is most common in the potassic (*e.g.*, Woodjam) and phyllic (*e.g.*, Casino) zones, more rarely within calcic-sodic (Highland Valley Copper), propylitic (Woodjam), and argillic (Casino) alteration zones (Figure 2-2). In zones of potassic alteration, TSM occur as disseminations or mineral replacements and also as veins with potassic alteration halos. Veins of TSM with potassic (bleached white alkali-feldspar) alteration halos are most common (*e.g.*, Byrne *et al.*

2020; Escolme *et al.* 2020). Additionally, TSM can be found less commonly in regions of significant biotite alteration, as disseminated grains or clots of multiple grains. In zones of phyllic alteration, TSM form as veins and pods associated with quartz, white mica, and pyrite (*e.g.*, Baksheev *et al.* 2012; Bozkaya *et al.* 2020). In the calcic-sodic zone, TSM forms in veins with quartz, albite, and actinolite (*e.g.*, Carten 1986; Byrne *et al.* 2020). In zones of propylitic alteration, TSM forms as veins and selective alteration in association with epidote, chlorite, quartz, and carbonate (*e.g.*, Baksheev *et al.* 2012; Li *et al.* 2021). Finally, TSM are also found in zones of argillic alteration, in association with clay minerals (Li *et al.* 2021).

2.6.1.4 Mineral Inclusions

Mineral inclusions in TSM from porphyry deposits are relatively limited (<1% of TSM grains investigated) in terms of type and abundance based on the samples examined in this study. Common mineral inclusions in the samples in this study are zircon, rutile, Fe-oxides, apatite, albite, quartz, titanite, epidote, barite, chalcopyrite, and molybdenite (Table 2-2, Figure 2-6). Due to the paucity and irregularity of the inclusions and inclusion populations, definitive statements cannot be made. However, zircon and rutile were noted in TSM in multiple samples from multiple deposits, while other mineral inclusions are considerably rarer. It is noteworthy that no sulfide inclusions were observed, further supporting the early paragenesis of TSM. Only sulfides developed on later-formed fractures are noted.

2.6.1.5 Internal textures in TSM: Backscattered-Electron Imaging (BSEI)

The TSM generally display a high degree of chemical heterogeneity in terms of both their major- and minor-element characters. Examination of TSM using BSEI reveals four distinct textural features, with two considered to be primary in origin: 1) oscillatory/concentric growth zoning,

recognized by the development of sharp chemical boundaries developed parallel to [001] (Figure 2-5a), and 2) sector zoning, recognized by the partitioning of elements in distinct sectors (Figure 2-5b). Oscillatory zonation is interpreted to record rapidly changing fluid conditions at the mineral surface scale, potentially due to surface-limited diffusion from fast crystallization rates (Dutrow and Henry 2018). Similarly, sector zonation forms under conditions of rapid growth such that equilibrium between different sectors cannot be maintained (Henry *et al.* 1999). These sectors initially form when elements are preferentially incorporated at specific growth surfaces and survive throughout crystal growth (van Hinsberg 2006). Further, several uncommon textures considered to be secondary in origin were also observed: 1) patchy/irregular growth common in recrystallized/brecciated TSM, with diffuse grain boundaries, developed perpendicular to [001] (Figure 2-5c), and 2) overgrowth or replacement features (Figure 2-5d). The development of regions of high porosity, giving rise to textures similar to those observed in plagioclase (Putnis 2009), are considered as products of coupled dissolution reprecipitation. Such textures could be included in the patchy/irregular group. These dissolution re-precipitation textures correspond to major-element changes, primarily involving Fe and Mg (*i.e.*, $Mg\#$ variations) typically reflected in the replacement of early Fe-rich (schorl) by Mg-rich (dravite) overgrowths. This observation is somewhat counterintuitive in that Mg is the smaller cation and would preferentially be incorporated before larger ones (in this case Fe). Variations in chemical zonation could reflect the relative abundance of these two elements in the fluid, competition for Fe with other co-crystallizing phases (*e.g.*, sulfides or oxides?), or additionally reflecting a fast rate of crystallization.

2.6.2 Mineral Chemistry

Results from SEM-EDS analyses and the recalculated empirical formula (summary of data in Table 2-3) show that the majority of the TSM analyzed (>80 %) are dravite, with the remainder being schorl. All belong to the Na-dominant (Figure 2-7a), alkali TSM group, with the majority following the oxy-dravite – povondraite (O-P) trend (Figure 2-7b) and to a lesser extent, the schorl–dravite trend (primarily the Casino samples; Figure 2-7c). A significant portion of the TSM analyzed show $\text{Fe}^{3+}_{(\text{calc})}$, suggesting a moderate relationship with prevailing oxidizing conditions. Analyses with the highest $\text{Fe}^{3+}_{(\text{calc})}$ concentrations are associated with the most Fe-rich and Al-depleted regions of individual grains. The TSM from all the porphyry systems analyzed contain some $\text{Fe}^{3+}_{(\text{calc})}$, with those from Casino having the fewest number of analyses with calculated $\text{Fe}^{3+}_{(\text{calc})}$ (~2 % of analyses totaling 23 grains). A limited number of analyses ($n = 203$) from the Donoso Breccia contain the highest calculated $\text{Fe}^{3+}_{(\text{calc})}$ values (1.38 *apfu avg.*), with a rare number ($n = 3$) having sufficient Fe^{3+} to classify as povondraite. The predominance of Fe^{3+} could reflect the oxidized nature of early porphyry fluids or could arise *via* boiling mechanisms (Yang and Jang 2002).

The variation in major- and minor-element concentrations in the TSM from the various deposits examined in this study is remarkably small, despite there being relatively large differences in age, host lithology, porphyry classification (calc-alkalic and alkalic), associated alteration, tectonic setting, and metal associations. The average major element composition for all porphyry related TSM ($n = 2896$ analyses from ~750 grains) analyzed (range in wt. %) are as follows; Na 1.70 (0.64 – 2.36), Ca 0.69 (<LOD – 2.64), Ti 0.34 (<LOD – 2.15), Mg 4.75 (1.60 – 7.29), Fe_{tot} 6.47 (0.20 – 24.85), Al 15.95 (6.45 – 20.09), and Si 16.91 (14.42 – 18.76). The average (range) in *apfu* are as follows; Na 0.74 (0.28 – 1.04), Ca 0.15 (<LOD – 0.70), Vac 0.12 (nil – 0.54), Ti

0.05 (<LOD – 0.45), Mg 1.94 (0.69 – 2.89), Fe_{tot} 1.17 (0.03 – 4.97), Al 5.85 (2.69 – 7.14), and Si 5.98 (5.53 – 6.25). Results show that based on occupancy of the *X*-site, the TSM analyzed predominantly plot in the alkali-dominant field, with a limited number (<2 %) plotting in the *X*-vacant and calcic fields (Figure 2-7a). The greatest compositional variation in terms of major and minor element chemistry is observed in the *Y*- and *Z*- crystallographic sites, these sites house Al as well as metals, predominantly Mg and Fe (Figure 2-7b, 7c). Calculated Fe²⁺ and Fe³⁺ contents show an average of Fe²⁺ 0.94 *apfu* (range: 0.03 – 2.41) and Fe³⁺ 0.24 *apfu* (range: <LOD – 3.20). No regular or systematic core-rim chemical changes could be discerned at the deposit scale or among the entire data set, based on the identification of grains with core-rim zonation and comparing the Al-Mg-Fe values did not show any repeatable patterns. Additionally, no difference in TSM chemistry exists when the data were sorted based on the TSM occurrence (*i.e.*, breccia, vein, and disseminated) suggesting macroscopic textures have no control on major or minor element chemistry.

The TSM exhibit variable chemical zonation within a single bedrock sample, between different samples from the same deposit, and between deposit types. Among the TSM analyzed from the different deposits examined, some minor differences can be discerned (Figure 2-7 and Figure 2-8); 1) the TSM from Casino show the highest *avg.* Al (6.36 *apfu*) amongst the deposits examined and the greatest proportion of *X*-site vacancies (0.17 *apfu*) along with the lowest *avg.* concentrations of Ti (0.03 *apfu*), Fe (0.62 *apfu*), and Ca (0.06 *apfu*), 2) those from Coxheath are not remarkable in their chemistry and are intermediate schorl-dravite in composition, 3) those from the Donoso breccia show the highest *avg.* Na (0.81 *apfu*), Fe_{tot} (2.95 *apfu*), and Fe³⁺_{calc} (1.38 *apfu*) with the lowest Al (4.47 *apfu*), 4) those from HVC are intermediate in composition, 5) those from New Afton show a high *avg.* Ti (0.09 *apfu*), 6) those from Schaft Creek contain the

highest *avg.* Ca (0.30 *apfu*) and Mg (2.15 *apfu*) and lowest *X*-site vacancies (0.02 *apfu*) as well as high *avg.* Ti (0.09 *apfu*) and, 7) those from Woodjam contain the lowest *avg.* Na (0.65 *apfu*). Samples of TSM are observed in a wide range of alteration styles (Figure 2-2). Although hand-sample and petrographic observations indicate TSM to be, in general, paragenetically earlier than alteration, an examination of major- and minor-elements was made to investigate whether any correlations exist amongst alteration styles (Figure 2-9). Some minor differences in major and minor elements can be observed among TSM and the alteration assemblages in which they are found. Analyses of TSM from zones of potassic alteration do not show any unique differences in major or minor-element chemistry in comparison to TSM from other alteration zones. However, those from Na-Ca alteration zones exhibit unique mineral chemistry, containing the highest *avg.* Fe (1.85 *apfu*) as well as high Ca (0.26 *apfu*) coupled with the lowest *avg.* Al (5.26 *apfu*). Grains forming in phyllic alteration zones show the highest *avg.* Na (0.76 *apfu*) coupled with low *avg.* Ca (0.10 *apfu*). Grains of TSM forming in propylitic alteration show the highest Mg (2.14 *apfu*) and high Ca (0.31 *apfu*) values. Finally, argillic alteration shows the highest Al (6.47 *apfu*) and Vac (0.20 *apfu*) coupled with the lowest *avg.* Fe (0.61 *apfu*) and Ca (0.08 *apfu*) values. The contrast in major element chemistry between phyllic and propylitic TSM is comparable to that presented by Baksheev *et al.* (2012); here, TSM associated with phyllic were noted to be enriched in Na, Vac, and Al while propylitic TSM has a higher *avg.* Ca and Fe.

2.7 Discussion

The physical characteristics including color, grain size, morphology, color in plane-polarized light, mineral associations, and inclusions found in TSM, are highly similar amongst the seven mineralized porphyry systems examined in this study. In hand sample, all TSM appear black but

can range from colorless to dark brown to black under the binocular microscope. Although TSM can occur in a wide range of colors in other geologic environments (Hawthorne and Dirlam 2011), color alone cannot be uniquely used to identify TSM derived from a mineralized porphyry system but can be an effective first pass in separating prospective grains (*i.e.*, dark brown to black in hand sample). However, as color is in part related to chemistry and considering the uniformity in color observed in the TSM analyzed from the seven porphyry systems examined in this study, the implication suggests a uniformity in TSM genesis in mineralized porphyry systems. They occur in relatively uniform grain sizes ranging from microns to millimeters in diameter, forming most commonly as sub- to euhedral radiating prismatic grains in groups or clusters and are very rarely found as isolated individual crystals. The uniformity in grain size could reflect similar cooling rates or degrees of undercooling (Kirkpatrick 1975). Under polarized light, TSM are moderate to weakly pleochroic and range in color from light green to blue, light brown to brown, and are even colorless and non-pleochroic in some rare cases. Optical zonation is ubiquitous as fine-scale (μm) concentric zonation perpendicular to the *c*-axis. As mentioned, TSM exhibit a range of internal textures (zonation), which in some cases can be recognized using plane-polarized light noting changes in color but is most evident with BSEI that highlights both major and more subtle changes in mineral chemistry. The two primary zonation types (concentric and sector) are observed. Concentric zonation (most common) is evident as distinct fine (μm scale) chemical zones (primarily Al-Mg-Fe exchange) that are separated by sharp and not gradational chemical variations. Concentric zonation in minerals can result from 1) changes in the chemical composition of a melt or fluid, or 2) crystal face kinetics and diffusion limitations of a chemical species (García-Ruiz and Otálora 2015). Sector zonation results from the preferential incorporation of elements on specific growth surfaces (van Hinsberg and

Schumacher 2006). Additionally, sector zonation indicates rapid crystallization such that equilibrium is not maintained (Henry *et al.* 1999). Considering the variation in chemistry between zones (Figure 2-5a, 5b), it is unlikely to reflect changes in bulk fluid composition (based on the inconsistency of TSM zoning chemistry of paragenetically simultaneous grains) but more likely records local changes in chemistry at the mineral surface during rapid crystal growth. The abundance of primary zonation features in TSM in porphyry systems and exceptionally low abundance of secondary zonation features suggest a single TSM forming event rather than multiple crystalizing events.

Samples of TSM recovered from till and stream sediments surrounding known porphyry deposits have been shown to contain abundant inclusions (Beckett-Brown *et al.* 2021). Mineral inclusions are rare in occurrence (<1% of grains) for TSM in mineralized porphyry systems examined in this study, but when present, zircon, and rutile are the most common. As such, the integration of such physical (such as inclusion types presented here) and chemical data (major and traces discussed below and traces in Chapter 3) of these minerals in mineralized porphyry systems could provide valuable insight both into the formation of these systems and the exploration for them (*e.g.*, their use as indicator minerals in sediment samples). Mineral inclusions in TSM are also present in other environments. Quartz inclusions in TSM from granites, schists, and gneiss have been observed (van Hinsberg and Schumacher 2011; Marger *et al.* 2019; Cheng *et al.* 2021). Samples of TSM from metamorphic rocks such as tourmalinites and serpentinites have been reported to contain inclusions of zircon and titanite (Dietrich 1985). Pegmatitic TSM has also been reported to contain inclusions such as apatite and rutile (Dunn 1977; Dietrich 1985). Grains of TSM from orogenic Au deposits occasionally contain inclusions of quartz, calcite, chlorite, and amphibole (*e.g.*, Sciuba *et al.* 2021). In VMS deposits, TSM are reported to contain

inclusions of quartz, zircon, and sphalerite (Slack and Coad 1989). Thus, the presence of inclusions could be an important first-pass filter to examine large quantities of TSM, which may indicate porphyry mineralization, therefore warranting further investigation, whereas those that contain quartz inclusions could be omitted from further investigation.

Given the complexity of the crystal structure of TSM and their ability to incorporate a wide-range in elements (alkalis, HFSE, semi-metals, *etc.*), it is necessary to consider the various sites possible and their occupants as revealed in this study. Beginning with the *X*-site, TSM chemistry in porphyry deposits may, in principle, be linked to the specific alteration assemblage (potassic, calcic-sodic, phyllic, propylitic, and argillic) with which they are associated even though in many cases the TSM form prior to the alteration minerals that characterize these assemblages. The contents of the *X*-site (0.74 Na *apfu* avg.) in TSM forming in porphyry systems are similar, with >95 % of analyses plotting in the Alkali-dominant field (Figure 2-7a). However, correlations exist between *X*-site populations and alteration assemblage. For example, TSM associated with sodic-calcic and propylitic alteration contain higher average proportions of Ca than other alteration types with contents of 0.26 and 0.31 *apfu* respectively, potentially reflecting the Ca-rich nature of the fluids. Phyllic alteration TSM can be identified by high average concentrations of Na (0.76 *apfu*) coupled with low Ca (0.10 *apfu*) that could reflect the low Ca and higher Na contents of the fluid. The TSM associated with argillic alteration zones contains the highest average Vac (0.20 *apfu*) reflecting the lower alkali contents of these environments. There are no distinct major-element differences for TSM developing in potassic alteration. This lack of difference could reflect the timing of TSM formation (*i.e.*, before potassic alteration) but could also reflect the extreme difficulty of K incorporation into TSM, which is a function of *P*, with high *P* needed to incorporate any meaningful concentrations of K (Berryman *et al.* 2015). Thus,

in mineralized porphyry systems, concentrations of K in TSM cannot be used as a guide for identifying zones of potassic alteration. The *X*-site composition of TSM forming in other environments can be similar with grains (on average) from orogenic Au deposits (0.64 *apfu* Na: Sciuba *et al.* 2021), VMS (0.64 *apfu* Na: Slack and Coad 1989; Slack 1993), orbicular tourmaline granites (0.74 *apfu* Na: Andreozzi *et al.* 2020), W-Sn-Cu polymetallic deposits (0.65 *apfu* Na: Codeço *et al.* 2017) and even many pegmatitic TSM (0.61 *apfu* Na: Gadas *et al.* 2012; López de Azarevich *et al.* 2021) dominated by Na in the *X*-site. *X*-site vacant dominant TSM including Mg-foitite, foitite, rossmanite, and oxy-foitite form in unique environments (*e.g.*, such as alkali-deficient portions of pegmatites) but their occurrence is extremely rare (*e.g.*, Bačík *et al.* 2015) and are not found in mineralized porphyry systems. Calcium dominant *X*-site TSM (*e.g.*, uvite, feruvite, fluor-uvite, fluor-liddicoatite, luchesiite, and adachiite) form in Ca-rich environments generally associated with mafic to ultramafic rocks (*e.g.*, Jiang *et al.* 1996). The *X*-site of TSM can contain Na, Ca, K, and Vac components in major concentrations with those forming in mineralized porphyry systems being exclusively sodic dominant.

In many systems, TSM have been regarded as a passive accessory phase that reflects changes in the local environment and does not control it (Henry and Dutrow 2018). The majority of porphyry TSM major element variability involves Al, Mg, and Fe at the *Y*- and *Z*-sites and has served as the basis for the development of the Al-Fe_(tot)-Mg classification ternary (Henry and Guidotti 1985), which has in turn been used as an environment of formation discriminator for TSM. As these fields only denote TSM forming in non-mineralized settings, what becomes key is the trends in the data for porphyry TSM (Figure 2-7b). Results from SEM-EDS show that TSM from porphyry systems plot on the O-P trend reflecting the substitution of Al³⁺ for Fe³⁺ with reasonably constant Mg contents (~2 *apfu*, 1.94 ± 0.29 *apfu*). This finding is consistent with

those from previous studies (*e.g.*, Lynch and Ortega 1997; Rabbia 2003; Baksheev *et al.* 2012), indicating that TSM from all porphyry systems must arise from similar geochemical and geological processes. The O-P trend can be observed in other non-porphyry environments (Henry *et al.* 1999; Kalliomäki *et al.* 2017) but it is distinctive relative to the more common schorl-dravite substitution trend observed for TSM in other environments *e.g.*, orogenic (Sciuba *et al.* 2021), W-Sn-Cu polymetallic deposits (Codeço *et al.* 2017; Codeço *et al.* 2019; Codeço *et al.* 2020), pegmatitic (Novak *et al.* 2011; Gadas *et al.* 2012), and VMS (Slack and Coad 1989). The O-P trend that characterizes TSM that forms in porphyry systems may distinguish it from other deposit types listed above, but not from other environments that also display the O-P trend (*e.g.*, Orogenic TSM). It is important to note that the type-locality for povondraite is from a schist near Villa Tunari, Bolivia with analyses plotting along the O-P trend (Grice *et al.* 1993). The fact that TSM from porphyry deposits chemically follows the O-P trend highlights the essential nature of the $\text{Al}^{3+} \leftrightarrow \text{Fe}^{3+}$ substitution and at least the partial role in their formation. If the porphyry systems are grouped based on their emplacement depth it reveals that deposits that form at greater depths >2 km contain higher $\text{Fe}^{3+}_{(\text{calc})}$ (*i.e.*, plot closer to povondraite, Figure 2-7b) than samples that form closer to the surface (>2 km) which plot closer to oxy-dravite (*i.e.*, contain less Fe^{3+} and more Al^{3+}). This O-P trend displays a transition from early oxidized conditions towards more reducing conditions, potentially reflecting the change in oxidation of arc magmas during their evolution and ascent (Sun *et al.* 2015). Conversely, this trend could reflect conditions or initiation of boiling, similar to the interpretations of other authors (Lynch and Ortega 1997; Baksheev *et al.* 2011). Given that Al is relatively fluid-immobile, the observed enrichment in TSM could suggest a local source rather than derived from an external fluid. The

hydrothermal alteration of primary magmatic minerals (*e.g.*, feldspars, biotite, and amphibole) could contribute to the Al required to form TSM.

There exists debate within the literature regarding the beginning of subduction and specifically its occurrence in the Precambrian (Wyman *et al.* 2002; Bédard *et al.* 2013). Porphyry deposits in the Precambrian have been used to infer the presence of subduction (*e.g.*, Malanjkhand, India; Stein *et al.* 2004). The focus of this manuscript is not to address the above but rather compare the TSM from a Precambrian porphyry-like system which may shed light on the link between Precambrian and more recent “typical” porphyry systems. Due to the robust nature and high closure temperature, TSM are an ideal phase to assess similarities and differences among recent and Precambrian systems. The Precambrian Coxheath Cu-Mo-Au system age is problematic when it comes to the initiation of plate tectonics. Importantly, Coxheath shares many features similar to typical porphyry systems (*e.g.*, large concentric zoned alteration, continental margin, stockwork mineralization, mineralized breccias, *etc.*). The TSM from the Coxheath deposit share many similarities with TSM characteristics from typical porphyry systems. This similarity includes color in hand sample and under transmitted light, grain size and morphology, inclusion types, absolute major and minor element chemistry, and porphyry major-element chemical trends (*i.e.*, the O-P trend) as well as trace element analyses (Chapter 3). The overwhelming similarity in TSM physical and chemical characteristics indicates that they have similar geological processes of formation. The implication is that porphyry or porphyry-like systems may be more common in the Precambrian than was previously thought and that the TSM found in these systems have developed under broadly similar conditions to modern porphyry systems. Subsequently, TSM could help identify possible porphyry systems in the Precambrian where there still exists debate as to their origin.

Although historically it has not been regarded as a significant accessory phase, considering the number of deposits including major deposits that report it (Figure 2-1), TSM should be considered an important accessory phase. The recognition of boron-bearing minerals, notably tourmaline, is likely under reported considering the abundance of boron (~500 ppm *avg.*) observed in porphyry fluid inclusions (Wagner *et al.* 2016). There are no apparent correlations of Cu concentration or age *vs.* ore tonnage when the presence or absence of TSM is considered (Figure 2-10). It is important to note the binary relationship of these diagrams and that modal abundance, chemistry, texture, *etc.* are not assessed, thus the interpretations being made are limited. Considering the direct overlap of data for deposits that contain TSM and those that do not, it begs the question of why some deposits do not contain TSM. The most likely explanation is that TSM are not reported in available literature or misidentified for other minerals (epidote, amphibole, biotite). A detailed study, especially of notable systems which do not contain TSM (*e.g.*, examining drill logs or re-logging key intervals), could significantly increase the number of porphyry systems that have been reported to contain TSM as an accessory phase. If TSM prove to be a significant phase in mineralized porphyry system, their presence in turn reflects a contribution of boron in the system. Considering that boron (in the form of borax) is used as a flux to reduce the melting point of metals for metallurgical processes (Davies 1992), perhaps it plays a similar role in the complexing of metals in porphyry mineralizing fluids.

2.8 Conclusions

Tourmaline should be considered a significant accessory phase in mineralized porphyry systems due to its repeated occurrence in many porphyry systems worldwide (Figure 2-1) and its presence highlights the importance of hydrothermal boron in crustal ore-forming processes.

The physical characteristics of TSM (*e.g.*, color, grain size, morphology, color in PPL) can provide some but not decisive information that can be used in distinguishing porphyry-related TSM from that forming in other environments. Although tourmaline major element chemistry is commonly reported, it has not been demonstrated to be a definitive tool in discriminating TSM forming in mineralized versus unmineralized settings. New insights from this study about TSM forming in mineralized porphyry systems that may be useful in discriminating between environments:

- 1) All TSM studied are exclusively black to dark brown at the macro-scale, occurring as radiating euhedral to subhedral masses of interlocking grains and are almost never observed as individual isolated grains. In transmitted light, grains are weakly pleochroic and range from green, brown, blue, to colorless. While inclusions are rarely observed, when present, zircon and rutile are most common.
- 2) In most porphyry systems, TSM form paragenetically early and exhibit a wide range of zonation textures including oscillatory, sector, patchy, and overgrowths with oscillatory being most common.
- 3) Major-element chemical trends of TSM forming in porphyry systems are not unique compared to TSM forming in other systems (*e.g.*, some Orogenic TSM) but among the porphyry systems presented in this study, and those presented in the literature, they are remarkably consistent. The grains are dominated by Na in the *X*-site but can contain minor concentrations of Ca and Vacancy components. They are Mg-Fe rich, ranging from predominantly dravite to schorl in composition with remarkably consistent *Mg apfu* values of ~ 2.0 (1.94 ± 0.29) and follow the O-P trend.

- 4) Physical and major element data alone cannot definitively distinguish TSM forming in mineralized porphyry systems. However, the integration of physical and chemical data (including trace element data, *i.e.*, Chapter 3) provides an effective method for distinguishing TSM that has formed in mineralized porphyry systems from that originating in any other geologic environment.

2.9 Figures

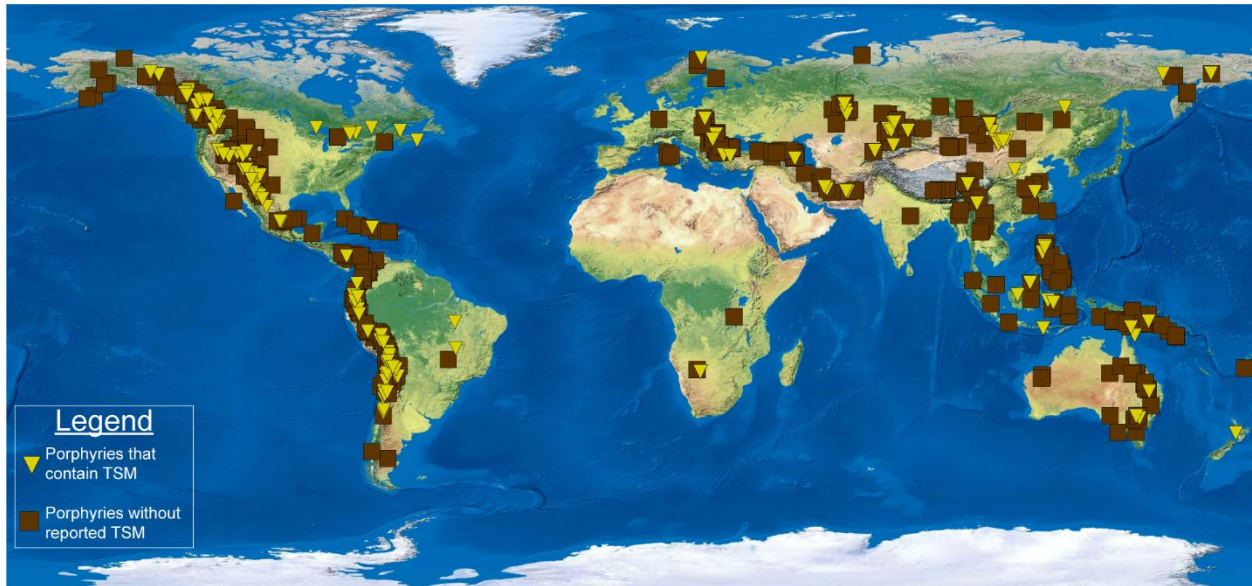


Figure 2-1: World map showing the distribution of porphyry deposits that contain TSM

World map overlain by the world porphyry database (USGS porphyry database; Singer *et al.*

2008). Yellow symbols represent porphyry systems that contain reported TSM and brown squares represent porphyry deposits that do not contain TSM. Note how the occurrences of TSM correspond to the major porphyry belts and some of the most well-endowed, mineralized porphyries worldwide. The presence of TSM is compiled from the USGS porphyry database and from additional references that are listed in Chapter 2.11. It is important to note that the porphyry systems included in the world porphyry database range from world-class deposits to small occurrences of little economic significance.

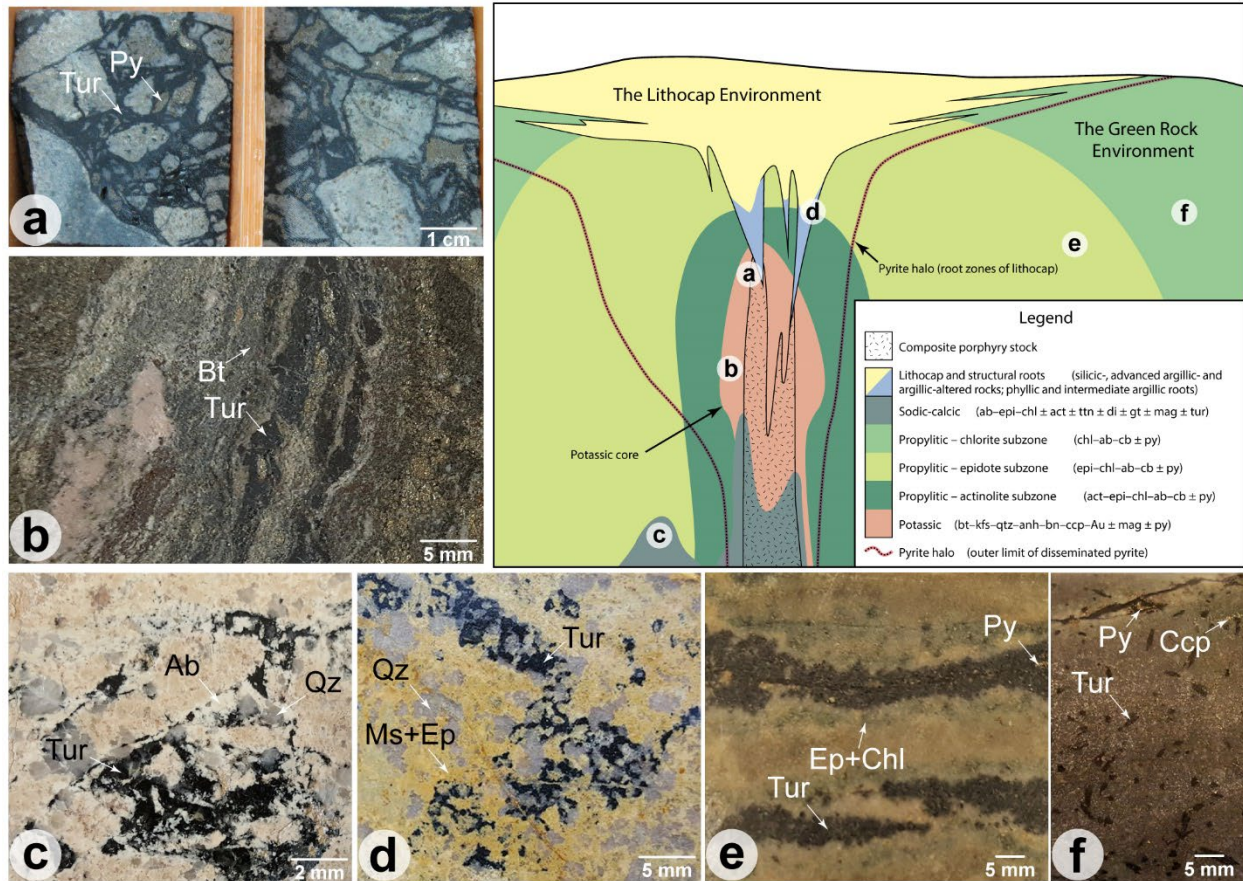


Figure 2-2: Porphyry alteration zonation schematic overlain with TSM distribution

Porphyry alteration schematic (modified after Cooke *et al.* 2020b; Hollings and Orovan 2020).

Tourmaline (tur) can be observed in all the alteration zones in a porphyry deposit. a) An example of a TSM breccia (Donoso Breccia – Los Bronces), which tend to develop at the contact with the intrusive stock, but not always. b) An example of TSM in a zone of potassic alteration with biotite (Bt) – New Afton. c) An example of TSM in a zone of sodic-calcic alteration with albite (Ab) – Highland Valley. d) An example of TSM in a zone of phyllic alteration with muscovite (Ms), epidote (Ep), and quartz (Qz) – Casino. e) An example of TSM in a zone of propylitic alteration with epidote (Ep) and chlorite (Chl) – Woodjam. (f) An example of TSM in “green rock” (chlorite subzone of propylitic alteration) zone – Schaft Creek.

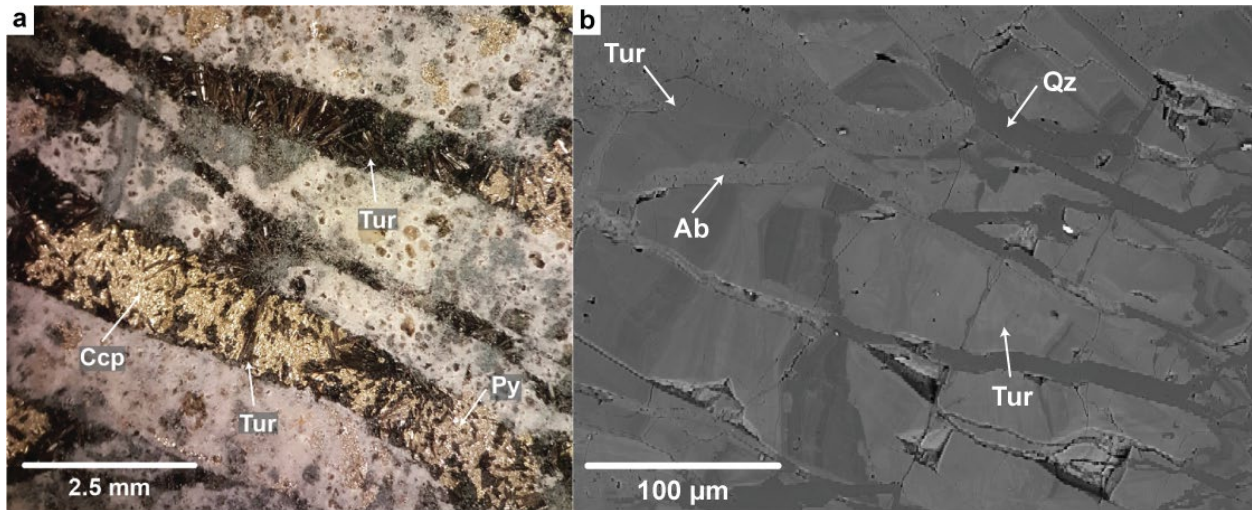


Figure 2-3: Tourmaline paragenesis.

a) A TSM breccia with chalcopyrite (ccp) and pyrite (py). Tourmaline (Tur) forms as prismatic euhedral crystals, which grow into the open space, that are overgrown/infilled (forming paragenetically later) by sulfides (ccp, py). b) BSE image (Schaft Creek) of early formed TSM, which has been later disrupted and broken, with quartz (qz) and albite (ab) infilling the spaces.

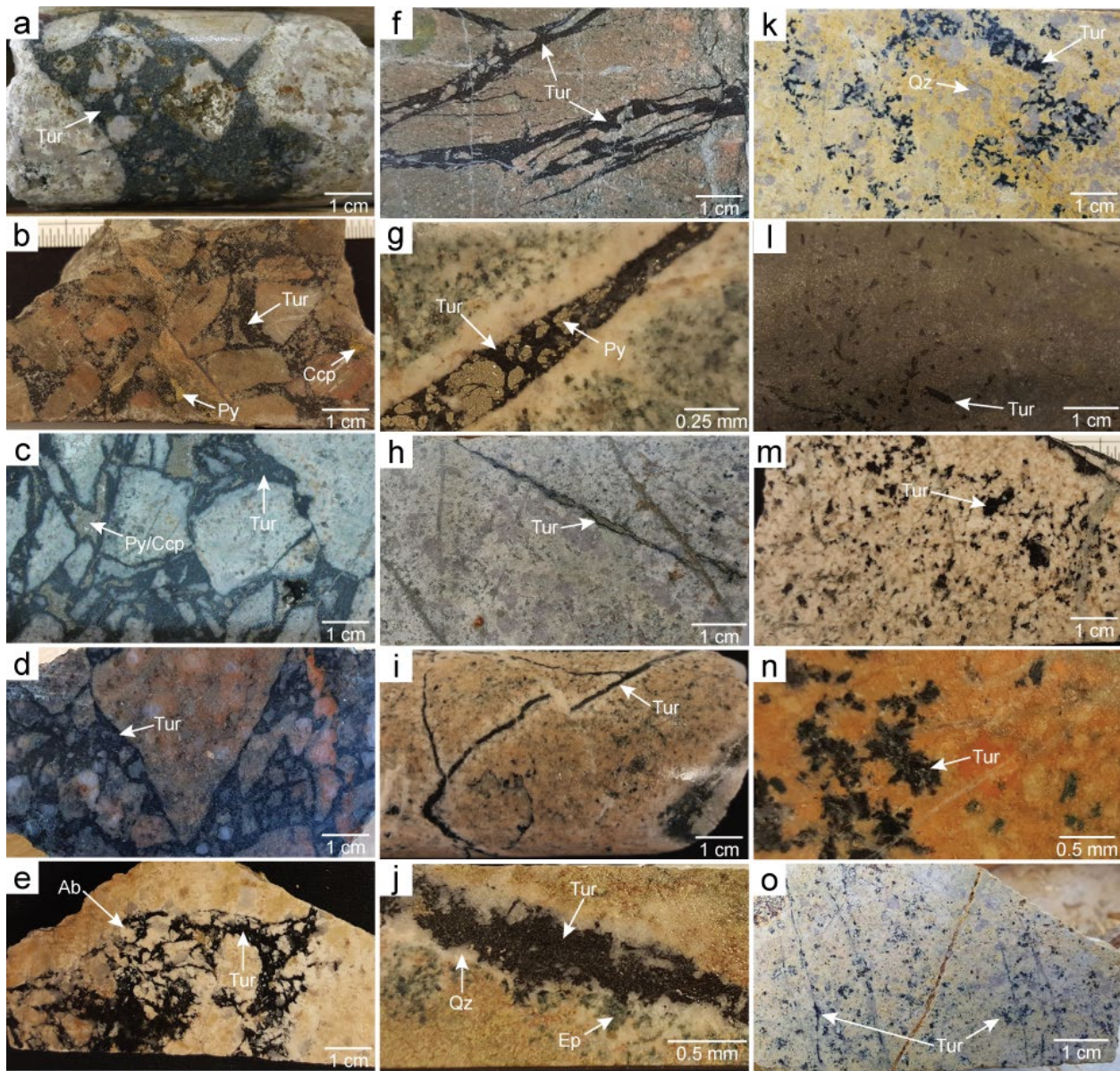


Figure 2-4: Hand sample photographs highlighting the textural styles of TSM

Hand sample photographs of core and rock samples showing the variable textural styles of TSM (black mineral in all images) from mineralized porphyry systems. a) TSM breccia from the Casino deposit-YT, forming with ancillary quartz and sulfides (mostly pyrite). b) mineralized TSM breccia with chalcopyrite (Schaft Creek-BC). c) TSM breccia from the phyllic zone with pyrite and chalcopyrite (Los Bronces – Donoso Breccia-Chile). d) TSM breccia with minor pyrite (Coxheath-NS). e) TSM breccia with quartz-hematite and albite in the matrix (Highmont

Pit-Highland Valley Copper-BC). f) veins of black tourmaline forming in phyllic alteration (New Afton-BC). g) vein of tourmaline and pyrite with a pronounced white alteration halo (mostly albite), forming in propylitic alteration (Woodjam-BC). h) veins of TSM and pyrite, with TSM forming along the edge of the vein and pyrite forming in the center (Casino-Y). i) monomineralic veins of tourmaline with subtle white alteration halo (Schaff Creek-BC). j) irregular walled veins of TSM with quartz and minor epidote-green (Takom - Woodjam-BC). k) disseminated clots of black TSM forming in the phyllic zone (Casino-YT) with quartz, muscovite and minor epidote. l) disseminated individual TSM crystals forming in green-rock (chlorite) alteration (Woodjam-BC). m) disseminated clots of TSM forming in a potassic alteration zone (Schaff Creek-BC). K-feldspar grains here appear as bleached white grains. n) clots of tourmaline forming in a potassic alteration zone with hematite-stained K-feldspar grains (Woodjam-BC). o) disseminated clots (as well as minor veins) of tourmaline forming in phyllic alteration (Casino-YT).

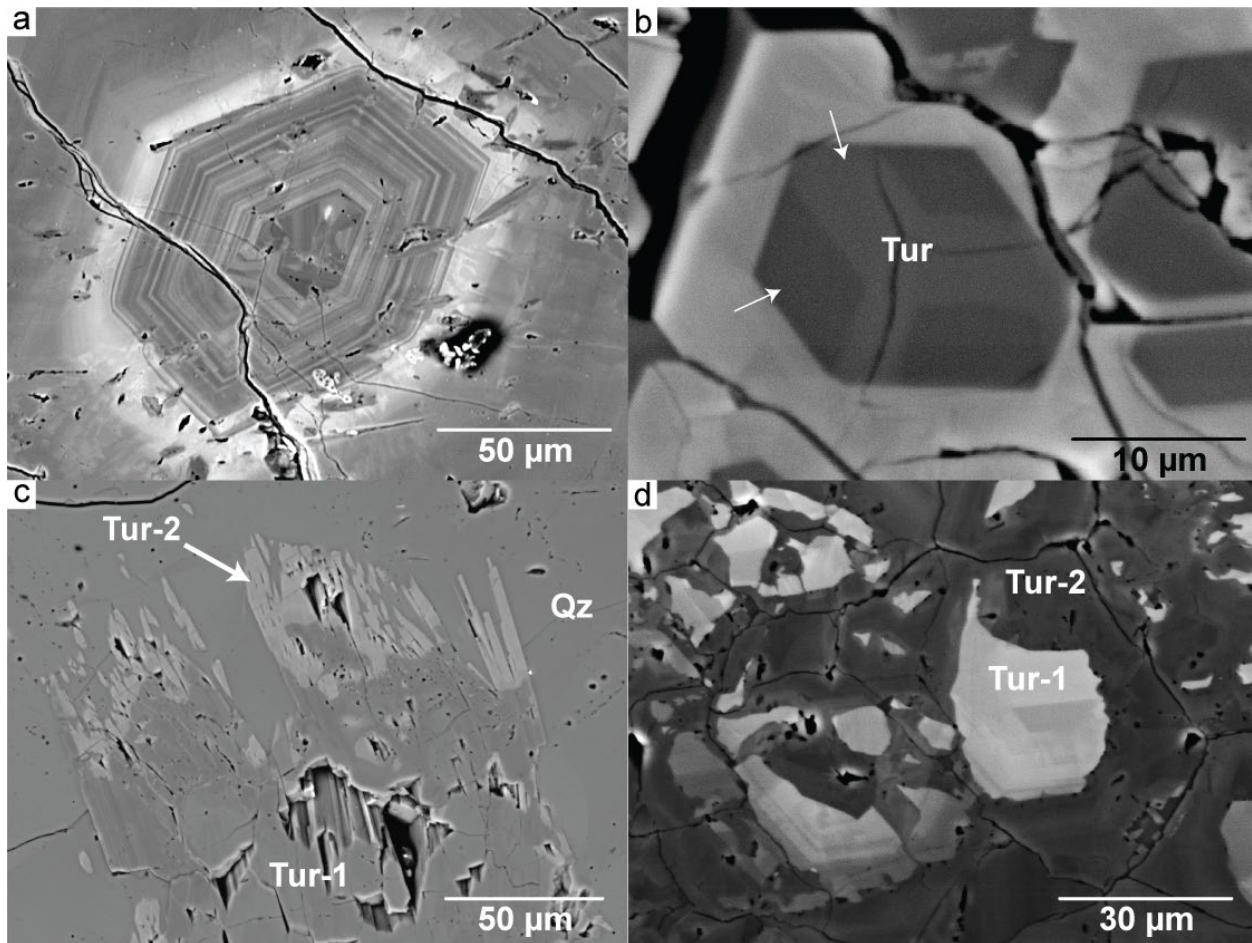


Figure 2-5: Backscattered electron images of internal TSM textures

Backscattered electron images showing internal textures of TSM grains a) An example of concentric zonation of a TSM oriented perpendicular to the c -axis with alternating Fe- and Mg-rich regions – Shaft Creek, BC; b) An example of sector zonation perpendicular to the c -axis with the arrows denoting different sectors – Highland Valley Copper, BC; c) An example of overgrowth texture (Tur-1 darker grey with higher Mg/Fe values, Tur-2 lighter grey with lower Mg/Fe values) – Casino, YT; d) An example of irregular/patchy zonation resulting from the recrystallization of pre-existing Tur-1, of which some primary fragments still remain, by Tur-2. Tur-2 is more Mg-rich – Shaft Creek, BC.

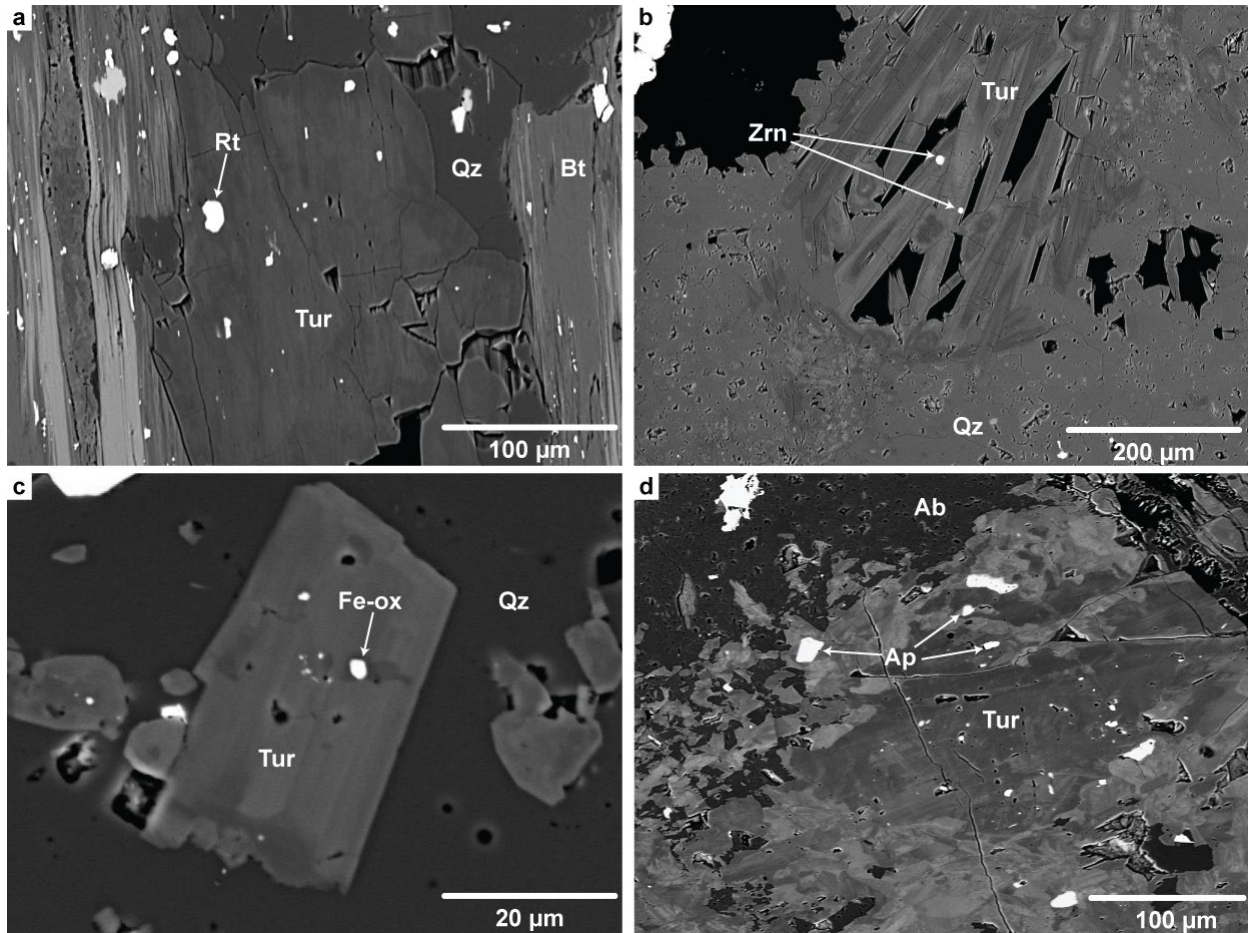


Figure 2-6: Examples of mineral inclusions in TSM

Less than one percent of porphyry TSM grains contain inclusions. Examples of mineral inclusions in TSM from mineralized porphyry systems. Backscattered electron images showing inclusions in TSM: a) rutile (rt) inclusions in TSM surrounded by quartz (qz) and biotite (bt) – Casino-YT; b) zircon (zrn) inclusions in TSM – Casino-YT; c) hematite (hem) inclusion in TSM – Coxheath-NS; d) apatite (ap) inclusions in TSM surrounded by albite (ab) – Schaft Creek-BC.

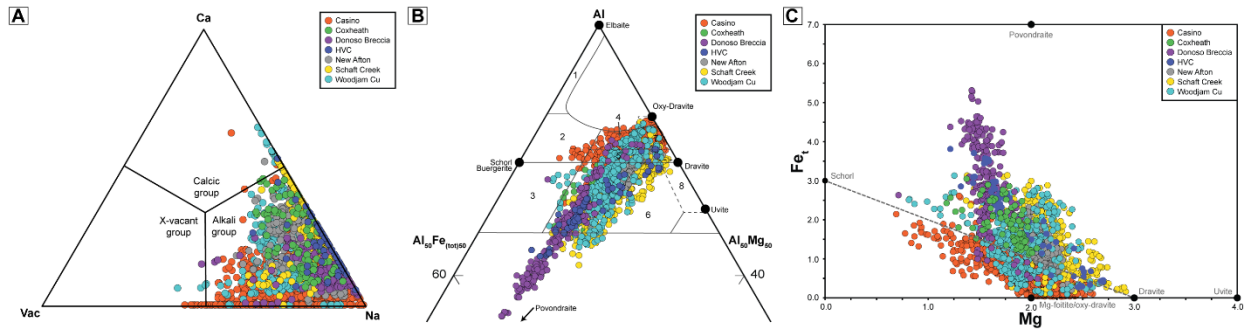


Figure 2-7: Major element diagrams of TSM chemistry

Major element plots of 2896 point analyses from ~750 TSM grains from 29 samples in *apfu*. Dot sizes roughly approximate the error of analyses. a) X-site classification ternary diagram showing the major constituents Na-Ca-Vac highlighting the consistency of Na dominant TSM in porphyry systems. Notice the Alkali group apex of the diagram does not include K as it was not observed above limit of detection (*via* EDS). b) Ternary diagram of tourmaline major element chemistry Al-Fe_(tot)-Mg for the porphyry tourmaline samples in this study, using ternary diagram of Henry and Guidotti (1985). The fields denote TSM compositions from: (1) Li-rich granitoid, pegmatites, aplites; (2) Li-poor granitoids, pegmatites, aplites; (3) Fe³⁺-rich quartz-tourmaline rocks; (4) metapelites and metapsammites with an Al-saturating phase; (5) metapelites and metapsammites without an Al-saturating phase; (6) Fe³⁺-rich quartz-tourmaline rocks, calc-silicate rocks, and metapelites; (7) low-Ca meta-ultramafics and Cr, V-rich metasediments; and (8) metacarbonates and meta-pyroxenites. This plot shows the overwhelming dominance of the O-P trend for the bulk of the deposits analyzed. c) binary plot of Mg-Fe *apfu* highlighting the general deviation (except for some Casino analyses) from the more typical Mg-Fe substitution between dravite and schorl end members.

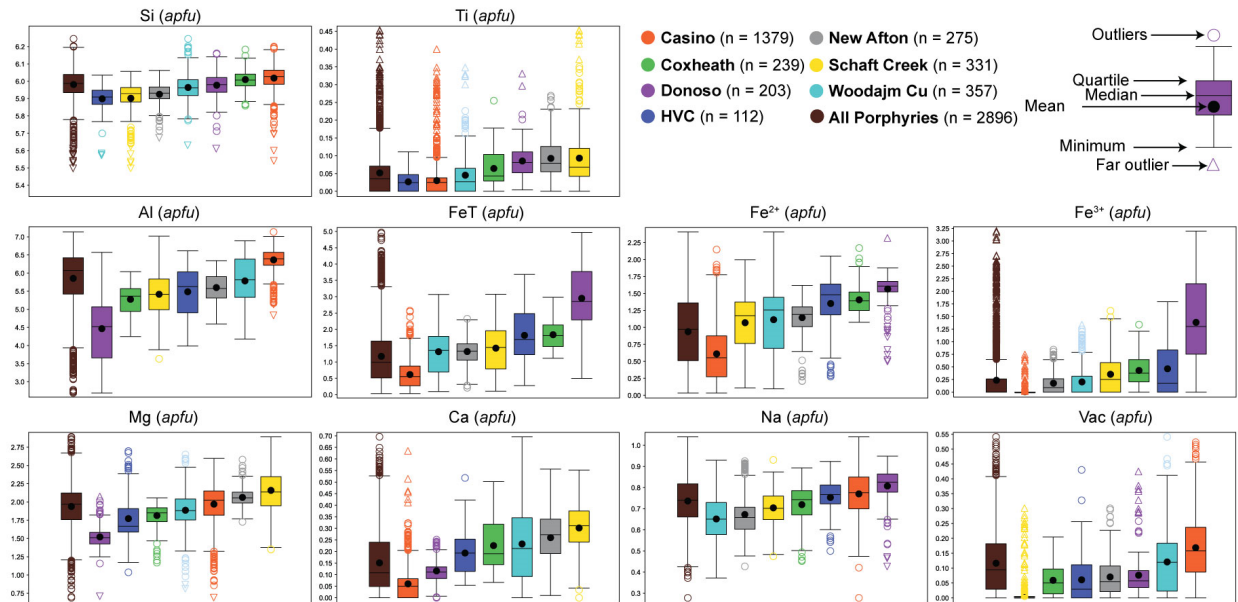


Figure 2-8: Major element tukey box plots of TSM deposit chemistry

Intra deposit variations of major-elements of 2896 point analyses from ~750 TSM grains from 29 samples presented in *apfu*. Tukey box plots, far outlier data, sorted by mean of major element *apfu* data, separated by the mineralized porphyry systems examined. Fe valence calculated using WinTcac (Yavuz *et al.* 2014). Outliers are classified as $1.5 \cdot (Q3 - Q1)$ and far outlier data classified as $3 \cdot (Q3 - Q1)$.

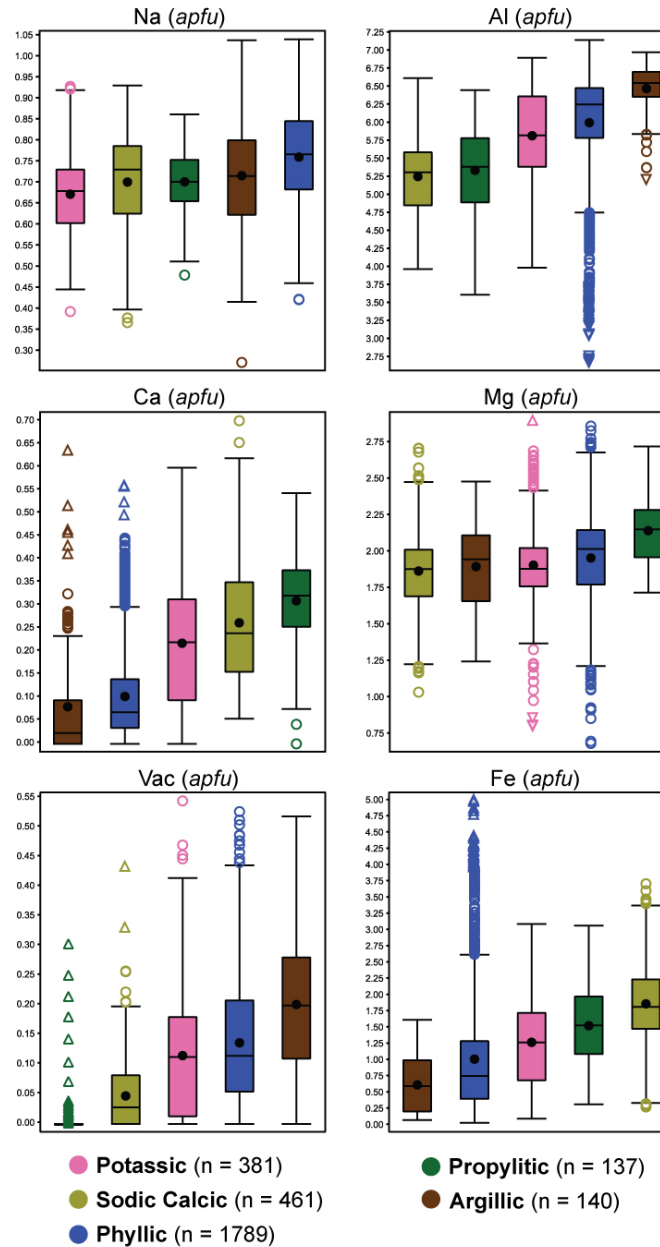


Figure 2-9: TSM major element chemistry and alteration

Samples are sorted based on their alteration assemblage. A total of 2908 analyses from two argillic, six sodic-calcic, 15 phyllic, three potassic, and two propylitic samples. Tukey box plots, far outlier data, sorted by mean of major element *apfu* data, separated by the alteration style. Outliers are classified as $1.5 \cdot (Q3 - Q1)$ and far outlier data is classified as $3 \cdot (Q3 - Q1)$.

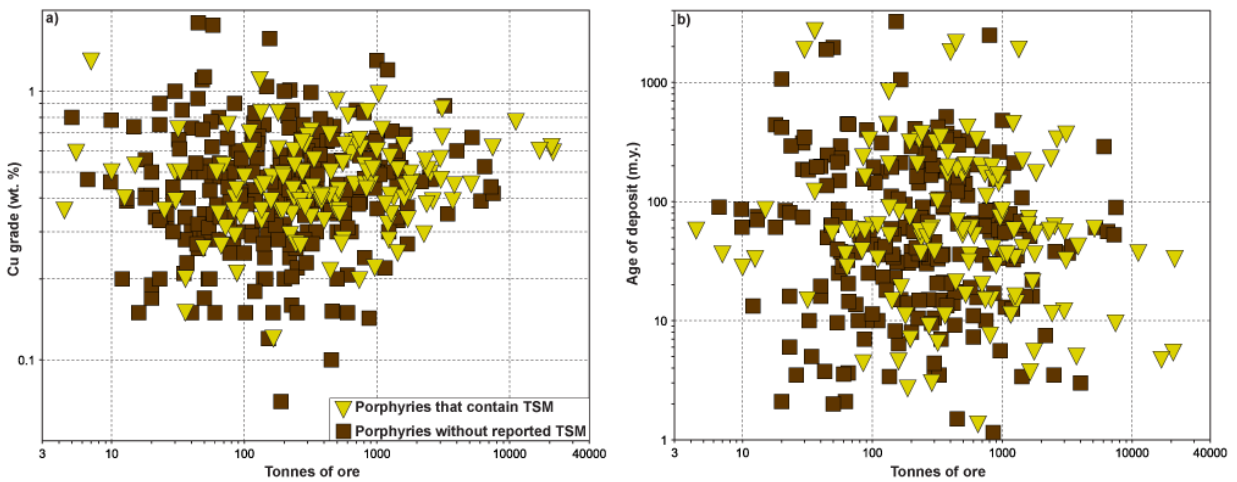


Figure 2-10: Binary plots of deposit tonnage vs. Cu grade and age of the deposit

Binary plots of porphyry deposit tonnage vs. Cu grade (wt. %) and age of deposit (m.y.). Values for tonnage, grade, and age from the USGS database (Singer *et al.* 2008). Yellow triangles represent deposits that contain TSM, brown squares represent deposits that have no reported TSM.

2.10 Tables

Table 2-1: Mineralized porphyry systems examined

Deposit	Location	Deposit Type and Tectonic Setting	Host lithology	Age (Ma)	Porphyry class	Metal Type	Emp. Depth (km)	*Alteration associated with TSM
Casino	300 km northwest of Whitehorse YT	Classic/Andean Continental margin	Quartz-monzonite	73	Calc-alkalic	Cu-Au-Mo	1.5	phyllic, argillic, propylitic
Coxheath	NE Nova Scotia, Canada	Classic?/Andean Continental margin?	Hornblende-Diorite	621	Calc-alkalic	Cu-Mo-Au	?	Sodic-calcic, propylitic
Donoso Breccia Los Bronces	50 km NE of Santiago, Chile	Plutonic?/Andean Continental margin	Quartz-monzonite	4.7	Calc-alkalic	Cu-Mo	3	phyllic
Highland Valley Copper	South-central BC, Canada	Plutonic/Island Arc	Granodiorite	206-210	Calc-alkalic	Cu-Mo	4	sodic-calcic, phyllic, propylitic
New Afton	13 km West of Kamloops, BC, Canada	Volcanic Alkalic/Island Arc	Monzonite	205	Silica-saturated alkalic	Cu-Au	1	potassic, phyllic, propylitic
Schaft Creek	375 km NW of Smithers, BC, Canada	Volcanic Calc-alkaline/Island Arc	Granodiorite	220	Calc-alkalic	Cu-Au-Mo	0.5	potassic, phyllic, propylitic
Woodjam (Deerhorn and Takom)	50 km E of Williams Lake, BC, Canada	Volcanic Calc-alkaline/Island Arc	Monzonite	197	High K calc-alkaline	Cu-Au	TK ~3, DH ~1.7	potassic, phyllic, propylitic

Ma – Millions of years. Km – Kilometres. Emp – emplacement. Data compiled from Singer *et al.* (2008); Osatenko *et al.* (2021); del Real *et al.* (2017) *Organized from most to least common in terms of spatial association.

Table 2-2: Tourmaline physical and optical characteristics

Deposit	Hand-sample features	Transmitted light features	Inclusions	Mineral associations	Other Notes
Casino	mm to sub-mm sized euhedral to subhedral radiating prismatic to acicular grains	Pleochroism: moderate to weak green-blue, light brown-brown to colorless. Intense fine-scale (μm) oscillatory zonation from core to rim in some grains.	rt, zrn, ccp, REE-ap, mo	qz, kfs, bt, ms, chl py, ccp, cv	Grains appear to replace primary magmatic minerals. Minor occurrences of second generation of TSM overgrowing earlier TSM.
Coxheath	sub-mm sized subhedral to euhedral prismatic to massive grains	Pleochroism: moderate to weak blue-green, light brown-brown. Intense fine-scale (μm) oscillatory zonation from core to rim.	hem, zrn, ap	qz, pl, ms, ap, bt, ilm, chl, ep py, ccp	TSM in general are very fine-grained and dark in color (greens/browns in transmitted light).
Donoso Breccia	mm to sub mm size euhedral radiating prismatic grains	Pleochroism: moderate to weak dark brown-pale brown to blue. Fine-scale (μm) oscillatory zonation from core to rim.	ccp ¹ , py ¹	qz, hem ccp, py, bn	Grains form as breccia cement and replace minerals within the host rocks.
HVC	sub-mm sized euhedral radiating prismatic to acicular grains	Pleochroism: moderate to weak light green, brown. Intense fine-scale (μm) oscillatory zonation from core to rim.	qz, act ²	cal, ep, ap, ab, qz, hem, act	Minor occurrences of 2 nd generation of TSM overgrowing earlier Tur.
New Afton	sub-mm sized subhedral clots of prismatic grains	Pleochroism: moderate to weak green-light green to colorless, dark green-brown.	qz, ab, zrn	bt, ms, qz, kfs, ep, dol, cal	Evidence of euhedral grains being fractured and suspended in later mineral phases (qz and cal)
Schaft Creek	mm to sub-mm sized euhedral to subhedral radiating prismatic to acicular grains	Pleochroism: moderate to weak green-blue, light brown-brown to colorless. Intense fine-scale (μm) oscillatory zonation from core to rim in some grains while others appear absent.	rt, zrn, qz, ap, brt, ab, Fe-ox	hem, dol, qz, py,	
Woodjam	mm to sub-mm sized euhedral to subhedral radiating prismatic grains	Pleochroism: moderate to weak dark green-green, light brown-brown to colorless. Intense fine-scale (μm) oscillatory zonation from core to rim	rt, ttn, Fe-ox, ap, ep	qz, ep, dol, ms, kfs, brt, py	Drastic grain size difference between breccia (smaller - μm scale) and other TSM types (larger - mm scale)
Generalized Porphyry Tourmaline	mm to sub-mm sized euhedral to subhedral radiating prismatic grains	Pleochroism: moderate to weak dark green-green, light brown-brown to blue, and more rarely colorless.	zrn, rt, \pm Fe-ox, \pm ap	qz, ep, ap, py	

All TSM examined at the deposits is black in hand sample. ¹-Skewes *et al.* (2003) denoted ccp and py inclusions, whereas only ccp and py forming along fractures were noted in this study. ²-Bryne denoted actinolite inclusions in tourmaline and suggested that the Tur replaced act. Mineral abbreviations after Whitney and Evans (2009).

Table 2-3: Major and minor element analyses of tourmaline from the deposits examined.

	Casino (<i>n</i> = 1379)			Coxheath (<i>n</i> = 239)			HVC (<i>n</i> = 112)			Donoso (<i>n</i> = 203)		
	Avg	Min	Max	Avg	Min	Max	Avg	Min	Max	Avg	Min	Max
SiO ₂	36.95	31.17	39.96	35.42	33.57	38.36	35.46	30.85	37.12	33.72	31.08	36.30
TiO ₂	0.24	<LOD	3.25	0.50	<LOD	1.99	0.34	<LOD	0.87	0.64	0.03	2.49
Al ₂ O ₃	33.15	24.28	37.30	26.41	20.82	31.91	28.06	18.93	35.24	21.46	12.19	33.24
FeO	4.48	0.257	17.36	12.90	8.00	20.11	12.90	2.08	25.27	19.79	3.47	31.97
MgO	8.12	2.653	11.01	7.18	4.48	8.24	7.18	4.06	11.41	5.76	2.80	8.17
CaO	0.34	<LOD	3.55	1.23	0.36	2.74	1.08	0.31	2.87	0.61	0.00	1.33
Na ₂ O	2.44	0.863	3.18	2.19	1.34	2.76	2.34	1.60	2.94	2.35	1.29	2.76
<i>apfu</i> (atoms per formula unit) normalized to 15 cations (<i>T</i> + <i>Z</i> + <i>Y</i>)												
Si(<i>T</i>)	6.018	5.528	6.245	6.010	5.859	6.183	5.899	5.571	6.035	5.977	5.610	6.161
Al(<i>T</i>)	0.018	0.000	0.461	0.008	0.000	0.141	0.081	0.000	0.423	0.018	0.000	0.347
Σ(<i>T</i>)	6.036			6.018			5.980			5.995		
Al(<i>Z</i>)	5.975	2.690	6.000	5.267	4.248	6.000	5.372	3.985	6.000	4.429	2.690	6.000
Mg(<i>Z</i>)	0.018	0.000	0.950	0.304	0.000	0.638	0.163	0.000	0.579	0.187	0.000	0.572
Fe ³⁺ _(calc) (<i>Z</i>)	0.006	0.000	0.738	0.429	0.000	1.339	0.463	0.000	1.795	1.384	0.000	1.795
Σ(<i>Z</i>)	5.999			6.000			6.000			6.000		
Al(<i>Y</i>)	0.370	0.000	0.968	0.000	0.000	0.039	0.031	0.000	0.387	0.018	0.000	0.478
Ti(<i>Y</i>)	0.030	0.000	0.453	0.064	0.000	0.255	0.027	0.000	0.111	0.085	0.004	0.330
Mg(<i>Y</i>)	1.952	0.569	2.771	1.511	0.727	1.888	1.610	0.967	2.563	1.335	0.641	2.071
Fe ²⁺ (<i>Y</i>)	0.610	1.077	2.170	1.407	0.000	1.339	1.352	0.276	2.053	1.566	0.494	2.317
Σ(<i>Y</i>)	2.962			2.982			3.020			3.004		
Ca(<i>X</i>)	0.060	0.000	0.696	0.225	0.066	0.502	0.193	0.054	0.518	0.116	0.000	0.251
Na(<i>X</i>)	0.770	0.278	1.040	0.719	0.452	0.893	0.753	0.500	0.924	0.807	0.426	0.949
Vac	0.169	0.000	0.541	0.059	0.000	0.205	0.061	0.000	0.430	0.076	0.000	0.424
Σ(<i>X</i>)	0.999			1.003			1.007			0.999		
Fe ²⁺ /(Fe ²⁺ +Fe ³⁺)	0.91			0.77			0.74			0.53		

Average analyses consist of an equal combination of core, intermediate, and rim chemical zones. Analyses are from 2896 points from ~750 TSM grains from 29 samples.

Table 2-3 Continued.

	New Afton (<i>n</i> = 275)			Schaft Creek (<i>n</i> = 331)			Woodjam (<i>n</i> = 357)		
	Avg	Min	Max	Avg	Min	Max	Avg	Min	Max
SiO ₂	35.79	33.63	39.45	35.71	33.25	39.00	36.08	32.65	38.96
TiO ₂	0.74	<LOD	2.20	0.74	<LOD	3.59	0.36	0.00	2.69
Al ₂ O ₃	28.73	22.90	34.07	27.78	17.67	37.96	29.79	20.37	37.60
FeO	9.50	1.58	16.43	10.29	0.85	20.74	9.39	0.73	21.15
MgO	8.36	6.77	10.91	8.74	5.06	12.09	7.66	3.15	11.03
CaO	1.46	0.06	3.11	1.70	<LOD	3.02	1.29	<LOD	3.69
Na ₂ O	2.10	1.31	2.97	2.19	1.47	2.83	2.04	1.09	2.95
<i>apfu</i> (atoms per formula unit) normalized to 15 cations (<i>T</i> + <i>Z</i> + <i>Y</i>)									
Si(<i>T</i>)	5.925	5.672	6.063	5.908	5.528	6.057	5.964	5.630	6.245
Al(<i>T</i>)	0.067	0.000	0.317	0.080	0.000	0.457	0.044	0.000	0.370
Σ(<i>T</i>)	5.992			5.988			6.008		
Al(<i>Z</i>)	5.521	4.562	6.000	5.295	3.633	6.000	5.580	4.175	6.000
Mg(<i>Z</i>)	0.302	0.000	0.675	0.341	0.000	0.950	0.217	0.000	0.834
Fe ³⁺ _(calc) (<i>Z</i>)	0.176	0.000	0.843	0.358	0.000	1.614	0.202	0.000	1.334
Σ(<i>Z</i>)	5.999			5.994			5.999		
Al(<i>Y</i>)	0.011	0.000	0.337	0.028	0.000	0.893	0.159	0.000	0.887
Ti(<i>Y</i>)	0.093	0.000	0.269	0.093	0.000	0.453	0.045	0.000	0.347
Mg(<i>Y</i>)	1.760	1.248	2.580	1.810	0.925	2.771	1.669	0.569	2.650
Fe ²⁺ (<i>Y</i>)	1.144	0.209	1.619	1.080	0.108	1.996	1.114	0.096	2.408
Σ(<i>Y</i>)	3.008			3.011			2.987		
Ca(<i>X</i>)	0.260	0.010	0.556	0.303	0.000	0.552	0.233	0.000	0.696
Na(<i>X</i>)	0.673	0.427	0.925	0.703	0.475	0.931	0.651	0.372	0.929
Vac	0.070	0.000	0.301	0.019	0.000	0.301	0.121	0.000	0.541
Σ(<i>X</i>)	1.003			1.025			1.005		
Fe ²⁺ /(Fe ²⁺ +Fe ³⁺)	0.87			0.75			0.85		

2.11 References for TSM at the deposits displayed in Fig. 2-1

(Wendt 1938; Legge 1939; Kuhn 1941; Lynch 1967; Goossens and Hollister 1973; Sillitoe 1973; Hollister and Sirvas 1974; Spatz 1974; Gustafson and Hunt 1975; Panteleyev 1976; Ambrus 1977; Ashley *et al.* 1978; Coochey and Eckman 1978; Panteleyev 1978; Storey 1978; Kwong 1981; Schwartz 1981; Meinert 1982; Bashkirov 1983; Hunt *et al.* 1983; Parry *et al.* 1984; Taylor 1984; Warnars *et al.* 1985; Carten 1986; Palacios *et al.* 1986; Robison 1987; King and Kerrich 1989; Clark 1990; Barr and Reid 1992; Dilles and Einaudi 1992; Lubis *et al.* 1994; Meldrum *et al.* 1994; Bower *et al.* 1995; Dirom *et al.* 1995; Kirkham *et al.* 1995; Arancibia and Clark 1996; Dugmore *et al.* 1996; Lynch and Ortega 1997; Hedenquist *et al.* 1998; Peng *et al.* 1998; Perea 1999; Palacios *et al.* 2001; Perello *et al.* 2001; Sotnikov *et al.* 2001; Landtwing *et al.* 2002; Morozumi 2003; Quang *et al.* 2003; Cannell 2004; Harris *et al.* 2004; Barra *et al.* 2005; Imai 2005; Kirwin *et al.* 2005; Volp 2005; Bouzari and Clark 2006; Norris 2006; Cooke *et al.* 2007; Ferrari *et al.* 2007; Franchini *et al.* 2007; Scott *et al.* 2008; Singer *et al.* 2008; Heberlein and Samson 2010; Lori 2010; Palacios *et al.* 2010; Zukowski 2010; Lefort *et al.* 2011; Baksheev *et al.* 2012; Dill *et al.* 2012; Djouka-Fonkwe *et al.* 2012; Herve *et al.* 2012; Mathur *et al.* 2012; Torro *et al.* 2012; Asadi *et al.* 2013; Del Rio Salas *et al.* 2013; Malla 2013; Pardo *et al.* 2015; Cao *et al.* 2016; Iveson *et al.* 2016; Oliveira *et al.* 2016; Bienko 2017; Maydagán *et al.* 2017; Ochoa-Landín *et al.* 2017; Gibbons 2018; Siddiqui *et al.* 2018; Byrne 2019; Salazar *et al.* 2019; Sokolović *et al.* 2019; Chaffee 2020; Kelley and Graham 2020; Meng *et al.* 2020; Moshefi *et al.* 2020; Skarmeta 2020; Warlo *et al.* 2020; Osatenko *et al.* 2021).

2.12 References

- Ahmed, A.D., Fisher, L., Pearce, M., Escolme, A., Cooke, D.R., Howard, D. and Belousov, I., 2020. A Microscale Analysis of Hydrothermal Epidote: Implications for the Use of Laser Ablation-Inductively Coupled Plasma-Mass Spectrometry Mineral Chemistry in Complex Alteration Environments. *Economic Geology*, 115(4): 793-811.
<http://doi.org/10.5382/econgeo.4705>
- Ambrus, J., 1977. Geology of the La Abra Porphyry Cu deposit, Chile. *Economic Geology*, 72(6): 1062-1085. <http://doi.org/10.2113/gsecongeo.72.6.1062>
- Andreozzi, G.B., Bosi, F., Celata, B., Capizzi, L.S., Stagno, V. and Beckett-Brown, C.E., 2020. Crystal-chemical behavior of Fe²⁺ in tourmaline dictated by structural stability: insights from a schorl with formula Na^Y(Fe²⁺Al)^Z(Al₅Fe²⁺)(Si₆O₁₈)(BO₃)₃(OH)₃(OH,F) from Seagull batholith (Yukon Territory, Canada). *Physics and Chemistry of Minerals*, 47(6).
<http://doi.org/10.1007/s00269-020-01094-7>
- Arancibia, O.N. and Clark, A.H., 1996. Early magnetite-amphibole-plagioclase alteration-mineralization in the Island Copper porphyry copper-gold-molybdenum deposit, British Columbia. *Economic Geology*, 91(2): 402-438.
<http://doi.org/10.2113/gsecongeo.91.2.402>
- Asadi, S., Moore, F., Zarasvandi, A. and Khosrojerdi, M., 2013. First report on the occurrence of CO₂-bearing fluid inclusions in the Meiduk porphyry copper deposit, Iran: implications for mineralisation processes in a continental collision setting. *Geologos*, 19(4): 301-320.
<http://doi.org/10.2478/logos-2013-0019>

- Ashley, P.M., Billington, W.G., Graham, R.L. and Neale, R.C., 1978. Geology of the Coalstoun Porphyry Copper Prospect Southeast Queensland Australia. *Economic Geology*, 73(5): 945-965. <http://doi.org/10.2113/gsecongeo.73.5.945>
- Bačík, P., Ertl, A., Števkó, M., Giester, G. and Sečkář, P., 2015. Acicular Zoned Tourmaline (Magnesio-Foitite to Foitite) from a Quartz Vein near Tisovec, Slovakia: The Relationship between Crystal Chemistry and Acicular Habit. *The Canadian Mineralogist*, 53(2): 221-234. <http://doi.org/10.3749/canmin.1400085>
- Baker, M.J., Wilkinson, J.J., Wilkinson, C.C., Cooke, D.R. and Ireland, T., 2020. Epidote Trace Element Chemistry as an Exploration Tool in the Collahuasi District, Northern Chile. *Economic Geology*, 115(4): 749-770. <http://doi.org/10.5382/econgeo.4739>
- Baksheev, I.A., Chitalin, A.F., Yapaskurt, V.O., Vígasina, M.F., Bryzgalov, I.A. and Ustinov, V.I., 2010. Tourmaline in the Vetka porphyry copper-molybdenum deposit of the Chukchi Peninsula of Russia. *Moscow University Geology Bulletin*, 65(1): 27-38. <http://doi.org/10.3103/s0145875210010035>
- Baksheev, I.A., Prokof'ev, V.Y., Yapaskurt, V.O., Vígasina, M.F., Zorina, L.D. and Solov'ev, V.N., 2011. Ferric-iron-rich tourmaline from the Darasun gold deposit, Transbaikalia, Russia. *The Canadian Mineralogist*, 49(1): 263-276. <http://doi.org/10.3749/canmin.49.1.263>
- Baksheev, I.A., Trumbull, R.B., Popov, M.P., Erokhin, Y.V., Kudryavtseva, O.E., Yapaskurt, V.O., Khiller, V.V., Vovna, G.M. and Kiselev, V.I., 2017. Chemical and boron isotopic composition of tourmaline from the Mariinsky emerald deposit, Central Urals, Russia. *Mineralium Deposita*, 53(4): 565-583. <http://doi.org/10.1007/s00126-017-0759-z>

- Baksheev, I.A., Yu Prokofev, V., Zارايسкий, G.P., Chitalin, A.F., Yapaskurt, V.O., Nikolaev, Y.N., Tikhomirov, P.L., Nagornaya, E.V., Rogacheva, L.I., Gorelikova, N.V. and Kononov, O.V., 2012. Tourmaline as a prospecting guide for the porphyry-style deposits. *European Journal of Mineralogy*, 24(6): 957-979. <http://doi.org/10.1127/0935-1221/2012/0024-2241>
- Barr, J.M. and Reid, D.L., 1992. Hydrothermal alteration at the Haib porphyry copper deposit, Namibia: Stable isotope and fluid inclusion patterns. *Communs Geological Survey Namibia*, 8: 23-35.
- Barra, F., Ruiz, J., Valencia, V.A., Ochoa-Landín, L.H., Chesley, J.T. and Zurcher, L., 2005. Laramide Porphyry Cu-Mo mineralization in Northern Mexico: Age Constraints from Re-Os Geochronology in Molybdenite. *Economic Geology*, 100(8): 1605-1616. <http://doi.org/10.2113/gsecongeo.100.8.1605>
- Bashkirov, B.G., 1983. Explosion breccias in the Kounrad porphyry-copper deposit. *International Geology Review*, 25(4): 373-380. <http://doi.org/10.1080/00206818309466714>
- Beckett-Brown, C.E., McDonald, A.M., McClenaghan, M.B., Plouffe, A. and Ferbey, T., 2021. Investigation of tourmaline characteristics in bedrock and surficial sediment samples from two Canadian porphyry copper systems. In: E. Schestelaar and A. Plouffe (Editors), Targeted Geoscience Initiative 5: contributions to the understanding and exploration of porphyry deposits, Geological Survey of Canada, pp. 109-135. <http://doi.org/10.4095/327989>

- Bédard, J.H., Harris, L.B. and Thurston, P.C., 2013. The hunting of the snArc. *Precambrian Research*, 229: 20-48. <http://doi.org/10.1016/j.precamres.2012.04.001>
- Berryman, E.J., Wunder, B., Wirth, R., Rhede, D., Schettler, G., Franz, G. and Heinrich, W., 2015. An experimental study on K and Na incorporation in dravitic tourmaline and insight into the origin of diamondiferous tourmaline from the Kokchetav Massif, Kazakhstan. *Contributions to Mineralogy and Petrology*, 169(3).
<http://doi.org/10.1007/s00410-015-1116-9>
- Bienko, T., 2017. The Sierra Gorda porphyry Cu-Mo-(Au) deposit Chile. *Przegląd Geologiczny*, 65(9): 555-559.
- Bosi, F., 2018. Tourmaline crystal chemistry. *American Mineralogist*, 103(2): 298-306.
<http://doi.org/10.2138/am-2018-6289>
- Bosi, F. and Lucchesi, S., 2004. Crystal chemistry of the schorl-dravite series. *European Journal of Mineralogy*, 16(2): 335-344. <http://doi.org/10.1127/0935-1221/2004/0016-0335>
- Bosi, F. and Lucchesi, S., 2007. Crystal chemical relationships in the tourmaline group: Structural constraints on chemical variability. *American Mineralogist*, 92(7): 1054-1063.
<http://doi.org/10.2138/am.2007.2370>
- Bouzari, F. and Clark, A.H., 2006. Prograde Evolution and Geothermal Affinities of a Major Porphyry Copper Deposit: The Cerro Colorado Hypogene Protore, I Region, Northern Chile. *Economic Geology*, 101(1): 95-134. <http://doi.org/10.2113/gsecongeo.101.1.95>
- Bower, B., Payne, J., DeLong, C. and Rebagliati, C.M., 1995. The oxide-gold, supergene and hypogene zones at the Casino gold-copper-molybdenum deposit, west central Yukon In: T. Schroeter (Editor), *Porphyry Copper Deposits of the Northwestern Cordillera of North*

- America. Canadian Institute of Mining and Metallurgy and Petroleum, Montreal, Quebec, pp. 352-366.
- Bozkaya, Ö., Baksheev, I.A., Hanilçi, N., Bozkaya, G., Prokofiev, V.Y., Öztaş, Y. and Banks, D.A., 2020. Tourmaline Composition of the Kışladağ Porphyry Au Deposit, Western Turkey: Implication of Epithermal Overprint. *Minerals*, 10(9).
<http://doi.org/10.3390/min10090789>
- Briskey, J.A. and Bellamy, J.R., 1976. Bethlehem Copper's Jersey, East Jersey, Huestis and Iona deposits. In: A. Sutherland Brown (Editor), *Porphyry Deposits of the Canadian Cordillera*. Canadian Institute of Mining and Metallurgy and Petroleum, Montreal, Quebec, pp. 105-119.
- Byrne, K., 2019. Diagnostic Features of the Rocks and Minerals Peripheral to the Highland Valley Copper District, British Columbia, Canada: Implications for the genesis of porphyry Cu systems and their footprints. PhD Thesis, University of Alberta, Edmonton, 211 pp.
- Byrne, K., Trumbull, R.B., Lesage, G., Gleeson, S.A., Ryan, J., Kyser, K. and Lee, R.G., 2020. Mineralogical and Isotopic Characteristics of Sodic-Calcic Alteration in the Highland Valley Copper District, British Columbia, Canada: Implications for Fluid Sources in Porphyry Cu Systems. *Economic Geology*, 115(4): 841-870.
<http://doi.org/10.5382/econgeo.4740>
- Cannell, J., 2004. Teniente porphyry copper-molybdenum deposit, Central Chile. PhD Thesis, University of Tasmania, Australia.

- Cao, M.J., Li, G.M., Qin, K.Z., Evans, N.J. and Seitmuratova, E.Y., 2016. Assessing the magmatic affinity and petrogenesis of granitoids at the giant Aktogai porphyry Cu deposit, Central Kazakhstan. *American Journal of Science*, 316(7): 614-668.
<http://doi.org/10.2475/07.2016.02>
- Carten, R.B., 1986. Sodium-calcium metasomatism; chemical, temporal, and spatial relationships at the Yerington, Nevada, porphyry copper deposit. *Economic Geology*, 81(6): 1495-1519. <http://doi.org/10.2113/gsecongeo.81.6.1495>
- Casselmann, S.C. and Brown, H., 2017. Casino porphyry copper-gold-molybdenum deposit, central Yukon (Yukon MINFILE 115J028); *in* Yukon Exploration and Geology Overview 2016, (ed.) K.W. MacFarlane; Yukon Geological Survey, p. 61–74, plus digital appendices.
- Chaffee, M.A., 2020. Geochemical and Mineralogical Study of the Red Mountain Porphyry Copper-Molybdenum Deposit and Vicinity, Santa Cruz County, Arizona. *USGS Scientific Investigations Report*: 164. <http://doi.org/10.3133/sir20195077>
- Cheng, L., Zhang, C., Liu, X., Yang, X., Zhou, Y., Horn, I., Weyer, S. and Holtz, F., 2021. Significant boron isotopic fractionation in the magmatic evolution of Himalayan leucogranite recorded in multiple generations of tourmaline. *Chemical Geology*, 571. <http://doi.org/10.1016/j.chemgeo.2021.120194>
- Clark, A.H., 1990. The slump breccias of the Toquepala porphyry Cu (-Mo) deposit, Peru: Implications for fragment rounding in hydrothermal breccias. *Economic Geology*, 85(7): 1677-1685. <http://doi.org/10.2113/gsecongeo.85.7.1677>

- Clarke, D.B., Reardon, N.C., Chatterjee, A.K. and Gregoire, D.C., 1989. Tourmaline Composition as a Guide to Mineral Exploration - a Reconnaissance Study from Nova-Scotia Using Discriminant Function-Analysis. *Economic Geology*, 84(7): 1921-1935. <http://doi.org/10.2113/gsecongeo.84.7.1921>
- Codeço, M.S., Weis, P., Trumbull, R.B., Glodny, J., Wiedenbeck, M. and Romer, R.L., 2019. Boron Isotope Muscovite-Tourmaline Geothermometry Indicates Fluid Cooling During Magmatic-Hydrothermal W-Sn Ore Formation. *Economic Geology*, 114(1): 153-163. <http://doi.org/10.5382/econgeo.2019.4625>
- Codeço, M.S., Weis, P., Trumbull, R.B., Pinto, F., Lecumberri-Sanchez, P. and Wilke, F.D.H., 2017. Chemical and boron isotopic composition of hydrothermal tourmaline from the Panasqueira W-Sn-Cu deposit, Portugal. *Chemical Geology*, 468: 1-16. <http://doi.org/10.1016/j.chemgeo.2017.07.011>
- Codeço, M.S., Weis, P., Trumbull, R.B., Van Hinsberg, V., Pinto, F., Lecumberri-Sanchez, P. and Schleicher, A.M., 2020. The imprint of hydrothermal fluids on trace-element contents in white mica and tourmaline from the Panasqueira W–Sn–Cu deposit, Portugal. *Mineralium Deposita*, 56(3): 481-508. <http://doi.org/10.1007/s00126-020-00984-8>
- Coochey, D.V. and Eckman, P., 1978. Geology of the La Verde Copper Deposits, Michoacan, Mexico, Proceeding of the porphyry copper symposium. Arizona Geological Society Digest XI, pp. 129-137.
- Cooke, D.R., Agnew, P., Hollings, P., Baker, M., Chang, Z., Wilkinson, J.J., Ahmed, A., White, N.C., Zhang, L., Thompson, J., Gemmell, J.B., Danyushevsky, L. and Chen, H., 2020a. Recent advances in the application of mineral chemistry to exploration for porphyry

- copper–gold–molybdenum deposits: detecting the geochemical fingerprints and footprints of hypogene mineralization and alteration. *Geochemistry: Exploration, Environment, Analysis*, 20(2): 176-188. <http://doi.org/10.1144/geochem2019-039>
- Cooke, D.R., Wilkinson, J.J., Baker, M., Agnew, P., Phillips, J., Chang, Z., Chen, H., Wilkinson, C.C., Inglis, S., Hollings, P., Zhang, L., Gemmell, J.B., White, N.C., Danyushevsky, L. and Martin, H., 2020b. Using Mineral Chemistry to Aid Exploration: A Case Study from the Resolution Porphyry Cu-Mo Deposit, Arizona. *Economic Geology*, 115(4): 813-840. <http://doi.org/10.5382/econgeo.4735>
- Cooke, D.R., Wilkinson, J.J. and Pacey, A., 2020c. Chlorite and Epidote Mineral Chemistry in Porphyry Ore Systems: A Case Study of the Northparkes District, New South Wales, Australia. *Economic Geology*, 115(4): 701-727. <http://doi.org/10.5382/econgeo.4700>
- Cooke, D.R., Wilson, A.J., House, M.J., Wolfe, R.C., Walshe, J.L., Lickfold, V. and Crawford, A.J., 2007. Alkalic porphyry Au – Cu and associated mineral deposits of the Ordovician to Early Silurian Macquarie Arc, New South Wales. *Australian Journal of Earth Sciences*, 54(2-3): 445-463. <http://doi.org/10.1080/08120090601146771>
- Davies, A., 1992. *The Science and Practice of Welding: Volume 1*, 1. Cambridge University Press.
- del Real, I., Bouzari, F., Bissig, T., Blackwell, J., Sherlock, R., Thompson, J.F.H. and Hart, R.J., 2017. Spatially and temporally associated porphyry deposits with distinct Cu/Au/Mo Ratios, Woodjam District, Central British Columbia. *Economic Geology*, 112(7): 1673-1717. <http://doi.org/10.5382/econgeo.2017.4526>

- Del Rio Salas, R., Ochoa-Landín, L., Ruiz, J., Eastoe, C., Meza-Figueroa, D., Zuñiga-Hernández, H., Mendivil-Quijada, H. and Quintanar-Ruiz, F., 2013. Geology, stable isotope, and U–Pb geochronology of the Mariquita porphyry copper and Lucy Cu–Mo deposits, Cananea District, Mexico: A contribution to regional exploration. *Journal of Geochemical Exploration*, 124: 140-154. <http://doi.org/10.1016/j.gexplo.2012.08.016>
- Dietrich, R.V., 1985. The Tourmaline Group. Van Nostrand Reinhold Company, New York. <http://doi.org/10.1007/978-1-4684-8085-6>
- Dill, H.G., Garrido, M.M., Melcher, F., Gomez, M.C. and Luna, L.I., 2012. Depth-related variation of tourmaline in the breccia pipe of the San Jorge porphyry copper deposit, Mendoza, Argentina. *Ore Geology Reviews*, 48: 271-277. <http://doi.org/10.1016/j.oregeorev.2012.04.006>
- Dilles, J.H. and Einaudi, M., 1992. Wall-rock alteration and hydrothermal flow paths about the Ann-Mason porphyry copper deposit, Nevada-A 6-Km vertical reconstruction. *Economic Geology*, 87(8): 1963-2001. <http://doi.org/10.2113/gsecongeo.87.8.1963>
- Dirom, G.E., Dittrick, M.P., McArthur, D.R., Orgryzlo, P.L., Pardoe, A.J. and Stothart, P.G., 1995. Bell and Granisle porphyry copper-gold mines, Babine region, west-central British Columbia. In: T. Schroeter (Editor), *Porphyry Copper Deposits of the Northwestern Cordillera of North America*. Canadian Institute of Mining and Metallurgy and Petroleum, Montreal, Quebec, pp. 256-289.
- Djouka-Fonkwe, M.L., Kyser, K., Clark, A.H., Urqueta, E., Oates, C.J. and Inlenfeld, C., 2012. Recognizing Propylitic Alteration Associated with Porphyry Cu-Mo Deposits in Lower Greenschist Facies Metamorphic Terrain of the Collahuasi District, Northern Chile—

- Implications of Petrographic and Carbon Isotope Relationships. *Economic Geology*, 107(7): 1457-1478. <http://doi.org/10.2113/econgeo.107.7.1457>
- Dugmore, M.A., Leaman, P.W. and Philip, R., 1996. Discovery of the Mt. Bini porphyry copper-gold-molybdenum deposit in the Owen Stanley Ranges, Papua New Guinea - A geochemical case history. *Journal of Geochemical Exploration*, 57(1-3): 89-100. [http://doi.org/10.1016/s0375-6742\(96\)00018-0](http://doi.org/10.1016/s0375-6742(96)00018-0)
- Dunn, P.J., 1977. Uvite, a newly classified gem tourmaline. *The Journal of Gemmology*, 15(6): 300-308.
- Dutrow, B.L. and Henry, D.J., 2018. Tourmaline compositions and textures: reflections of the fluid phase. *Journal of Geosciences*: 99-110. <http://doi.org/10.3190/jgeosci.256>
- Escolme, A., Cooke, D.R., Hunt, J., Berry, R.F., Maas, R. and Creaser, R.A., 2020. The Productora Cu-Au-Mo Deposit, Chile: A Mesozoic Magmatic-Hydrothermal Breccia Complex with Both Porphyry and Iron Oxide Cu-Au Affinities. *Economic Geology*, 115(3): 543-580. <http://doi.org/10.5382/econgeo.4718>
- Ferrari, L., Valencia-Moreno, M.n. and Bryan, S., 2007. Magmatism and tectonics of the Sierra Madre Occidental and its relation with the evolution of the western margin of North America. *Geology of Mexico: Celebrating the Centenary of the Geological Society of Mexico*. [http://doi.org/10.1130/2007.2422\(01\)](http://doi.org/10.1130/2007.2422(01))
- Franchini, M., Impiccini, A., Meinert, L., Grathoff, G. and Schalamuk, I.B.A., 2007. Clay Mineralogy and Zonation in the Campana Mahuida Porphyry Cu Deposit, Neuquén, Argentina: Implications for Porphyry Cu Exploration. *Economic Geology*, 102: 27-34.

- Frikken, P.H., Cooke, D.R., Walshe, J.L., Archibald, D., Skarmeta, J., Serrano, L. and Vargas, R., 2005. Mineralogical and isotopic zonation in the Sur-Sur tourmaline breccia, Río Blanco-Los Bronces Cu-Mo deposit, Chile: Implications for ore genesis. *Economic Geology*, 100(5): 935-961. <http://doi.org/10.2113/gsecongeo.100.5>
- Gadas, P., Novak, M., Stanek, J., Filip, J. and Galiova, M.V., 2012. Compositional Evolution of Zoned Tourmaline Crystals from Pockets in Common Pegmatites of the Moldanubian Zone, Czech Republic. *The Canadian Mineralogist*, 50(4): 895-912. <http://doi.org/10.3749/canmin.50.4.895>
- Galbraith, C.G., Clarke, D.B., Trumbull, R.B. and Wiedenbeck, M., 2009. Assessment of tourmaline compositions as an indicator of emerald mineralization at the Tsa da Glisza prospect Yukon Territory, Canada. *Economic Geology*, 104(5): 713-731. <http://doi.org/10.2113/gsecongeo.104.5.713>
- García-Ruiz, J.M. and Otálora, F., 2015. Crystal Growth in Geology: Patterns on the Rocks, Handbook of crystal growth. Elsevier, pp. 1-43.
- Gibbons, J., 2018. Magmatic-hydrothermal evolution of the Pampa Escondida porphyry copper deposit northern Chile. PhD Thesis, University of Arizona, Arizona, 288 pp.
- Godwin, C.I., 1975. Alternative Interpretations for the Casino Complex and Klotassin Batholith in the Yukon Crystalline Terrane. *Canadian Journal of Earth Sciences*, 12(11): 1910-1916. <http://doi.org/10.1139/e75-168>
- Goossens, P.J. and Hollister, V.F., 1973. Structural Control And Hydrothermal Alteration Patter of Chaucha Porphyry Copper, Ecuador. *Mineralium Deposita*, 8(4). <http://doi.org/10.1007/bf00207515>

Grice, J.D., Ercit, T.C. and Hawthorne, F.C., 1993. Povondraite, a redefinition of the tourmaline ferridravite. *American Mineralogist*, 78(3-4): 433-436.

Griffin, W.L., Slack, J.F., Ramsden, A.R., Win, T.T. and Ryan, C.G., 1996. Trace elements in tourmalines from massive sulfide deposits and tourmalinites Geochemical controls and exploration application. *Economic Geology*, 91(4): 657-675.

<http://doi.org/10.2113/gsecongeo.91.4.657>

Gustafson, L.B. and Hunt, J.P., 1975. The porphyry copper deposit at El Salvador, Chile.

Economic Geology, 70(5): 857-912. <http://doi.org/10.2113/gsecongeo.70.5.857>

Harris, A.C., Allen, C.M., Bryan, S.E., Campbell, I.H., Holcombe, R.J. and Palin, J.M., 2004.

LA-ICP-MS U-Pb zircon geochronology of regional volcanism hosting the Bajo de la Alumbrera Cu-Au deposit: implications for porphyry-related mineralization. *Mineralium Deposita*, 39(1): 46-67. <http://doi.org/10.1007/s00126-003-0381-0>

Hawthorne, F.C. and Dirlam, D.M., 2011. Tourmaline the Indicator Mineral: From Atomic Arrangement to Viking Navigation. *Elements*, 7(5): 307-312.

<http://doi.org/10.2113/gselements.7.5.307>

Heberlein, D.R. and Samson, H., 2010. An Assessment of Soil Geochemical Methods for Detecting Copper-Gold Porphyry Mineralization through Quaternary Glaciofluvial Sediments at the Kwanika Central Zone, North-Central British Columbia. In: Geoscience BC, Report 2010-03.

Hedenquist, J.W., Arribas Jr, A. and Reynolds, T.J., 1998. Evolution of an intrusion-centered hydrothermal system: Far Southeast-Lepanto porphyry and epithermal Cu-Au deposits,

- Philippines. *Economic Geology*, 93(4): 373-404.
<http://doi.org/10.2113/gsecongeo.93.4.373>
- Henry, D.J. and Dutrow, B.L., 2018. Tourmaline studies through time: contributions to scientific advancements. *Journal of Geosciences*: 77-98. <http://doi.org/10.3190/jgeosci.255>
- Henry, D.J. and Guidotti, C.V., 1985. Tourmaline as a petrogenetic indicator mineral an example from the staurolite-grade metapelites of NW Maine. *American Mineralogist*, 70: 1-15.
- Henry, D.J., Kirkland, B.L. and Kirkland, D.W., 1999. Sector-zoned tourmaline from the cap rock of a salt dome. *European Journal of Mineralogy*, 11(2): 263-280.
<http://doi.org/10.1127/ejm/11/2/0263>
- Henry, D.J., Sun, H., Slack, J.F. and Dutrow, B.L., 2008. Tourmaline in meta-evaporites and highly magnesian rocks: perspectives from Namibian tourmalinites. *European Journal of Mineralogy*, 20(5): 889-904. <http://doi.org/10.1127/0935-1221/2008/0020-1879>
- Herve, M., Sillitoe, R.H., Wong, C., Fernandez, P., Crignola, F., Ipinza, M. and Urzua, F., 2012. Geologic Overview of the Escondida Porphyry Copper District, Northern Chile. In: J.W. Hedenquist, M. Harris and F. Camus (Editors), *Geology and Genesis of Major Copper Deposits and Districts of the World: A tribute to Richard H. Sillitoe*. Society of Economic Geologists, Littleton, CO, pp. 55-78. <http://doi.org/10.5382/sp.16.03>
- Hollings, P. and Orovan, E., 2020. Exploring the Green Rock Environment: An Introduction. *Economic Geology*, 115(4): 695-700. <http://doi.org/10.5382/econgeo.4751>
- Hollister, V.F. and Sirvas, E.B., 1974. The Michiquillay Porphyry Copper Deposit *Mineralium Deposita*, 9(3): 261-269. <http://doi.org/10.1007/bf00204000>

- Hunt, J.P., Bratt, J.A. and Marquardt, J.C., 1983. Quebrada-Blanca, Chile - an Enriched Porphyry Copper-Deposit. *Mining Engineering*, 35(6): 636-644.
- Imai, A., 2005. Evolution of hydrothermal system at the Dizon porphyry Cu-Au deposit, Zambales, Philippines. *Resource Geology*, 55(2): 73-90. <http://doi.org/10.1111/j.1751-3928.2005.tb00230.x>
- Iveson, A.A., Webster, J.D., Rowe, M.C. and Neill, O.K., 2016. Magmatic–hydrothermal fluids and volatile metals in the Spirit Lake pluton and Margaret Cu–Mo porphyry system, SW Washington, USA. *Contributions to Mineralogy and Petrology*, 171(3): 20. <http://doi.org/10.1007/s00410-015-1224-6>
- Jiang, S.Y., Palmer, M.R., McDonald, A.M., Slack, J.F. and Leitch, C.H.B., 1996. Feruvite from the Sullivan Pb-Zn-Ag deposit, British Columbia. *Canadian Mineralogist*, 34: 733-740.
- Kalliomäki, H., Wagner, T., Fusswinkel, T. and Sakellaris, G., 2017. Major and trace element geochemistry of tourmalines from Archean orogenic gold deposits: Proxies for the origin of gold mineralizing fluids? *Ore Geology Reviews*, 91: 906-927. <http://doi.org/10.1016/j.oregeorev.2017.08.014>
- Kelley, K.D. and Graham, G.E., 2020. Hydrogeochemistry in the Yukon-Tanana upland region of east-central Alaska: Possible exploration tool for porphyry-style deposits. *Applied Geochemistry*, 124: 104821. <http://doi.org/10.1016/j.apgeochem.2020.104821>
- King, R.W. and Kerrich, R.W., 1989. Strontium Isotope Compositions of Tourmaline from Lode Gold Deposits of the Archean Abitibi Greenstone-Belt (Ontario Quebec, Canada) - Implications for Source Reservoirs. *Chemical Geology*, 79(3): 225-240. [http://doi.org/10.1016/0168-9622\(89\)90031-6](http://doi.org/10.1016/0168-9622(89)90031-6)

- Kirkham, R. V. and Margolis, J., 1995. Overview of the Sulphurets area, northwestern British Columbia. In: T. Schroeter (Editor), *Porphyry Copper Deposits of the Northwestern Cordillera of North America*. Canadian Institute of Mining and Metallurgy and Petroleum, Montreal, Quebec, 46, pp. 473-483.
- Kirkpatrick, R.J., 1975. Crystal growth rate from the melt: a review. *American Mineralogist*, 60: 798-814.
- Kirwin, D.J., Turmagnai, W.D. and Wolfe, R., 2005. Exploration history, geology, and mineralisation of the Kharmagtai gold-copper porphyry district, south Gobi Region, Mongolia, Geodynamics and metallogeny of Mongolia with a special emphasis on copper and gold deposits. SEG-IAGOD field trip.
- Kontak, D.J., DeWolfe, J. and Finck, P.W., 2001. The Coxheath Plutonic-Volcanic Belt (NTS 11K/01): A Linked Porphyry-Epithermal Mineralized System of Precambrian Age. In: M.a.M.B.R.o. Activities (Editor), pp. 69-87.
- Kuhn, T.H., 1941. Pipe deposits of the copper creek area, Arizona. *Economic Geology*, 36(5): 512-538. <http://doi.org/10.2113/gsecongeo.36.5.512>
- Kwong, Y.-T.J., 1981. A new look at the Afton copper mine in light of mineral distributions, host rock geochemistry and irreversible mineral-solution interactions. PhD Thesis, University of British Columbia.
- Landtwing, M., Dillenbeck, E.D., Leake, M.H. and Heinrich, C.A., 2002. Evolution of the Breccia-Hosted Porphyry Cu-Mo-Au Deposit at Agua Rica, Argentina: Progressive Unroofing of a Magmatic Hydrothermal System. *Economic Geology*, 97(6): 1273-1292. <http://doi.org/10.2113/gsecongeo.97.6.1273>

- Launay, G., Sizaret, S., Guillou-Frottier, L., Gloaguen, E. and Pinto, F., 2018. Deciphering fluid flow at the magmatic-hydrothermal transition: A case study from the world-class Panasqueira W–Sn–(Cu) ore deposit (Portugal). *Earth and Planetary Science Letters*, 499: 1-12. <http://doi.org/10.1016/j.epsl.2018.07.012>
- Lefort, D., Hanley, J.J. and Guillong, M., 2011. Subepithermal Au-Pd Mineralization Associated with an Alkalic Porphyry Cu-Au Deposit, Mount Milligan, Quesnel Terrane, British Columbia, Canada. *Economic Geology*, 106(5): 781-808. <http://doi.org/10.2113/econgeo.106.5.781>
- Legge, J.A., 1939. Paragenesis of the ore minerals of the Miami Mine Arizona. MSc Thesis, University of Arizona, Arizona, 48 pp.
- Li, W., Qiao, X., Zhang, F. and Zhang, L., 2021. Tourmaline as a potential mineral for exploring porphyry deposits: a case study of the Bilihe gold deposit in Inner Mongolia, China. *Mineralium Deposita*: 1-22. <http://doi.org/10.1007/s00126-021-01051-6>
- López de Azarevich, V., Fulignati, P., Gioncada, A. and Azarevich, M., 2021. Rare element minerals' assemblage in El Quemado pegmatites (Argentina): insights for pegmatite melt evolution from gahnite, columbite-group minerals and tourmaline chemistry and implications for minerogenesis. *Mineralogy and Petrology*, 115(5): 497-518. <http://doi.org/10.1007/s00710-021-00752-0>
- Lori, J.D.L., 2010. Investigations of grade control, Macarthur mine, Yerrington, Nevada: an oxidized porphyry copper system. MSc Thesis, University of Texas, 336 pp.
- Lubis, H., Prihatmoko, S. and James, L.P., 1994. Bulagidun prospect: a copper, gold and tourmaline bearing porphyry and breccia system in northern Sulawesi, Indonesia. *Journal*

- of Geochemical Exploration*, 50(1-3): 257-278. [http://doi.org/10.1016/0375-6742\(94\)90027-2](http://doi.org/10.1016/0375-6742(94)90027-2)
- Lynch, D.W., 1967. The geology of the esperanza mine and vicinity pima county, Arizona. MSc Thesis, University of Arizona, 70 pp.
- Lynch, G. and Ortega, S., 1997. Hydrothermal alteration and tourmaline-albite equilibria at the Coxheath porphyry Cu-Mo-Au deposit, Nova Scotia. *Canadian Mineralogist*, 35(1): 79-94.
- Malla, F.P.O., 2013. Estudio de geología, mineralización y alteraciones en la concesión minera Cascabel Provincia de Imbabura. BSc Thesis, Escuela Politécnica Nacional.
- Manéglia, N., Beaudoin, G. and Simard, M., 2018. Indicator minerals of the Meliadine orogenic gold deposits, Nunavut (Canada), and application to till surveys. *Geochemistry: Exploration, Environment, Analysis*, 18(3): 241-251. <http://doi.org/10.1144/geochem2017-036>
- Marger, K., Luisier, C., Baumgartner, L.P., Putlitz, B., Dutrow, B.L., Bouvier, A.-S. and Dini, A., 2019. Origin of Monte Rosa whiteschist from in-situ tourmaline and quartz oxygen isotope analysis by SIMS using new tourmaline reference materials. *American Mineralogist*, 104(10): 1503-1520. <http://doi.org/10.2138/am-2019-7012>
- Marschall, H.R. and Jiang, S.Y., 2011. Tourmaline Isotopes: No Element Left Behind. *Elements*, 7(5): 313-319. <http://doi.org/10.2113/gselements.7.5.313>
- Mathur, R., Ruiz, J., Casselman, M.J., Megaw, P. and van Egmond, R., 2012. Use of Cu isotopes to distinguish primary and secondary Cu mineralization in the Cañariaco Norte porphyry

- copper deposit, Northern Peru. *Mineralium Deposita*, 47(7): 755-762.
<http://doi.org/10.1007/s00126-012-0439-y>
- Maydagán, L., Franchini, M., Chiaradia, M., Bouhier, V., Di Giuseppe, N., Rey, R. and Dimieri, L., 2017. Petrogenesis of Quebrada de la Mina and Altar North porphyries (Cordillera of San Juan, Argentina): Crustal assimilation and metallogenic implications. *Geoscience Frontiers*, 8(5): 1135-1159. <http://doi.org/10.1016/j.gsf.2016.11.011>
- McMillan, N.J. and Panteleyev, A., 1988. Ore Deposit Models - Porphyry Copper Deposits. *Geoscience Canada*, 7(2): 52-63.
- Meinert, L., 1982. Skarn, Manto, and Breccia Pipe Formation in Sedimentary Rocks of the Cananea Mining District, Sonora, Mexico. *Economic Geology*, 77(4): 919-949.
<http://doi.org/10.2113/gsecongeo.77.4.919>
- Meldrum, S.J., Aquino, R.S., Gonzales, R.I., Burke, R.J., Suyadi, A., Irianto, B. and Clarke, D.S., 1994. The Batu Hijau porphyry copper-gold deposit, Sumbawa Island, Indonesia. *Journal of Geochemical Exploration*, 50(1-3): 203-220. [http://doi.org/10.1016/0375-6742\(94\)90025-6](http://doi.org/10.1016/0375-6742(94)90025-6)
- Meng, X., Richards, J., Mao, J., Ye, H., DuFrane, S.A., Creaser, R., Marsh, J. and Petrus, J., 2020. The Tongkuangyu Cu Deposit, Trans-North China Orogen: A Metamorphosed Paleoproterozoic Porphyry Cu Deposit. *Economic Geology*, 115(1): 51-77.
<http://doi.org/10.5382/econgeo.4693>
- Morozumi, H., 2003. Geochemical Characteristics of Granitoids of the Erdenet Porphyry Copper Deposit, Mongolia. *Resource Geology*, 53(4): 311-316.
<http://doi.org/10.1111/j.1751-3928.2003.tb00180.x>

Moshefi, P., Hosseinzadeh, M.R., Moayyed, M. and Lentz, D.R., 2020. Distinctive geochemical features of biotite types from the subeconomic Sonajil porphyry-type Cu deposit, northwestern Iran: Implications for analysis of porphyry copper deposit mineralization potential. *Journal of Geochemical Exploration*, 214.

<http://doi.org/10.1016/j.gexplo.2020.106543>

Norris, J.R., 2006. Evolution of Alteration and mineralization at the Red Chris Cu-Au Porphyry Deposit East Zone, Northwestern British Columbia, Canada. MSc Thesis, University of British Columbia, Vancouver, 194 pp.

Novak, M., Skoda, R., Filip, J., Macek, I. and Vaculovic, T., 2011. Compositional trends in tourmaline from intragranitic NYF pegmatites of the Trebic pluton, Czech Republic: an electron microprobe, Mossbauer and LA-ICP-MS study. *The Canadian Mineralogist*, 49(1): 359-380. <http://doi.org/10.3749/canmin.49.1.359>

Ochoa-Landín, L.H., Valencia-Moreno, M., Calmus, T., Del Rio-Salas, R., Mendivil-Quijada, H., Meza-Figueroa, D., Flores-Vásquez, I. and Zúñiga-Hernández, L.G., 2017. Geology and geochemistry of the Suaqui Verde deposit: A contribution to the knowledge of the Laramide porphyry copper mineralization in south central Sonora, Mexico. *Ore Geology Reviews*, 81: 1158-1171. <http://doi.org/10.1016/j.oregeorev.2016.10.011>

Oliveira, C.G.d., Oliveira, F.B.d., Giustina, M.E.S.D., Marques, G.C., Dantas, E.L., Pimentel, M.M. and Buhn, B.M., 2016. The Chapada Cu–Au deposit, Mara Rosa magmatic arc, Central Brazil: Constraints on the metallogenesis of a Neoproterozoic large porphyry-type deposit. *Ore Geology Reviews*, 72: 1-21.

<http://doi.org/10.1016/j.oregeorev.2015.06.021>

- Osatenko, M., Riedell, K.B. and Lang, J.R., 2021. Characteristics of porphyry copper and porphyry molybdenum deposits in the northwestern Cordillera: A comprehensive compilation. In: E.R. Sharman, J.R. Lang and J.B. Chapman (Editors), *Porphyry Deposits of the Northwestern Cordillera of North America: A 25-Year Update*. The Canadian Institute Of Mining, Metallurgy and Petroleum, Montmagny, Quebec, Canada, pp. 726.
- Pacey, A., Wilkinson, J.J., Boyce, A.J. and Millar, I.L., 2020. Magmatic Fluids Implicated in the Formation of Propylitic Alteration: Oxygen, Hydrogen, and Strontium Isotope Constraints from the Northparkes Porphyry Cu-Au District, New South Wales, Australia. *Economic Geology*, 115(4): 729-748. <http://doi.org/10.5382/econgeo.4732>
- Palacios, C., Hein, U.F. and Dulski, P., 1986. Behaviour of rare earth elements during hydrothermal alteration at the Buena Esperanza copper-silver deposit, northern Chile. *Earth and Planetary Science Letters*, 80(3-4): 208-216. [http://doi.org/10.1016/0012-821x\(86\)90105-6](http://doi.org/10.1016/0012-821x(86)90105-6)
- Palacios, C., Herail, G., Townley, B., Maksaev, V. and Sepulveda, F., 2001. The composition of gold in the Cerro Casale gold-rich porphyry deposit, Maricunga belt, Northern Chile. *Canadian Mineralogist*, 39(3): 907-915. <http://doi.org/10.2113/gscanmin.39.3.907>
- Palacios, C., Rouxel, O., Reich, M., Cameron, E.M. and Leybourne, M.I., 2010. Pleistocene recycling of copper at a porphyry system, Atacama Desert, Chile: Cu isotope evidence. *Mineralium Deposita*, 46(1): 1-7. <http://doi.org/10.1007/s00126-010-0315-6>
- Panteleyev, A., 1976. Geologic Setting, Mineralization, and Aspects of Zoning at the Berg Porphyry Copper-Molybdenum Deposit, Central British Columbia, University of British Columbia, Vancouver, 235 pp.

- Panteleyev, A., 1978. Gnat Pass Deposit. In: Geological Fieldwork 1977 Reports of Project Geologists Metallic Investigations Northwest BC, British Columbia Geological Survey (Editor) Brown, A.S. and Carter N.C., 4: 43-45.
- Pardo, A.R., Ausburn, K., Aguilera, M. and Rubio, M., 2015. Implications of expansive mineralogy on the production process in the Fortuna de Cobre mine. Lomas Bayas, II Region of Antofagasta, Chile. Conference: XIV Congreso Geológico Chileno, La Serena, Chile. October 2015. *Conference paper*.
- Parry, W.T., Ballantyne, J.M. and Jacobs, D.C., 1984. Geochemistry of hydrothermal sericite from Roosevelt Hot Springs and the Tintic and Santa Rita porphyry copper systems. *Economic Geology*, 79(1): 72-86. <http://doi.org/10.2113/gsecongeo.79.1.72>
- Peng, Z., Watanabe, M., Hoshino, K., Sueoka, S., Yano, T. and Nishido, H., 1998. The Machangqing copper-molybdenum deposits, Yunnan, China- an example of Himalayan porphyry-hosted Cu-Mo mineralization. *Mineralogy and Petrology*, 63(1-2): 95-117. <http://doi.org/10.1007/bf01162770>
- Perea, V.J.E., 1999. Magmatic Evolution and Geochemistry of the Piedras Verdes Deposit, Sonora, Mexico. MSc Thesis, University of Arizona, Arizona, 114 pp.
- Perello, J., Cox, D.F., Garamjav, D., Sanjdorj, S., Diakov, S., Schissel, D., Munkhbat, T.-O. and Oyun, G., 2001. Oyu Tolgoi, Mongolia: Siluro-Devonian porphyry Cu-Au-(Mo) and high-sulfidation Cu mineralization with a Cretaceous chalcocite Blanket. *Economic Geology*, 96(6): 1407-1428. <http://doi.org/10.2113/gsecongeo.96.6.1407>
- Putnis, A., 2009. Mineral Replacement Reactions. *Reviews in Mineralogy and Geochemistry*, 70(1): 87-124. <http://doi.org/10.2138/rmg.2009.70.3>

- Qiao, X., Li, W., Zhang, L., White, N.C., Zhang, F. and Yao, Z., 2019. Chemical and boron isotope compositions of tourmaline in the Hadamiao porphyry gold deposit, Inner Mongolia, China. *Chemical Geology*, 519: 39-55.
<http://doi.org/10.1016/j.chemgeo.2019.04.029>
- Quang, C.X., Clark, A.H., Lee, J.K.W. and Guillen B, J., 2003. ^{40}Ar - ^{39}Ar Ages of hypogene and supergene mineralization in the Cerro Verde-Santa Rosa porphyry Cu-Mo cluster, Aequipa, Peru. *Economic Geology*, 98: 1683. <http://doi.org/0361-0128/01/3398/1683-14>
- Rabbia, K.R.W.H., O. M. and Lopez-Escobar, L., 2003. Tourmaline and Tourmaline Breccia Pipes From the Supergiant Porphyry Copper Deposits of the El Teniente Belt, Central Chile, *10th Congreso Geologico Chileno*.
- Reed, A. and Jambor, J., 1976. Highmont: Linearly zoned copper-molybdenum porphyry deposits and their significance in the genesis of the Highland Valley ores. In: A. Sutherland Brown (Editor), *Porphyry Deposits of the Canadian Cordillera*, A. Sutherland Brown (ed.), Canadian Institute of Mining, Metallurgy and Petroleum, CIM Special, pp. 163-181.
- Robison, L.C., 1987. Geology and geochemistry of Proterozoic volcanic rocks bearing massive sulfide ore deposits, Bagdad, Arizona. MSc Thesis, University of Arizona, Arizona, 142 pp.
- Salazar, E., Barra, F., Reich, M., Simon, A., Leisen, M., Palma, G., Romero, R. and Rojo, M., 2019. Trace element geochemistry of magnetite from the Cerro Negro Norte iron oxide-apatite deposit, northern Chile. *Mineralium Deposita*, 55(3): 409-428.
<http://doi.org/10.1007/s00126-019-00879-3>

- Schwartz, M.O., 1981. The porphyry copper deposit at La Granja, Peru. *Economic Geology*, 77(2): 482-488. <http://doi.org/10.2113/gsecongeo.77.2.482>
- Sciuba, M., Beaudoin, G. and Makvandi, S., 2021. Chemical composition of tourmaline in orogenic gold deposits. *Mineralium Deposita*, 56(3): 537-560. <http://doi.org/10.1007/s00126-020-00981-x>
- Scott, J.E., Richards, J.P., Heaman, L.M., Creaser, R.A. and Salzar, G.A., 2008. The Schaft Creek Porphyry Cu-Mo-(Au) Deposit, Northwestern British Columbia. *Exploration and Mining Geology*, 17(3-4): 163-196. <http://doi.org/10.2113/gsemg.17.3-4.163>
- Siddiqui, R.H., Aftab, S.M. and Chaudhry, A.H., 2018. Hydrothermal Alteration in Porphyry Cu-Mo-Au Mineralizations of the Chagai Arc, Balochistan, Pakistan, Conf. Series: Materials Science and Engineering, pp. 012033. <http://doi.org/10.1088/1757-899x/414/1/012033>
- Sillitoe, R.H., 1973. Geology of the Los Pelambres Porphyry Copper Deposit, Chile. *Economic Geology*, 68(1): 1-10. <http://doi.org/10.2113/gsecongeo.68.1.1>
- Sillitoe, R.H., 2010. Porphyry copper systems. *Economic Geology*, 105(1): 3-41. <http://doi.org/0.2113/gsecongeo.105.1.3>
- Singer, D.A., Berger, V.I. and Moring, B.C., 2008. Porphyry copper deposits of the world: Database and grade and tonnage models: USGS Open-File Report 2008-1155. *USGS: Reston, VA, USA*. <http://doi.org/10.3133/ofr20081155>
- Skarmeta, J., 2020. Structural Controls on Alteration Stages at the Chuquicamata Copper-Molybdenum Deposit, Northern Chile. *Economic Geology*, 116(1): 1-28. <http://doi.org/10.5382/econgeo.4769>

- Skewes, M.A., Arevalo, A., Floody, R., Zuniga, P.H. and Stern, C.R., 2002. The Giant El Teniente Breccia Deposit: Hypogene Copper Distribution and Emplacement. In: R.J. Goldfarb and R.L. Nielsen (Editors), *Integrated Methods for Discovery: Global Exploration in the 21st Century*. Society of Economic Geologists, pp. 299-332.
<http://doi.org/10.5382/sp.09.14>
- Skewes, M.A., Holmgren, C. and Stern, C.R., 2003. The Donoso copper-rich, tourmaline-bearing breccia pipe in central Chile: petrologic, fluid inclusion and stable isotope evidence for an origin from magmatic fluids. *Mineralium Deposita*, 38(1): 2-21.
<http://doi.org/10.1007/s00126-002-0264-9>
- Slack, J.F., 1996. Tourmaline Associations with Hydrothermal Ore Deposits. In: L.M. Anovitz and E.S. Grew (Editors), *Boron. Reviews in Mineralogy and Geochemistry*. Mineralogical Society of America, Oak Ridge, Tennessee, USA, pp. 559-644.
<http://doi.org/10.1515/9781501509223-013>
- Slack, J.F. and Coad, P.R., 1989. Multiple hydrothermal and metamorphic events in the Kidd Creek volcanogenic massive sulphide deposit, Timmins, Ontario: Evidence from tourmalines and chlorites. *Canadian Journal of Earth Sciences*, 26(4): 694-715.
<http://doi.org/10.1139/e89-059>
- Slack, J.F. and Trumbull, R.B., 2011. Tourmaline as a Recorder of Ore-Forming Processes. *Elements*, 7(5): 321-326. <http://doi.org/10.2113/gselements.7.5.321>
- Slack, J.F.P., M. R.; Stevens, B. P.; Barnes, R. G.; , 1993. Origin and significance of tourmaline-rich rocks in the Broken Hill district, Australia. *Economic Geology*, 88(3): 505-541.
<http://doi.org/10.2113/gsecongeo.88.3.505>

- Sokolović, J., Stanojlović, R., Andrić, L., Štirbanović, Z. and Ćirić, N., 2019. Flotation studies of copper ore Majdanpek to enhance copper recovery and concentrate grade with different collectors. *Journal of Mining and Metallurgy A: Mining*, 55(1): 53-65.
<http://doi.org/10.5937/jmma1901053s>
- Sotnikov, V., Berzina, A.N., Economou-Eliopoulos, M. and Eliopoulos, D.G., 2001. Palladium, platinum and gold distribution in porphyry Cu±Mo deposits of Russia and Mongolia. *Ore Geology Reviews*, 18(1-2): 95-111. [http://doi.org/10.1016/s0169-1368\(01\)00018-x](http://doi.org/10.1016/s0169-1368(01)00018-x)
- Spatz, D.M., 1974. Geology and alteration-mineralization zoning of the Pine Flat porphyry copper occurrence, Yavapai County, Arizona, University of Arizona, Arizona, 148 pp.
- Stein, H.J., Hannah, J.L., Zimmerman, A., Markey, R.J., Sarkar, S.C. and Pal, A.B., 2004. A 2.5 Ga porphyry Cu–Mo–Au deposit at Malanjhand, central India: implications for Late Archean continental assembly. *Precambrian Research*, 134(3-4): 189-226.
<http://doi.org/10.1016/j.precamres.2004.05.012>
- Storey, L.O., 1978. Geology and Mineralization for the lights creek stock plumas country, California. *Arizona Geological Survey Digest*, 11: 49-58.
- Sun, W., Huang, R.-f., Li, H., Hu, Y.-b., Zhang, C.-c., Sun, S.-j., Zhang, L.-p., Ding, X., Li, C.-y., Zartman, R.E. and Ling, M.-x., 2015. Porphyry deposits and oxidized magmas. *Ore Geology Reviews*, 65: 97-131. <http://doi.org/10.1016/j.oregeorev.2014.09.004>
- Taylor, B.P., M.; Slack, J., 1999. Mineralizing Fluids in the Kidd Creek Massive Sulfide Deposit, Ontario: Evidence from Oxygen, Hydrogen, and Boron Isotopes in Tourmaline, The Giant Kidd Creek Volcanogenic Massive Sulfide Deposit, Western Abitibi Subprovince, Canada, pp. 389-414. <http://doi.org/10.5382/mono.10.15>

- Taylor, B.S., J., 1984. Tourmalines from Appalachian-Caledonian massive sulfide deposits: textural, chemical, and isotopic relationships. *Economic Geology*, 79(7): 1703-1726. <http://doi.org/10.2113/gsecongeo.79.7.1703>
- Torro, L., Proenza, J.A., Melgarejo, J.C., Carrasco, C., Dominguez, H. and Lewis, J.F., 2012. Tourmaline Composition near a Diorite Intrusive Body under La Cuaba Lithocap (Ampliación Pueblo Viejo District, Dominican Republic). *sociedad española de mineralogía*, 16: 1-2.
- Trumbull, R.B., Slack, J.F., Krienitz, M.S., Belkin, H.E. and Wiedenbeck, M., 2011. Fluid sources and metallogenesis in the Blackbird Co-Cu-Au-Bi-Y-REE district, Idaho, U.S.A.: insights from major-element and boron isotopic compositions of tourmaline. *The Canadian Mineralogist*, 49(1): 225-244. <http://doi.org/10.3749/canmin.49.1.225>
- van Hinsberg, V.J., 2006. Hourglass sector zoning in metamorphic tourmaline and resultant major and trace-element fractionation. *American Mineralogist*, 91(5-6): 717-728. <http://doi.org/10.2138/am.2006.1920>
- van Hinsberg, V.J., 2011. Preliminary experimental data on trace-element partitioning between tourmaline and silicate melt. *The Canadian Mineralogist*, 49(1): 153-163. <http://doi.org/10.3749/canmin.49.1.153>
- van Hinsberg, V.J., Henry, D.J. and Marschall, H.R., 2011. Tourmaline: an ideal indicator of its host environment. *The Canadian Mineralogist*, 49(1): 1-16. <http://doi.org/10.3749/canmin.49.1.1>

- van Hinsberg, V.J. and Schumacher, J.C., 2006. Intersector element partitioning in tourmaline: a potentially powerful single crystal thermometer. *Contributions to Mineralogy and Petrology*, 153(3): 289-301. <http://doi.org/10.1007/s00410-006-0147-7>
- van Hinsberg, V.J. and Schumacher, J.C., 2011. Tourmaline as a petrogenetic indicator mineral in the Haut-Allier metamorphic suite, Massif Central, France. *The Canadian Mineralogist*, 49(1): 177-194. <http://doi.org/10.3749/canmin.49.1.177>
- Volp, K.M., 2005. The Estrela copper deposit, Carajás, Brazil: Geology and implications of a Proterozoic copper stockwork. *Mineral Deposit Research: Meeting the Global Challenge*. Springer Berlin Heidelberg, Berlin, Heidelberg, pp. 1085-1088.
- Vry, V.H., Wilkinson, J.J., Seguel, J. and Millán, J., 2010. Multistage intrusion, brecciation, and veining at El Teniente, Chile: Evolution of a nested porphyry system. *Economic Geology*, 105(1): 119-153. <http://doi.org/10.2113/gsecongeo.105.1.119>
- Wagner, T., Fusswinkel, T., Wälle, M. and Heinrich, C.A., 2016 Microanalysis of Fluid Inclusions in Crustal Hydrothermal Systems using Laser Ablation Methods. *Elements*, 12(October): 323-328. <http://doi.org/10.2113/gselements.12.5.323>
- Warlo, M., Wanhainen, C., Martinsson, O. and Karlsson, P., 2020. Mineralogy and character of the Liikavaara Östra Cu-(W-Au) deposit, northern Sweden. *Gff*, 142(3): 169-189. <http://doi.org/10.1080/11035897.2020.1753807>
- Warnaars, F.W., Holmgren, C. and Barassi, S., 1985. Porphyry Copper and Tourmaline Breccias at Los-Bronces-Rio-Blanco, Chile. *Economic Geology*, 80(6): 1544-1565. <http://doi.org/10.2113/gsecongeo.80.6.1544>

- Wendt, C.J., 1938. Geology, alteration, and mineralization of the Batamote Ranch area, northern Sonora, Mexico. MSc Thesis, University of Arizona, Arizona, 96 pp.
- Wilkinson, C.C., Cooke, D.R., Baker, M.J. and Wilkinson, J.J., 2020. Exploration Targeting in Porphyry Cu Systems Using Propylitic Mineral Chemistry: A Case Study of the El Teniente Deposit, Chile. *Economic Geology*, 115(4): 771-791.
<http://doi.org/10.5382/econgeo.4738>
- Wyman, D.A., Kerrich, R.W. and Polat, A., 2002. Assembly of Archean cratonic mantle lithosphere and crust: plume–arc interaction in the Abitibi–Wawa subduction–accretion complex. *Precambrian Research*, 115(1-4): 37-62. [http://doi.org/10.1016/s0301-9268\(02\)00005-0](http://doi.org/10.1016/s0301-9268(02)00005-0)
- Yang, K. and Jang, J.-Y., 2002. Geochemistry of tourmalines in the Ilgwang Cu-W breccia-pipe deposit, Southeastern Gyeongsang Basin. *Journal of Petrology Society of Korea*, 11: 259-270.
- Yavuz, F., Iskenderoglu, A. and Jiang, S.Y., 1999. Tourmaline compositions from the Salikvan porphyry Cu-Mo deposit and vicinity, northeastern Turkey. *Canadian Mineralogist*, 37: 1007-1023.
- Yavuz, F., Karakaya, N., Yıldırım, D.K., Karakaya, M.Ç. and Kumral, M., 2014. A Windows program for calculation and classification of tourmaline-supergroup (IMA-2011). *Computers & Geosciences*, 63: 70-87. <http://doi.org/10.1016/j.cageo.2013.10.012>
- Zukowski, W., 2010. Geology and Mineralisation of the Endeavour 41 Gold Deposit, Cowal District, NSW, Australia. PhD Thesis, University of Tasmania, 275 pp.

Chapter 3

3 Recognizing tourmaline in mineralized porphyry systems Part II: trace-element characteristics of tourmaline: development and application to discrimination among source regions

3.1 Abstract

Samples of tourmaline supergroup minerals (TSM) from mineralized porphyry systems (Cu \pm Au, \pm Mo, \pm Ag) including Casino (Yukon Territory, Canada), Coxheath (Nova Scotia, Canada), Donoso Breccia (Chile), Highland Valley Copper (British Columbia, Canada), New Afton (British Columbia, Canada), Schaft Creek (British Columbia, Canada), and Woodjam (British Columbia, Canada) were examined to characterize their trace-element signatures and to evaluate discriminating variables that distinguish them from TSM forming in other environments. Trace-element analyses, conducted *via* LA-ICP-MS, reveal striking similarities in trace-element character among the mineralized environments examined in contrast to those considered to be barren. Key concentrations of elements (Sr, Pb, Zn, Cu, and Ga) and select element ratios (Sr/Pb and Zn/Cu), were found to be useful as discriminators. These discriminators are presented and compared to that of TSM forming in other geologic environments. The TSM from porphyry systems is characterized by high Sr/Pb values (*avg*: 241) and relatively low Zn/Cu (*avg*: 1.5) values. A ternary of Sr/Pb-Zn/Cu-Ga is most useful in distinguishing porphyry-related TSM from that of other geologic environments. Compared to porphyry TSM grains, the TSM derived from felsic pegmatites have lower Sr/Pb values (*avg*: 2.91) and higher Zn/Cu (*avg*: 472); those from orogenic Au deposits have high Sr/Pb (*avg*: 193) similar to the porphyry TSM but intermediate Zn/Cu (*avg*: 223) and lower Ga (*avg*: 43 ppm); and those considered to be derived

from metamorphic environments (greenschist to amphibolite) form in the center of the ternary trending away from the Zn/Cu apex. Utilizing an understanding of both intrinsic and extrinsic controls on TSM chemistry is an effective approach to distinguish TSM forming in porphyry bedrock samples from TSM forming in other geologic environments and ore systems. More broadly, this work has implications for using TSM recovered from surficial sediments to identify prospective areas for further porphyry exploration.

3.2 Introduction

Tourmaline supergroup minerals (TSM) are common accessories found in many geologic environments and deposit types (Slack 1996; Slack and Trumbull 2011) and their major-, minor-, and trace-element chemistries have been widely used as indicators of the primary environments of formation, primarily owing to the wide variation in elements that may be accommodated (*e.g.*, Henry and Guidotti 1985; van Hinsberg *et al.* 2011; Li *et al.* 2021a; Sciuba *et al.* 2021). In general, TSM are found as a trace to minor mineral constituents in many hydrothermal environments, which has led to numerous studies into the occurrence, chemistry, and stable-isotope features to better understand the origin and development of a variety of mineralized systems including volcanogenic massive sulfides (VMS), orogenic gold, polymetallic W-Sn-Cu deposits, porphyry Cu-Au-Mo deposits, and even emerald mineralization (Palmer 1989; Slack 1993; Griffin *et al.* 1996; Frikken 2003; Frikken *et al.* 2005; Galbraith *et al.* 2009; Baksheev *et al.* 2010; Baksheev *et al.* 2011; Baksheev *et al.* 2012; Baksheev *et al.* 2017; Codeço *et al.* 2017; Kalliomäki *et al.* 2017; Manégliia *et al.* 2018; Codeço *et al.* 2019; Codeço *et al.* 2020; Sciuba *et al.* 2021). Whereas several key mineral groups have been evaluated as potential indicators of mineralized porphyry systems (*e.g.*, apatite, epidote, and chlorite group minerals; Cooke *et al.*

2020b), no comprehensive studies involving TSM trace-elements have similarly been conducted to date.

Numerous studies of the trace-element chemistry of TSM from porphyry systems can be found in the literature (Iveson *et al.* 2016; Qiao *et al.* 2019; Li *et al.* 2021a) but such studies are generally restricted to the deposit-scale (Smith 1985; Warnars *et al.* 1985; Koval *et al.* 1991; Lynch and Ortega 1997; Yavuz *et al.* 1999; Skewes *et al.* 2003; Frikken *et al.* 2005; Baksheev *et al.* 2010; Baksheev *et al.* 2011; Dill *et al.* 2012; Bačík *et al.* 2016; Baksheev *et al.* 2017; Testa *et al.* 2018; Baksheev *et al.* 2019) with only very few having been conducted at the broader scale (Beckett-Brown *et al.* 2021; Li *et al.* 2021a). It is within this context that the need for a comprehensive, broad-scale study of the trace-element features present, along with their respective trends and ratios, has been deemed timely and critical considering the number of porphyry systems that contain TSM.

Tourmaline is a relatively common accessory mineral that develops in porphyry systems, not all of which are necessarily mineralized (Sillitoe and Sawkins 1971). In terms of the latter, TSM are present in some of the most prolific porphyry deposits world-wide *e.g.*, El Teniente (Chile), Los Bronces-Rio Blanco district (Chile), Highland Valley (BC-Canada), Cadia district (eastern Australia), and Yerington district (NV-USA). A detailed understanding of which trace-elements are present, the ranges in the concentrations of those traces, their internal chemical zoning relationships to other trace-elements, and how these relate to the environments in which they occur are key factors to developing a holistic understanding of the genesis and evolution of the porphyry environment and in turn how that is reflected in TSM trace-element chemistry. The purpose of this study is to investigate and evaluate the applicability and efficacy of TSM trace-element chemistry to identify porphyry Cu (\pm Au, \pm Mo) related TSM. Several key elements of

porphyry tourmaline trace-elements will be addressed, including: 1) elements present, 2) concentrations, 3) their relationship with texture development (internal and external texture, spatial distribution *etc.*), 4) inter/intra deposit variations, and 5) determination of those important trace-element concentrations or ratios that have the highest efficacy of distinguishing TSM in mineralized porphyries from other geologic environments. This contribution will provide the first detailed documentation and comparison of the trace-elements that occur in TSM associated with seven different mineralized porphyry systems and builds on the textural and major element characterization of Chapter 2, with an emphasis on using these as tools useful in the discrimination between mineralized and unmineralized porphyry systems. The longer-term goal is to develop a methodology that applies to a wide range of sample media, spanning those found in-situ in bedrock to those obtained from surficial sediment samples.

3.3 Trace-elements in tourmaline from porphyry deposits: A review

An evaluation of ~470 porphyry systems world-wide (that report grade) shows that nearly 30 % are reported to contain TSM (using the USGS porphyry Cu database; Singer *et al.* 2008; and data compiled in this study Chapter 2).

3.3.1 Metals and Semi-Metals

At the Salikvan Cu-Mo porphyry system (Turkey), it was demonstrated that those TSM associated with a TSM-dominant rock had higher Zn/(Zn+Pb) and Sr values than those associated with TSM in veins (Yavuz *et al.* 1999). Concentrations of Zn, Pb, and Mn of TSM from the Cadia East Cu-Au porphyry (Australia) were used to highlight variations with alteration types and stratigraphic depth, with higher concentrations of Zn, Pb, and Mn being linked to the shallow and late forming tourmaline (Cooke *et al.* 2017). At the Hadamiao porphyry Au deposit,

China, two broad groups of TSM were identified, magmatic and hydrothermal. The authors suggested that hydrothermal TSM have lower Sr and higher Pb, Zn, and Cu concentrations than magmatic tourmalines in the Hadamiao deposit (Qiao *et al.* 2019).

An investigation of TSM from porphyry Cu systems in Mongolia and Russia reported that TSM contain the highest As contents amongst tourmaline from any mineralized systems (Koval *et al.* 1991).

3.3.2 Discrimination

An investigation of TSM from the Bilihe porphyry Au deposit (Inner Mongolia, China; Li *et al.* 2021a) found that hydrothermal vein TSM show a negative Eu anomaly whereas TSM replacing magmatic plagioclase feldspar show a positive Eu anomaly. Li *et al.* (2021a) also presented a series of plots potentially applicable in the discrimination between porphyry deposits, orogenic Au deposits, IOCG deposits, and TSM forming in unmineralized granitic rocks using a variety of elements including: (Sn + Li) vs. (Ni + V + Zn), (\sum REE + Y + Zr) vs. (Ni + V + Zn) and V vs. Zn. Unfortunately, a clear justification for the selection of elements or why they are beneficial for discriminating environment of formation of TSM was not presented.

3.4 Tourmaline Systems Examined

A detailed description of the deposits examined in this study can be found in Beckett-Brown *et al.* (2021b), with a summary presented below. Samples of TSM from Casino (Yukon Territory, Canada), Coxheath (Nova Scotia, Canada), Donoso Breccia (Chile), Highland Valley Copper (British Columbia, Canada), New Afton (British Columbia, Canada), Schaft Creek (British Columbia, Canada), and Woodjam (British Columbia, Canada) were examined. The Casino deposit is a calc-alkaline Cu-Au-Mo porphyry deposit hosted in Late Cretaceous quartz-

monzonite and associated breccias (Casselmann and Brown 2017). The Coxheath deposit is a calc-alkaline Cu-Mo-Au porphyry system hosted in a Precambrian hornblende diorite (Lynch and Ortega 1997). The Donoso breccia is the youngest breccia in the Rio-Blanco – Los Bronces copper district where TSM breccias host a large volume of the mineralization (Warnaars *et al.* 1985). The Highland Valley Copper district is hosted in the Late Triassic calc-alkaline granodiorite, referred to as the Guichon Creek batholith (Byrne 2019). The New Afton Cu-Au porphyry system is a silica-saturated alkalic deposit hosted in the Late Triassic Iron Mask Batholith (Kwong 1981). The calc-alkaline Schaft Creek Cu-Mo-Au deposit is hosted by late Triassic volcanics and associated with porphyritic granodiorite dikes of the Hickman batholith (Scott *et al.* 2008). The Woodjam Cu-Au deposits are hosted in calc-alkaline high K-monzonite porphyries.

The prequel companion study to this (Chapter 2), the textural and major/minor element characteristics of TSM from the seven porphyry systems discussed above were described and discussed. Noteworthy results to set the stage for reporting the findings in this paper are summarized. Tourmaline should be considered a significant phase in porphyry systems as it occurs in nearly 30% of worldwide porphyry occurrences. The physical characteristics of TSM from porphyry systems are remarkably consistent in terms of macro color, grain size, morphology, paragenetic position, and color in transmitted light. These features provide some information for discrimination of TSM in mineralized porphyry systems compared to that in other geologic environments. Some generalities that exist in porphyry TSM include their black to dark brown color at the macro-scale, weak pleochroism (green, brown, and blue), and rare presence of inclusions, with zircon and rutile being the most common when present. Porphyry TSM forms early in the paragenesis of these systems denoted by their euhedral morphology and

repeated observations of alteration and mineralization crosscutting individual grains. Major-element chemistry of porphyry TSM is characterized by sodic group TSM, primarily dravite with some schorl compositions with remarkably consistent Mg *apfu* values of ~ 2.0 and almost exclusively follow the O-P trend. In short, although there are some trends, the physical and major/minor element data alone can not definitively distinguish TSM in porphyry systems from that in other geologic environments. The integration of these data with the findings of the trace-element data presented here provides an effective method for which TSM in mineralized porphyry systems can be distinguished. Data for TSM from a variety of mineralized systems as well as unmineralized geologic settings are compiled and compared for reference. Data for TSM in porphyry Au deposits is compiled from Qiao *et al.* (2019) and Li *et al.* (2021a). Data for TSM forming in granites is compiled from: Drivenes *et al.* (2015); Kalliomaki *et al.* (2017); Zall *et al.* (2019); Zhao *et al.* (2019); Xiang *et al.* (2020); Aysal *et al.* (2021); Hong *et al.* (2021); Zhao *et al.* (2021a); and unpublished analyses collected by the author from the Seagull Batholith-Yukon Territory. Data for TSM in pegmatites is compiled from: Marks *et al.* (2013); Copjakova *et al.* (2015); Zhao *et al.* (2019); Chakraborty and Upadhyay (2020); Long *et al.* (2021); Sciuba *et al.* (2021); Zhao *et al.* (2021c); and unpublished analyses collected by the author from the Usakos Pegmatite-Namibia as well as the Beryl pit-Ontario. Data for TSM in metamorphic rocks is compiled from: van Hinsberg (2011); Kalliomaki *et al.* (2017); Wang *et al.* (2018); Hong *et al.* (2021); and unpublished analyses collected by the author from Jordan Falls-Nova Scotia. Data for TSM in orogenic Au deposits is compiled from: Jiang *et al.* (2002); Kalliomaki *et al.* (2017); Trumbull *et al.* (2018); Jin and Sui (2020); and Sciuba *et al.* (2021). Data for TSM in VMS deposits is compiled from: Slack *et al.* (1999); Klemme *et al.* (2011); and Sciuba *et al.* (2021). Data for TSM in polymetallic W \pm Sn \pm Cu deposits are compiled from: Jiang *et al.* (2004);

Codeco *et al.* (2017); Lunay *et al.* (2018); Harlaux *et al.* (2019); Carocci *et al.* (2020); Carr *et al.* (2020); Harlaux *et al.* (2020); Hu and Jiang (2020); Xiang *et al.* (2020); Ghosh *et al.* (2021); and Zhao *et al.* (2021b). Data for TSM from other localities were also compiled including samples from a Be-U system (Zhu *et al.* 2021) and a Au-Co system (Tapio *et al.* 2021).

3.5 Analytical Conditions

3.5.1 Laser-Ablation Inductively Coupled-Plasma Mass-Spectrometry

Trace-element analyses of TSM grains were made *in-situ* on polished thin sections using laser-ablation inductively coupled-plasma mass spectrometry (LA-ICP-MS) at Laurentian University. Samples were ablated using Resonetic Resolution M-50 coupled to a Thermo Electron X-Series II quadrupole ICP-MS. This employs a 193 nm ArF excimer laser which was operated at a rate of 8 Hz with a 30 μm beam and a line scan speed between 5 $\mu\text{m}/\text{s}$ and 15 $\mu\text{m}/\text{s}$ with a measured fluence of $\sim 3 \text{ j}/\text{cm}^2$. Beam size was optimized to be large enough for better count resolution but also small enough to collect enough data of individual chemical zones. Slow line scans were conducted to allow for an investigation of variations across complex chemically zoned grains (generally oriented perpendicular to *c*-axis) allowing for the integration and processing of data from individual chemical zones while also allowing for the ability to remove contamination from inclusions. External reference materials included: 1) NIST 610 (Jochum *et al.* 2011); 2) NIST 612 (Jochum *et al.* 2011); and 3) BHVO2G (Raczek *et al.* 2001). The NIST 610 standard served as the primary reference material, with Si (obtained from SEM-EDS analyses; Chapter 2) being used as the internal standard. Drift and data reproducibility were assessed using NIST 612, BHVO2G, and an in-house tourmaline standard. Standards were ablated before and after every 10-15 analyses made on TSM. Although TSM from porphyry systems rarely contain inclusions

(Chapter 2), they are present and need to be avoided or removed during data processing. During data processing, specific attention was paid to P, Ti, and Zr which account for the most common inclusion observed (apatite, oxides, and zircon). Additionally, channels of B and Si were also referenced to assure that count rates were consistent across zones that were integrated for analyses. A drift correction was applied using the baseline-reduction scheme available in Iolite (Paton *et al.* 2011). Detection limits were calculated in Iolite following the method of Pettke *et al.* (2012). A summary of the average trace-element data for porphyry-related TSM are presented in Table 3-1.

3.6 Results

3.6.1 General Overview

Trace-element analyses (LA-ICP-MS) were completed on 516 TSM grains from 24 samples from the seven porphyry deposits examined in this study (Figure 3-1). A large number of elements were found to be at or below the lower detection limit (Li, Be, Mo, Ag, Cs, Ta, Bi, and Hf). The elements detected were divided into three populations, based on the concentrations obtained. Elements in minute concentrations (0.5-10 ppm *avg*) include LILE: Rb, Ba, and Pb; HFSE: Y, Zr, Nb, U; and semi-metals: Ge, In, and Sb. Others were present in low concentrations (10-100 ppm *avg*) including transition metals: Sc, Cr, Co, Ni, Cu, and Zn; semi-metals: Ga, Ge, As, and Sn; and HFSE: Th. The remainder, Alkali and Alkali-Earths: K and Sr; and transition metals: Ti, V, and Mn were found to occur in intermediate concentrations (100-1000s of ppm *avg*).

Two key trace-elements were carefully examined. The first is Li, which has been used as a discriminator based on its abundance in TSM among deposit types in other studies (Kalliomäki

et al. 2017; Codeço *et al.* 2020; Li *et al.* 2021a). Results from this current study found Li to be present in concentrations at or below the limit of detection (~10 ppm), in contrast to the higher concentrations (*e.g.*, orogenic Au TSM contain 10s of ppm Li and the Panasqueira W-Sn-Cu deposit TSM contains 100s of ppm Li) noted in other studies (Kalliomäki *et al.* 2017; Codeço *et al.* 2020). The second group of elements that warranted careful examination were the REEs. In many cases, a number of the MREE occurred below the limit of detection. In cases where REEs concentrations were above detection, the resulting distribution patterns are concave, with variable Eu anomalies (0.04 – 59.43 and 2.11 *avg*). Depletion of MREEs is consistent with amphibole fractionation, typical for hydrous porphyry magmas (Chiaradia *et al.* 2012; Loucks 2014). A dichotomy in Eu anomalies was observed with HVC, Los Bronces, Schaft Creek, and Woodjam samples exhibiting negative Eu anomalies on average while the Casino, Coxheath, and New Afton samples exhibited positive Eu anomalies. These positive and negative anomalies for two groups of samples potentially reflects differing fluid sources or if the breakdown of plagioclase was involved in the formation of TSM.

3.6.2 Inter-deposit Variations

The results from this study show that porphyry TSM contain variable concentrations of large ion lithophile elements (LILE) include K (763 ppm *avg*, range: 72-25930), Rb (2.78 ppm *avg*, range: <LOD-61.5), Sr (353 ppm *avg*, range: 35-977), Ba (17.9 ppm *avg*, range: 0.15-1059), and Pb (3.63 ppm *avg*, range: 0.03-51) expected to reside in the X-site of TSM. High field strength elements (HFSE) include Ti (2637 ppm *avg*, range: 111-9239), Zr (9 ppm *avg*, range: 0.59-116), Nb (0.90 ppm *avg*, range: 0.02-32.6), and Th (1.3 ppm *avg*, range: <LOD-20.3). Transition metals include V (641 ppm *avg*, range: 51-3076), Cr (70 ppm *avg*, range: <LOD-1241), Mn (184 ppm *avg*, range: 16-1300), Co (13.3 ppm *avg*, range: <LOD-260), Ni (17.8 ppm *avg*, range:

<LOD-120), Cu (24.7 ppm *avg*, range: <LOD-510), and Zn (36 ppm *avg*, range: 2.5-172).

Finally, semi-metals include Ga (58 ppm *avg*, range: 21-114), As (88 ppm *avg*, range: <LOD-1499), Sn (11.9 ppm *avg*, range: 1-62), and Sb (1.7 ppm *avg*, range: <LOD-41.5). The latter elements (As, Sn, and Sb) potentially reflecting a higher-level portion of these systems.

Among the deposits examined in this study, important inter-deposit TSM trace-element variations exist, notably in terms of the following elements: LILE – K, Sr, and Pb; transition metals – Ti, V, Mn, and Cu; and semi-metals; As and Sn; and REEs – La for which the average values are presented below. Inter-deposit variations are important in that they likely reflect physiochemical differences amongst the deposits examined. Among the deposits examined in this study, Coxheath contains the highest K (2169 ppm), while Woodjam contains the lowest (135 ppm). Strontium is consistent between the deposits, 298 ppm for porphyry TSM, with the Casino deposit being the exception with a lower concentration (132 ppm). The Donoso breccia additionally contains the highest Pb concentration (8 ppm), while Woodjam contains the lowest (0.6 ppm). With regards to the transition metals, the Donoso breccia contains the highest Ti concentration (6284 ppm), which is much higher than any other breccia samples examined, whereas the Casino samples contain the lowest (1396 ppm). New Afton contains the highest V contents (1392 ppm), while HVC contains the lowest 127 ppm. Highland Valley contains the highest Mn (341 ppm), while Casino contains the lowest 65 ppm. The Donoso breccia contains the highest Cu (30 ppm), while HVC contains the lowest (3.5 ppm). Finally, for the semi-metals, the Donoso breccia contains the highest As (344 ppm), while New Afton contains the lowest (3 ppm). The Casino deposit contains the highest Sn (19 ppm), while Coxheath contains the lowest (3.7 ppm). The Donoso Breccia contains the highest La (12.7 ppm), while Coxheath contains the lowest (0.7 ppm).

3.6.3 Intra-grain variations

Intra-grain variations exist in all the deposits examined and reflect changes in the local environment during crystallization. A LA-ICP-MS trace-element map was collected for a TSM grain from Woodjam that showed a particularly complicated BSEI, *i.e.*, combination of concentric and ‘patchy’ zoning (Figure 3-2). This grain is described here as it highlights both of the common internal textures observed in TSM from porphyry systems. Similar intra-grain features were observed in other porphyry deposits, specifically the trends reflected in the concentric zones. The variations in grey tones primarily reflect changes in major element chemistry, specifically Al and Fe, with the lighter areas having a higher concentration of Fe (13.16 wt. % *avg.*) and depleted in Al (11.74 wt. % *avg.*) relative to the darker zones. In general Mg (~5.5 wt %) remains relatively constant from core to rim (Figure 3-2). Several trace-elements associations are evident: LILE, HFSE, metals, semi-metals, and REEs. Regarding the LILE: K, Sr, and Pb are the principal elements detected, capable of substituting into the $[IX]X$ -site along with Na and Ca. Potassium concentrations are concentrated in the core and weakly correlated with the observed concentric zonation pattern, with some correlation with the patchy zonation as well, although that is less clear (Figure 3-2). Strontium is distinct, in that it is not correlated with the concentric zonation patterns but closely follows the patchy zonation (Figure 3-2). This decoupling reflects the lack of oscillatory zonation of Na for which Sr substitutes. Higher Sr concentrations are found predominantly in the brighter (BSEI) areas that coincide with areas of Fe enrichment and Al depletion. Lead is homogeneous in its distribution across the grain (not shown). The HFSE including Ti and Zr are both enriched in the core regions but have some inverse relationships (Figure 3-2). The small <10 μm bright spots in the Zr map (Figure 3-2) likely reflect zircon inclusions. The Ti distribution pattern is similar to that of Sr described above,

but the inverse is present for Zr (Figure 3-2). Many metals, including Cr, Ni, and Cu are homogeneously distributed (*i.e.*, shows no visible zonation in trace-element grain maps), while a few key elements, including V, Mn, and Zn are not. For example, V (not shown in Figure 3-2) reflects the oscillatory zonation, a pattern similar to that observed for Zn (Figure 3-2).

Manganese shows a similar pattern to Zn (Figure 3-2). Vanadium is concentrated in the rim and less abundant in the core, which is also similar to Zn (Figure 3-2). Manganese exhibits a similar enrichment in the rim of this grain but is concentrated closer to the contact with the core region rather than closer to the edges of the grain (Figure 3-2). The V and Mn distributions exhibit subtle variations matching the patchy zonation but dissimilar to that for Sr (Figure 3-2).

Variations in semi-metal concentrations (*e.g.*, Ga and As) are less pronounced and appear to coincide with the observed oscillatory zonation (Figure 3-2). Gallium is slightly enriched in the rim relative to the core, whereas As (not shown) and Sn are enriched in the core compared to the rim (Figure 3-2). Overall, the REEs follow both oscillatory and patchy zonation patterns (Figure 3-2). There does appear to be a difference between LREE and HREE concentrations: LREE correlates with bright (BSEI) patchy regions in the core while the HREE appears inverse with higher concentrations in the dark (BSEI) patchy regions of the core (Figure 3-2).

3.7 Discussion

The trace element variations present in a mineral (and TSM in particular) are dependent on several factors including (but not limited to) fluid/melt composition (Slack and Trumbull 2011), nature of co-crystallizing minerals (Taylor 1984; Slack 1999), host rock compositions (Galbraith *et al.* 2009), metamorphic grade (Sciuba *et al.* 2021), *P-T* conditions (van Hinsberg *et al.* 2011), oxygen fugacity (van Hinsberg *et al.* 2011), and crystal structure constraints (Bosi 2018). To effectively understand the variation in the overall trace-element composition of TSM is to

holistically understand the interplay amongst the inter- and intra-variables during crystallization must be considered. Doing so requires an appreciation of the fact that while a complex set of parameters may be in operation collectively or independently, the sum of their effects has been encapsulated within the TSM. Further, the potential use of such variations to discriminate between TSM from different environments of formation becomes an important, feasible outcome and it is this latter aspect, specifically with respect to those characteristics of TSM from mineralized porphyry systems that serves as the locus of this present study.

Interpretation of the trace-element data and patterns in TSM requires knowledge of both the intrinsic and extrinsic factors that collectively control the chemical composition, especially when absolute concentrations are unable to effectively discriminate TSM from different environments (Figure 3-3). Intrinsic factors are those related to the crystal-chemistry and structure of a TSM, including the ideal size of a given crystallographic site, ionic radii, valence, and differences of substituting ions (*i.e.*, size, charge and compatibility with the crystallographic site) for simple ionic substitution or composite ionic radii for more complex substitutions. The TSM are characterized by the general formula: $XY_3Z_6T_6O_{18}(BO_3)_3V_3W$, with $X = Na^+, K^+, Ca^{2+}, \square$ (vacancy); $Y = Al^{3+}, Cr^{3+}, V^{3+}, Fe^{2+/3+}, Mg^{2+}, Mn^{2+}, Li^+, Ti^{4+}$; $Z = Al^{3+}, Cr^{3+}, V^{3+}, Fe^{2+/3+}, Mg^{2+}$; $T = Si^{4+}, Al^{3+}, B^{3+}$; $B = B^{3+}$, $V = (OH)^-, O^{2-}$; $W = (OH)^-, F^-, O^{2-}$ are the common major constituents. The characters in the general formula represent groups of cations including: $^{[9]}X$, $^{[6]}Y$, $^{[6]}Z$, $^{[4]}T$, and $^{[3]}B$. The characters V and W represent groups of anions $^{[3]}O3$ and $^{[3]}O1$ sites (Bosi 2018). The systematics of trace-element cation incorporation into the TSM structure has been relatively unexplored in terms of crystal chemistry, but an understanding of the intrinsic constraints on the trace-element incorporation is necessarily crucial. The most basic manner by which any element can be considered as potentially substituting for another is by considering the

relative differences between the ions in terms of radii (primarily) and charge (secondarily). The ideal radii for various crystallographic sites is known: $r_X = 1.28 \text{ \AA}$, $r_Y = 0.68 \text{ \AA}$, $r_Z = 0.56 \text{ \AA}$, and $r_T = 0.24 \text{ \AA}$, determined from site dimensions from a TSM of intermediate schorl-dravite composition (van Hinsberg 2011). This is presented to be a simplistic overview and should not be taken as concrete parameters for element incorporation. The TSM crystal structure is incredibly flexible and can incorporate a wide range of elements that theoretically should not easily fit (*e.g.*, potassium). Figure 3-4 shows each cation site and the potential substituents. The ideal site size is denoted on the respective diagrams with 5% and 15% fields also denoted which encapsulate the most likely substituents into their respective sites. Although the ideal crystallographic site size will differ depending on the TSM end member, the vast majority of the TSM examined in this study lies within the schorl-dravite solid-solution. Given the size of the *X*-site, the size of ^[9]REE (1.032 - 1.216 Å) and the incorporation of elements (*e.g.*, alkaline earths like Ca) here, suggests their incorporation into the *X*-site. Using the diagram, it is predicted that the REE patterns for TSM should show evidence for LREE enrichment, given that the HREE are >15% smaller than the ideal *X*-site size (Figure 3-4a). Other *X*-site trace-elements unlikely to be found in significant concentrations include U and Th due to their large size and significant charge difference as well as Rb and Cs due to their significantly larger (>15% of the ideal size) ionic radius. The *Z*-site, most commonly occupied by Al, can be expected to accommodate a range of trace-elements including As, Cr, Co, Ga, and V, whereas the *Y*-site, most commonly occupied by Fe and Mg can also incorporate Ni, Li, Cu, Zn, Co, Mn, and Sc (Figure 3-4b). The *T*-site commonly occupied by Si is unlikely to contain large concentrations of trace elements due to the small site size and abundance of Si in hydrothermal fluids (Figure 3-4c). Elements such as Be could also fit but Be does not occur in concentrations above the limit of detection in the samples from this study. Due

to the flexibility of the TSM structure, it is important to consider radii of perspective crystallographic sites in the TSM structure. It must also be considered that differences in ionic radii among substituting ions may also be, in part, accommodated through relativistic effects associated with substitution in local or adjacent crystallographic sites. The latter may lead to the development of ordering patterns (short- or long-range) (Bosi 2008; Bosi *et al.* 2018; Andreozzi *et al.* 2020).

Alternatively, extrinsic controls are those that are imparted by the environment of formation on the formation of a crystal which may include temperature, pressure, melt/fluid composition, fO_2 , *etc.* that will directly affect the potential trace element substitution. A recent study has indicated that the partitioning of trace elements between TSM and a silicate melt (800 °C and 7.5 kbar) is close to one (van Hinsberg 2011), suggesting that the trace-element data of a TSM can closely indicate the composition of the melt from which it crystallized. In terms of overall porphyry chemical signatures, porphyry magmas have been shown to exhibit high contents of Sr relative to Y as well as V relative to Sc (Richards 2011; Chiaradia *et al.* 2012; Loucks 2014). Other geochemical pathfinders for porphyry deposits include: Cu, Mo, and Au (proximal pathfinders) as well as Zn, Ag, Pb, As, Sb, and Mn (distal pathfinders) (Cooke *et al.* 2020a) that are also many of the key elements for distinguishing TSM in porphyry systems.

The high Sr content present in porphyry-related TSM (*avg.*: 353 ppm) is consistent with the enrichment observed in porphyry type magmas (≥ 400 ppm) and their associated fluids, a feature ascribed to the suppression of plagioclase crystallization in tandem with fractionation of amphibole \pm garnet in the lower crust (Richards and Kerrich 2007; Chiaradia *et al.* 2012; Loucks 2014). The enrichment in Sr in porphyry TSM is also consistent with observations made of Sr in plagioclase from intrusions related to porphyry deposits, such plagioclase contains ~ 1000 s of

ppm Sr while plagioclase forming in non-mineralized environments contains less ~100 ppm Sr on average (Aigner-Torres *et al.* 2007; Chiaradia *et al.* 2012; Cao *et al.* 2019). It is interesting to note that the Sr content of TSM associated with granitic pegmatites is lower by an order of magnitude (*avg*: 35 ppm, data compiled in this study), which may be related to the formation of paragenetically earlier feldspars. The Sr content of TSM from TSM granites (magmatic tourmaline: Andreozzi *et al.* 2020) is even lower (*avg*: 5 ppm) reflecting the competition with other phases such as feldspars. In TSM granites specifically, TSM formation is shown to be one of the last phases in the paragenesis (Samson 1992; Sinclair and Richardson 1992; Hong *et al.* 2019).

The Pb concentrations (*avg*: 3.6 ppm) in porphyry-related TSM are an order of magnitude lower than those of Sr, resulting in consistently high values of Sr/Pb. The incorporation of Pb into TSM are linked the availability and competition with other crystallizing minerals, most importantly, alkali feldspars and sulfides which both have high affinities for Pb, $D_{\text{feldspar/melt}} = 0.989-2.72$ and $D_{\text{sulfide melt/silicate melt}} = 140-3300$ respectively (Aigner-Torres *et al.* 2007; Li *et al.* 2021b).

Concentrations of Pb and Zn increase with increasing distance from the porphyry center (Jones 1992). Thus, the variations of Pb-Zn in TSM should reveal this, in which case the Pb and Zn concentrations would decrease towards the core of the porphyry system. In contrast, Pb concentrations in granitic pegmatites for example, are higher (*avg*: 22 ppm). Interestingly, Pb-rich TSM, with up to 17.5 wt. % PbO have been recorded (Sokolov and Martin 2009) and Pb-rich TSM have been synthesized at 700 °C and 200 MPa (Vereshchagin *et al.* 2020).

The concentration of Zn is strongly correlated with the nature of the environment of formation. For example, TSM from mineralized porphyries contains relatively low concentrations of Zn (*avg*: 36 ppm) whereas granitic pegmatites show more pronounced enrichments (*avg*: 450 ppm,

data compiled in this study). In porphyry systems, higher concentrations of Zn are observed to be distal to the porphyry center (Jones 1992). To date, the highest recorded concentration in a TSM, 7.37 wt. % ZnO, is from a transitional NYF-LCT granitic pegmatite (Pieczka *et al.* 2018). In medium to high-grade metapelitic rocks, it has been argued that the principal hosts of Zn (that are not sphalerite), ranked in terms of decreasing concentrations are: gahnite > staurolite > tourmaline (Henry and Dutrow 2018). In this regard, along with their generally high modal abundances, TSM must be considered an important sink for Zn, in not only metamorphic rocks but also in other environments that contain elevated concentrations of Zn *e.g.*, pegmatites, especially those that lack gahnite. In systems where gahnite is present (values up to 43.75 wt. % ZnO), TSM can still contain significant concentrations of ZnO up to 0.75 wt.% (Henry and Dutrow 2001). The fact that Zn is considered to be highly mobile in the presence of a fluid phase may in part explain its enrichment during fluid exsolution leading to pegmatite formation (Telus *et al.* 2012).

The concentration of Cu in porphyry-related TSM is generally higher (*avg*: 24 ppm) than other environments. The relative enrichment of Cu in porphyry TSM may be in part related to the high Cu concentrations found in porphyry mineralizing fluids (Hedenquist and Richards 1998; Ulrich *et al.* 1999). The concentration of Cu also appears to strongly correlate with its environment of formation. The exception for high Cu concentrations are Paraiba and Paraiba-like material (pegmatitic TSM with a striking blue color) where TSM-elbaite contains up to 2.50 wt. % CuO (Abduriyim *et al.* 2006). The enrichment of Cu in these TSM has been attributed to pegmatitic melts mixing with ultramafic rocks rich in Cu (Beurlen *et al.* 2011). Additionally, these Cu-bearing to Cu-rich TSM can be distinguished by their low concentrations of Sr which are generally <10 ppm (Abduriyim *et al.* 2006), making them easily distinguished from porphyry

TSM. Typical pegmatitic TSM, in contrast, has much lower concentrations of Cu (*avg*: 1.2 ppm). Variation along the Zn/Cu–Ga side of the diagram (Figure 3-5) of pegmatitic TSM grains could in part be explained by variability in the parental granitic melts. These melts can arise from single sources but also from the anatexis of multiple rock types, which could lead to considerable chemical variability in the resulting TSM (Černý *et al.* 2012).

Gallium has an average concentration in the Earth's upper continental crust of 17.5 ppm (Rudnick 2003). The presence of Ga³⁺ (^{VI}0.62 Å), owing to its similarity in charge and size, substitutes for Al³⁺ (^{VI}0.535 Å) or Fe³⁺ (^{VI}0.645 Å). Gallium is compatible with TSM, fitting into either the *Y* or *Z* sites. The fact that Ga exhibits a wide range in concentrations (Figure 3-3) from 1 to 100s of ppm in TSM makes it a potential discriminator. Studies of Ga in natural melts and fluids show that the highest concentrations are associated with fluids of magmatic origin (Prokof'ev *et al.* 2016) even though Ga relative to Al concentrations have been shown to increase during fractionation (Breiter *et al.* 2013). The concentration of Ga in TSM has been shown to be useful for separating magmatic and hydrothermal samples, with hydrothermal grains having lower concentrations (their Fig. 11h; Sciuba *et al.* 2021). It is unclear if this observation is widespread or whether *P*, *T* or both, contribute to the observed Ga contents of TSM.

Concentrations of Ga in other minerals such as igneous magnetite are higher than that of hydrothermal magnetite (Nadoll *et al.* 2014), potentially further linking Ga incorporation as a function of temperature. Similar results were found in this current study when TSM from porphyry *vs.* orogenic settings are considered. Here porphyry and orogenic TSM (hydrothermal) contain lower concentrations of Ga than granitic TSM (magmatic).

It is also important to consider the partition coefficient values ($D_{\text{tur/melt}}$) in relation to the elements used for discrimination as well as mineral-mineral coefficients when available. As

noted earlier, the only study that provides any such data for TSM is that of van Hinsberg (2011) that reported K values of ~ 1 for most elements. Although this study cannot in any way encapsulate and reflect all the possible conditions under which TSM may develop, it does provide a baseline from which obtained trace-element data may be discussed. For example, the $D_{\text{tur/melt}} \text{Sr} = 1.05$ which is close to unity making Sr incorporation a good indicator as well as a discriminator of the bulk melt Sr composition and relatively unaffected by the crystallization of other phases. In the discrimination diagram presented here, a Sr/Pb ratio is considered, owing to the hypothesis that both elements are co-competing for the X -site. However, the $D_{\text{tur/melt}} \text{Pb} = 0.57$ (*i.e.*, slightly < 1), reflecting the fact that Pb favors the melt (under the conditions of the experiment) thus, Pb is not as favored in the TSM structure. For the Zn/Cu apex, the $D_{\text{tur/melt}} \text{Zn} = 0.66$ indicating a slight preference for the melt, empirically Zn concentrations in TSM have been a strong indicator for differentiating fractionation and magmatic *vs.* hydrothermal processes. Copper ($D_{\text{tur/melt}} = 1.86$) in TSM is another strong indicator for mafic systems which have not yet reached conditions of S-saturation or hydrothermal systems with elevated Cu concentrations (*i.e.*, porphyry deposits). In systems where S-saturation has occurred, $D_{\text{sulfide liquid/silicate melt}} \text{Cu} = 50 - 220$ (Li *et al.* 2021b), any subsequent TSM would be strongly depleted in Cu. In systems which are not actively crystalizing sulfides or have not reached S-saturation, Cu can readily partition into TSM with a reported $D_{\text{tur/melt}} \text{Cu} = 1.86$. Finally, Ga has a reported $D_{\text{tur/melt}} \text{Ga} = 0.76$ suggesting a slight preference for the melt. It has also been shown to be an indicator of magmatic and hydrothermal processes as well as metamorphic grade (Prokof'ev *et al.* 2016; Sciuba *et al.* 2021). Considering the partition coefficients (values from; van Hinsberg 2011) for the elements in the ternary plot proposed is wholly consistent with crystal-chemical considerations for TSM. The lack of major constraints on the incorporation of these elements in TSM further reinforces

the effectiveness of this diagram as a useful discriminator for its geological environment of formation.

Discrimination diagrams are numerous in the mineral chemistry literature (*e.g.*, Dare *et al.* 2012; Li *et al.* 2021a), but many authors fail to provide a scientifically valid justification for the use of specific elements, ratios, or addition of elements concentrations that were used in developing the discrimination plots presented. These diagrams (in general) rely simply on the visual separation of data and very few consider suitable explanations for the visual interpretations that have been made. Average trace-element concentrations can partially distinguish TSM in porphyry systems from that in other geologic environments, but ratios of key elements are most effective because much of the noise in the data is removed. Ratios may correct for the wide range of trace element concentrations and in part normalize the data, removing some of the intra-grain variations observed between chemical zones (Figure 3-2). Ratios can also be useful for evaluating the competition of elements for specific crystallographic sites. A number of ratios were examined including V/Sn, Sr/Sn (which were presented by: Sciuba *et al.* 2021), Ti/V, Cr/V, Co/Ni, Sr/Pb, and Zn/Cu, many of which showed little to no variation amongst the environments examined. Meaningful variations in Sr/Sn exist for the TSM groups examined but the overlap between orogenic and porphyry-related samples is its downfall. For Ti/V, little variation exists in Ti concentrations amongst the environments examined, while V is much more variable with pegmatitic and W-Sn samples having significantly lower concentrations with respect to other environments investigated. Unfortunately, this ratio is only effective at separating pegmatitic samples. Finally, V/Sn is effective for separating porphyry and orogenic samples but the high concentrations of V in the metamorphic samples overlaps with both porphyry and orogenic TSM, precluding differentiation. The ratios Sr/Pb and Zn/Cu are the most useful in discriminating

between TSM in mineralized porphyry systems and that from other potential environments (Figure 3-5). Development of this discrimination plot is based on several key features including 1) intrinsic (crystal-chemical), and 2) extrinsic (geologic environment) factors. In terms of the crystal structure of TSM, both Sr and Pb are known to occupy the *X*-site, while both Zn and Cu are known to compete for the *Y*-site (Beurlen *et al.* 2011; Ertl and Bačík 2020).

A ternary plot of Sr/Pb–Zn/Cu–Ga reveals that TSM associated with mineralized porphyry systems have trace-element compositions that predominantly occur along the Sr/Pb–Ga join. Porphyry TSM contain high Sr/Pb (*avg*: 241), variable Ga (*avg*: 58 ppm), and low Zn/Cu (*avg*: 1.5) values (Figure 3-5). Conversely, the TSM associated with orogenic Au deposits clusters along the Sr/Pb–Zn/Cu join, and those having a granitic or granitic pegmatite affiliation plot along the Zn/Cu–Ga join (Figure 3-5). In effect, the relatively simple Sr/Pb–Zn/Cu–Ga ternary plot is a powerful tool for discriminating among different types of TSM evaluated in this study. As a note, some of the TSM that have been classified as orogenic in origin (*e.g.*, those forming from hydrothermal fluids in orogenic Au systems), plot outside of what is considered the orogenic field. Such TSM is likely metamorphic in origin or may have experienced some overprinting effects related to metamorphism. These TSM warrant further investigation to their textural relationship with the mineralizing fluids. In general, metamorphic TSM plot in the center of the diagram trending from the Zn/Cu apex along a vector towards the center of the Sr/Pb and Ga side of the diagram (Figure 3-5). Even with the high degree of chemical variability that exists at the grain-scale for individual crystals of porphyry-related TSM, their distinct porphyry signature (*i.e.*, high Sr/Pb, low Zn/Cu and variable Ga) is still retained (Figure 3-5). However, some porphyry-related TSM plot to the left of the Sr/Pb – Ga join due to relative enrichments in Zn, which include some of the TSM from HVC. These TSM samples are from a late-stage dike

rather than within the porphyry and may explain the Zn enrichment, similar to the zonation of Zn seen in porphyry systems (Cooke *et al.* 2020a). Based on this assumption, samples of TSM with high Zn could potentially be considered less prospective (*i.e.*, typically have concomitant decreases in Cu) because they may be indicative of occurring distal from the porphyry center or entirely unrelated to the mineralizing process. Orogenic TSM, much like porphyry TSM, exhibit a wide variation along the Sr/Pb – Zn/Cu join. The bulk of this variation reflects changes in Sr and Pb which largely reflects the wide range of host rocks for these deposits. For TSM associated with VMS environments, the most recent data are from the La Ronde deposit (Quebec, Canada) (Sciuba *et al.* 2021). These data show that two populations exist, one that plots in the metamorphic field and the other that plots close to the top of the diagram in the orogenic field (due to high concentrations of Sr and low concentrations of Zn). Unfortunately, due to a paucity of data for TSM from VMS settings, conclusions cannot be made about their trace-element compositions in relation to the other environments examined in this study. However, based on TSM data from the select VMS systems (*e.g.*, Griffin *et al.* 1996; Slack 1999), elements that should be useful for discrimination include Cu, Pb, and Zn.

In order to determine how individual elements, affect the distribution on the ternary diagram, the absolute abundances (color-coded concentrations separated into 10 equal ranges) of each of the elements are overlain on the ternary diagram (Figure 3-6). The rationale of the elements plotted in Figure 3-6 (*i.e.*, Sr, Pb, Zn, Cu, and Ga) are explained above. Strontium concentrations are highest in porphyry and orogenic TSM samples and lowest in pegmatitic and granitic samples. Lead concentrations distinctly show lower concentrations towards the Sr/Pb apex, and higher concentrations towards the Zn/Cu-Ga line. Orogenic samples exclusively have low concentrations of Pb while the porphyry TSM increase in Pb concentrations towards the Ga

apex, likely reflecting TSM forming on the peripheries or in a higher-level setting where Pb is more concentrated. Gallium concentrations in TSM have been plotted to distinguish magmatic and hydrothermal origins and they also possibly reflect the temperature of formation. Granitic and pegmatitic TSM contain the highest concentrations of Ga followed by porphyry and orogenic related TSM. Zinc concentrations reflect competition with other phases and fractionation with porphyry TSM containing the lowest concentrations followed by orogenic, and granitic/pegmatitic, which have the highest concentrations. Finally, Cu concentrations are highest in porphyry-related tourmaline followed by pegmatitic and orogenic related TSM.

There are a variety of factors to consider when applying the discrimination diagram (Figure 3-5). To start, a thorough investigation of macro and micro textures should be undertaken (*e.g.*, grain size, morphology, color, inclusion populations, and internal zonation; discussed in Beckett-Brown 2022). Grains that do not fit the textural characteristics of porphyry TSM can not be considered porphyry derived. For example, grains forming as isolated individual grains with abundant inclusions are not derived from a porphyry system. Once the textures have been investigated then the major and minor elements should be investigated. Grains which contain >0.5 apfu Ca+K+Vac should not be considered further, additionally any Li bearing (>0.1 wt.%) should also be excluded from further consideration. Once all these parameters above have been investigated, then and only then should trace-element data be collected. Before plotting trace-element data on Figure 3-5, key trace-elements should first be examined, those including Li and Cr. Samples which contain Li concentrations >50 ppm should not be considered porphyry related while samples with high Cr >1500 ppm should be considered suspect and likely formed in ultramafic rocks. Finally, once these steps have been completed, trace-element data can be plotted on the discrimination diagram (Figure 3-5). Grains which plot with in the 99th percentile

field (the larger porphyry Cu TSM region with the line drawn at 10% line on the ternary) are prospective, those which plot in the 95th percentile field (the smaller region, drawn at the 3% line on the ternary) are highly prospective. This discrimination is for porphyry systems that contain Cu, those systems which are Au only will not fall within this region as there is no available Cu to substitute into the TSM. Additional work will be required to help separate those Au-only porphyries.

3.8 Conclusions

Tourmaline in porphyry Cu (\pm Au, \pm Mo) systems can be distinguished from that in other environments or deposit styles using trace-element data if intrinsic (crystal-chemical *i.e.*, site-specific partitioning) and extrinsic (geochemical environment, co-crystallizing minerals, and fluid chemistry) factors that affect the TSM chemistry are considered.

Large ions such as Sr and Pb are controlled by presence or absence of feldspars. Porphyry deposit intrusions are known for their anomalous Sr concentrations, whereby Sr is primarily hosted in feldspars. The breakdown of primary feldspars during hydrothermal activity contributes to the high concentrations in the resulting TSM. Transition metals including V, Cr, Co, Ni, Cu, and Zn are strongly affected by the presence of mafic rocks with porphyry TSM in general containing low concentrations of these elements. Copper is an exception as it can also be influenced by Cu-rich fluids found in porphyry systems. The Cu contents in TSM reflect its availability in the fluid, with porphyry TSM containing the highest Cu concentrations of the ore systems that were compared. Finally, Zn, in addition to being sensitive to host rock compositions also reflects fractionation and a lack of Zn-competing phases. Concentrations of Zn in porphyry TSM is the lowest amongst the environments examined. Gallium is used as a proxy for

temperature as well as an indication of magmatic, magmatic-hydrothermal, and hydrothermal samples. Rare earth concentrations in TSM from porphyry systems are generally low with LREE enriched patterns and variable Eu-anomalies.

From an investigation of these intrinsic trace-element effects as well as the role of extrinsic geochemical trends and factors, a ternary of Sr/Pb-Zn/Cu-Ga is proposed to effectively discriminate porphyry TSM from that forming in other unique geologic environments (Figure 3-5). Strontium and Pb readily substitute into the *X*-site, Zn and Cu readily substitute into the *Y*-site, and Ga substitutes into the *Z*-site. The partition coefficients close to one between TSM and a melt make these elements ideal indicators of distinct geochemical processes. Porphyry tourmaline is characterized by high Sr/Pb (*avg*: 241) and low Zn/Cu (*avg*: 1.5) and variable Ga (*avg*: 58 ppm). Orogenic tourmaline is characterized by low Sr/Pb (*avg*: 193) and high Zn/Cu (*avg*: 223) and variable Ga (*avg*: 43 ppm). Metamorphic tourmaline is characterized by low Sr/Pb (*avg*: 12) and high Zn/Cu (*avg*: 223) and variable Ga (*avg*: 72 ppm). Pegmatitic and granitic tourmaline is characterized by low Sr/Pb (*avg*: 2.91) and high Zn/Cu (*avg*: 472) and higher Ga (*avg*: 112 ppm).

3.9 Figures

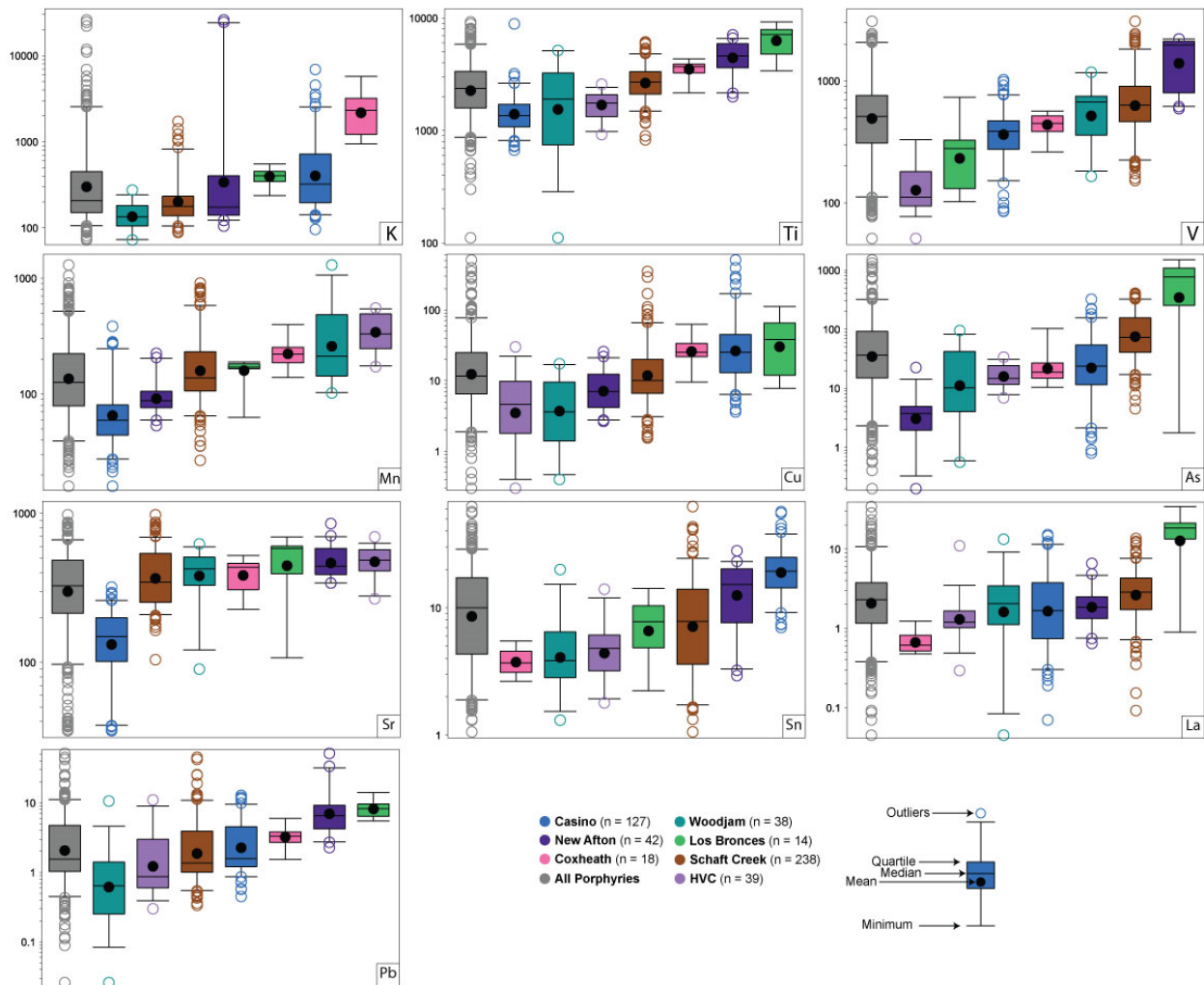


Figure 3-1: Tukey box plots of porphyry tourmaline trace-element data.

Tukey box plots, far outlier data, sorted by mean of TSM trace-element data determined by LA-ICP-MS of 516 grain analyses from 24 samples at the seven porphyry deposits examined.

Results show the variations in data between the porphyry deposits examined in this study. All concentrations shown are in parts per million. Outliers are classified as $1.5 \times (Q3 - Q1)$ and far outlier data is classified as $3 \times (Q3 - Q1)$.

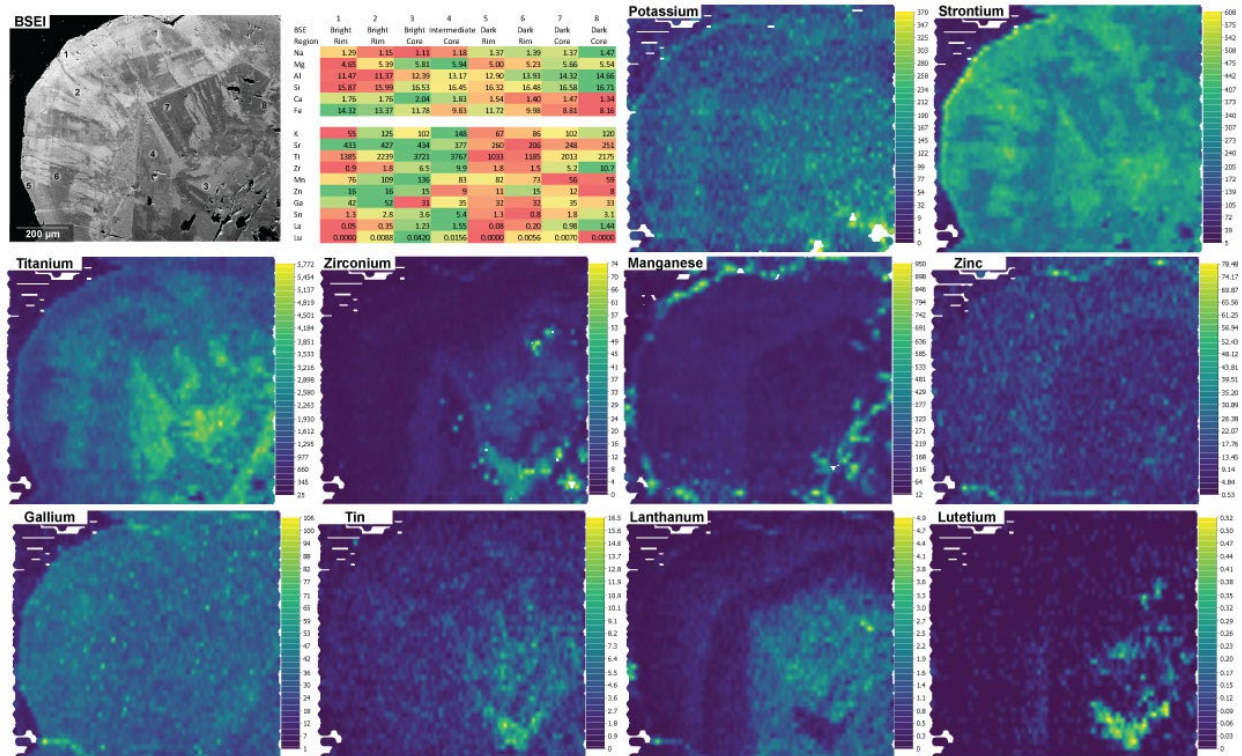


Figure 3-2: Tourmaline trace-element map.

LA-ICP-MS trace-element map of a TSM grain from the Woodjam deposits, BC. The top left tile is a backscattered electron image (BSEI) overlain with areas of interest (circled numbers). The adjacent tile is a summary of the major (data shown in wt %) and trace-element data (data shown in ppm) for the investigated grain. Subsequent tiles show select trace-element maps. Maps were constructed using the “grid” function in ioGAS™. Map cell size was 2.6 x 2.6 map units with a search radius of 7 cells and a minimum smoothing radius of 3 cells. The color scale presented is linear. The trace-element map concentration scales are presented in ppm. Anomalous values of K, Zr, and Mn were removed (due to the presence of inclusions or other phases forming along fractures) to allow for a linear scale to be used for all elements.

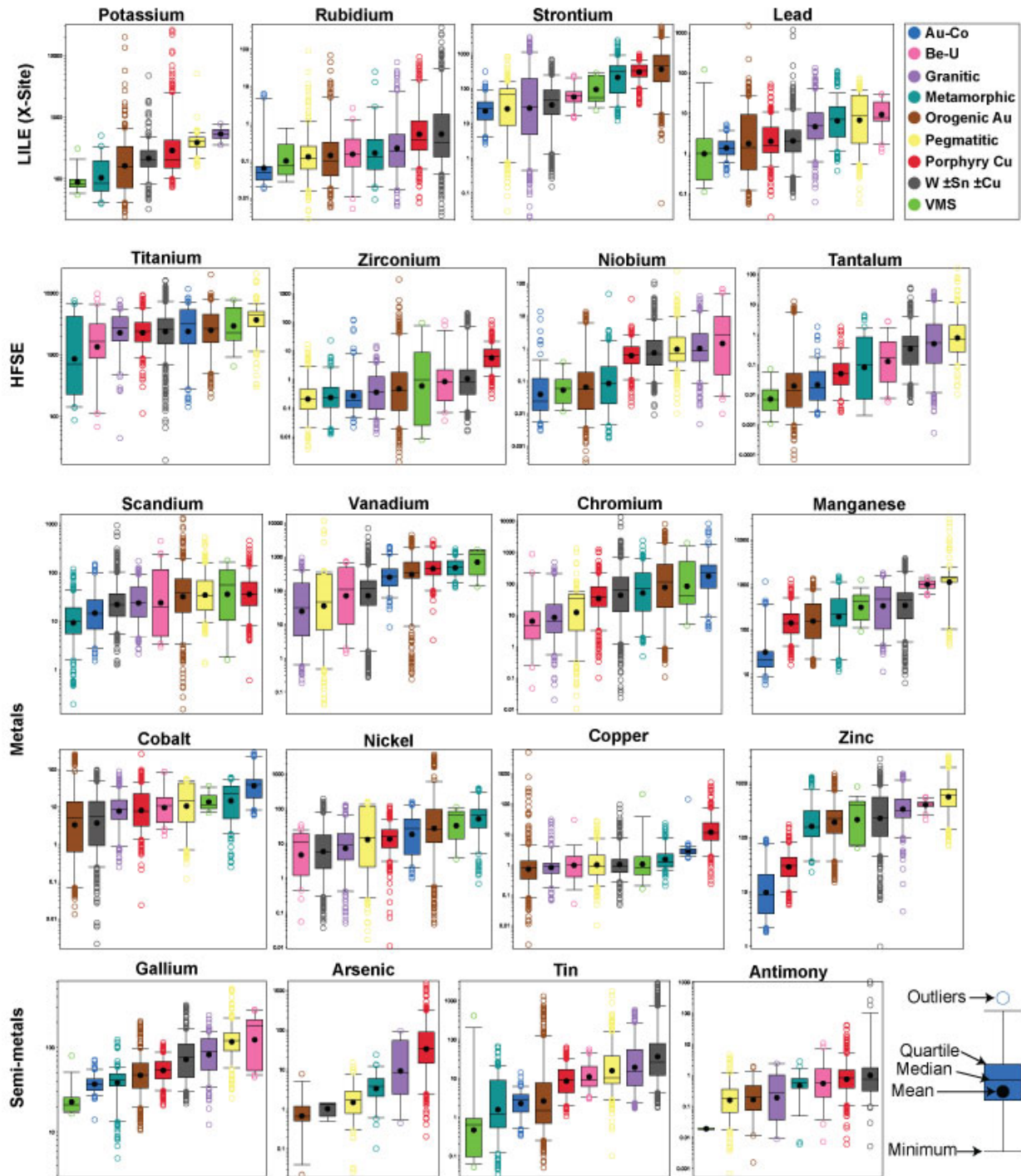
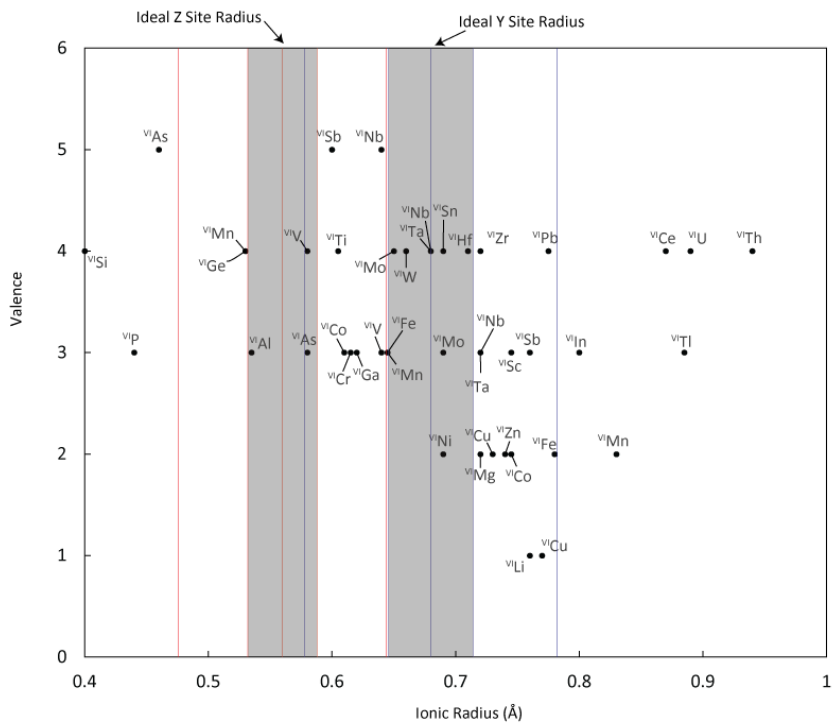
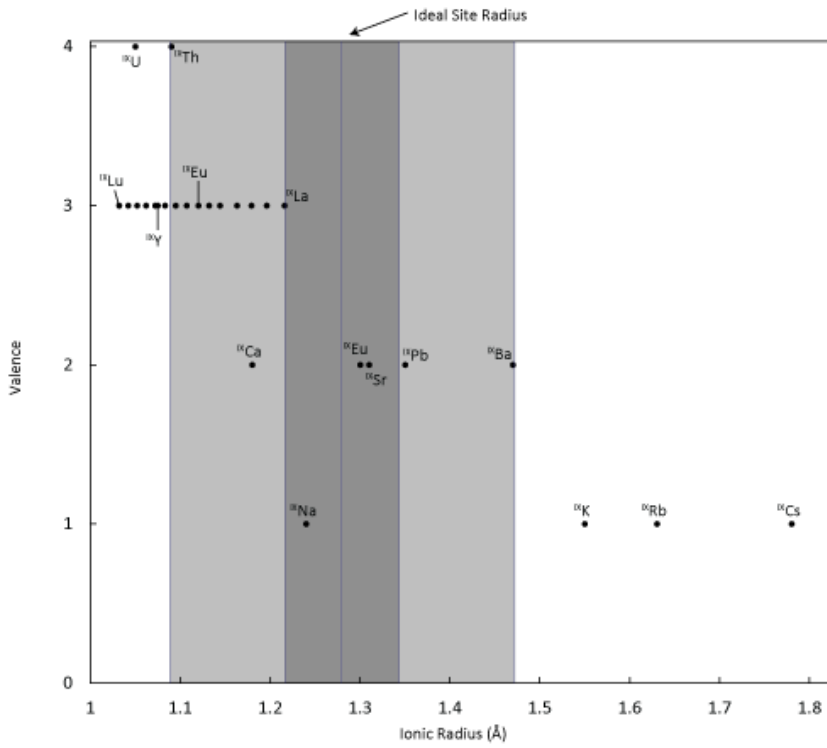


Figure 3-3: Percentile box plots of tourmaline trace-elements.

Percentile box plots, far outlier data, sorted by mean of TSM trace-element data determined by LA-ICP-MS showing the variations in data between some geologic environments in which TSM

are found. All concentrations shown are in parts per million. Outliers are classified as $1.5*(Q3-Q1)$ and far outlier data is classified as $3*(Q3-Q1)$. Data for TSM forming in granites is compiled from: Drivenes *et al.* (2015); Kalliomaki *et al.* (2017); Zall *et al.* (2019); Zhao *et al.* (2019); Xiang *et al.* (2020); Aysal *et al.* (2021); Hong *et al.* (2021); Zhao *et al.* (2021a); and unpublished analyses collected by the author from the Seagull Batholith-Yukon Territory. Data for TSM forming in pegmatites is compiled from: Marks *et al.* (2013); Copjakova *et al.* (2015); Zhao *et al.* (2019); Chakraborty and Upadhyay (2020); Long *et al.* (2021); Sciuba *et al.* (2021); Zhao *et al.* (2021c); and unpublished analyses collected by the author from the Usakos Pegmatite-Namibia as well as the Beryl pit-Ontario. Data for TSM forming in metamorphic rocks is compiled from: van Hinsberg (2011); Kalliomaki *et al.* (2017); Wang *et al.* (2018); Hong *et al.* (2021); and unpublished analyses collected by the author from Jordan Falls-Nova Scotia. Data for TSM forming in orogenic Au deposits is compiled from: Jiang *et al.* (2002); Kalliomaki *et al.* (2017); Trumbull *et al.* (2018); Jin and Sui (2020); and Sciuba *et al.* (2021). Data for TSM forming in VMS deposits is compiled from: Slack *et al.* (1999); Klemme *et al.* (2011); and Sciuba *et al.* (2021). Data for TSM forming in polymetallic $W \pm Sn \pm Cu$ deposits is compiled from: Jiang *et al.* (2004); Codeco *et al.* (2017); Lunay *et al.* (2018); Harlaux *et al.* (2019); Carocci *et al.* (2020); Carr *et al.* (2020); Harlaux *et al.* (2020); Hu and Jiang (2020); Xiang *et al.* (2020); Ghosh *et al.* (2021); and Zhao *et al.* (2021b). Some of the compiled trace-element data (*i.e.*, Mn, Ga, Pb) lack values as they were not analyzed by the respective authors or occur below limit of detection.



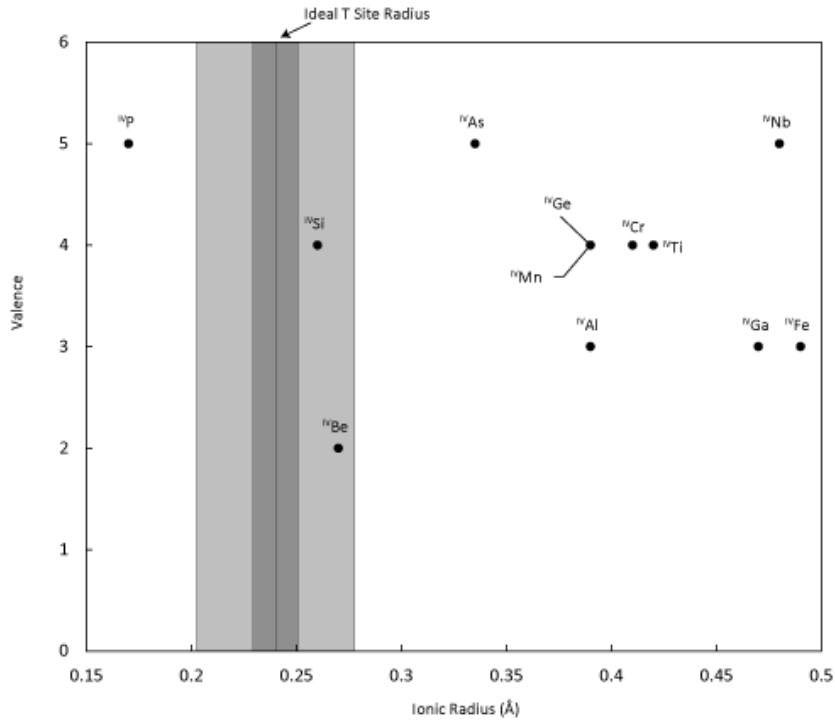


Figure 3-4: Size and valence substitution constraints for trace-elements.

An Ionic radius *versus* valence plot for ideal crystallographic site sizes corresponding to an intermediate schorl-dravite (van Hinsberg, 2011). Also indicated are fields corresponding to 5 and 15% relative size differences. **a.** *X*-site potential substituents, with an ideal site radius size of 1.28 Å. **b.** *Z*- and *Y*-site potential substituents, with an ideal site radius size of 0.56 Å and 0.68 Å respectively. **c.** *T*-site potential substituents, with an ideal site radius size of 0.24 Å.

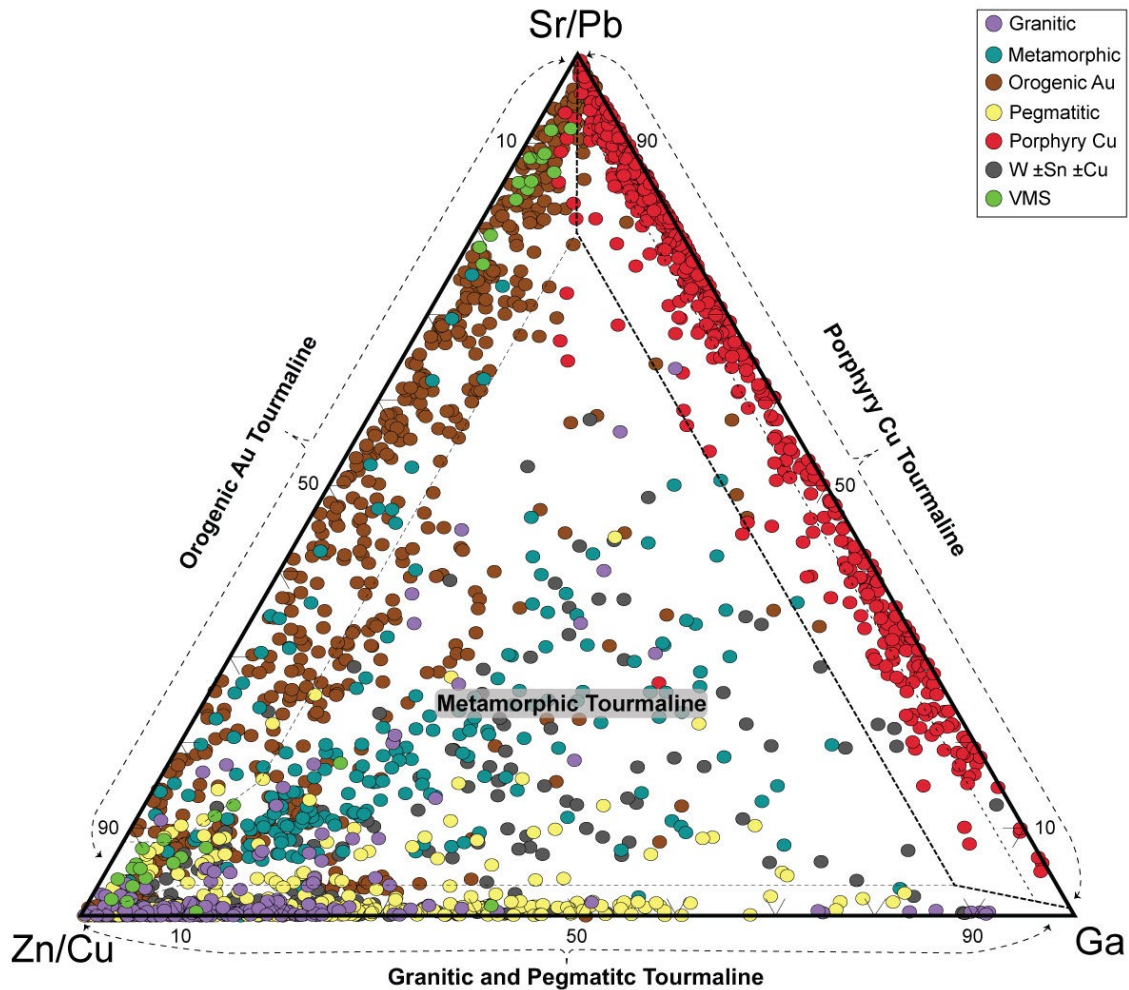


Figure 3-5: Tourmaline trace-element discrimination diagram.

Tourmaline trace-element classification diagram. The apices of the ternary are Sr/Pb–Zn/Cu–Ga. Dashed lines represent the typical field where TSM analyses from the respective environments listed plot. The porphyry Cu TSM field represents a 99th percentile region of porphyry TSM analyses drawn in a straight line. This coincides with the 10% marker on the ternary. The other fields on the diagram are less constrained as the bulk of the data is compiled and not as well constrained as the porphyry analyses. Overlap between metamorphic and orogenic samples is suspect and potentially a reflection of misclassification. Published data used for comparison are referenced in Figure 3-3.

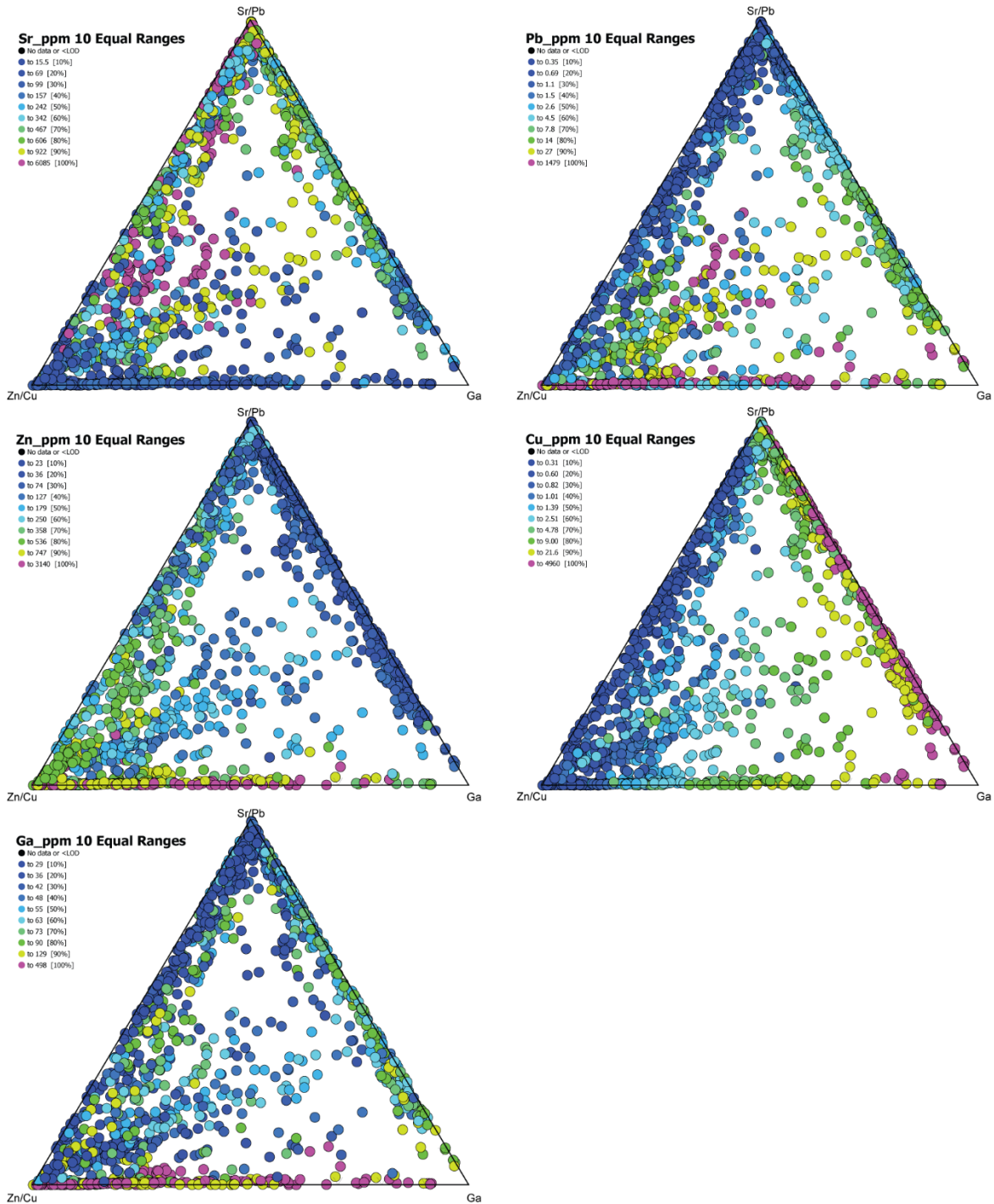


Figure 3-6: Discrimination diagram trace-element concentration overlays.

Tourmaline trace-element classification diagram from Figure 5 overlain with a hot-cold color scale of Sr, Pb, Zn, Cu, and Ga concentrations split into 10 equal ranges.

3.10 Tables

Table 3-1: Summary of tourmaline trace-element concentrations determined by LA-ICP-MS for the seven deposits examined

	LOD	Casino <i>n</i> = 127			Coxheath <i>n</i> = 18			HVC <i>n</i> = 39			Los Bronces <i>n</i> = 14		
		Mean	Min	Max	Mean	Min	Max	Mean	Min	Max	Mean	Min	Max
K	20	680	96	6900	2495	944	5736	NA			402	236	552
Sc	1	61	10	250	49	23	98	12	4	42	46	15	118
Ti	5	1517	668	8877	3544	2167	4336	1748	920	2580	6551	3394	9239
V	2	400	85	1022	443	262	566	141	51	330	268	102	732
Cr	0.1	68.3	11.5	347.0	27.6	18.8	39.2	21.7	1.7	71.0	71.0	5.1	206.0
Mn	3	80	16	384	230	139	398	364	172	552	164	63	189
Co	0.1	8.0	<LOD	41.3	53.6	28.2	84.2	18.9	9.5	29.8	36.8	12.8	58.8
Ni	0.1	14.0	0.2	44.2	45.6	10.8	79.0	6.1	0.1	11.1	80.4	46.9	120.1
Cu	0.1	44.9	3.6	510.0	28.5	9.5	62.6	6.3	0.3	30.0	44.1	7.7	112.2
Zn	0.1	29.5	5.7	105.0	62.5	34.8	106.7	29.7	16.9	48.1	40.1	18.8	58.8
Ga	0.1	49.7	23.7	103.0	61.7	31.3	79.2	41.7	20.7	61.0	67.2	52.7	88.1
Ge	0.1	7.0	2.3	15.7	1.7	0.9	2.5	4.9	1.3	11.6	5.9	0.6	7.9
As	2	41	<LOD	322	26	10	103	17	7	34	755	2	1499
Sr	0.2	149.1	34.8	319.5	394.2	226.8	520.6	484.8	267.0	694.0	498.8	107.5	692.8
Y	0.04	3.56	0.06	20.60	2.24	0.89	4.75	8.98	0.95	22.80	8.30	0.42	18.23
Zr	0.1	2.7	0.6	21.0	5.73	2.31	11.32	8.6	2.2	21.7	8.5	0.6	17.7
Nb	0.2	1.2	<LOD	32.6	0.81	0.38	1.83	1.9	0.7	3.8	2.3	0.5	4.8
In	0.1	0.4	<LOD	2.4	0.2	0.1	0.4	1.9	0.4	3.7	1.2	<LOD	1.6
Sn	0.5	20.6	7.0	57.0	3.8	2.6	5.5	4.9	1.8	14.0	7.5	2.2	14.2
Sb	0.2	2.7	<LOD	41.5	0.4	<LOD	0.7	0.4	<LOD	1.0	10.4	0.3	38.8
Ba	0.2	17.6	<LOD	300.0	36.3	12.4	80.4	2.3	0.7	11.0	2.4	0.6	5.7
La	0.03	2.93	0.07	15.20	0.69	0.48	1.24	1.63	0.29	11.00	17.36	0.90	34.32
Ce	0.03	4.62	0.22	23.00	0.98	0.64	1.62	2.56	0.56	24.00	23.79	0.95	54.04
Pr	0.01	0.38	<LOD	1.92	0.10	0.05	0.22	0.30	0.06	3.70	1.98	0.08	5.05
Nd	0.01	1.21	<LOD	5.10	0.43	0.22	0.92	1.08	0.11	16.40	5.71	0.14	14.71
Sm	0.01	0.19	<LOD	0.69	0.10	<LOD	0.28	0.18	<LOD	3.90	0.67	<LOD	1.39
Eu	0.03	0.09	<LOD	0.34	0.05	<LOD	0.10	0.04	<LOD	0.57	0.15	0.05	0.28
Gd	0.01	0.19	<LOD	1.20	0.14	<LOD	0.34	0.23	<LOD	1.80	0.62	<LOD	0.94
Tb	0.03	0.04	<LOD	0.29	0.03	<LOD	0.07	0.05	<LOD	0.38	0.11	<LOD	0.19
Dy	0.01	0.38	<LOD	2.84	0.23	0.09	0.59	0.60	<LOD	2.10	0.92	0.05	1.87
Ho	0.03	0.12	<LOD	0.75	0.07	0.02	0.16	0.22	<LOD	0.53	0.26	<LOD	0.66
Er	0.01	0.53	<LOD	2.43	0.33	0.13	0.74	1.12	0.04	3.01	0.98	0.02	2.05
Tm	0.03	0.11	<LOD	0.51	0.07	0.01	0.18	0.23	<LOD	0.63	0.18	<LOD	0.35
Yb	0.01	1.14	<LOD	3.83	0.65	0.28	1.61	2.19	0.23	5.40	1.27	<LOD	2.36
Lu	0.03	0.22	<LOD	0.74	0.17	0.07	0.40	0.53	0.06	1.23	0.23	<LOD	0.40
Pb	0.04	3.21	0.45	12.84	3.37	1.53	5.99	1.98	0.30	11.00	8.43	5.48	14.10
Th	0.04	1.67	<LOD	18.00	0.90	0.37	1.68	0.90	<LOD	2.56	4.35	0.08	20.26
U	0.04	0.60	<LOD	11.87	0.11	<LOD	0.36	0.18	<LOD	0.66	2.11	0.49	9.74

Table 3-1: Continued...

	New Afton <i>n</i> = 42			Schaft Creek <i>n</i> = 238			Woodjam <i>n</i> = 38			Porphyry TSM <i>avg.</i>			
	LOD	Mean	Min	Max	Mean	Min	Max	Mean	Min	Max	Mean	Min	Max
K	20	2500	105	25929	254	88	1720	143	72	274	730	72	25929
Sc	1	93	19	355	53	4	449	46	7	182	53	4	449
Ti	5	4656	1999	7092	2804	826	6131	2145	111	5150	2635	111	9239
V	2	1545	591	2208	738	152	3076	589	165	1175	630	51	3076
Cr	0.1	84.6	4.7	528.0	88.3	2.9	1241.1	4.1	<LOD	20.2	67.9	<LOD	1241.1
Mn	3	96	53	225	200	27	907	335.8	102	1300	184	16	1300
Co	0.1	2.9	0.2	5.5	10.0	0.3	90.0	29.1	5.4	260.0	14.2	<LOD	260.0
Ni	0.1	13.8	0.0	26.9	17.6	0.7	68.2	12.1	0.4	24.6	18.2	<LOD	120.1
Cu	0.1	8.6	2.6	25.8	21.0	1.5	350.0	6.2	0.4	17.3	24.4	<LOD	510.0
Zn	0.1	36.5	8.9	172.5	38.0	6.0	121.9	38.0	11.0	151.0	35.8	5.7	172.5
Ga	0.1	74.7	36.7	114.3	63.0	26.4	101.0	46.0	21.5	67.2	57.7	20.7	114.3
Ge	0.1	2.4	1.2	5.2	4.0	0.2	14.3	2.9	0.8	7.1	4.5	<LOD	15.7
As	2	4	<LOD	22	111	5	407	25	<LOD	95	85	<LOD	1499
Sr	0.2	340.2	853.3	476.3	399.2	104.2	977.0	405.66	90	623	354.9	34.8	977.0
Y	0.04	1.03	53.86	13.96	5.41	0.21	62.22	14.11	<LOD	73.00	6.31	<LOD	73.00
Zr	0.1	1.6	32.2	7.2	12.6	1.6	116.0	12.9	1.1	45.0	8.8	0.59	116.0
Nb	0.2	0.1	2.2	0.6	0.7	<LOD	3.3	0.3	<LOD	0.8	0.9	<LOD	32.6
In	0.1	0.3	<LOD	0.6	0.6	<LOD	2.7	0.4	<LOD	1.4	0.6	<LOD	3.7
Sn	0.5	14.6	2.9	28.1	10.0	1.1	62.4	5.0	1.3	20.0	11.6	1.1	62.4
Sb	0.2	0.3	<LOD	2.0	1.4	<LOD	8.1	0.7	<LOD	2.4	1.6	<LOD	41.5
Ba	0.2	90.1	1.1	1058.6	5.9	<LOD	82.0	10.9	0.8	130.0	17.2	<LOD	1058.6
La	0.03	2.08	0.64	6.60	3.31	0.09	13.60	2.71	0.05	13.30	3.14	0.05	34.32
Ce	0.03	3.41	0.81	12.03	4.74	0.21	16.50	5.85	0.05	29.40	4.75	0.05	54.04
Pr	0.01	0.32	<LOD	1.24	0.40	<LOD	1.75	0.69	<LOD	3.70	0.42	<LOD	5.05
Nd	0.01	1.16	0.17	4.64	1.36	0.03	5.75	2.64	<LOD	13.80	1.42	<LOD	16.40
Sm	0.01	0.18	0.02	0.69	0.19	<LOD	0.86	0.78	<LOD	4.20	0.22	<LOD	4.20
Eu	0.03	0.17	0.04	0.49	0.06	<LOD	0.29	0.08	<LOD	0.27	0.08	<LOD	0.57
Gd	0.01	0.36	0.06	1.38	0.24	<LOD	1.35	1.89	<LOD	9.80	0.31	<LOD	9.80
Tb	0.03	0.10	<LOD	0.40	0.05	<LOD	0.41	0.41	<LOD	1.91	0.07	<LOD	1.91
Dy	0.01	1.16	0.07	5.19	0.49	<LOD	5.00	2.59	<LOD	13.80	0.63	<LOD	13.80
Ho	0.03	0.44	0.05	1.56	0.16	<LOD	1.93	0.66	<LOD	2.69	0.20	<LOD	2.69
Er	0.01	1.98	0.27	7.18	0.73	<LOD	9.66	1.87	<LOD	7.98	0.85	<LOD	9.66
Tm	0.03	0.37	0.07	1.30	0.15	<LOD	1.72	0.29	<LOD	1.30	0.17	<LOD	1.72
Yb	0.01	3.20	0.72	10.28	1.41	0.03	15.16	2.25	<LOD	10.80	1.53	<LOD	15.16
Lu	0.03	0.66	0.13	1.77	0.33	<LOD	3.04	0.39	<LOD	1.63	0.33	<LOD	3.04
Pb	0.04	9.06	2.27	51.34	3.30	0.34	45.00	1.23	<LOD	10.60	3.57	<LOD	51.34
Th	0.04	0.34	0.09	1.31	1.31	0.05	10.40	0.53	<LOD	3.19	1.28	<LOD	20.26
U	0.04	0.10	<LOD	0.64	0.74	<LOD	13.80	0.28	<LOD	1.57	0.57	<LOD	13.80

3.11 References

- Abduriyim, A., Kitawaki, H., Furuya, M. and Schwartz, D., 2006. "Paraíba"-type copper-bearing tourmaline from Brazil, Nigeria, and Mozambique: chemical fingerprinting by LA-ICP-MS. *Gems & Gemology*, 42(1): 4-21. <http://doi.org/10.5741/gems.42.1.4>
- Aigner-Torres, M., Blundy, J., Ulmer, P. and Pettke, T., 2007. Laser Ablation ICP-MS study of trace element partitioning between plagioclase and basaltic melts: an experimental approach. *Contributions to Mineralogy and Petrology*, 153(6): 647-667. <http://doi.org/10.1007/s00410-006-0168-2>
- Andreozzi, G.B., Bosi, F., Celata, B., Capizzi, L.S., Stagno, V. and Beckett-Brown, C.E., 2020. Crystal-chemical behavior of Fe²⁺ in tourmaline dictated by structural stability: insights from a schorl with formula Na^Y(Fe²⁺²Al)^Z(Al₅Fe²⁺)(Si₆O₁₈)(BO₃)₃(OH)₃(OH,F) from Seagull batholith (Yukon Territory, Canada). *Physics and Chemistry of Minerals*, 47(6). <http://doi.org/10.1007/s00269-020-01094-7>
- Aysal, N., Öngen, S., Hanilçi, N., Kasapçı, C., Laçın, D., Boroğlu, M.Ş., Yesiltaş, M., Yılmaz, İ. and Azaz, D., 2020. Late magmatic – hydrothermal tourmaline occurrences within leucogranites in NW Anatolia (Turkey): Mineral chemistry and genetic implications. *Geochemistry*, 81(1). <http://doi.org/10.1016/j.chemer.2020.125676>
- Bačík, P., Koděra, P., Uher, P., Ozdín, D. and Jánošík, M., 2016. Chlorine-Enriched Tourmalines In Hydrothermally Altered Diorite Porphyry From the Biely Vrch Porphyry Gold Deposit (Slovakia). *The Canadian Mineralogist*, 53(4): 673-691. <http://doi.org/10.3749/canmin.1500013>

- Baksheev, I.A., Chitalin, A.F., Yapaskurt, V.O., Vigasina, M.F., Bryzgalov, I.A. and Ustinov, V.I., 2010. Tourmaline in the Vetka porphyry copper-molybdenum deposit of the Chukchi Peninsula of Russia. *Moscow University Geology Bulletin*, 65(1): 27-38.
<http://doi.org/10.3103/s0145875210010035>
- Baksheev, I.A., Prokof'ev, V.Y., Yapaskurt, V.O., Vigasina, M.F., Zorina, L.D. and Solov'ev, V.N., 2011. Ferric-iron-rich tourmaline from the Darasun gold deposit, Transbaikalia, Russia. *The Canadian Mineralogist*, 49(1): 263-276.
<http://doi.org/10.3749/canmin.49.1.263>
- Baksheev, I.A., Trumbull, R.B., Popov, M.P., Erokhin, Y.V., Kudryavtseva, O.E., Yapaskurt, V.O., Khiller, V.V., Vovna, G.M. and Kiselev, V.I., 2017. Chemical and boron isotopic composition of tourmaline from the Mariinsky emerald deposit, Central Urals, Russia. *Mineralium Deposita*, 53(4): 565-583. <http://doi.org/10.1007/s00126-017-0759-z>
- Baksheev, I.A., Vigasina, M.F., Yapaskurt, V.O., Bryzgalov, I.A. and Gorelikova, N.V., 2019. Tourmaline of the Solnechnoe tin deposit, Khabarovsk Krai, Russia. *Mineralogical Magazine*: 1-53. <http://doi.org/10.1180/mgm.2019.72>
- Baksheev, I.A., Yu Prokof'ev, V., Zaraisky, G.P., Chitalin, A.F., Yapaskurt, V.O., Nikolaev, Y.N., Tikhomirov, P.L., Nagornaya, E.V., Rogacheva, L.I., Gorelikova, N.V. and Kononov, O.V., 2012. Tourmaline as a prospecting guide for the porphyry-style deposits. *European Journal of Mineralogy*, 24(6): 957-979. <http://doi.org/10.1127/0935-1221/2012/0024-2241>
- Beckett-Brown, C.E., McDonald, A.M., McClenaghan, M.B., Plouffe, A. and Ferbey, T., 2021. Investigation of tourmaline characteristics in bedrock and surficial sediment samples

- from two Canadian porphyry copper systems. In: E. Schestelaar and A. Plouffe (Editors), Targeted Geoscience Initiative 5: contributions to the understanding and exploration of porphyry deposits, Geological Survey of Canada, pp. 109-135.
<http://doi.org/10.4095/327989>
- Beurlen, H., de Moura, O.J.M., Soares, D.R., Da Silva, M.R.R. and Rhede, D., 2011. Geochemical and geological controls on the genesis of gem-quality "Paraíba Tourmaline" in granitic pegmatites from northeastern Brazil. *The Canadian Mineralogist*, 49(1): 277-300. <http://doi.org/10.3749/canmin.49.1.277>
- Bosi, F., 2008. Disordering of Fe²⁺ over octahedrally coordinated sites of tourmaline. *American Mineralogist*, 93(10): 1647-1653. <http://doi.org/10.2138/am.2008.2722>
- Bosi, F., 2018. Tourmaline crystal chemistry. *American Mineralogist*, 103(2): 298-306. <http://doi.org/10.2138/am-2018-6289>
- Bosi, F., Andreozzi, G.B., Hålenius, U. and Skogby, H., 2018. Experimental evidence for partial Fe²⁺ disorder at the Y and Z sites of tourmaline: a combined EMP, SREF, MS, IR and OAS study of schorl. *Mineralogical Magazine*, 79(03): 515-528. <http://doi.org/10.1180/minmag.2015.079.3.01>
- Breiter, K., Gardenová, N., Kanický, V. and Vaculovič, T., 2013. Gallium and germanium geochemistry during magmatic fractionation and post-magmatic alteration in different types of granitoids: a case study from the Bohemian Massif (Czech Republic). *Geologica Carpathica*, 64(3): 171-180b. <http://doi.org/10.2478/geoca-2013-0018>
- Byrne, K., 2019. Diagnostic Features of the Rocks and Minerals Peripheral to the Highland Valley Copper District, British Columbia, Canada: Implications for the genesis of

- porphyry Cu systems and their footprints. PhD Thesis, University of Alberta, Edmonton, 211 pp.
- Cao, M., Evans, N.J., Reddy, S.M., Fougereuse, D., Hollings, P., Saxey, D.W., McInnes, B.I.A., Cooke, D.R., McDonald, B.J. and Qin, K., 2019. Micro- and nano-scale textural and compositional zonation in plagioclase at the Black Mountain porphyry Cu deposit: Implications for magmatic processes. *American Mineralogist*, 104(3): 391-402. <http://doi.org/10.2138/am-2019-6609>
- Carocci, E., Marignac, C., Cathelineau, M., Truche, L., Poujol, M., Boiron, M.-C. and Pinto, F., 2021. Incipient wolframite deposition at Panasqueira (Portugal): W-rutile and tourmaline compositions as proxies for early fluid composition. *Economic Geology*, 116(1), 123–146. <http://doi:10.5382/econgeo.4783>
- Carr, P., Norman, M.D., Bennett, V.C. and Blevin, P.L., 2020. Tin Enrichment in Magmatic-Hydrothermal Environments Associated with Cassiterite Mineralization at Ardlethan, Eastern Australia: Insights from Rb-Sr and Sm-Nd Isotope Compositions in Tourmaline. *Economic Geology*, 116: 147-167. <http://doi.org/10.5382/econgeo.4774>
- Casselmann, S.C. and Brown, H., 2017. Casino porphyry copper-gold-molybdenum deposit, central Yukon (Yukon MINFILE 115J028); in Yukon Exploration and Geology Overview 2016, (ed.) K.W. MacFarlane; Yukon Geological Survey, p. 61–74, plus digital appendices.
- Černý, P., London, D. and Novák, M., 2012. Granitic Pegmatites as Reflections of Their Sources. *Elements*, 8: 289-294.

Chakraborty, T. and Upadhyay, D., 2020. The geochemical differentiation of S-type pegmatites: constraints from major–trace element and Li–B isotopic composition of muscovite and tourmaline. *Contributions to Mineralogy and Petrology*, 175, 60.

<http://doi.org/10.1007/s00410-020-01697-x>

Chiaradia, M., Ulianov, A., Kouzmanov, K. and Beate, B., 2012. Why large porphyry Cu deposits like high Sr/Y magmas? *Scientific Reports*, 2: 1-7.

<http://doi.org/10.1038/srep00685>

Codeço, M.S., Weis, P., Trumbull, R.B., Glodny, J., Wiedenbeck, M. and Romer, R.L., 2019. Boron Isotope Muscovite-Tourmaline Geothermometry Indicates Fluid Cooling During Magmatic-Hydrothermal W-Sn Ore Formation. *Economic Geology*, 114(1): 153-163.

<http://doi.org/10.5382/econgeo.2019.4625>

Codeço, M.S., Weis, P., Trumbull, R.B., Pinto, F., Lecumberri-Sanchez, P. and Wilke, F.D.H., 2017. Chemical and boron isotopic composition of hydrothermal tourmaline from the Panasqueira W-Sn-Cu deposit, Portugal. *Chemical Geology*, 468: 1-16.

<http://doi.org/10.1016/j.chemgeo.2017.07.011>

Codeço, M.S., Weis, P., Trumbull, R.B., Van Hinsberg, V., Pinto, F., Lecumberri-Sanchez, P. and Schleicher, A.M., 2020. The imprint of hydrothermal fluids on trace-element contents in white mica and tourmaline from the Panasqueira W–Sn–Cu deposit, Portugal.

Mineralium Deposita, 56(3): 481-508. <http://doi.org/10.1007/s00126-020-00984-8>

Cooke, D.R., Hong, W., Fox, N., Zhang, L., Thompson, J., Goemann, K. and Fayek, M., 2017. Tourmaline mineral chemistry: a tool for vectoring and fertility assessments in porphyry Cu-Au and granite-related Sn deposits, Presentation, pp. 38.

Cooke, D.R., Wilkinson, J.J., Baker, M., Agnew, P., Phillips, J., Chang, Z., Chen, H., Wilkinson, C.C., Inglis, S., Hollings, P., Zhang, L., Gemmell, J.B., White, N.C., Danyushevsky, L. and Martin, H., 2020a. Using Mineral Chemistry to Aid Exploration: A Case Study from the Resolution Porphyry Cu-Mo Deposit, Arizona. *Economic Geology*, 115(4): 813-840. <http://doi.org/10.5382/econgeo.4735>

Cooke, D.R., Wilkinson, J.J. and Pacey, A., 2020b. Chlorite and Epidote Mineral Chemistry in Porphyry Ore Systems: A Case Study of the Northparkes District, New South Wales, Australia. *Economic Geology*, 115(4): 701-727. <http://doi.org/10.5382/econgeo.4700>

Čopjaková, R., Škoda, R., Galiová, M.V., Novák, M. and Cempírek, J., 2015. Sc- and REE-rich tourmaline replaced by Sc-rich REE-bearing epidote-group mineral from the mixed (NYF+LCT) Kracovice pegmatite (Moldanubian Zone, Czech Republic). *American Mineralogist*, 100(7): 1434-1451. <http://doi.org/10.2138/am-2015-4863>

Dare, S.A.S., Barnes, S.-J. and Beaudoin, G., 2012. Variation in trace element content of magnetite crystallized from a fractionating sulfide liquid, Sudbury, Canada: Implications for provenance discrimination. *Geochimica et Cosmochimica Acta*, 88: 27-50. <http://doi.org/10.1016/j.gca.2012.04.032>

Dill, H.G., Garrido, M.M., Melcher, F., Gomez, M.C. and Luna, L.I., 2012. Depth-related variation of tourmaline in the breccia pipe of the San Jorge porphyry copper deposit, Mendoza, Argentina. *Ore Geology Reviews*, 48: 271-277. <http://doi.org/10.1016/j.oregeorev.2012.04.006>

Drivenes, K., Larsen, R.B., Müller, A., Sørensen, B.E., Wiedenbeck, M. and Raanes, M.P., 2015. Late-magmatic immiscibility during batholith formation: assessment of B isotopes and

- trace elements in tourmaline from the Land's End granite, SW England. *Contributions to Mineralogy and Petrology*, 169(6): 27. <http://doi.org/10.1007/s00410-015-1151-6>
- Ertl, A. and Bačík, P., 2020. Considerations About Bi and Pb in the Crystal Structure of Cu-Bearing Tourmaline. *Minerals*, 10(8): 706-721. <http://doi.org/10.3390/min10080706>
- Frikken, P.H., 2003. Breccia-Hosted Copper-Molybdenum Mineralization at Rio Blanco, Chile. PhD Thesis, University of Tasmania.
- Frikken, P.H., Cooke, D.R., Walshe, J.L., Archibald, D., Skarmeta, J., Serrano, L. and Vargas, R., 2005. Mineralogical and isotopic zonation in the Sur-Sur tourmaline breccia, Río Blanco-Los Bronces Cu-Mo deposit, Chile: Implications for ore genesis. *Economic Geology*, 100(5): 935-961. <http://doi.org/10.2113/gsecongeo.100.5>
- Galbraith, C.G., Clarke, D.B., Trumbull, R.B. and Wiedenbeck, M., 2009. Assessment of tourmaline compositions as an indicator of emerald mineralization at the Tsa da Glisza prospect Yukon Territory, Canada. *Economic Geology*, 104(5): 713-731. <http://doi.org/10.2113/gsecongeo.104.5.713>
- Ghosh, U., Upadhyay, D., Abhinay, K. and Mishra, B., 2021. Nature of the mineralizing fluids in the Balda and Motiya W-prospects, western India: Constraints from chemical and B-isotope composition of tourmaline. *Chemical Geology*, 582. <http://doi.org/10.1016/j.chemgeo.2021.120439>
- Griffin, W.L., Slack, J.F., Ramsden, A.R., Win, T.T. and Ryan, C.G., 1996. Trace elements in tourmalines from massive sulfide deposits and tourmalinites Geochemical controls and exploration application. *Economic Geology*, 91(4): 657-675. <http://doi.org/10.2113/gsecongeo.91.4.657>

- Harlaux, M., Kouzmanov, K., Gialli, S., Laurent, O., Rielli, A., Dini, A., Chauvet, A., Menzies, A., Kalinaj, M. and Fontboté, L., 2020. Tourmaline as a Tracer of Late-Magmatic to Hydrothermal Fluid Evolution: The World-Class San Rafael Tin (-Copper) Deposit, Peru. *Economic Geology*, 115: 1665-1697. <http://doi.org/10.5382/econgeo.4762>
- Harlaux, M., Mercadier, J., Marignac, C., Villeneuve, J., Mouthier, B. and Cuney, M., 2019. Origin of the atypical Puy-les-Vignes W breccia pipe (Massif Central, France) constrained by trace element and boron isotopic composition of tourmaline. *Ore Geology Reviews*, 114. <http://doi.org/10.1016/j.oregeorev.2019.103132>
- Hazarika, P., Upadhyay, D. and Pruseth, K.L., 2016. Episodic tourmaline growth and re-equilibration in mica pegmatite from the Bihar Mica Belt, India: major- and trace-element variations under pegmatitic and hydrothermal conditions. *Geological Magazine*, 154(01): 68-86. <http://doi.org/10.1017/s0016756815000916>
- Hedenquist, J.W. and Richards, J.P., 1998. The influence of geochemical techniques on the development of genetic models for porphyry copper deposits. In: J.P. Richards and P.B. Larson (Editors), *Techniques in hydrothermal ore deposits geology*, pp. 235-256. <http://doi.org/10.5382/rev.10.10>
- Henry, D.J. and Dutrow, B.L., 2001. Compositional zoning and element partitioning in nickeloan tourmaline from a metamorphosed karstbauxite from Samos, Greece. *American Mineralogist*, 86(10): 1130-1142. <http://doi.org/10.2138/am-2001-1002>
- Henry, D.J. and Dutrow, B.L., 2018. Tourmaline studies through time: contributions to scientific advancements. *Journal of Geosciences*, 63: 77-98. <http://doi.org/10.3190/jgeosci.255>

Henry, D.J. and Guidotti, C.V., 1985. Tourmaline as a petrogenetic indicator mineral an example from the staurolite-grade metapelites of NW Maine. *American Mineralogist*, 70: 1-15.

Hong, W., Fox, N., Cooke, D.R., Zhang, L. and Fayek, M., 2019. B- and O-isotopic compositions of tourmaline constrain late-stage magmatic volatile exsolution in Tasmanian tin-related granite systems. *Mineralium Deposita*, 55(1): 63-78.

<http://doi.org/10.1007/s00126-019-00885-5>

Hong, T., Zhai, M.-G., Xu, X.-W., Li, H., Wu, C., Ma, Y.-C., Niu, L., Ke, Q. and Wang, C., 2021. Tourmaline and quartz in the igneous and metamorphic rocks of the Tashisayi granitic batholith, Altyn Tagh, northwestern China: Geochemical variability constraints on metallogenesis. *Lithos*, 400-401: 106358. <http://doi.org/10.1016/j.lithos.2021.106358>

Hu, D.-L. and Jiang, S.-Y., 2020. In-situ elemental and boron isotopic variations of tourmaline from the Maogongdong deposit in the Dahutang W-Cu ore field of northern Jiangxi Province, South China: Insights into magmatic-hydrothermal evolution. *Ore Geology Reviews*, 122. <http://doi.org/10.1016/j.oregeorev.2020.103502>

Iveson, A.A., Webster, J.D., Rowe, M.C. and Neill, O.K., 2016. Magmatic–hydrothermal fluids and volatile metals in the Spirit Lake pluton and Margaret Cu–Mo porphyry system, SW Washington, USA. *Contributions to Mineralogy and Petrology*, 171(3): 20.

<http://doi.org/10.1007/s00410-015-1224-6>

Jiang, S.-Y., Yu, J.-M. and Lu, J.-J., 2004. Trace and rare-earth element geochemistry in tourmaline and cassiterite from the Yunlong tin deposit, Yunnan, China: implication for migmatitic–hydrothermal fluid evolution and ore genesis. *Chemical Geology*, 209(3-4): 193-213. <http://doi.org/10.1016/j.chemgeo.2004.04.021>

- Jiang, S.Y., Palmer, M.R. and Yeats, C.J., 2002. Chemical and boron isotopic compositions of tourmaline from the Archean Big Bell and Mount Gibson gold deposits, Murchison Province, Yilgarn Craton, Western Australia. *Chemical Geology*, 188(3-4): 229-247. [http://doi.org/10.1016/S0009-2541\(02\)00107-9](http://doi.org/10.1016/S0009-2541(02)00107-9)
- Jin, X. and Sui, J., 2020. Geochemistry of Tourmaline from the Laodou Gold Deposit in the West Qinling Orogen, Central China: Implications for the Ore-Forming Process. *Minerals*, 10(8). <http://doi.org/10.3390/min10080647>
- Jochum, K.P., Weis, U., Stoll, B., Kuzmin, D., Yang, Q., Raczek, I., Jacob, D.E., Stracke, A., Birbaum, K., Frick, D.A., Günther, D. and Enzweiler, J., 2011. Determination of Reference Values for NIST SRM 610-617 Glasses Following ISO Guidelines. *Geostandards and Geoanalytical Research*, 35(4): 397-429. <http://doi.org/10.1111/j.1751-908X.2011.00120.x>
- Jones, B.K., 1992. Application of metal zoning to gold exploration in porphyry copper systems. *Journal of Geochemical Exploration*, 43: 127-155.
- Kalliomäki, H., Wagner, T., Fusswinkel, T. and Sakellaris, G., 2017. Major and trace element geochemistry of tourmalines from Archean orogenic gold deposits: Proxies for the origin of gold mineralizing fluids? *Ore Geology Reviews*, 91: 906-927. <http://doi.org/10.1016/j.oregeorev.2017.08.014>
- Klemme, S., Marschall, H.R., Jacob, D.E., Prowatke, S. and Ludwig, T., 2011. Trace-element partitioning and boron isotope fractionation between white mica and tourmaline. The *Canadian Mineralogist*, 49(1): 165-176. <http://doi.org/10.3749/canmin.49.1.165>

- Koval, P.V., Zorina, L.D., Kitajev, N.A., Spiridonov, A.M. and Ariunbileg, S., 1991. The Use of Tourmaline in Geochemical Prospecting for Gold and Copper Mineralization. *Journal of Geochemical Exploration*, 40(1-3): 349-360. [http://doi.org/10.1016/0375-6742\(91\)90047-X](http://doi.org/10.1016/0375-6742(91)90047-X)
- Kwong, Y.-T.J., 1981. A new look at the Afton copper mine in light of mineral distributions, host rock geochemistry and irreversible mineral-solution interactions. PhD Thesis, University of British Columbia.
- Launay, G., Sizaret, S., Guillou-Frottier, L., Gloaguen, E. and Pinto, F., 2018. Deciphering fluid flow at the magmatic-hydrothermal transition: A case study from the world-class Panasqueira W–Sn–(Cu) ore deposit (Portugal). *Earth and Planetary Science Letters*, 499: 1-12. <http://doi.org/10.1016/j.epsl.2018.07.012>
- Li, W., Qiao, X., Zhang, F. and Zhang, L., 2021a. Tourmaline as a potential mineral for exploring porphyry deposits: a case study of the Bilihe gold deposit in Inner Mongolia, China. *Mineralium Deposita*: 1-22. <http://doi.org/10.1007/s00126-021-01051-6>
- Li, Y., Audétat, A., Liu, Z. and Wang, F., 2021b. Chalcophile element partitioning between Cu-rich sulfide phases and silicate melt and implications for the formation of Earth's continental crust. *Geochimica et Cosmochimica Acta*, 302: 61-82. <http://doi.org/10.1016/j.gca.2021.03.020>
- Long, Z., Yu, X. and Zheng, Y., 2021. Ore formation of the Dayakou emerald deposit (Southwest China) constrained by chemical and boron isotopic composition of tourmaline. *Ore Geology Reviews*, 135. <http://doi.org/10.1016/j.oregeorev.2021.104208>

- Loucks, R.R., 2014. Distinctive composition of copper-ore-forming arc magmas. *Australian Journal of Earth Sciences*, 61(1): 5-16. <http://doi.org/10.1080/08120099.2013.865676>
- Lynch, G. and Ortega, S., 1997. Hydrothermal alteration and tourmaline-albite equilibria at the Coxheath porphyry Cu-Mo-Au deposit, Nova Scotia. *Canadian Mineralogist*, 35(1): 79-94.
- Manégliá, N., Beaudoin, G. and Simard, M., 2018. Indicator minerals of the Meliadine orogenic gold deposits, Nunavut (Canada), and application to till surveys. *Geochemistry: Exploration, Environment, Analysis*, 18(3): 241-251. <http://doi.org/10.1144/geochem2017-036>
- Marks, M.A.W., Marschall, H.R., Schühle, P., Guth, A., Wenzel, T., Jacob, D.E., Barth, M. and Markl, G., 2013. Trace element systematics of tourmaline in pegmatitic and hydrothermal systems from the Variscan Schwarzwald (Germany): The importance of major element composition, sector zoning, and fluid or melt composition. *Chemical Geology*, 344: 73-90. <http://doi.org/10.1016/j.chemgeo.2013.02.025>
- Nadoll, P., Angerer, T., Mauk, J.L., French, D. and Walshe, J., 2014. The chemistry of hydrothermal magnetite: A review. *Ore Geology Reviews*, 61: 1-32. <http://doi.org/10.1016/j.oregeorev.2013.12.013>
- Novak, M., Skoda, R., Filip, J., Macek, I. and Vaculovic, T., 2011. Compositional trends in tourmaline from intragranitic NYF pegmatites of the Trebic pluton, Czech Republic: an electron microprobe, Mossbauer and LA-ICP-MS study. *The Canadian Mineralogist*, 49(1): 359-380. <http://doi.org/10.3749/canmin.49.1.359>

- Palmer, M.R.a.S., J. F., 1989. Boron isotope composition of tourmaline from massive sulfide deposits and tourmalinites. *Contributions to Mineralogy and Petrology*, 103(4): 434-451. <http://doi.org/10.1007/bf01041751>
- Paton, C., Hellstrom, J., Paul, B., Woodhead, J. and Hergt, J., 2011. Iolite: Freeware for the visualisation and processing of mass spectrometric data. *Journal of Analytical Atomic Spectrometry*, 26(12). <http://doi.org/10.1039/c1ja10172b>
- Pettke, T., Oberli, F., Audetat, A., Guillong, M., Simon, A.C., Hanley, J.J. and Klemm, L.M., 2012. Recent developments in element concentration and isotope ratio analysis of individual fluid inclusions by laser ablation single and multiple collector ICP-MS. *Ore Geology Reviews*, 44: 10-38. <http://doi.org/10.1016/j.oregeorev.2011.11.001>
- Pieczka, A., Gołębiowska, B., Jeleń, P., Włodek, A., Szełęg, E. and Szuszkiewicz, A., 2018. Towards Zn-Dominant Tourmaline: A Case of Zn-Rich Fluor-Elbaite and Elbaite from the Julianna System at Piława Górna, Lower Silesia, SW Poland. *Minerals*, 8(4). <http://doi.org/10.3390/min8040126>
- Prokof'ev, V.Y., Naumov, V.B. and Dorofeeva, V.A., 2016. Gallium concentration in natural melts and fluids. *Geochemistry International*, 54(8): 691-705. <http://doi.org/10.1134/s0016702916080097>
- Qiao, X., Li, W., Zhang, L., White, N.C., Zhang, F. and Yao, Z., 2019. Chemical and boron isotope compositions of tourmaline in the Hadamiao porphyry gold deposit, Inner Mongolia, China. *Chemical Geology*, 519: 39-55. <http://doi.org/10.1016/j.chemgeo.2019.04.029>

- Raczek, I., Stoll, B., Hofmann, A.W. and Peter Jochum, K., 2001. High-Precision Trace Element Data for the USGS Reference Materials BCR-1, BCR-2, BHVO-1, BHVO-2, AGV-1, AGV-2, DTS-1, DTS-2, GSP-1 and GSP-2 by ID-TIMS and MIC-SSMS. *Geostandards and Geoanalytical Research*, 25(1): 77-86. <http://doi.org/10.1111/j.1751-908X.2001.tb00789.x>
- Richards, J.P., 2011. High Sr/Y arc magmas and porphyry Cu +/- Mo +/- Au deposits: just add water. *Economic Geology*, 106(7): 1075-1081. <http://doi.org/10.2113/econgeo.106.7.1075>
- Richards, J.P. and Kerrich, R.W., 2007. Special Paper: Adakite-Like Rocks: Their Diverse Origins and Questionable Role in Metallogenesis. *Economic Geology*, 102(4): 537-576. <http://doi.org/10.2113/gsecongeo.102.4.537>
- Rudnick, R.L.a.G., S. , 2003. Composition of the continental crust. *Treatise on Geochemistry*: 1-51. <http://doi.org/10.1016/b978-0-08-095975-7.00301-6>
- Samson, I.M.a.S., W. D., 1992. Magmatic Hydrothermal Fluids and the Origin of Quartz _ Tourmaline Orbicules in the Seagull Batholith, Yukon Territory. *Canadian Mineralogist*, 30: 937-954.
- Sciuba, M., Beaudoin, G. and Makvandi, S., 2021. Chemical composition of tourmaline in orogenic gold deposits. *Mineralium Deposita*, 56(3): 537-560. <http://doi.org/10.1007/s00126-020-00981-x>
- Scott, J.E., Richards, J.P., Heaman, L.M., Creaser, R.A. and Salzar, G.A., 2008. The Schaft Creek Porphyry Cu-Mo-(Au) Deposit, Northwestern British Columbia. *Exploration and Mining Geology*, 17(3-4): 163-196. <http://doi.org/10.2113/gsemg.17.3-4.163>

- Sillitoe, R.H. and Sawkins, F.J., 1971. Geologic, mineralogic and fluid inclusion studies relating to the origin of copper-bearing tourmaline breccia pipes, Chile. *Economic Geology*, 66(7): 1028-1041. <http://doi.org/10.2113/gsecongeo.66.7.1028>
- Sinclair, W.D. and Richardson, J.M., 1992. Quartz-Tourmaline Orbicules Batholith, in the Seagull Yukon Territory. *Canadian Mineralogist*, 30: 923-935.
- Singer, D.A., Berger, V.I. and Moring, B.C., 2008. Porphyry copper deposits of the world: Database and grade and tonnage models: USGS Open-File Report 2008-1155. *USGS: Reston, VA, USA*. <http://doi.org/10.3133/ofr20081155>
- Skewes, M.A., Holmgren, C. and Stern, C.R., 2003. The Donoso copper-rich, tourmaline-bearing breccia pipe in central Chile: petrologic, fluid inclusion and stable isotope evidence for an origin from magmatic fluids. *Mineralium Deposita*, 38(1): 2-21. <http://doi.org/10.1007/s00126-002-0264-9>
- Slack, J.F., 1996. Tourmaline Associations with Hydrothermal Ore Deposits. In: L.M. Anovitz and E.S. Grew (Editors), *Boron. Reviews in Mineralogy and Geochemistry*. Mineralogical Society of America, Oak Ridge, Tennessee, USA, pp. 559-644. <http://doi.org/10.1515/9781501509223-013>
- Slack, J.F. and Trumbull, R.B., 2011. Tourmaline as a Recorder of Ore-Forming Processes. *Elements*, 7(5): 321-326. <http://doi.org/10.2113/gselements.7.5.321>
- Slack, J.F.P., M. R.; Stevens, B. P.; Barnes, R. G.; , 1993. Origin and significance of tourmaline-rich rocks in the Broken Hill district, Australia. *Economic Geology*, 88(3): 505-541. <http://doi.org/10.2113/gsecongeo.88.3.505>

- Slack, J.F.R., A.R.; Griffin, W.L.; Win, T. T.; French D. H.; Ryan, C. G., 1999. Trace Elements in Tourmaline from the Kidd Creek Massive Sulfide Deposit and Vicinity, Timmins, Ontario A Proton Microprobe Study, The Giant Kidd Creek Volcanogenic Massive Sulfide Deposit, Western Abitibi Subprovince, Canada. *Economic Geology Monograph*, pp. 415-429. <http://doi.org/10.5382/mono.10.16>
- Smith, S., 1985. Trace element variation in hydrothermal tourmalines associated with mineralization: El Correo Sonora Mexico. MSc Thesis, Colorado School of Mines, 171 pp.
- Sokolov, M. and Martin, R.F., 2009. A Pb-dominant member of the tourmaline group, Minh Tien granitic pegmatite, Luc Yen district, Vietnam. *Estudios Geológicos*, 19(2): 352-353.
- Tapio, J., Ranta, J.-P., Cook, N., Lahaye, Y. and O'Brien, H., 2021. Paleoproterozoic Rajapalot Au-Co system associated with evaporites: Chemical composition and boron isotope geochemistry of tourmaline, and sulfur isotopes of sulfates, Peräpohja belt, northern Finland. *Precambrian Research*, 365. <http://doi.org/10.1016/j.precamres.2021.106410>
- Taylor, B.S., J., 1984. Tourmalines from Appalachian-Caledonian massive sulfide deposits: textural, chemical, and isotopic relationships. *Economic Geology*, 79(7): 1703-1726. <http://doi.org/10.2113/gsecongeo.79.7.1703>
- Telus, M., Dauphas, N., Moynier, F., Tissot, F.L.H., Teng, F.-Z., Nabelek, P.I., Craddock, P.R. and Groat, L.A., 2012. Iron, zinc, magnesium and uranium isotopic fractionation during continental crust differentiation: The tale from migmatites, granitoids, and pegmatites. *Geochimica et Cosmochimica Acta*, 97: 247-265. <http://doi.org/10.1016/j.gca.2012.08.024>

- Testa, F., Villanueva, C., Cooke, D. and Zhang, L., 2018. Lithological and Hydrothermal Alteration Mapping of Epithermal, Porphyry and Tourmaline Breccia Districts in the Argentine Andes Using ASTER Imagery. *Remote Sensing*, 10(2).
<http://doi.org/10.3390/rs10020203>
- Trumbull, R.B., Garda, G.M., Xavier, R.P., Cavalcanti, J.A.D. and Codeço, M.S., 2018. Tourmaline in the Passagem de Mariana gold deposit (Brazil) revisited: major-element, trace-element and B-isotope constraints on metallogenesis. *Mineralium Deposita*, 54(3): 395-414. <http://doi.org/10.1007/s00126-018-0819-z>
- Ulrich, T., Gunther, D. and Heinrich, C.A., 1999. Gold concentrations of magmatic brines and the metal budget of porphyry copper deposits. *Letters to Nature*, 399(6737): 676-679.
<http://doi.org/10.1038/21406>
- van Hinsberg, V.J., 2011. Preliminary experimental data on trace-element partitioning between tourmaline and silicate melt. *The Canadian Mineralogist*, 49(1): 153-163.
<http://doi.org/10.3749/canmin.49.1.153>
- van Hinsberg, V.J., Henry, D.J. and Marschall, H.R., 2011. Tourmaline: an ideal indicator of its host environment. *The Canadian Mineralogist*, 49(1): 1-16.
<http://doi.org/10.3749/canmin.49.1.1>
- van Hinsberg, V.J. and Schumacher, J.C., 2011. Tourmaline as a petrogenetic indicator mineral in the Haut-Allier metamorphic suite, Massif Central, France. *The Canadian Mineralogist*, 49(1): 177-194. <http://doi.org/10.3749/canmin.49.1.177>
- Vereshchagin, O.S., Wunder, B., Britvin, S.N., Frank-Kamenetskaya, O.V., Wilke, F.D.H., vlasenko, N.S. and Shilovskikh, V.V., 2020. Synthesis and crystal structure of Pb-

- dominant tourmaline. *American Mineralogist*, 105: 1589-1592.
<http://doi.org/10.2138/am-2020-7457>
- Wang, Z., Chen, B. and Yan, X., 2018. Geochemistry and boron isotopic compositions of tourmaline from the Paleoproterozoic amphibolites, NE China: Implications for the origin of borate deposit. *Precambrian Research*. <http://doi.org/10.1016/j.precamres.2018.01.006>
- Warnaars, F.W., Holmgren, C. and Barassi, S., 1985. Porphyry Copper and Tourmaline Breccias at Los-Bronces-Rio-Blanco, Chile. *Economic Geology*, 80(6): 1544-1565.
<http://doi.org/10.2113/gsecongeo.80.6.1544>
- Xiang, L., Wang, R., Romer, R.L., Che, X., Hu, H., Xie, L. and Tian, E., 2020. Neoproterozoic Nb-Ta-W-Sn bearing tourmaline leucogranite in the western part of Jiangnan Orogen: Implications for episodic mineralization in South China. *Lithos*, 360-361.
<http://doi.org/10.1016/j.lithos.2020.105450>
- Yavuz, F., Iskenderoglu, A. and Jiang, S.Y., 1999. Tourmaline compositions from the Salikvan porphyry Cu-Mo deposit and vicinity, northeastern Turkey. *Canadian Mineralogist*, 37: 1007-1023.
- Zall, F., Tahmasbi, Z., Jiang, S.-Y., Danyushevsky, L.V. and Harris, C., 2019. Elemental and B-O-H isotopic compositions of tourmaline and associated minerals in biotite-muscovite granite of Mashhad, NE Iran: Constraints on tourmaline genesis and element partitioning. *Lithos*, 324-325: 803-820. <http://doi.org/10.1016/j.lithos.2018.12.012>
- Zhao, H.-D., Zhao, K.-D., Palmer, M.R. and Jiang, S.-Y., 2019. In-situ elemental and boron isotopic variations of tourmaline from the Sanfang granite, South China: Insights into

magmatic-hydrothermal evolution. *Chemical Geology*, 504: 190-204.

<http://doi.org/10.1016/j.chemgeo.2018.11.013>

Zhao, H.-D., Zhao, K.-D., Palmer, M.R., Jiang, S.-Y. and Chen, W., 2021a. Magmatic-Hydrothermal Mineralization Processes at the Yidong Tin Deposit, South China: Insights from In Situ Chemical and Boron Isotope Changes of Tourmaline. *Economic Geology*, 116(7): 1625-1647. <http://doi.org/10.5382/econgeo.4868>

Zhao, K.-D., Zhang, L.-H., Palmer, M.R., Jiang, S.-Y., Xu, C., Zhao, H.-D. and Chen, W., 2021b. Chemical and boron isotopic compositions of tourmaline at the Dachang Sn-polymetallic ore district in South China: Constraints on the origin and evolution of hydrothermal fluids. *Mineralium Deposita*. <http://doi.org/10.1007/s00126-021-01045-4>

Zhao, Z., Yang, X., Liu, Q., Lu, Y., Chen, S., Sun, C., Zhang, Z., Wang, H. and Li, S., 2021c. In-situ boron isotopic and geochemical compositions of tourmaline from the Shangbao Nb-Ta bearing monzogranite, Nanling Range: Implication for magmatic-hydrothermal evolution of Nb and Ta. *Lithos*, 386-387. <http://doi.org/10.1016/j.lithos.2021.106010>

Zhu, Y., Li, X., Zhang, L., Zhang, D. and Wang, C., 2021. Chemical and boron isotopic compositions of tourmaline at the Baiyanghe Be U deposit, northwest China: Implications for Be U mineralization. *Chemical Geology*, 569. <http://doi.org/10.1016/j.chemgeo.2021.120146>

Chapter 4

4 Investigation of tourmaline characteristics in bedrock and surficial sediment samples from two Canadian porphyry copper systems

4.1 Abstract

Colour, texture, and chemistry were used to determine the source of tourmaline grains in local surficial (detrital) sediments from two Canadian porphyry systems (Woodjam and Casino). Tourmaline from porphyry bedrock is generally dark brown to black. Crystals frequently exhibit oscillatory and sector zoning, with overgrowth, irregular, and patchy patterns. Major-element analyses show ranges from schorl (Fe^{2+} -rich; 0.04–3.07 *apfu*, *avg.* 0.76) to dravite (Mg-rich, *avg.* 2.00 *apfu*), with a minor povondraite (Fe^{3+}) component. The alkali- and alkaline-earth element concentrations are relatively constant, with $\text{Na} > \text{Ca} > \square$ and $\text{OH}^- > \text{O}^{2-}$ dominant. Tourmaline from porphyry systems is characterized by high Sr/Pb values (*avg.*: 241) and relatively low Zn/Cu (*avg.*: 1.5) values. Detrital tourmaline occurs as euhedral grains and contains similar Fe and Mg concentrations and textural zonation patterns to porphyry tourmaline. Its trace-element content shows similarities but with larger ranges of values, likely related to the presence of non-porphyry detrital tourmaline. Overall, a combination of physical and chemical characteristics including 1) macro-color, 2) morphology, 3) inclusion populations, 4) *X*-site composition, 5) *W*-site composition, and 6) trace-element compositions are useful in discriminating between porphyry- versus non-porphyry-derived (or related) tourmaline in both bedrock and surficial sediments.

4.2 Introduction

Exploration for new mineral deposits is becoming increasingly challenging as discovery rates decrease, expenditures increase, and exploration switches from surface-based methods to those that can detect buried deposits. Indicator mineral identification is one such technique that can detect mineral deposits buried beneath cover.

Recent studies have identified two groups of porphyry copper indicator minerals (Plouffe and Ferbey 2017). Group 1 includes minerals that can be directly linked to porphyry copper mineralization based on their spatial distribution and abundance in surficial sediments (*e.g.*, chalcopyrite, pyrite, gold, jarosite; Averill 2011; Kelley *et al.* 2011; Plouffe and Ferbey 2017; Plouffe *et al.* 2021a; Plouffe *et al.* 2021b). Group 2 includes minerals that are common in many geological environments but have specific chemical characteristics tied directly to mineralized porphyry systems, such as zircon (Lu *et al.* 2016), epidote (Cooke *et al.* 2014, 2020b, 2020c), apatite (Bouzari *et al.* 2016; Mao *et al.* 2016), titanite (Xu *et al.* 2014), and magnetite (Dare *et al.* 2014; Canil *et al.* 2016). Studies of indicator minerals typically focus either on those present in the bedrock environment (*e.g.*, Cooke *et al.* 2020c) or those found in surficial sediment such as till (Plouffe and Ferbey 2017; Plouffe *et al.* 2021a). This study combines multidimensional analyses of a specific supergroup of indicator minerals, tourmaline, derived from both bedrock and surficial (till and stream) sediments.

Several mineral groups have been evaluated as indicator minerals for mineralized porphyry systems (*e.g.*, apatite, epidote, and chlorite group minerals; Wilkinson *et al.* 2015; Baker *et al.* 2020; Cooke *et al.* 2020a; Wilkinson *et al.* 2020), but to date, the tourmaline supergroup has been overlooked. Tourmaline is a common constituent of many felsic rocks, notably pegmatites, but it is also common in the calc-alkaline to alkaline environments that characterize porphyry

systems. Because of its colour, habit, and specific gravity, tourmaline can often be overlooked or mistaken for similar minerals (*e.g.*, epidote, amphibole). Its hardness and resistance to chemical and physical weathering allow tourmaline to potentially serve as an effective indicator mineral. Tourmaline has proven extremely useful in other geological applications, including as a successful petrogenetic indicator mineral of its host rocks (Henry and Guidotti 1985). The characteristics of tourmaline that make it an ideal long-term recorder of petrogenetic conditions include 1) the ability to accommodate a wide range of elements, 2) high hardness (7 on Mohs scale) and a lack of cleavage, and 3) insolubility under most terrestrial conditions. The overall long-term stability of tourmaline in the surficial environment also allows it to potentially record fluid evolution (including magmatic, magmatic-hydrothermal, and hydrothermal ore-forming fluids) during its crystallization history (Henry and Dutrow 1996; Henry *et al.* 2011; Marschall and Jiang 2011; van Hinsberg *et al.* 2011a). In this sense, the growth history of a tourmaline crystal has the potential to record not only major features, but also subtle ones (*e.g.*, trace-element variations). Tourmaline should, therefore, closely reflect the chemical zonation that develops within a mineralized porphyry system.

Tourmaline is a common accessory mineral in hydrothermal deposits worldwide (Slack 1996) and has been used to understand the development and evolution of select ore systems, including volcanogenic massive sulfide (VMS), orogenic gold, Sn-W, porphyry deposits and even emerald mineralization (Clarke *et al.* 1989; Slack and Coad 1989; Slack 1993; Griffin *et al.* 1996; Jiang *et al.* 1996; Slack 1996; Yavuz *et al.* 1999; Frikken *et al.* 2005; Galbraith *et al.* 2009; Baksheev *et al.* 2010; Baksheev *et al.* 2011; Slack and Trumbull 2011; Baksheev *et al.* 2012; Baksheev *et al.* 2017; Kalliomäki *et al.* 2017; Launay *et al.* 2018; Manégliia *et al.* 2018; Codeço *et al.* 2019; Byrne *et al.* 2020; Codeço *et al.* 2020; Sciuba *et al.* 2021).

The purpose of this study is to investigate and evaluate the applicability and usefulness of tourmaline as an indicator of mineralized porphyry copper systems. It also examines the distance from which porphyry derived tourmaline can be identified in surficial sediments (till and stream sediments). We focused on two sites, Woodjam in British Columbia, and Casino in Yukon, examining tourmaline in the mineralized porphyry system (bedrock) as well as in local surficial sediments (stream sediments or till). This paper provides detailed documentation and comparisons of several key elements in tourmaline, including 1) chemical zonation and textural features, 2) major- and minor-element chemistry, and 3) trace-element chemistry. The comparison of tourmaline derived from the different media (*i.e.*, surficial and bedrock) is crucial to the evaluation of the effectiveness of tourmaline as an indicator for porphyry deposits.

4.3 Geological Background

4.3.1 Bedrock Samples

The Casino deposit is a mineralized porphyry Cu-Mo-Au deposit located 300 km northwest of Whitehorse, Yukon. It is hosted in Late Cretaceous calc-alkalic quartz monzonite of the Casino suite (Casselmann and Brown 2017). Tourmaline is found throughout the deposit, including in breccias and veins, and as disseminations. Samples of all three textures of tourmaline were used in this study.

The Woodjam cluster is located in the Cariboo district, 50 km east of Williams Lake, British Columbia. Several types of mineralized porphyry systems hosted in Early Jurassic calc-alkaline intrusions (del Real *et al.* 2017) have been identified in the cluster: Megabuck and Deerhorn (Au-Cu), Southeast Zone (Cu-Mo), and Three Firs and Takom (Au-Cu). The tourmaline samples used in our study are from the Deerhorn and Takom deposits, where tourmaline occurs as an

early alteration of the host rock, as disseminations, in breccias, and veins. The tourmaline investigated formed in a variety of alteration types, including 1) potassic, 2) phyllic, and 3) propylitic.

For comparison, we also analyzed tourmaline-bearing samples from other mineralized porphyry systems, including 1) Coxheath (Nova Scotia, Canada), 2) Donoso Breccia (Chile), 3) Highland Valley Copper (British Columbia, Canada), 4) New Afton (British Columbia, Canada), and 5) Schaft Creek (British Columbia, Canada). A suite of background tourmaline (*i.e.*, non-porphyry) samples was also examined to provide a frame of reference for comparing tourmaline associated with mineralized porphyry systems to tourmaline not associated with mineralization (see Chapter 3 for a complete list).

4.3.2 Surficial Samples

The Casino deposit is a deeply weathered porphyry that is largely intact due to minimal to no glacial erosion of the region during the past 2 million years (Godwin 1975; Bond and Lipovsky 2011). Bulk (10–15 kg) stream-sediment samples were collected in 2017 from local first- and second-order streams (*e.g.*, Casino Creek) located in narrow V-shaped valleys (Figure 4-1b). Sampling details are reported in McCurdy *et al.* (2019) and McClenaghan *et al.* (2021).

At the time of the original GSC study, the Woodjam till samples were processed by Overburden Drilling Management Ltd. (ODM) to produce mid-density (2.8–3.2 specific gravity (SG)) and heavy (>3.2 SG) mineral concentrates for counting indicator minerals in the 0.25 to 0.5 mm non-ferromagnetic fraction.

Tourmaline abundance was reported as 1) a percentage of the total heavy minerals in the greater than 3.2 SG fraction, 2) a percentage of the total minerals in the 2.8 to 3.2 SG fraction, and 3) a total number of grains in the 2.8 to 3.2 and greater than 3.2 SG fractions.

Maps showing the distribution of tourmaline in till at Woodjam were presented by Chapman *et al.* (2015), and Plouffe and Ferbey (2017) in which they showed the number of grains in the 2.8 to 3.2 SG fraction normalized to 10 kg sample mass. In 2015, 50 tourmaline grains were removed from the 2.8 to 3.5 SG fraction of four of the till samples for mineral chemistry, the results of which are reported in Chapman *et al.* (2015), however, the mineral chemistry data from his study were never published.

4.4 Methods

4.4.1 Sample Processing

Surficial sediment samples (till at Woodjam and stream sediment at Casino) were collected by the GSC and processed by ODM to produce nonferromagnetic HMCs. Processing followed protocols outlined by Plouffe and Ferbey (2016) and McClenaghan *et al.* (2020) that included tabling to prepare a concentrate, ferromagnetic separations, and heavy liquid separations at 2.8 SG and 3.2 SG. The nonferromagnetic 2.8 to 3.2 SG and the >3.2 SG fractions were then visually examined using a binocular microscope and the tourmaline grains counted. Tourmaline grains were primarily recovered in the sand-sized (0.25–0.5 mm) mid-density (2.8–3.2 SG) fraction of the surficial sediment samples, with minor amounts (approximately 1%) also recovered from the heavy (>3.2 SG) fraction. Tourmaline grains were visually identified by their dark brown color, prismatic crystal habit, parallel striations on crystal faces, and conchoidal fracture (Figure 4-2a).

The archived 2.8 to 3.2 SG and greater than 3.2 SG Woodjam concentrates were re-examined in 2016 by ODM as part of our current study. The original tourmaline count data (Plouffe and Ferbey 2016), the number of grains removed in 2015 for mineral chemistry, and the 2016 tourmaline recount data are summarized in Appendix 4-1. There are important differences between the counts reported in 2013 and 2016, specifically for the 2.8 to 3.2 SG fraction. The 2016 tourmaline grain count is more than 50% higher in 75 of 91 samples. It is difficult to visually identify tourmaline in heavy mineral concentrates (HMC) based on its optical and physical properties alone; the differences in abundance show that the visual identification method can be highly subjective. Given that the 2016 recounts were specifically targeted at the identification of tourmaline and were completed by a senior mineralogist, we assert that the 2016 counts are more accurate. A new tourmaline abundance map for the 2.8 to 3.2 SG fraction of till around the Woodjam deposits that is based on the 2016 recount data is presented in Figure 4-1a. Selected grains were mounted in 2.5 cm epoxy pucks for imaging and chemical analysis. Grains were mounted in circular epoxy grain mounts perpendicular and parallel to the *c*-axis (elongation direction) to provide favorable orientations to examine any variations in chemical zonation with respect to the *c*-axis. Polished thin sections (PTS) of tourmaline-bearing bedrock samples from both deposits were also prepared.

4.4.2 Major- and minor-element chemistry

Chemical analyses of major and minor elements in tourmaline grains in PTS and epoxy grain mounts were conducted by scanning electron microscopy–energy-dispersive spectroscopy (SEM-EDS) at Laurentian University on a JEOL 6400 SEM, with an accelerating voltage of 20 kV, a beam current of 1.0 nA, and 15 s counting times. Data were processed using INCA software. The primary standards were well-characterized materials, including diopside ($MgK\alpha$, $CaK\alpha$, $SiK\alpha$),

albite ($AlK\alpha$, $NaK\alpha$), chalcopyrite ($FeK\alpha$), and syn $CaTiO_3(TiK\alpha)$. Chemical analyses of select samples are presented in Table 4-1. The chemical data were reduced to atoms per formula unit (*apfu*) based on 31 anions and this calculation was completed using *WinTcac* (Yavuz *et al.* 2014). Tourmaline ubiquitously exhibits zonation, typically about the *c*-axis, thus individual chemical zones were analyzed. A total of 1757 analyses from ~250 grains from bedrock and 2954 analyses from 1507 grains from sediment samples were analyzed.

4.4.3 Trace-element chemistry

In-situ trace-element analyses of tourmaline in bedrock samples and mounted grains from surficial sediment samples were carried out using laser-ablation inductively coupled plasma mass spectrometry (LA-ICP-MS) at Laurentian University. Samples were ablated using a Resonetics RESOLUTION M-50 laser ablation system coupled to a Thermo Fisher X-Series 2 quadrupole ICP-MS. The Resonetics laser uses a 193 nm argon fluoride excimer laser operated at a rate of 8 Hz for line scans with a 30 μm beam and a scan speed between 10 and 15 $\mu\text{m}/\text{s}$ with a measured fluence of approximately 3 J/cm^2 . External reference materials included NIST 610 (Jochum *et al.* 2011), NIST 612 (Jochum *et al.* 2011), and BHVO2G (Raczek *et al.* 2001). The NIST 610 standard was used as the primary reference material with Si as the internal standard (values collected from SEM-EDS were used for Si). Drift and data reproducibility were assessed using NIST 612, BHVO2G, and an in-house tourmaline standard. Standards were ablated before and after each 10 to 15 tourmaline sample analysis. Drift correction was applied using the baseline reduction scheme in iolite (Paton *et al.*, 2011). Samples were analyzed for major and trace elements, including ^7Li , ^9Be , ^{11}B , ^{28}Si , ^{31}P , ^{33}S , ^{39}K , ^{45}Sc , ^{47}Ti , ^{51}V , ^{52}Cr , ^{55}Mn , ^{59}Co , ^{60}Ni , ^{65}Cu , ^{66}Zn , ^{71}Ga , ^{72}Ge , ^{75}As , ^{85}Rb , ^{88}Sr , ^{89}Y , ^{90}Zr , ^{93}Nb , ^{95}Mo , ^{107}Ag , ^{115}In , ^{118}Sn , ^{121}Sb , ^{133}Cs , ^{137}Ba , ^{139}La , ^{140}Ce , ^{141}Pr , ^{146}Nd , ^{147}Sm , ^{153}Eu , ^{157}Gd , ^{159}Tb , ^{163}Dy , ^{165}Ho , ^{166}Er , ^{169}Tm , ^{172}Yb , ^{175}Lu ,

^{178}Hf , ^{208}Pb , ^{232}Th , and ^{238}U . A summary of the trace-element data are presented in Table 4-2 for bedrock samples and Table 4-3 for surficial sediment samples. Data on a large number of elements were collected to create a baseline for future comparison.

4.5 Results

4.5.1 Tourmaline textures

4.5.1.1 Bedrock Samples

Three distinct styles of bedrock tourmaline have been recognized in samples from Casino and Woodjam: breccia, vein, and disseminated (Figure 4-3). One important characteristic is that all three styles of tourmaline are variably associated with sulfide mineralization. Sulfides, including chalcopyrite and pyrite, were observed overgrowing prismatic to acicular, subhedral to euhedral tourmaline crystals. Alteration minerals (quartz and albite) are also observed overgrowing euhedral tourmaline crystals; therefore, tourmaline is interpreted to be one of the earliest forming hydrothermal phases in these two deposits (Figure 4-4). In hand sample, tourmaline ranges in color from usually dark-colored or black to less common colorless and is generally massive in form. Examination of tourmaline in PTS using backscattered-electron (BSE) imaging reveals evidence of complex chemical zonation, dissolution, overgrowths and various mineral inclusions (rutile, ilmenite, quartz, and apatite), although inclusions are rare and occur in <1% of grains. Although typically black in hand sample, in thin section under cross-polarized light tourmaline ranges from brown, pale green to green, blue, or nearly colorless. Pleochroism is generally weak compared to that observed in tourmaline from other geological settings; porphyry tourmaline pleochroism is colorless to blue-green in most cases.

4.5.1.1.1 *Tourmaline in breccias*

Tourmaline breccias are the most widely recognized style of tourmaline in porphyry deposits (Sillitoe, 2010), which is consistent with our observations in this study of the Casino and Woodjam deposits. The tourmaline in the matrix material as a cement (Figure 4-3a). Although the matrix can be greater than 90% tourmaline, quartz and sulfides (chalcopyrite and pyrite) that postdate tourmaline may also be present as matrix cement. The tourmaline grains in the breccia typically occur as radial aggregates of prismatic to acicular crystals that average approximately 50 μm but range from sub-micron up to millimeters in diameter in rare cases.

4.5.1.1.2 *Tourmaline in veins*

The crystals of tourmaline in veins (Figure 4-3b) are the smallest among the three tourmaline mineralization styles, typically approximately 20 μm in diameter and only rarely up to 100 μm in length. The veins are millimeters to centimeters in thickness, and tourmaline is associated with paragenetically later quartz and sulfide. The veins are variable in width and commonly have bleached white selvages, mainly of feldspar and quartz (Figure 4-3b). Tourmaline grains are randomly oriented with respect to vein margins and tend to occur in densely packed aggregates, the interstices of which are predominantly occupied by quartz and, to a lesser extent, sulfides.

4.5.1.1.3 *Disseminated tourmaline*

Of the three styles observed in the porphyry systems, disseminated tourmaline (Figure 4-3c) forms the largest crystals, with grains up to several centimetres in length. Texturally, disseminated tourmaline closely resembles breccia-hosted tourmaline (*i.e.*, acicular to prismatic radiating masses, commonly infilled by quartz), but the tourmaline develops in discrete anhedral clots instead of the radiating interlocking masses observed in breccias. Some of the

clots appear to represent the dissolution of pre-existing phases (*e.g.*, biotite or feldspars), based on the shape of the cavities they infill. Disseminated tourmaline can also be found in association with paragenetically later sulfides (pyrite and chalcopyrite).

4.5.1.2 Surficial sediment samples

Tourmaline recovered from surficial sediment samples is predominantly subhedral and brown to black in colour, or rarely yellow, green, or blue (Figure 4-2a, 2b). In general, tourmaline occurs in sediments as individual grains and only rarely as agglomerations (Figure 4-2c). The types of mineral inclusions identified in detrital tourmaline grains in polished epoxy mounts are summarized in Table 4-4 for the Woodjam deposit and Table 4-5 for the Casino deposit. Of the 1507 tourmaline grains examined, 60% contain mineral inclusions; most are (listed in decreasing abundance) zircon, quartz, rutile, ilmenite, epidote, and chalcopyrite (*e.g.*, Figure 4-2d). There are differences in the type and abundance of inclusions at the two study areas. At Woodjam, approximately 50% of the grains contain inclusions (Table 4-4) and at Casino, approximately 75% of detrital grains contain inclusions (Table 4-5). Ilmenite inclusions are twice as common in Woodjam tourmaline grains than in Casino tourmaline grains, but pyrite is more abundant in the Casino tourmaline. Detrital tourmaline grains also contain inclusions or attached grains of pyrite (Figure 4-2c), chalcopyrite, galena, sphalerite, jarosite, or barite.

4.5.2 Mineral chemistry

4.5.2.1 Backscattered electron imaging

4.5.2.1.1 *Tourmaline in bedrock*

Minerals in the tourmaline supergroup are able to accommodate a wide range of elements during their crystallization histories (van Hinsberg *et al.* 2011b). The tourmaline from Casino and Woodjam bedrock samples examined in this study exhibits, in general, a high degree of chemical heterogeneity and zonation. These grain-scale features are best observed with BSE imaging, which highlights differences in average atomic number in a given sample. Based on BSE imaging, four types of compositional growth textures are observed in the bedrock samples (Figure 4-5). These textures are further subdivided by whether they are likely to be primary (developed at the time of crystallization) or secondary (developed post-crystallization) in origin, as suggested by Slack and Trumbull (2011). Primary features include growth texture type 1) oscillatory/concentric growth zoning, interpreted to reflect changes in local fluid composition, displaying sharp chemical boundaries or zones developed parallel to [001] (Figure 4-5a); and type 2) sector/polar zoning that reflects selective partitioning of elements in distinct sectors (Figure 4-5b). Secondary textures include growth texture type 3) patchy/irregular growth features (Figure 4-5c), commonly observed in recrystallized tourmaline, with diffuse grain boundaries, developed perpendicular to [001], and overgrowth or replacement features (Figure 4-5d). Coupled dissolution-reprecipitation textures (similar to those developed in minerals such as plagioclase) are not currently included in the texture classification but could be grouped with the patchy/irregular growth features that result from recrystallization. These dissolution-reprecipitation textures correlate with the change from primary Fe-rich (schorl) compositions to

more Mg-rich (dravite) ones. Diffusion-like textures are also occasionally observed (Figure 4-6a, 6b).

4.5.2.1.2 *Tourmaline in surficial sediments*

Tourmaline from surficial samples exhibits a high degree of chemical heterogeneity and zonation at the individual grain scale. All four types of compositional growth textures observed in bedrock are also observed in grains from the surficial samples, with more than 50% of surficial grains exhibiting some type of chemical zonation. Atypical linear internal textures overprinting concentric zonation, similar to those observed in some of the bedrock tourmaline grains from Woodjam were also observed in surficial grains from samples surrounding the deposit cluster (Figure 4-6c).

4.5.3 Major- and minor-element chemistry (SEM-EDS)

4.5.3.1 *Tourmaline in bedrock*

Tourmaline from the Casino and Woodjam bedrock samples primarily plot within the compositional space of schorl, dravite, and povondraite (Figure 4-7), regardless of the deposit or tourmaline textural style. The dominant substitution can be summarized by: $R^{2+} + Na^+ \leftrightarrow Al^{3+} + \square$ ($R^2 = 0.90$) and $Fe^{2+} + (OH)^- \leftrightarrow Al^{3+} + O^{2-}$ ($R^2 = 0.90$). The average (range) proportions of major elements, expressed in wt. %, are Na = 1.75 (0.64–2.36), Ca = 0.49 (< LOD–2.64), Ti = 0.27 (< LOD–1.95), Mg = 4.85 (1.60–6.65), Fe = 4.27 (0.20–16.44), Al = 17.19 (10.78–19.90), and Si = 17.20 (15.52–18.68). The average (range) proportions expressed in *apfu* are Na = 0.75 (0.28–1.00), Ca = 0.10 (< LOD–0.70), Ti = 0.03 (< LOD–0.40), Mg = 1.95 (0.69–2.65), Fe = 0.76 (0.04–3.07), Al = 6.24 (4.18–7.14), and Si = 6.01 (5.60–6.55). In general, broad chemical variations conform to the oxy-dravite–povondraite trend, superimposed on a weaker schorl–

dravite trend; the oxy-dravite–povondraite trend within this series reflects the increase in Fe^{3+} (and decrease in Al^{3+}) that may reflect conditions of increasing oxidation (*i.e.*, $f\text{O}_2$; Figure 4-7a, 7b). The predominance of the oxy-dravite–povondraite trend has been previously reported for tourmaline from mineralized porphyry systems in Russia (Baksheev *et al.* 2012) as well as previously at the Woodjam deposit (Chapman *et al.* 2015). The oxy-dravite–povondraite trend is more developed for Woodjam bedrock samples than the Casino ones, this likely reflects the relative erosional levels between the two systems with Woodjam not having an intact supergene zone whereas the bulk of the samples from Casino are from the supergene zone.

4.5.3.2 *Tourmaline in surficial sediments*

The chemistry and range in composition of detrital tourmaline is somewhat similar with sediment samples plots as a large cluster centered on the trends for bedrock for each deposit but is a much broader cloud. In terms of end members, most tourmaline grains plot as schorl, dravite, and povondraite, with some grains plotting as uvite-feruvite. The average (range) of major elements, expressed in weight per cent, are Na = 1.58 (0.74–2.58), Ca = 0.72 (<LOD– 3.17), Ti = 0.43 (<LOD–2.20), Mg = 4.55 (0.13–7.66), Fe = 4.91 (0.21–15.31), Al = 17.43 (12.06–22.92), and Si = 17.19 (15.54–18.88). The average (range) proportions expressed in *apfu* are Na = 0.69 (0.30–1.00), Ca = 0.17 (< LOD–0.75), Ti = 0.08 (< LOD–0.47), Mg = 1.82 (0.05–3.00), Fe = 0.85 (0.04–2.71), Al = 6.27 (4.49–7.71), and Si = 5.95 (5.51–6.21). These data show that there is a greater spread in data for the sediment samples, likely reflecting TSM from other bedrock sources.

4.5.4 Trace-element chemistry

4.5.4.1 Tourmaline in bedrock

Trace-element analyses (LA-ICP-MS) for 51 elements were completed on 145 tourmaline grains from 15 samples between the Casino and Woodjam deposits (Table 4-2). Concentrations of many elements, including Li, Be, Rb, Nb, Mo, Ag, In, Sb, Cs, Ba, Hf, and rare-earth elements (REE), are at or below the lower detection limit. Many, including Co, Ni, Ge, Y, Zr, Sn, Pb, Th, and U, are present in very low concentrations (1–20 ppm), and the remainder, including K, Sc, Ti, V, Cr, Mn, Cu, Zn, Ga, As, and Sr, occur at higher concentrations (hundreds to thousands of ppm). Significant effort was made to identify relationships between the elements, but very few strong correlations were found. Noteworthy ones include positive correlations between Mn and Zn ($R^2 = 0.61$) and Mn and Sr ($R^2 = 0.48$). Trace-element concentration variations in a single, zoned tourmaline grain can be profound, with variations of several magnitudes possible. For example, concentrations of Ti, V, and Mn can vary over an order of magnitude, from hundreds to thousands of ppm, between zones within a grain.

Given the high degree of variation in trace-element concentration from point to point, attempts were made to discern general trends in tourmaline grains using LA-ICP-MS maps (Figure 4-8). The tourmaline grain shown in the figure is from the Woodjam deposit and exhibits concentric zonation (zones with sharp boundaries developed parallel to [001]) and complex patchy zonation (areas with diffuse boundaries, developed perpendicular to [001]) that in some places crosses the concentric zone boundaries. Examination of the maps produced for Sc and Mn indicates that elemental distribution is, in part, linked to concentric zonation (Figure 4-8). In contrast, high concentrations of other elements, such as Ti, Sr, and Zr, appear to positively correlate with the a-

typical zonation. Closer inspection of Ti and Sr show differences in their zonation patterns, including high concentrations of Ti in the core and intermediate regions but is absent in the rim. Strontium concentrations, in contrast, accentuate the a-typical zonation throughout the grain and in the rim. In summary, patterns in trace elements are very complex and may or may not correlate with the observed zonation type in all cases.

4.5.4.2 *Tourmaline in surficial sediments*

A total of 1507 individual tourmaline grains in epoxy grain mounts were analyzed from 26 surficial sediment samples from Casino and Woodjam (Table 4-3). Some of the elements analyzed occur at or below the lower detection limit, including Li, Be, Rb, Nb, Mo, Ag, In, Sb, Cs, Ba, Hf, and REE. The average concentration range of Co, Cu, Ge, As, Y, Zr, Sn, Pb, Th, and U is 1 to 20 ppm, whereas K, Sc, Ti, V, Cr, Mn, Ni, Zn, Ga, and Sr occur in much higher concentrations (hundreds to thousands of ppm). The positive correlations between Mn and Zn and Mn and Sr observed in tourmaline from bedrock samples were not found in tourmaline grains from surficial sediments; however, a strong correlation between Co and Ni ($R^2 = 0.74$), not noted in the bedrock material, was observed.

4.6 Discussion

Using tourmaline as an indicator for mineralized porphyry systems necessarily involves identification of key features in the mineralized bedrock samples, examination of grains from the surficial sediments to search for these same features, and comparison of these features in tourmaline from a variety of geological settings (*i.e.*, pegmatites; granites; and VMS, orogenic Au, and polymetallic W-Sn-Cu deposits). Observations made as part of this study and a compilation of material from the published literature is provided.

Tourmaline is commonly black in most rock types, except in pegmatites where it can be green, blue, pink, and yellow. The tourmaline from mineralized porphyry systems in this study is predominantly black and, less commonly, pale brown or colorless. The grain size of tourmaline in bedrock from all geological environments is highly variable and is not a distinctive feature, but the largest tourmaline grains (commonly cm in length) are known to have formed in pegmatite and granitic settings. Fibrous tourmaline is a morphology not observed in porphyry deposits; it is most typically associated with felsic pegmatites (Dutrow and Henry 2017).

A comprehensive review of inclusions found within tourmaline in all geological settings does not exist. From the limited literature available, zircon appears to be a ubiquitous inclusion in tourmaline from all geological settings, as is quartz (Henry and Guidotti 1985; Novak *et al.* 2011; Sciuba *et al.* 2021). The morphology of quartz inclusions is variable; however, anhedral, well-rounded quartz grains commonly occur in tourmaline derived from metamorphic terranes, and subhedral to euhedral quartz grains are found in tourmaline from most other geological environments (*e.g.*, in pegmatites and granites). Tourmaline from porphyry deposits does not contain rounded inclusions of quartz.

Tourmaline grains can also be classified using internal growth textures. The presence of complex growth features, such as those observed in the tourmaline crystals analyzed in this study, can be useful for graphically documenting the variations in pressure-temperature-time (P - T - X) experienced by an evolving crystal (Slack and Trumbull 2011). Concentric and sector zonation is widely observed in tourmaline from a range of geological settings, but the presence of patchy/irregular to even atypical growth features is not common. All tourmaline grains from mineralized porphyry systems examined in this study exhibited zonation of one type or another, including both concentric and sector zonation; patchy or irregular zonation within concentric or

sector zones was also observed (Figure 4-6, Figure 4-8a). The a-typical zonation is particularly unusual; it does not destroy the concentric or sector zonation, which suggests it is unlikely to be a product of recrystallization. It is possible that this a-typical zonation (Figure 4-6) is produced through chemical diffusion, although the commonly accepted view is that diffusion is negligible in tourmaline (Palmer *et al.* 1992; Henry and Dutrow 1996). Still, degrees of chemical diffusion involving major, and some trace elements have been noted in tourmaline that has undergone deformation under moderate to high-grade conditions (*e.g.*, mylonite metamorphosed to the amphibolite facies; Buttner and Kasemann 2007). Tourmaline has also exhibited greater diffusion along the *c*-axis (Desbois and Ingrin 2007). For bedrock samples in this study, the effect of deformation can be ignored because the host rocks are undeformed. Diffusion features, if present, align well with the orientation perpendicular to [001] of the grains from this study (Figure 4-6, Figure 4-8). The orientation of these diffusion features could also be related to the weak cleavage present in tourmaline [10-10], which has been reported by Hawthorne and Dirlam (2011).

There is only one comprehensive study of the major-element chemistry of tourmaline from porphyry systems, that of Baksheev *et al.* (2012). They showed that generally, the tourmaline that is present belongs to the schorl–dravite series (Fe²⁺-Mg substitution), with a strong oxydravite–povondraite trend overprint. Both of these compositional trends are observed in tourmaline in the Casino and Woodjam bedrock samples. As identified by our research, the alkali/alkaline-earth site can be used to help identify non-porphyry tourmaline because porphyry-related tourmaline almost exclusively contains greater than 0.4 *apfu* Na; however, major elements alone cannot definitively distinguish porphyry copper-related tourmaline from tourmaline that has formed in other geological settings.

In general, the application of LA-ICP-MS in the characterization of tourmaline is in its infancy and important issues still need to be resolved, including the complex nature and wide chemical variation of tourmaline, paired with the difficulty of developing appropriate reference materials and internal element standards. This study has demonstrated that high-quality tourmaline trace-element data can be obtained by LA-ICP-MS. Data from the existing literature show that there are wide variations in the trace-element composition of tourmaline found in differing geological environments (Slack 1999; Novak *et al.* 2011; Marks *et al.* 2013; Hazarika *et al.* 2015; Kalliomäki *et al.* 2017). A detailed understanding of what trace elements are present, the ranges in their concentrations, and their internal relationships to other trace elements and textures are all key to understanding the provenance of tourmaline in the surficial environment. Before interpreting tourmaline trace-element data, the intrinsic and extrinsic controls on tourmaline crystal chemistry must be understood and considered. Intrinsic, or crystal-chemical, controls include ideal site size, ionic radius, and valence; extrinsic controls relate to the roles that the geological environment of formation play in affecting elemental incorporation. A summary of trace-element generalizations for tourmaline from a variety of geological environments is listed in Table 4-6.

Tourmaline from the Casino and Woodjam porphyry systems, as well as others examined in this PhD research (see Chapter 3) generally contain low concentrations of Li (<15 ppm), high Sr/Pb (*avg*: 241), variable Ga (*avg*: 58 ppm), low Zn/Cu (*avg*: 1.5) values and have light REE-enriched patterns despite having low overall REE concentrations (<10 ppm Σ REE). To explore and better explain the trace-element concentrations observed in our study, data from the literature and our data are compiled and presented as percentile box plots (Figure 4-9). Tourmaline from granites and pegmatites generally have high Li concentrations >50 ppm, low Sr <100 ppm, and

high Zn and Ga concentrations Table 4-6. Metamorphic and VMS tourmaline are both similar in that they have high relative V concentrations >275 ppm (Table 4-6). Tourmaline from orogenic Au deposits is characterized by high Sr concentrations (>150 ppm) whereas polymetallic W-Sn-Cu tourmaline is characterized by high Li >35 ppm, and Sn >11 ppm (Table 4-6). Tourmaline from mineralized porphyry deposits has been characterized in terms of textural, major, minor, and trace-element chemistry (Chapter 3). A decision tree has been developed to aid in the discrimination of tourmaline grains recovered in the surficial environment (Figure 4-10). Figure 4-11 shows the contrast of trace-element composition between surficial and bedrock samples in this study and highlights the predominance of non-porphyry tourmaline in the surficial sediments, especially for the Woodjam samples. The recovery of tourmaline grains from the surficial sediments around the Woodjam and Casino deposits provides an opportunity to apply our understanding of bedrock tourmaline to tourmaline of unknown origin. We classified tourmaline grains from surficial sediment samples using the physical and chemical criteria presented in Chapters 2 and 3 and simplified in Figure 4-10. Some of the tourmaline grains in surficial sediment samples have trace-element chemical compositions consistent with those formed in porphyry deposits (Figure 4-11). Based on the observed physical and chemical characteristics of the surficial tourmaline examined, porphyry-derived tourmaline can be observed down-ice and downstream of known deposits. The samples collected surrounding the Casino deposit contain a much higher percentage of porphyry-derived tourmaline than do the Woodjam samples. Using the 10% cut-off presented for the ternary diagram (Figure 4-11) ~ 44 % of Casino surficial samples are porphyry derived while ~ 7 % of the Woodjam surficial samples are porphyry derived Table 4-7.

At the Casino deposit a large number of tourmaline grains from sediment sample 115J171018 (n= 385 grains) collected downstream of the deposit in Canadian Creek, which drains the north side of the deposit, have been classified as porphyry-derived tourmaline. In contrast, tourmaline grains from Casino Creek on the south side of the deposit, have lower overall abundances of tourmaline per sample (n= 3 to 43) and a smaller percentage of porphyry-derived grains (Figure 4-12). The highest concentration of porphyry-derived tourmaline comes from the Excelsior Creek (sample 115J171015) with 100% of the tourmaline grains (n= 14) classified as such, although it's important to note that only 3 tourmaline grains were recovered at this sample site, and thus it should not be taken to be representative. Interest should be paid to samples 115J171025 (n= 385 grains) and 115J171026 (n= 354 grains) which are downstream of the north side of the Casino deposit and contain 63% and 55% porphyry-derived tourmaline, respectively. These results show that greater than 90% of the grains in the surficial sediments were likely not derived from the nearby Woodjam deposits. The bulk of the surficial grains, especially in till samples around the deposit, are likely of metamorphic origin based on their physical (inclusion populations; rounded quartz inclusions, epidote, apatite, etc.) and trace-element characteristics (low Sr: tens of ppm, hundreds of ppm Zn, and >5000 ppm Ti). Only 7 % of the grains in the till samples exhibit physical and chemical characteristics of tourmaline that indicate that they are likely derived from the Woodjam deposit cluster (Figure 4-12). The small proportion of tourmaline grains that have a composition similar to porphyry-derived grains may be due to tourmaline abundance of tourmaline in the rocks in Woodjam porphyry system that were exposed to glaciation. For example, till samples collected down ice of mineralization contain less than 7% porphyry-derived tourmaline, except for two samples: sample 11PMA012A01 overlying the deposit contains 85.7% porphyry-derived tourmaline and sample 11PMA614A01, collected

11 km west-southwest (down-ice) from the Takom South deposit, contains 7.1% porphyry-derived tourmaline. The greater abundance of non-porphyry-derived tourmaline in till samples is expected down ice of the Woodjam deposit, as compared to the Casino sediment samples, because the size of the bedrock source area for the till is much greater (crosses drainage divides) than the source area for the stream sediments at the Casino deposit (within single drainage basins on the north or south side of the deposit). Despite the overwhelming expanse of non-porphyry-bedrock terrane up ice of the Woodjam till samples, porphyry-derived tourmaline, it is still identifiable in the samples.

4.7 Conclusions

The physical characteristics of tourmaline (*e.g.*, color, grain size, morphology, color in PPL) can assist in the classification of environment of formation. One physical characteristic that has proven useful is identifying inclusion populations (type and texture), specifically within the tourmaline grains recovered in the surficial sediments. The identification of inclusions can be carried out rapidly using SEM scans of grains in epoxy grain mounts prior to LA ICP-MS analysis. Methods such as MLA or TIMA would be useful at an early stage to find the inclusions and identify their composition. Porphyry tourmaline specifically contains a dearth of mineral inclusions and as such, grains recovered in the surficial environment that contain inclusions are likely not derived from a porphyry setting.

A stepwise decision tree to aid in the classification of tourmaline grains in bedrock and sediment samples using physical and chemical observations is presented (Figure 4-10). Step 1) macro tourmaline color: If grain is black or dark brown it could be porphyry related. Other colors are not observed in porphyry tourmaline; Step 2) inclusion populations: porphyry-related tourmaline

grains rarely contain mineral inclusions (zircon and rutile are most common). Rounded quartz inclusions in tourmaline grains, if present, are not considered to be derived from a porphyry system.; Step 3) Na dominant *X*-site: porphyry-derived tourmaline exclusively is dominated by Na in the *X*-site; Step 4) Porphyry-derived tourmaline has an oxy or hydroxy dominant (*i.e.*, OH⁻ + O²⁻) *W*-site; Step 5) Porphyry-related tourmaline does not contain >0.5 *apfu* F + Cl; Step 6) Trace-element discrimination using the Sr/Pb–Zn/Cu–Ga ternary diagram presented in Chapter 3: samples that plot outside the porphyry field are unlikely to be derived from a mineralized porphyry system.

Results from this study show that recognizing tourmaline grains in sediment samples that are from a mineralized porphyry system can be challenging, even if the sediments are proximal to a deposit. For example, at the Woodjam deposit, porphyry-related tourmaline in the surficial environment accounts for less than 5% of the total tourmaline content, except for one sample located near mineralization (85.7% porphyry tourmaline) and a second sample located 11 km down-ice from mineralization (7.1% porphyry tourmaline). Up to 63% porphyry-related tourmaline in stream sediments was identified in the Casino area, but only in samples from the northern drainage basin. The bulk of the brown to black tourmaline recovered from the sediment samples at both study sites appears to be of metamorphic origin. The small size (<0.25 mm) and fractured nature of the tourmaline associated with porphyry mineralization could be limiting factors for its recovery in detrital sediments.

4.8 Figures

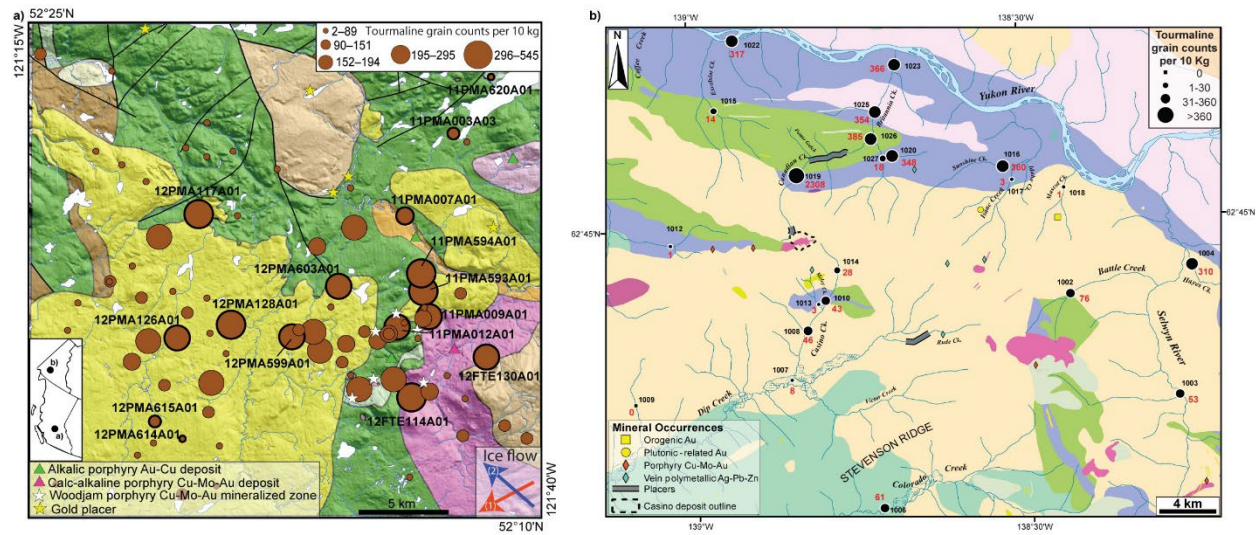


Figure 4-1: Location of surficial sediment samples (Woodjam-BC and Casino-YT)

Location of surficial sediment samples from which tourmaline grains were recovered and examined in this study; inset map shows the location of a) the Woodjam deposit in British Columbia and b) the Casino deposit in Yukon: a) Proportional dot map of tourmaline abundance (grain counts normalized to 10 kg) in the mid-density (2.8–3.2 SG) 0.25 to 0.5 mm fraction of till samples collected down ice of the Woodjam deposit cluster, British Columbia (unpublished Geological Survey of Canada data). See Plouffe and Ferbey (2017) for bedrock geology. Dots with thick black outline indicate till samples from which tourmaline grains were investigated in the study; b) the location of stream-sediment sample sites (black sample numbers) around the Casino deposit, Yukon, and abundance of tourmaline (grain counts, normalized to 10 kg, in red) in the 2.8 to 3.2 SG, 0.25 to 0.5 mm fraction. See McClenaghan *et al.* (2021) for Casino bedrock geology.

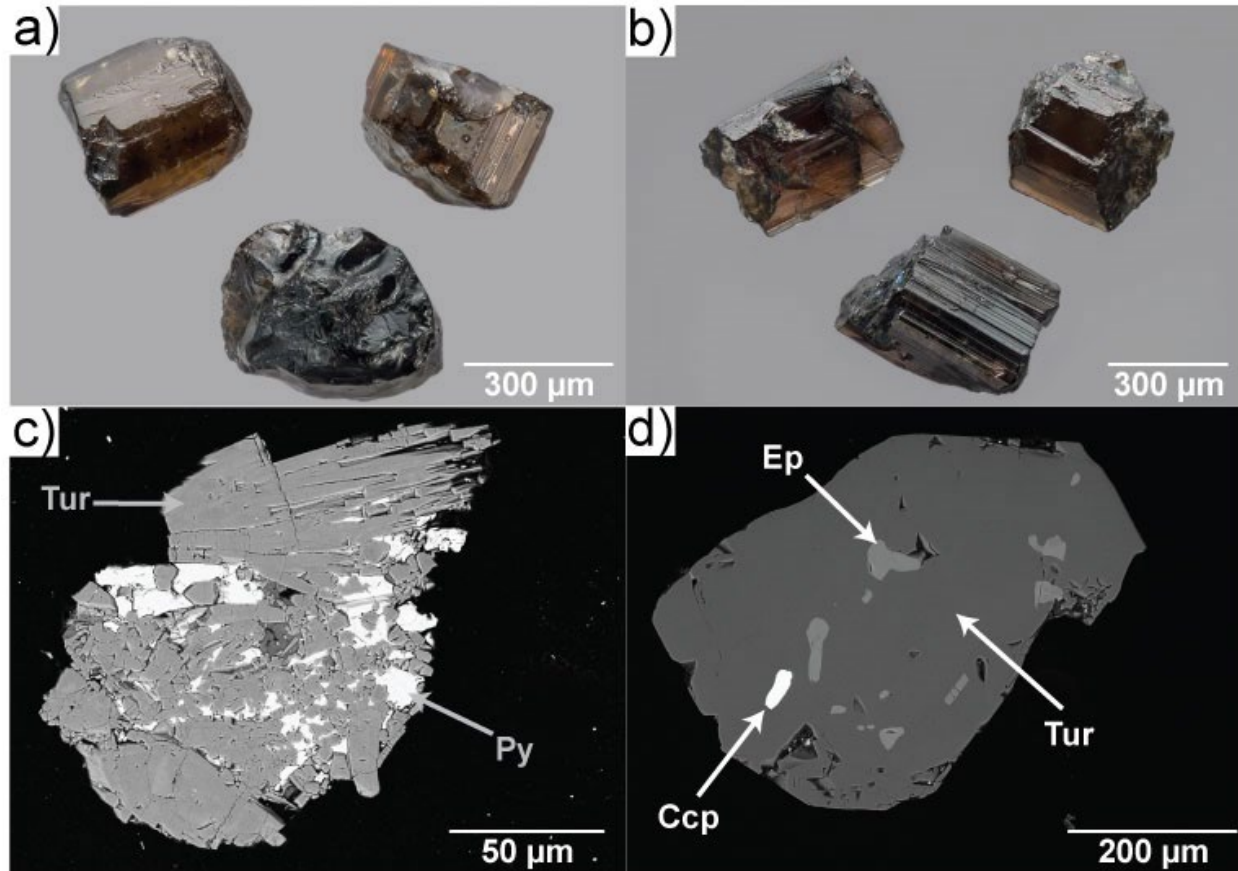


Figure 4-2: Tourmaline from the surficial environment

Brown tourmaline grains from the mid-density (2.8–3.2 SG) fraction of: a) Geological Survey of Canada (GSC) till sample 11-PMA-009A01, collected less than 1 km northwest (up-ice) of a Woodjam cluster mineralized zone (photograph by Michael J. Bainbridge Photography); b) GSC stream-sediment sample 115171003, collected downstream of the Cockfield porphyry occurrence, 30 km east of the Casino deposit (photograph by Michael J. Bainbridge Photography); c) backscattered electron image of a tourmaline (Tur) grain (from Woodjam till sample 11PMA012A01) infilled by pyrite (Py); and d) backscattered electron image of a tourmaline grain (from Casino stream-sediment sample 115J171025) containing inclusions of chalcopyrite (Ccp) and epidote (Ep).

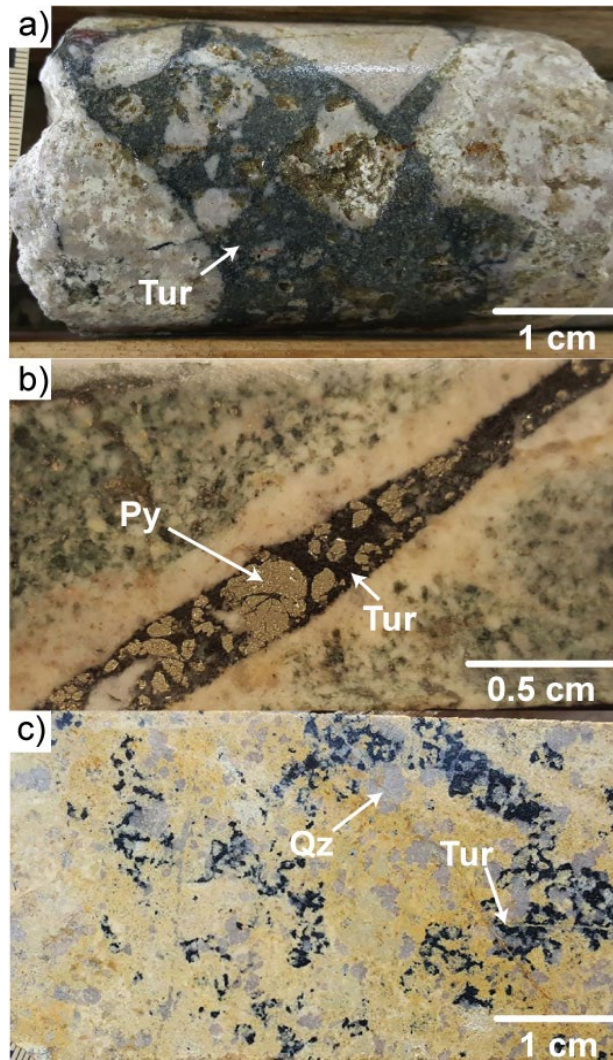


Figure 4-3: Hand sample images of tourmaline textures in bedrock

Hand samples of core showing the variable textural styles of tourmaline (Tur) in bedrock: a) tourmaline cemented breccia from the Casino deposit (Photograph by C.E. Beckett Brown; NRCan photo 2020-128); b) tourmaline from the Woodjam deposit cluster forming as monomineralic veins (Photograph by C.E. Beckett-Brown; NRCan photo 2020-129); c) tourmaline from the Casino deposit forming as isolated disseminated clots (Photograph by C.E. Beckett-Brown; NRCan photo 2020-130).

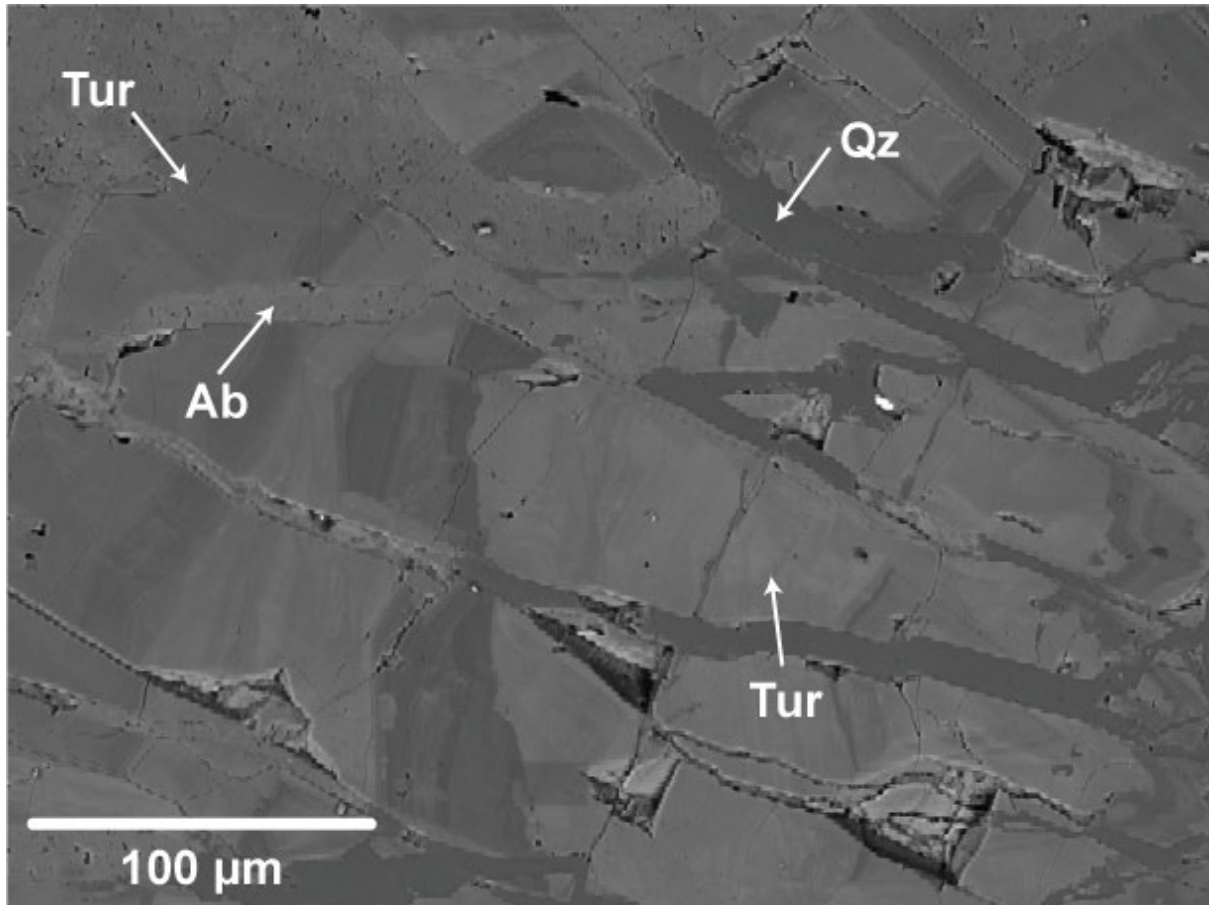


Figure 4-4: Paragenetic position of tourmaline

Backscattered-electron image showing the paragenetic relationship of tourmaline in which albite and quartz have infilled fractures in the tourmaline. Tur: tourmaline; Ab: albite; Qz: quartz.

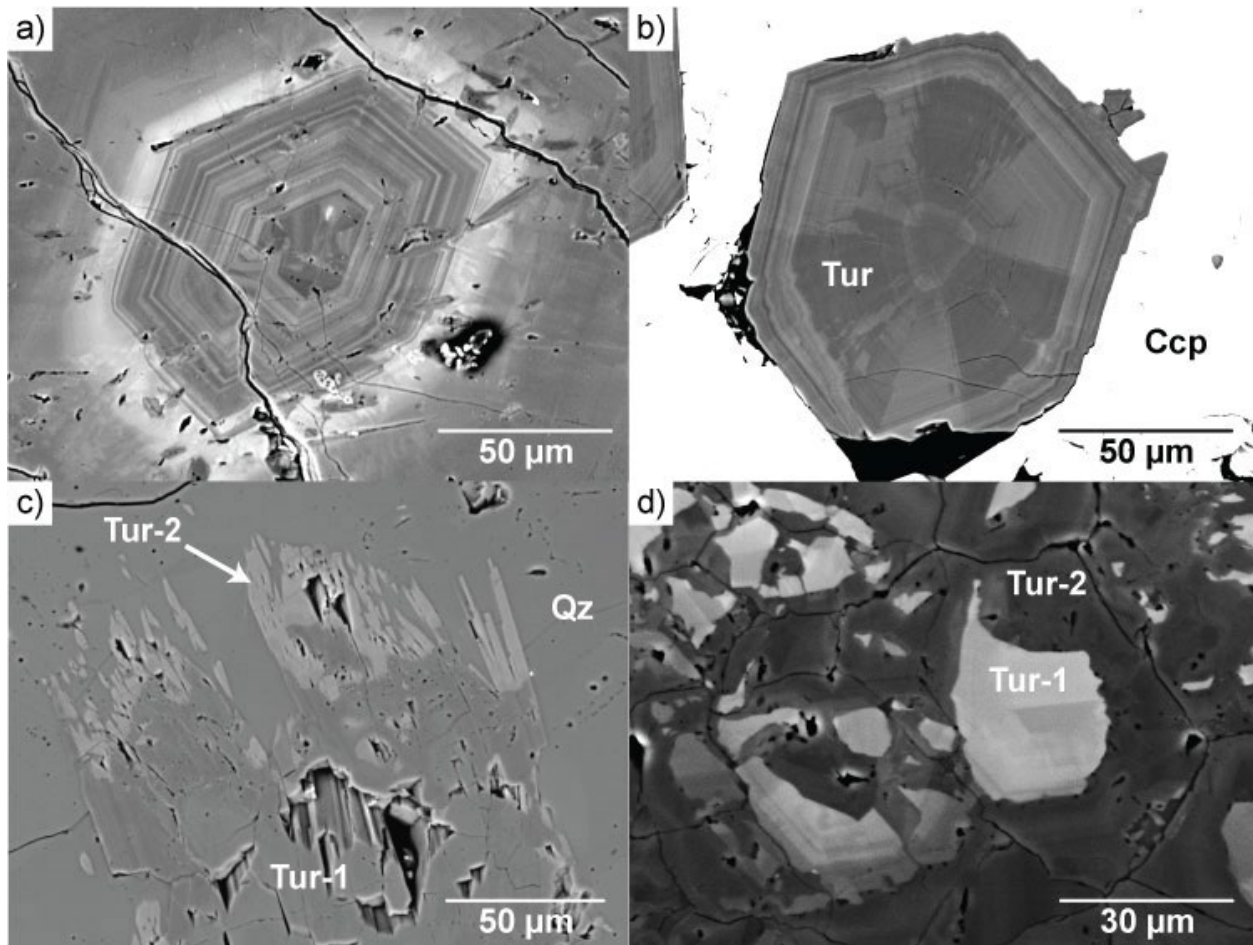


Figure 4-5: Internal zonation textures of tourmaline

Backscattered-electron images showing the internal textures of tourmaline grains from bedrock samples: a) oscillatory zonation; b) sector zonation; c) overgrowth (Tur-1 is dark, Tur-2 is lighter); d) irregular/patchy zonation resulting from recrystallization of pre-existing Tur-1, of which some primary fragments still remain, to Tur-2. The primary chemical difference between Tur-1 and Tur-2 is that Tur-2 contains more Mg than Fe.

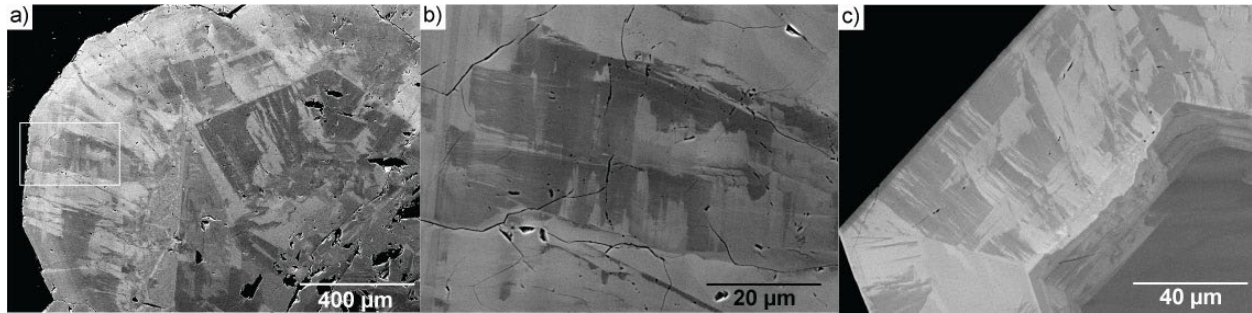


Figure 4-6: Comparison of internal textures (Bedrock-till: Woodjam-BC)

Backscattered-electron images of bedrock and till samples collected at the Woodjam deposit showing tourmaline internal textures in: **a)** a tourmaline grain in a Woodjam bedrock sample showing a combination of oscillatory and sector zoning features as well as some patchy zonation; **b)** magnified view of the white box in a) showing patchy zonation; **c)** a tourmaline grain from a till sample near the Woodjam deposit cluster showing similar atypical patch zonation overprinting concentric zonation to those observed in the Woodjam bedrock sample in (a).

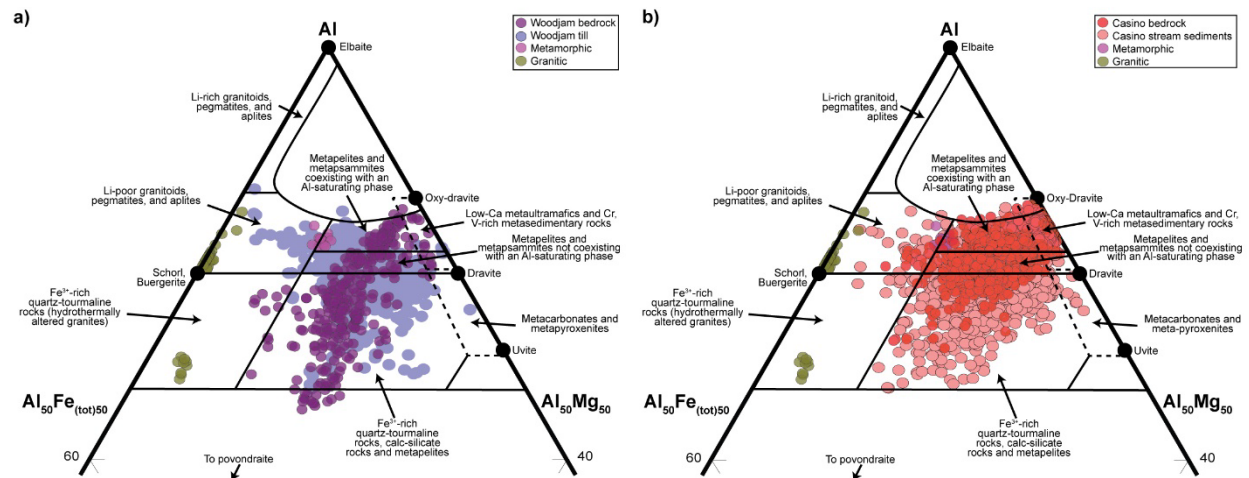


Figure 4-7: Major element trends of bedrock and surficial tourmaline

Tourmaline major-element chemistry Al-Mg-Fe for grains from a) Woodjam deposit and b) Casino deposit bedrock and surficial sediment samples analyzed in this study, plotted using the ternary diagram of Henry and Guidotti (1985). Background unmineralized bedrock is represented by grains classified as metamorphic that are from a gneiss from Jordan Falls, Nova Scotia, and grains classified as granitic that are from the Seagull batholith, Yukon.

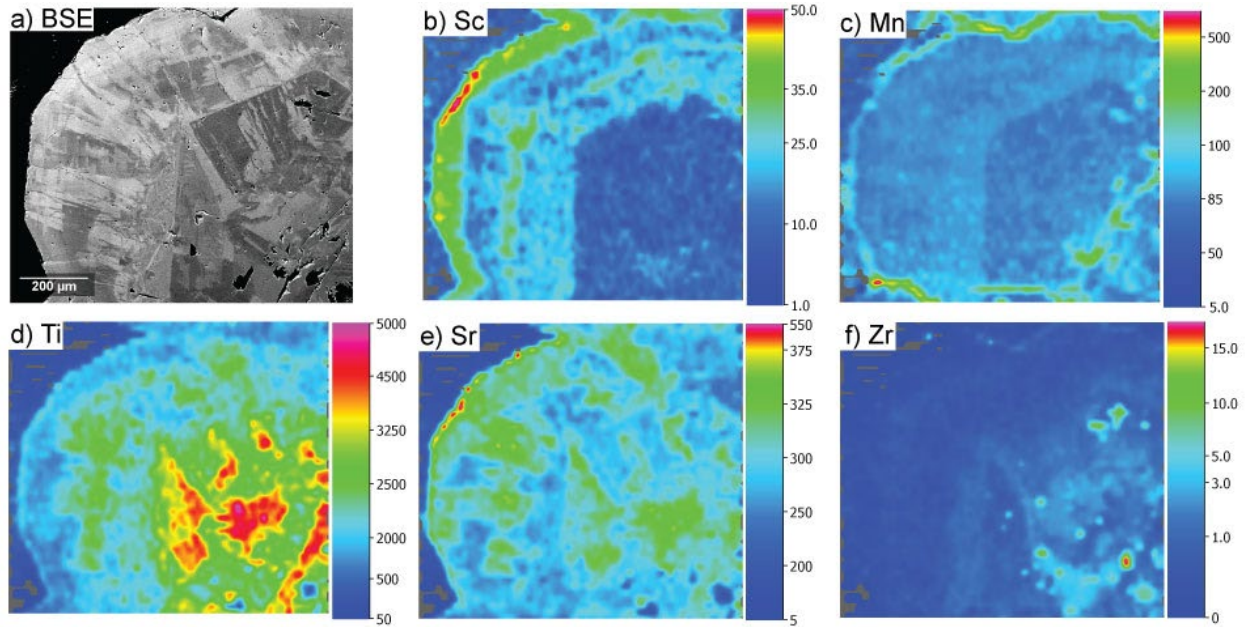


Figure 4-8: Trace-element grain map of tourmaline

Element maps of a single tourmaline grain from sample 13CDBWJ05: a) backscatter electron image; b) to f) laser-ablation inductively coupled plasma mass spectrometry maps of trace-element content for b) Sc, c) Mn, d) Ti, e) Sr, and f) Zr. Element scales are semi-quantitative (ppm) and indicate relative changes in element concentrations.

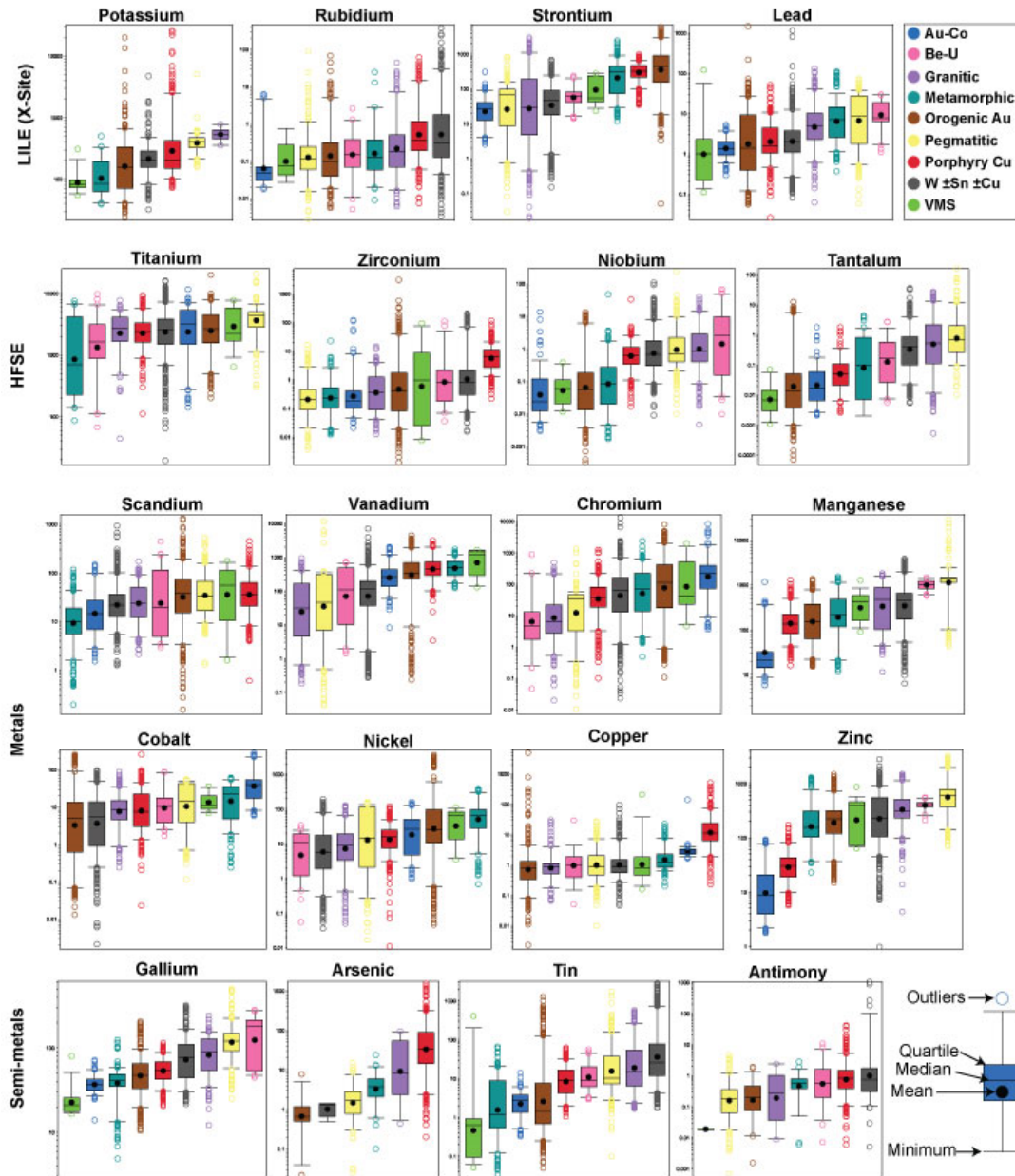


Figure 4-9: Percentile box plots of tourmaline trace-element data for common environments of formation

Percentile box plots, far outlier data, sorted by mean of TSM trace-element data determined by LA-ICP-MS showing the variations in data between some geologic environments in which TSM are found. All concentrations shown are in parts per million. Outliers are classified as $1.5 \times (Q3 - Q1)$ and far outlier data is classified as $3 \times (Q3 - Q1)$. Data for TSM forming in granites is

compiled from: Drivenes *et al.* (2015); Kalliomaki *et al.* (2017); Zall *et al.* (2019); Zhao *et al.* (2019); Xiang *et al.* (2020); Aysal *et al.* (2021); Hong *et al.* (2021); Zhao *et al.* (2021a); and unpublished analyses collected by the author from the Seagull Batholith-Yukon Territory. Data for TSM forming in pegmatites is compiled from: Marks *et al.* (2013); Copjakova *et al.* (2015); Zhao *et al.* (2019); Chakraborty and Upadhyay (2020); Long *et al.* (2021); Sciuba *et al.* (2021); Zhao *et al.* (2021c); and unpublished analyses collected by the author from the Usakos Pegmatite-Namibia as well as the Beryl pit-Ontario. Data for TSM forming in metamorphic rocks is compiled from: van Hinsberg (2011); Kalliomaki *et al.* (2017); Wang *et al.* (2018); Hong *et al.* (2021); and unpublished analyses collected by the author from Jordan Falls-Nova Scotia. Data for TSM forming in orogenic Au deposits is compiled from: Jiang *et al.* (2002); Kalliomaki *et al.* (2017); Trumbull *et al.* (2018); Jin and Sui (2020); and Sciuba *et al.* (2021). Data for TSM forming in VMS deposits is compiled from: Slack *et al.* (1999); Klemme *et al.* (2011); and Sciuba *et al.* (2021). Data for TSM forming in polymetallic W ± Sn ± Cu deposits is compiled from: Jiang *et al.* (2004); Codeco *et al.* (2017); Lunay *et al.* (2018); Harlaux *et al.* (2019); Carocci *et al.* (2020); Carr *et al.* (2020); Harlaux *et al.* (2020); Hu and Jiang (2020); Xiang *et al.* (2020); Ghosh *et al.* (2021); and Zhao *et al.* (2021b). Some of the compiled trace-element data (*i.e.*, Mn, As, Ga, Pb) lack values as they were not analyzed by the respective authors.

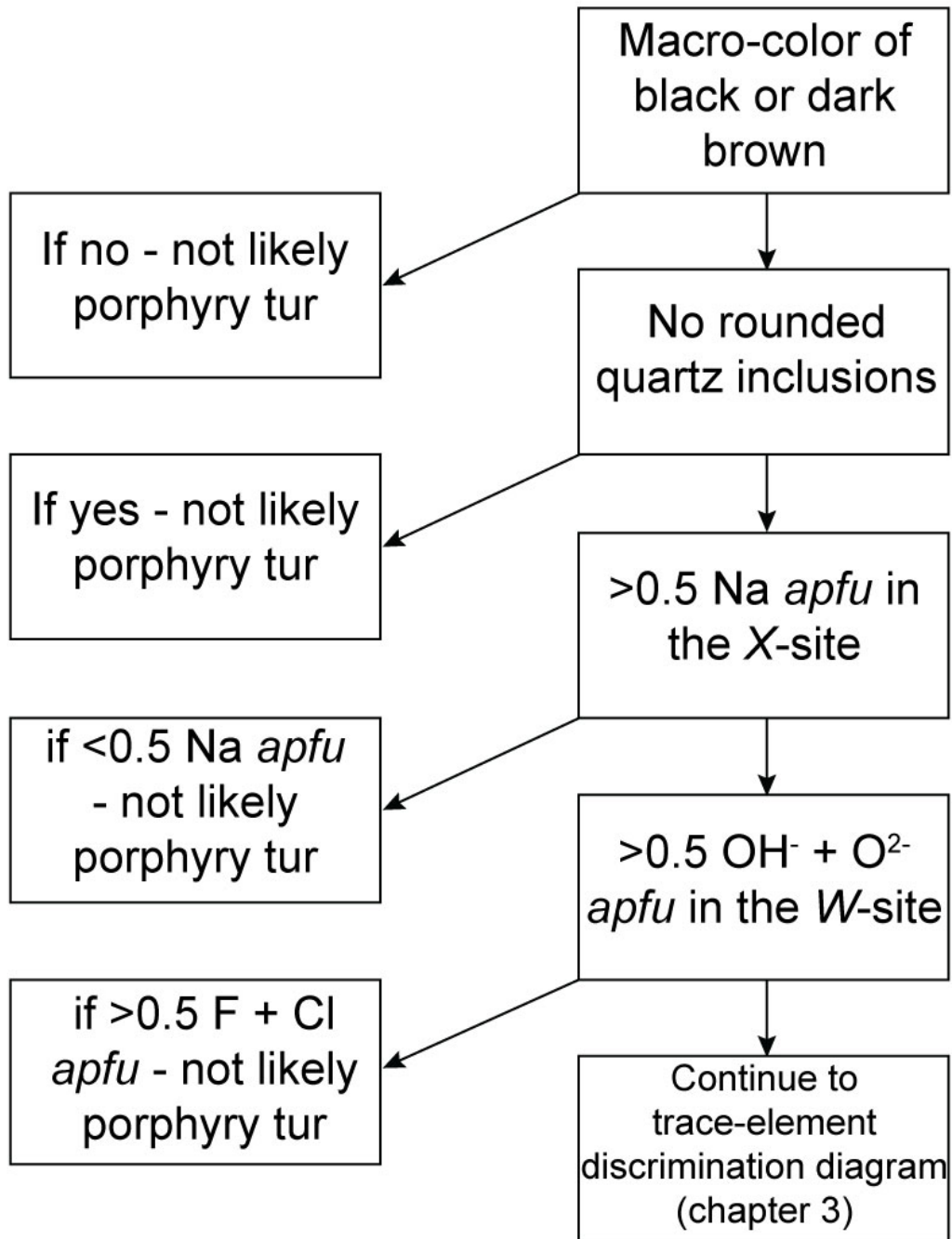


Figure 4-10: Decision Tree: porphyry tourmaline

Stepwise decision tree to aid in the classification of tourmaline grains in bedrock and sediment samples using physical and chemical observations. Step 1) macro tourmaline color: If grain is black or dark brown it could be porphyry related. Other colors are not observed in porphyry

tourmaline; Step 2) inclusion populations: porphyry-related tourmaline grains rarely contain mineral inclusions (zircon and rutile are most common). Rounded quartz inclusions in tourmaline grains, if present, are not considered to be derived from a porphyry system.; Step 3) Na dominant *X*-site: porphyry-derived tourmaline exclusively is dominated by Na in the *X*-site; Step 4) Porphyry-derived tourmaline has an oxy or hydroxy dominant (*i.e.*, OH⁻ + O²⁻) *W*-site; Step 5) Porphyry-related tourmaline does not contain >0.5 *apfu* F + Cl; Step 6) Trace-element discrimination using the Sr/Pb–Zn/Cu–Ga ternary diagram presented in Chapter 3: samples that plot outside the porphyry field are unlikely to be derived from a mineralized porphyry system.

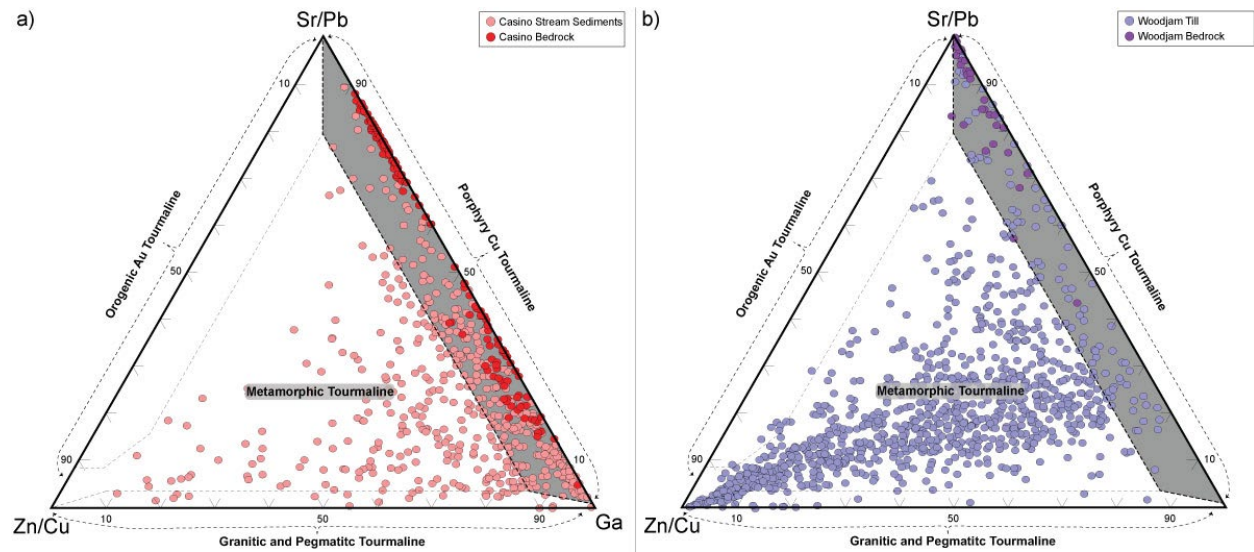


Figure 4-11: Ternary trace-element discrimination of surficial tourmaline grains.

Ternary trace-element discrimination diagram (developed presented in Chapter 3, Figure 3-5). a) Casino deposit tourmaline grain compositions for six bedrock samples and 423 stream sediment grains. b) Woodjam deposit tourmaline grain composition in three bedrock samples and 1084 till grains.

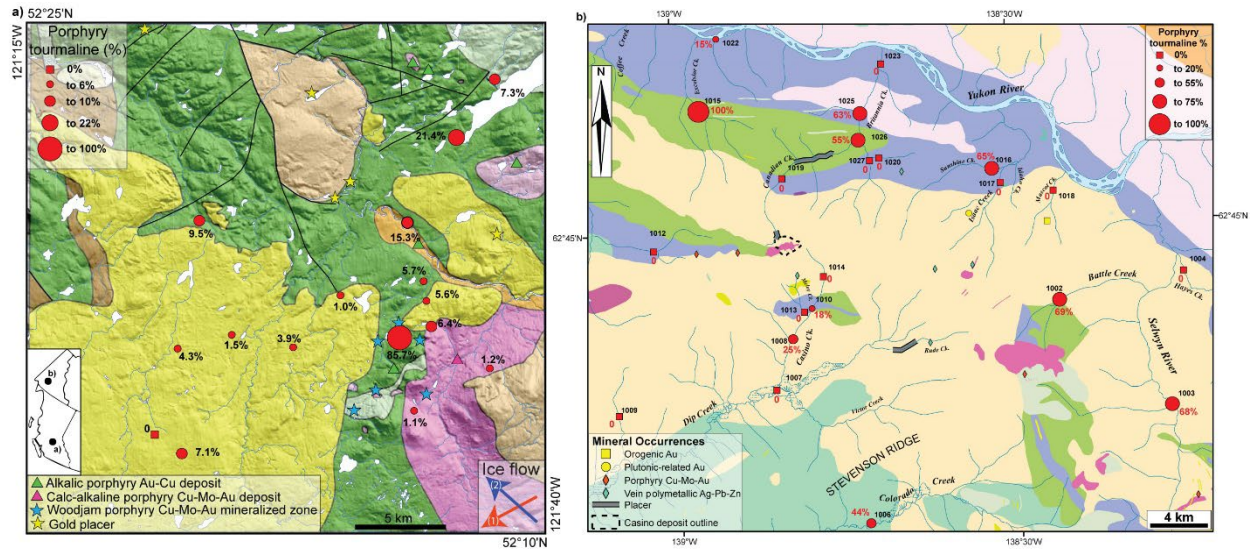


Figure 4-12: Porphyry tourmaline dispersion maps (Woodjam and Casino).

Percentage of tourmaline grains in selected sediment samples for which chemical analysis of the tourmaline grains was conducted (Table 4-7). Tourmaline were identified as being derived from mineralized porphyry bedrock using criteria established in this study (Figure 4-10). Red numbers are individual percentages of the grains analyzed that were classified as “porphyry-derived”.

Inset map shows the location of (a) the Woodjam deposit in British Columbia and (b) the Casino deposit in Yukon. a) till samples around the Woodjam deposit, see Plouffe and Ferbey (2017) for bedrock geology. b) stream sediment samples around the Casino deposit, see McClenaghan *et al.* (2021) for bedrock geology.

4.9 Tables

Table 4-1: Select major element compositions of tourmaline from bedrock, till, and stream sediment samples collected at the Woodjam and Casino deposits.

	13CDB-WJ09 C2 6-2	13CDB-WJ05 C2 4-1	CEBB-031 C32-3	CEBB-005 C2 4-1	CEBB-7 SOI1-4 2	11PMA-009-01	12PMA-126A-01	Casino-1010-A6	Casino-1026-B1
Deposit	Woodjam	Woodjam	Casino	Casino	Casino	Woodjam	Woodjam	Casino	Casino
Sample type	Bedrock	Bedrock	Bedrock	Bedrock	Bedrock	Till	Till	Stream sediment	Stream sediment
SiO ₂	35.88	34.27	37.76	38.76	36.33	37.18	36.50	36.30	36.13
TiO ₂	0.33	0.93	0.38		0.22	0.48	0.68	0.80	0.68
Al ₂ O ₃	30.70	20.46	33.03	36.41	34.97	32.65	32.57	34.39	29.61
FeO	9.17	18.96	7.55	2.12	0.45	6.02	5.47	3.98	8.21
MgO	7.03	7.79	6.83	9.55	10.58	7.03	8.11	7.49	8.41
CaO	1.46	3.04				0.15	0.46	0.94	1.74
Na ₂ O	1.78	1.43	2.63	2.24	2.70	2.36	2.40	1.77	2.21
Si(T)	5.949	5.938	6.059	5.952	5.806	6.093	5.947	5.912	5.960
Al(T)	0.051	0.004	0.000	0.048	0.194	0.000	0.053	0.088	0.040
B(T)	0.000	0.058	0.000	0.000	0.000	0.000	0.000	0.000	0.000
Al(Z)	5.949	4.175	0.247	6.000	6.000	6.000	6.000	6.000	5.716
Mg(Z)	0.051	1.825	0.000	0.000	0.000	0.000	0.000	0.000	0.284
Al(Y)	0.000	0.000	0.247	0.541	0.393	0.305	0.202	0.511	0.000
Ti(Y)	0.042	0.122	0.046	0.000	0.026	0.060	0.084	0.098	0.085
Mg(Y)	1.686	0.188	1.634	2.186	2.520	1.717	1.969	1.819	1.783
Fet(Y)	1.272	2.748	1.013	0.273	0.060	0.825	0.745	0.541	1.132
Ca(X)	0.259	0.564	0.000	0.000	0.000	0.027	0.081	0.164	0.307
Na(X)	0.572	0.480	0.818	0.666	0.480	0.749	0.758	0.558	0.707
Vac	0.169	0.000	0.182	0.334	0.165	0.224	0.161	0.279	0.000

apfu (atoms per formula unit) calculated based on 31 anions. Vac: vacancy in the X-site.

Table 4-2: Summary of trace-element analyses in TSM from bedrock samples at Woodjam and Casino

Element	Samples above LOD	Av. LOD (ppm)	Abundance (ppm)				
			Minimum	Maximum	Mean	Median	Standard deviation
³⁹ K	145	20	73	6900	600	240	915
⁴⁵ Sc	145	1	7	250	56	46	40
⁴⁷ Ti	145	5	111	5150	1688	1521	932
⁵¹ V	145	2	85	1175	439	389	217
⁵² Cr	143	0.1	< LOD	347	50.5	39.1	52.4
⁵⁵ Mn	145	3	21	1300	152	79	186
⁵⁹ Co	145	0.1	0.6	260	14.2	5.4	25.6
⁶⁰ Ni	145	0.1	0.2	31.7	12.8	10.9	8.4
⁶⁵ Cu	140	0.1	< LOD	510	37.8	19.0	68.1
⁶⁶ Zn	145	0.1	5.7	151	34.0	20.1	28.1
⁶⁹ Ga	145	0.1	21.5	103	47.7	47.1	12.3
⁷² Ge	145	0.1	0.8	13.9	5.4	5.2	2.5
⁷⁵ As	143	1	< LOD	322	37.7	21.8	48.7
⁸⁵ Rb	134	0.2	< LOD	25.8	2.4	0.8	4.4
⁸⁸ Sr	145	0.2	34.8	623	209.6	164	143.2
⁸⁹ Y	143	0.03	< LOD	73	6.6	2.9	11.5
⁹⁰ Zr	145	0.1	0.6	45.0	5.3	2.2	7.8
⁹³ Nb	143	0.2	< LOD	2.9	0.7	0.6	0.6
⁹⁵ Mo	143	0.1	< LOD	51	4.6	1.3	6.6
¹¹⁵ In	140	0.01	< LOD	1.4	0.3	0.2	0.2
¹¹⁸ Sn	145	0.5	1.3	57.0	17.1	16.5	10.9
¹²¹ Sb	143	0.2	< LOD	41.5	2.4	0.9	5.3
¹³⁷ Ba	143	0.2	< LOD	300	17.4	5.4	35.6
¹³⁹ La	143	0.03	< LOD	15.20	3.02	2.01	3.31
¹⁴⁰ Ce	145	0.03	0.05	29.4	5.14	2.80	5.63
¹⁴¹ Pr	143	0.03	< LOD	3.7	0.47	0.25	0.56
¹⁴⁶ Nd	142	0.01	< LOD	13.80	1.59	0.72	2.00
¹⁴⁷ Sm	104	0.01	< LOD	4.20	0.31	0.17	0.52
¹⁵³ Eu	136	0.03	< LOD	0.34	0.09	0.08	0.06
¹⁵⁷ Gd	114	0.01	< LOD	9.8	0.49	0.18	1.13
¹⁵⁹ Tb	119	0.03	< LOD	1.91	0.10	0.04	0.23
¹⁶³ Dy	132	0.01	< LOD	13.8	0.88	0.35	1.83
¹⁶⁵ Ho	133	0.03	< LOD	2.69	0.24	0.11	0.42
¹⁶⁶ Er	142	0.01	< LOD	7.98	0.90	0.49	1.33
¹⁶⁹ Tm	140	0.03	< LOD	1.30	0.16	0.10	0.20
¹⁷² Yb	143	0.01	< LOD	10.8	1.49	1.04	1.54
¹⁷⁵ Lu	141	0.03	< LOD	1.63	0.28	0.21	0.25
¹⁷⁸ Hf	131	0.04	< LOD	2.53	0.31	0.12	0.48
²⁰⁸ Pb	143	0.04	< LOD	11.50	2.55	1.37	2.70
²³² Th	143	0.04	< LOD	18.00	1.26	0.59	1.82
²³⁸ U	135	0.04	< LOD	1.59	0.37	0.28	0.31

Table 4-3: Summary of trace-element analyses of tourmaline from surficial sediments at the Woodjam and Casino porphyry deposits.

Element	Samples above LOD	Av. LOD (ppm)	Abundance (ppm)				
			Minimum	Maximum	Mean	Median	Standard deviation
³⁹ K	1373	20	< LOD	2900	315	252	265
⁴⁵ Sc	1565	1	< LOD	993	27	11	56
⁴⁷ Ti	1585	5	108	70000	4645	4540	2791
⁵¹ V	1583	2	< LOD	18900	404	227	921
⁵² Cr	1575	0.1	< LOD	7200	333	243	466
⁵⁵ Mn	1584	3	< LOD	12900	164	76	434
⁵⁹ Co	1572	0.1	< LOD	114	23.5	19.4	16.1
⁶⁰ Ni	1542	0.1	< LOD	672	69.3	45.4	70.4
⁶⁵ Cu	1377	0.1	< LOD	2100	27.1	7.9	107.9
⁶⁶ Zn	1585	0.1	10.3	3020	201	169	178
⁶⁹ Ga	1582	0.1	< LOD	187	37.2	32.4	18.8
⁷² Ge	1200	0.1	< LOD	25	2.5	1.6	2.8
⁷⁵ As	1325	1	< LOD	670	7	3	26
⁸⁵ Rb	1140	0.2	< LOD	31.0	1.5	0.6	3.1
⁸⁸ Sr	1584	0.2	< LOD	2740	300	229	261
⁸⁹ Y	1277	0.03	< LOD	378	1.22	0.11	12.20
⁹⁰ Zr	1516	0.1	< LOD	6200	13.1	0.6	196
⁹³ Nb	1415	0.2	< LOD	340	0.8	0.1	9.2
⁹⁵ Mo	1369	0.1	< LOD	150	21.4	0.6	4.4
¹¹⁵ In	1108	0.01	< LOD	4.80	0.14	0.04	0.36
¹¹⁸ Sn	1544	0.5	< LOD	497	6.6	1.7	23.1
¹²¹ Sb	1362	0.2	< LOD	360	1.1	0.3	9.9
¹³⁷ Ba	1309	0.2	< LOD	460	6.1	0.9	23.2
¹³⁹ La	1543	0.03	< LOD	21.80	1.90	1.00	2.60
¹⁴⁰ Ce	1555	0.03	< LOD	77.00	3.23	1.60	4.90
¹⁴¹ Pr	1381	0.03	< LOD	4.30	0.33	0.17	0.47
¹⁴⁶ Nd	1283	0.01	< LOD	11.60	1.15	0.59	1.61
¹⁴⁷ Sm	541	0.01	< LOD	4.40	0.27	0.13	0.42
¹⁵³ Eu	1362	0.03	< LOD	2.48	0.39	0.30	0.36
¹⁵⁷ Gd	427	0.01	< LOD	5.50	0.24	0.10	0.48
¹⁵⁹ Tb	345	0.03	< LOD	1.50	0.04	0.04	0.48
¹⁶³ Dy	332	0.01	< LOD	18.00	0.39	0.06	1.49
¹⁶⁵ Ho	291	0.03	< LOD	11.60	0.15	0.04	0.78
¹⁶⁶ Er	266	0.01	< LOD	70.00	0.86	0.06	1.74
¹⁶⁹ Tm	211	0.03	< LOD	16.20	0.25	0.04	1.24
¹⁷² Yb	268	0.01	< LOD	158	1.89	0.10	10.91
¹⁷⁵ Lu	274	0.03	< LOD	31.70	0.41	0.04	2.30
¹⁷⁸ Hf	320	0.04	< LOD	140	1.51	0.15	10.25
²⁰⁸ Pb	1585	0.04	0.27	260	18.73	15.50	15.12
²³² Th	625	0.04	< LOD	12.70	0.41	0.06	1.02
²³⁸ U	596	0.04	< LOD	13.00	0.21	0.05	0.78

Table 4-4: Mineral inclusions identified in detrital tourmaline grains in selected till samples at the Woodjam deposit.

		Total grains	Grains with inclusions	Zircon	Quartz	Rutile	Ilmenite	Biotite	Apatite	Alanite	Epidote	Muscovite	Fe-oxide	Albite	Chlorite	Apatite-REE	Pyrite	K-feldspar	Dumortierite	Titanite	Pentlandite	Ferrosilite	Galena	Calcite	Barite
All samples	# grains	1122	597	251	231	96	65	40	39	38	30	25	17	14	14	14	13	6	6	3	1	1	1	1	1
	%	–	53.2	22.4	20.6	8.6	5.8	3.6	3.5	3.4	2.7	2.2	1.5	1.3	1.3	1.3	1.2	0.5	0.5	0.3	<0.1	<0.1	<0.1	<0.1	<0.1
11PMA003A03	# grains	40	22	9	9	4	1	1	1	–	–	–	–	–	–	1	–	1	–	–	–	–	–	–	–
	%	–	55	22.5	22.5	10.0	2.5	2.5	2.5	–	–	–	–	–	–	2.5	–	2.5	–	–	–	–	–	–	–
11PMA007A01	# grains	70	34	13	11	4	3	2	1	4	1	–	–	1	1	1	–	2	–	–	–	–	–	–	–
	%	–	48.6	18.6	15.7	5.7	4.3	2.9	1.4	5.7	1.4	–	–	1.4	1.4	1.4	–	2.9	–	–	–	–	–	–	–
11PMA009A01	# grains	71	40	14	15	8	3	2	3	1	3	–	1	1	2	–	–	–	–	1	1	–	–	–	–
	%	–	56.3	19.7	21.1	11.3	4.2	2.8	4.2	1.4	4.2	–	1.4	1.4	2.8	–	–	–	–	1.4	1.4	–	–	–	–
11PMA012A01	# grains	28	13	3	4	2	1	–	1	1	1	–	5	1	–	–	–	–	–	–	–	–	–	–	–
	%	–	46.4	10.7	14.3	7.1	3.6	–	3.6	3.6	3.6	–	17.9	3.6	–	–	–	–	–	–	–	–	–	–	–
12PMA117A01	# grains	67	42	21	12	9	5	3	3	1	–	–	–	–	–	1	1	1	1	–	–	–	–	–	–
	%	–	62.7	31.3	17.9	13.4	7.5	4.5	4.5	1.5	–	–	–	–	–	1.5	1.5	1.5	1.5	–	–	–	–	–	–
12PMA126A01	# grains	93	40	15	17	7	3	3	3	3	2	5	1	–	1	–	–	–	2	–	–	–	1	–	–
	%	–	43	16.1	18.3	7.5	3.2	3.2	3.2	3.2	2.2	5.4	1.1	–	1.1	–	–	–	2.2	–	–	–	1.1	–	–
12PMA593A01	# grains	67	37	12	16	5	3	1	1	3	1	1	–	–	1	3	1	–	1	–	–	–	–	–	–
	%	–	55.2	17.9	23.9	7.5	4.5	1.5	1.5	4.5	1.5	1.5	–	–	1.5	4.5	1.5	–	1.5	–	–	–	–	–	–
12PMA128A01	# grains	92	53	26	19	8	4	3	2	–	5	2	5	2	3	1	2	–	1	–	–	–	–	–	–
	%	–	57.6	28.3	20.7	8.7	4.3	3.2	2.2	–	5.4	2.2	5.4	2.2	3.2	1.1	2.2	–	1.1	–	–	–	–	–	–
12PMA594A01	# grains	99	44	14	19	6	5	3	3	–	5	1	1	2	–	–	1	–	–	–	–	–	–	–	–
	%	–	44.4	14.1	19.2	6.1	5.1	3.0	3.0	–	5.1	1.0	1.0	2.0	–	–	1.0	–	–	–	–	–	–	–	–
12PMA599A01	# grains	95	47	18	21	6	7	4	4	7	1	6	–	1	–	3	3	–	–	1	–	–	1	–	–
	%	–	49.5	18.9	22.1	6.3	7.4	4.2	4.2	7.4	1.1	6.3	–	1.1	–	3.2	3.2	–	–	1.1	–	–	1.1	–	–
12PMA603A01	# grains	99	50	23	19	8	4	1	1	3	2	1	–	1	1	–	1	–	–	–	–	–	–	–	–
	%	–	50.5	23.2	19.2	8.1	4.0	1.0	1.0	3.0	2.0	1.0	–	1.0	1.0	–	1.0	–	–	–	–	–	–	–	–
12PMA614A01	# grains	42	22	9	8	4	3	1	3	–	–	–	–	–	2	2	–	–	–	–	–	–	–	–	–
	%	–	52.4	21.4	19.0	9.5	7.1	2.4	7.1	–	–	–	–	–	4.8	4.8	–	–	–	–	–	–	–	–	–
12PMA615A01	# grains	48	25	10	11	3	1	2	–	1	–	2	2	2	–	–	2	1	–	–	–	–	–	–	–
	%	–	52.1	20.8	22.9	6.3	2.1	4.2	–	2.1	–	4.2	4.2	4.2	–	–	4.2	2.1	–	–	–	–	–	–	–
12PMA620A01	# grains	40	27	13	12	8	4	3	1	3	–	1	–	–	–	–	–	–	–	1	–	–	–	–	–
	%	–	67.5	32.5	30.0	20.0	10.0	7.5	2.5	7.5	–	2.5	–	–	–	–	–	–	–	2.5	–	–	–	–	–
12TFE114A01	# grains	85	52	26	18	8	6	5	5	6	4	5	1	2	1	1	–	–	1	–	–	–	–	1	–
	%	–	61.2	30.6	21.2	9.4	7.1	5.9	5.9	7.1	4.7	5.9	1.2	2.4	1.2	1.2	–	–	1.2	–	–	–	–	1.2	–
12TFE130A01	# grains	86	50	25	20	6	12	6	6	5	5	1	1	1	2	1	2	1	–	–	–	–	–	–	1
	%	–	58.1	29.1	23.3	7.0	14.0	7.0	7.0	5.8	5.8	1.2	1.2	1.2	2.3	1.2	2.3	1.2	–	–	–	–	–	–	1.2

REE: Rare earth elements.

Table 4-5: Mineral inclusions identified in detrital tourmaline grains collected from stream sediments surrounding the Casino deposit.

		Total grains	Grains with inclusions	Zircon	Rutile	Quartz	Epidote	Fe-oxide	Apatite	Biotite	Muscovite	Pyrite	Apatite-REE	Alanite	Ilmenite	K-feldspar	Barite	Titanite	Albite	Chlorite	Calcopyrite	Jarosite	Galena	Sphalerite	Dumortierite	Zn-staurolite	Molybdenite	Calcite	Dioside	
All samples	# grains	423	331	129	112	74	48	37	34	33	33	33	27	26	22	17	15	12	8	6	5	4	3	3	3	2	1	1	1	
	%	–	78.3	30.5	26.5	17.5	11.3	8.7	8.0	7.8	7.8	7.8	6.4	6.1	5.2	4.0	3.5	2.8	1.9	1.4	1.2	0.9	0.7	0.7	0.7	0.5	0.2	0.2	0.2	
1002	# grains	16	10	1	2	2	–	1	2	–	–	–	–	1	1	2	–	–	–	–	–	–	–	–	–	–	–	–	–	
	%	–	62.5	6.3	12.5	12.5	–	6.3	12.5	–	–	–	–	6.3	6.3	12.5	–	–	–	–	–	–	–	–	–	–	–	–	–	–
1003	# grains	19	12	2	1	3	–	–	2	1	–	–	1	–	1	2	–	1	–	–	–	–	1	–	–	–	–	–	–	
	%	–	63.2	11.1	5.6	16.7	–	–	11.1	5.6	–	–	5.6	–	5.6	11.1	–	5.6	–	–	–	–	5.6	–	–	–	–	–	–	–
1006	# grains	18	16	4	3	8	2	3	–	–	–	1	1	7	2	3	–	1	–	–	–	–	–	–	1	–	–	–	–	
	%	–	88.9	22.2	16.7	44.4	11.1	16.7	–	–	–	5.6	5.6	–	11.1	16.7	–	5.6	–	–	–	–	–	–	5.6	–	–	–	–	–
1008	# grains	4	4	1	2	3	1	1	–	1	–	–	1	1	–	–	1	–	–	–	–	–	–	–	–	–	–	–	–	–
	%	–	100.0	25.0	50.0	75.0	25.0	25.0	–	25.0	–	–	25.0	25.0	–	–	25.0	–	–	–	–	–	–	–	–	–	–	–	–	–
1010	# grains	11	10	5	6	3	1	2	3	3	–	–	–	2	3	–	–	–	–	–	–	–	–	–	–	–	–	–	–	
	%	–	90.9	45.5	54.5	27.3	9.1	18.2	27.3	27.3	–	–	–	18.2	27.3	–	–	–	–	–	–	–	–	–	–	–	–	–	–	–
1015	# grains	3	3	–	1	2	2	–	1	–	–	–	–	3	–	–	–	–	–	–	–	–	–	–	–	–	–	–	–	
	%	–	100.0	–	33.3	66.6	66.6	–	33.3	–	–	–	–	100.0	–	–	–	–	–	–	–	–	–	–	–	–	–	–	–	–
1016	# grains	92	78	40	28	13	4	8	9	10	10	8	8	5	6	5	4	1	2	1	1	1	1	1	2	–	–	–	1	–
	%	–	84.8	43.5	30.4	14.1	4.3	8.7	9.8	10.9	10.9	8.7	8.7	5.4	6.5	5.4	4.3	1.1	2.2	1.1	1.1	1.1	1.1	1.1	2.2	–	–	–	1.1	–
1022	# grains	150	121	63	46	24	18	10	12	11	16	19	14	5	8	3	5	8	5	3	–	1	–	–	2	2	1	–	1	
	%	–	80.7	42.0	30.7	16.0	12.0	6.7	8.0	7.3	10.7	12.7	9.3	3.3	5.3	2.0	3.3	5.3	3.3	2.0	–	0.7	–	–	1.3	1.3	0.7	–	0.7	
1025	# grains	52	40	7	14	8	6	7	3	5	3	2	1	–	1	2	3	–	–	1	3	–	–	–	–	–	–	–	–	–
	%	–	76.9	13.5	26.9	15.4	11.5	13.5	5.7	9.6	5.7	3.8	1.9	–	1.9	3.8	5.7	–	–	1.9	5.7	–	–	–	–	–	–	–	–	–
1026	# grains	58	37	6	9	8	14	5	2	2	4	3	1	2	–	–	2	1	1	1	1	2	1	1	–	–	–	–	–	
	%	–	71.2	10.3	15.5	13.8	24.1	8.6	3.4	3.4	6.9	5.2	1.7	3.4	–	–	3.4	1.7	1.7	1.7	1.7	3.4	1.7	1.7	–	–	–	–	–	

REE: Rare earth elements.

Table 4-6: Generalizations of trace-element compositions for tourmaline from different geological settings.

	Granites	Pegmatites	Metamorphic	Orogenic Au	Polymetallic W-Sn-Cu	VMS	Porphyry Cu-Mo-Au
Li	H >50 ppm (70 avg)	H >50 ppm (95 avg)	L <25 ppm (11 avg)	L <35 ppm (16 avg)	H >35 ppm (72 avg)	L <35 ppm (8.6 avg)	L <15 ppm (7.8 avg)
LILE	K	ID	ID	L <330 ppm (162 avg)	N (214 avg)	L <200 ppm (88 avg)	wide-range (287 avg)
	Sr	L <100 ppm (27 avg)	L <100 ppm (26 avg)	H >75 ppm (210 avg)	H >150 ppm (359 avg)	N (94 avg)	H >100 ppm (298 avg)
	Pb	H >2 ppm (4.6 avg)	H >2 ppm (6.6 avg)	H >2 ppm (6.4 avg)	N (1.7 avg)	N (2.0 avg)	L <2 ppm (1.0 avg)
HFSE	Ti	N (2269 avg)	wide-range (3664 avg)	wide-range (853 avg)	N (2490 avg)	wide-range (2368 avg)	N (2271 avg)
	Zr	L <1.5 ppm (0.36 avg)	L <0.5 ppm (0.21 avg)	L <0.6 ppm (0.23 avg)	wide-range (0.47 avg)	L <2.5 ppm (1.1 avg)	wide-range (0.59 avg)
	Nb	H >0.4 ppm (1.00 avg)	H >0.4 ppm (0.93 avg)	L <0.3 ppm (0.08 avg)	L <0.2 ppm (0.06 avg)	H >0.3 ppm (0.73 avg)	L <0.1 (0.05 avg)
	Ta	H >0.11 ppm (0.49 avg)	H >0.25 (0.76 avg)	wide-range (0.08 avg)	wide-range (0.02 avg)	H >0.1 (0.33 avg)	L <0.01 (0.007 avg)
Metals	V	L <200 ppm (24 avg)	L <300 ppm (35 avg)	H >285 ppm (471 avg)	wide-range (298 avg)	wide-range (70 avg)	H >300 ppm (689 avg)
	Cr	L 25< ppm (8 avg)	L 45< ppm (12 avg)	H >15 ppm (51 avg)	H >20 ppm (76 avg)	wide-range (43 avg)	H >25 ppm (83 avg)
	Mn	L 900< ppm (avg)	H >1000 ppm (1134 avg)	L <500 ppm (191 avg)	L <375 ppm (152 avg)	L <650 ppm (342 avg)	L <585 ppm (311 avg)
	Cu	L <1.2 ppm (0.8 avg)	L <2.0 ppm (1.0 avg)	L <2.3 ppm (1.5 avg)	L <1.3 ppm (0.7 avg)	L <1.5 ppm (1.0 avg)	L <1.8 ppm (1.0 avg)
	Zn	H >235 ppm (331 avg)	H >375 ppm (559 avg)	H >105 ppm (160 avg)	H >120 ppm (190 avg)	H >105 ppm (224 avg)	H >75 ppm (212 avg)
Semi-metals	Ga	H >55 ppm (83 avg)	H >92 ppm (117 avg)	L <50 ppm (39 avg)	L <65 ppm (47 avg)	H >45 ppm (73 avg)	L <26 ppm (23 avg)
	As	ID	L <3 ppm (1.5 avg)	L <6 ppm (3.3 avg)	ID	ID	H >14 ppm (33 avg)
	Sn	H >6.5 ppm (19 avg)	H >7 ppm (16 avg)	L <9 ppm (1.6 avg)	L <7.5 ppm (2.6 avg)	H >11 ppm (36 avg)	L <0.9 ppm (0.46 avg)
	Sb	L <1.0 ppm (0.19 avg)	L <0.4 ppm (0.16 avg)	H >0.38 ppm (0.46 avg)	L <0.47 ppm (0.17 avg)	H >0.31 ppm (1.0 avg)	ID
ΣREE	H >4 ppm (10.9 avg)	H >2.8 ppm (9.0 avg)	L <6.2 ppm (3.3 avg)	L <9.8 ppm (3.0 avg)	H >3.9 ppm (8.3 avg)	L <2.3 ppm (0.98 avg)	H >6.6 ppm (11.3 avg)

ID: insufficient data (*i.e.*, less than 50 analyses), L: lower, N: neutral, H: higher. Bold values denote elements which can be distinctive for that environment.

Table 4-7a: Number of surficial porphyry derived tourmaline grains in the 2.8 to 3.2 SG fraction of till samples from the Woodjam deposit

Woodjam	# of tourmaline Recovered	# of porphyry related tourmaline	% of porphyry related tourmaline
11PMA003A03	42	9	21.4
11PMA007A01	72	11	15.3
11PMA009A01	78	5	6.4
11PMA012A01	28	24	85.7
12PMA117A01	63	6	9.5
12PMA126A01	93	4	4.3
12PMA128A01	68	1	1.5
12PMA593A01	90	5	5.6
12PMA594A01	105	6	5.7
12PMA599A01	102	4	3.9
12PMA603A01	99	1	1.0
12PMA614A01	42	3	7.1
12PMA615A01	60	0	-
12PMA620A01	41	3	7.3
12TFE114A01	94	1	1.1
12FTE130A01	85	1	1.2

Porphyry tourmaline grains classified based on Figure 4-10.

Table 4-8b: Number of surficial porphyry derived tourmaline grains in the 2.8 to 3.2 SG fraction of stream sediment samples from the Casino deposit

Casino	# of tourmaline Recovered	# of porphyry related tourmaline	% of porphyry related tourmaline
115J171002	16	11	68.8
115J171003	19	13	68.4
115J171004	0	0	-
115J171006	18	8	44.4
115J171007	0	0	-
115J171008	4	1	25.0
115J171009	0	0	-
115J171010	11	2	18.2
115J171012	0	0	-
115J171013	0	0	-
115J171014	0	0	-
115J171015	3	3	100.0
115J171016	92	60	65.2
115J171017	0	0	-
115J171018	0	0	-
115J171019	0	0	-
115J171020	0	0	-
115J171022	150	23	15.3
115J171023	0	0	-
115J171025	52	33	63.5
115J171026	58	32	55.2
115J171027	0	0	-

Porphyry tourmaline grains classified based on Figure 4-10.

4.10 Appendix

4.10.1 Appendix 1:

Detrital tourmaline recount data for the 0.25-0.5 mm 2.8-3.2 SG and the >3.2 SG fractions of GSC till samples collected around the Woodjam deposits.

4.11 References

- Averill, S.A., 2011. Viable indicator minerals in surficial sediments for two major base metal deposit types: Ni-Cu-PGE and porphyry Cu. *Geochemistry: Exploration, Environment, Analysis*, 11(4): 279-291. <http://doi.org/10.1144/1467-7873/10-im-022>
- Baker, M.J., Wilkinson, J.J., Wilkinson, C.C., Cooke, D.R. and Ireland, T., 2020. Epidote Trace Element Chemistry as an Exploration Tool in the Collahuasi District, Northern Chile. *Economic Geology*, 115(4): 749-770. <http://doi.org/10.5382/econgeo.4739>
- Baksheev, I.A., Chitalin, A.F., Yapaskurt, V.O., Vigasina, M.F., Bryzgalov, I.A. and Ustinov, V.I., 2010. Tourmaline in the Vetka porphyry copper-molybdenum deposit of the Chukchi Peninsula of Russia. *Moscow University Geology Bulletin*, 65(1): 27-38. <http://doi.org/10.3103/s0145875210010035>
- Baksheev, I.A., Prokof'ev, V.Y., Yapaskurt, V.O., Vigasina, M.F., Zorina, L.D. and Solov'ev, V.N., 2011. Ferric-iron-rich tourmaline from the Darasun gold deposit, Transbaikalia, Russia. *The Canadian Mineralogist*, 49(1): 263-276. <http://doi.org/10.3749/canmin.49.1.263>
- Baksheev, I.A., Trumbull, R.B., Popov, M.P., Erokhin, Y.V., Kudryavtseva, O.E., Yapaskurt, V.O., Khiller, V.V., Vovna, G.M. and Kiselev, V.I., 2017. Chemical and boron isotopic composition of tourmaline from the Mariinsky emerald deposit, Central Urals, Russia. *Mineralium Deposita*, 53(4): 565-583. <http://doi.org/10.1007/s00126-017-0759-z>

- Baksheev, I.A., Yu Prokofev, V., Zاراisky, G.P., Chitalin, A.F., Yapaskurt, V.O., Nikolaev, Y.N., Tikhomirov, P.L., Nagornaya, E.V., Rogacheva, L.I., Gorelikova, N.V. and Kononov, O.V., 2012. Tourmaline as a prospecting guide for the porphyry-style deposits. *European Journal of Mineralogy*, 24(6): 957-979. <http://doi.org/10.1127/0935-1221/2012/0024-2241>
- Bond, J.D. and Lipovsky, P.S., 2011. Surficial geology, soils and permafrost of the northern Dawson Range. In: K.E. MacFarlane, L.H. Weston and C. Relf (Editors), Yukon Exploration and Geology 2010. Yukon Geological Survey, pp. 19-32.
- Bouzari, F., Hart, C.J.R., Bissig, T. and Barker, S., 2016. Hydrothermal Alteration Revealed by Apatite Luminescence and Chemistry: A Potential Indicator Mineral for Exploring Covered Porphyry Copper Deposits. *Economic Geology*, 111(6): 1397-1410. <http://doi.org/10.2113/econgeo.111.6.1397>
- Buttner, S.H. and Kasemann, S.A., 2007. Deformation-controlled cation diffusion in tourmaline: A microanalytical study on trace elements and boron isotopes. *American Mineralogist*, 92(11-12): 1862-1874. <http://doi.org/10.2138/am.2007.2567>
- Byrne, K., Trumbull, R.B., Lesage, G., Gleeson, S.A., Ryan, J., Kyser, K. and Lee, R.G., 2020. Mineralogical and Isotopic Characteristics of Sodic-Calcic Alteration in the Highland Valley Copper District, British Columbia, Canada: Implications for Fluid Sources in Porphyry Cu Systems. *Economic Geology*, 115(4): 841-870. <http://doi.org/10.5382/econgeo.4740>

- Canil, D., Grondahl, C., Lacourse, T. and Pisiak, L.K., 2016. Trace elements in magnetite from porphyry Cu–Mo–Au deposits in British Columbia, Canada. *Ore Geology Reviews*, 72: 1116-1128. <http://doi.org/10.1016/j.oregeorev.2015.10.007>
- Casselman, S.C. and Brown, H., 2017. Casino porphyry copper-gold-molybdenum deposit, central Yukon (Yukon MINFILE 115J028); *in* Yukon Exploration and Geology Overview 2016, (ed.) K.W. MacFarlane; Yukon Geological Survey, p. 61–74, plus digital appendices.
- Chapman, J.B., Plouffe, A. and Ferbey, T., 2015. Tourmaline: the universal indicator?, Association of Applied Geochemists, 27th International Applied Geochemistry Symposium, Short Course No. 2, pp. 25-31.
- Clague, J.J. and Ward, B.W., 2011. Pleistocene glaciation of British Columbia - a closer look. In: J. Ehlers, P.L. Gibbard and P.D. Hughes (Editors), *Developments in Quaternary Sciences*, pp. 563-573. <http://doi.org/10.1016/B978-0-444-53447-7.00044-1>
- Clarke, D.B., Reardon, N.C., Chatterjee, A.K. and Gregoire, D.C., 1989. Tourmaline Composition as a Guide to Mineral Exploration - a Reconnaissance Study from Nova-Scotia Using Discriminant Function-Analysis. *Economic Geology*, 84(7): 1921-1935. <http://doi.org/10.2113/gsecongeo.84.7.1921>
- Codeço, M.S., Weis, P., Trumbull, R.B., Glodny, J., Wiedenbeck, M. and Romer, R.L., 2019. Boron Isotope Muscovite-Tourmaline Geothermometry Indicates Fluid Cooling During Magmatic-Hydrothermal W-Sn Ore Formation. *Economic Geology*, 114(1): 153-163. <http://doi.org/10.5382/econgeo.2019.4625>

- Codeço, M.S., Weis, P., Trumbull, R.B., Van Hinsberg, V., Pinto, F., Lecumberri-Sanchez, P. and Schleicher, A.M., 2020. The imprint of hydrothermal fluids on trace-element contents in white mica and tourmaline from the Panasqueira W–Sn–Cu deposit, Portugal. *Mineralium Deposita*, 56(3): 481-508. <http://doi.org/10.1007/s00126-020-00984-8>
- Cooke, D.R., Agnew, P., Hollings, P., Baker, M., Chang, Z., Wilkinson, J.J., Ahmed, A., White, N.C., Zhang, L., Thompson, J., Gemmell, J.B., Danyushevsky, L. and Chen, H., 2020a. Recent advances in the application of mineral chemistry to exploration for porphyry copper–gold–molybdenum deposits: detecting the geochemical fingerprints and footprints of hypogene mineralization and alteration. *Geochemistry: Exploration, Environment, Analysis*, 20(2): 176-188. <http://doi.org/10.1144/geochem2019-039>
- Cooke, D.R., Hollings, P., Wilkinson, J.J. and Tosdal, R.M., 2014. 13.14 - Geochemistry of Porphyry Deposits, In: Heinrich D. Holland, Karl K. Turekian (Editors), *Treatise on Geochemistry*, pp. 357-381. <http://doi.org/10.1016/b978-0-08-095975-7.01116-5>
- Cooke, D.R., Wilkinson, J.J., Baker, M., Agnew, P., Phillips, J., Chang, Z., Chen, H., Wilkinson, C.C., Inglis, S., Hollings, P., Zhang, L., Gemmell, J.B., White, N.C., Danyushevsky, L. and Martin, H., 2020b. Using Mineral Chemistry to Aid Exploration: A Case Study from the Resolution Porphyry Cu-Mo Deposit, Arizona. *Economic Geology*, 115(4): 813-840. <http://doi.org/10.5382/econgeo.4735>
- Cooke, D.R., Wilkinson, J.J. and Pacey, A., 2020c. Chlorite and Epidote Mineral Chemistry in Porphyry Ore Systems: A Case Study of the Northparkes District, New South Wales, Australia. *Economic Geology*, 115(4): 701-727. <http://doi.org/10.5382/econgeo.4700>

- Čopjaková, R., Škoda, R., Galiová, M.V., Novák, M. and Cempírek, J., 2015. Sc- and REE-rich tourmaline replaced by Sc-rich REE-bearing epidote-group mineral from the mixed (NYF+LCT) Kracovice pegmatite (Moldanubian Zone, Czech Republic). *American Mineralogist*, 100(7): 1434-1451. <http://doi.org/10.2138/am-2015-4863>
- Dare, S.A.S., Barnes, S.-J., Beaudoin, G., Méric, J., Boutroy, E. and Potvin-Doucet, C., 2014. Trace elements in magnetite as petrogenetic indicators. *Mineralium Deposita*, 49(7): 785-796. <http://doi.org/10.1007/s00126-014-0529-0>
- del Real, I., Bouzari, F., Bissig, T., Blackwell, J., Sherlock, R., Thompson, J.F.H. and Hart, R.J., 2017. Spatially and temporally associated porphyry deposits with distinct Cu/Au/Mo Ratios, Woodjam District, Central British Columbia. *Economic Geology*, 112(7): 1673-1717. <http://doi.org/10.5382/econgeo.2017.4526>
- Desbois, G. and Ingrin, J., 2007. Anisotropy of hydrogen diffusion in tourmaline. *Geochimica et Cosmochimica Acta*, 71(21): 5233-5243. <http://doi.org/10.1016/j.gca.2007.08.027>
- Dutrow, B.L. and Henry, D.J., 2017. Fibrous Tourmaline: A Sensitive Probe of Fluid Compositions and Petrologic Environments. *The Canadian Mineralogist*, 54(1): 311-335. <http://doi.org/10.3749/canmin.1600019>
- Frikken, P.H., Cooke, D.R., Walshe, J.L., Archibald, D., Skarmeta, J., Serrano, L. and Vargas, R., 2005. Mineralogical and isotopic zonation in the Sur-Sur tourmaline breccia, Río Blanco-Los Bronces Cu-Mo deposit, Chile: Implications for ore genesis. *Economic Geology*, 100(5): 935-961. <http://doi.org/10.2113/gsecongeo.100.5>

- Galbraith, C.G., Clarke, D.B., Trumbull, R.B. and Wiedenbeck, M., 2009. Assessment of tourmaline compositions as an indicator of emerald mineralization at the Tsa da Glisza prospect Yukon Territory, Canada. *Economic Geology*, 104(5): 713-731.
<http://doi.org/10.2113/gsecongeo.104.5.713>
- Godwin, C.I., 1975. Geology of Casino Porphyry Copper-Molybdenum Deposit, Dawson Range, Y. T., University of British Columbia, Vancouver BC.
- Griffin, W.L., Slack, J.F., Ramsden, A.R., Win, T.T. and Ryan, C.G., 1996. Trace elements in tourmalines from massive sulfide deposits and tourmalinites Geochemical controls and exploration application. *Economic Geology*, 91(4): 657-675.
<http://doi.org/10.2113/gsecongeo.91.4.657>
- Hawthorne, F.C. and Dirlam, D.M., 2011. Tourmaline the Indicator Mineral: From Atomic Arrangement to Viking Navigation. *Elements*, 7(5): 307-312.
<http://doi.org/10.2113/gselements.7.5.307>
- Hazarika, P., Mishra, B. and Pruseth, K.L., 2015. Diverse Tourmaline Compositions from Orogenic Gold Deposits in the Hutti-Maski Greenstone Belt, India: Implications for Sources of Ore-Forming Fluids. *Economic Geology*, 110.
- Henry, D.J. and Dutrow, B.L., 1996. Metamorphic Tourmaline and its petrologic applications. In: Reviews in Mineralogy and Geochemistry 33(1) Boron, E.S. Grew (Editor), 503-557.
- Henry, D.J. and Guidotti, C.V., 1985. Tourmaline as a petrogenetic indicator mineral an example from the staurolite-grade metapelites of NW Maine. *American Mineralogist*, 70: 1-15.

- Henry, D.J., Novak, M., Hawthorne, F.C., Ertl, A., Dutrow, B.L., Uher, P. and Pezzotta, F., 2011. Nomenclature of the tourmaline-supergroup minerals. *American Mineralogist*, 96(5-6): 895-913. <http://doi.org/10.2138/am.2011.3636>
- Jiang, S.Y., Palmer, M.R., McDonald, A.M., Slack, J.F. and Leitch, C.H.B., 1996. Feruvite from the Sullivan Pb-Zn-Ag deposit, British Columbia. *Canadian Mineralogist*, 34: 733-740.
- Jochum, K.P., Weis, U., Stoll, B., Kuzmin, D., Yang, Q., Raczek, I., Jacob, D.E., Stracke, A., Birbaum, K., Frick, D.A., Günther, D. and Enzweiler, J., 2011. Determination of Reference Values for NIST SRM 610-617 Glasses Following ISO Guidelines. *Geostandards and Geoanalytical Research*, 35(4): 397-429. <http://doi.org/10.1111/j.1751-908X.2011.00120.x>
- Kalliomäki, H., Wagner, T., Fusswinkel, T. and Sakellaris, G., 2017. Major and trace element geochemistry of tourmalines from Archean orogenic gold deposits: Proxies for the origin of gold mineralizing fluids? *Ore Geology Reviews*, 91: 906-927. <http://doi.org/10.1016/j.oregeorev.2017.08.014>
- Kelley, K.D., Eppinger, R.G., Lang, J., Smith, S.M. and Fey, D.L., 2011. Porphyry Cu indicator minerals in till as an exploration tool: example from the giant Pebble porphyry Cu-Au-Mo deposit, Alaska, USA. *Geochemistry: Exploration, Environment, Analysis*, 11(4): 321-334. <http://doi.org/10.1144/1467-7873/10-im-041>
- Launay, G., Sizaret, S., Guillou-Frottier, L., Gloaguen, E. and Pinto, F., 2018. Deciphering fluid flow at the magmatic-hydrothermal transition: A case study from the world-class

- Panasqueira W–Sn–(Cu) ore deposit (Portugal). *Earth and Planetary Science Letters*, 499: 1-12. <http://doi.org/10.1016/j.epsl.2018.07.012>
- Lu, Y.-J., Loucks, R.R., Fiorentini, M., McCuaig, T.C., Evans, N.J., Yang, Z.-M., Hou, Z.-Q., Kirkland, C.L., Parra-Avila, L.A. and Kobussen, A., 2016. Zircon Compositions as a Pathfinder for Porphyry Cu ± Mo ± Au Deposits. *Economic Geology*, 19: 329-347.
- Manéglia, N., Beaudoin, G. and Simard, M., 2018. Indicator minerals of the Meliadine orogenic gold deposits, Nunavut (Canada), and application to till surveys. *Geochemistry: Exploration, Environment, Analysis*, 18(3): 241-251.
<http://doi.org/10.1144/geochem2017-036>
- Mao, M., Rukhlov, A.S., Rowins, S.M., Spence, J. and Coogan, L.A., 2016. Apatite Trace Element Compositions: A Robust New Tool for Mineral Exploration. *Economic Geology*, 111(5): 1187-1222. <http://doi.org/10.2113/econgeo.111.5.1187>
- Marks, M.A.W., Marschall, H.R., Schühle, P., Guth, A., Wenzel, T., Jacob, D.E., Barth, M. and Markl, G., 2013. Trace element systematics of tourmaline in pegmatitic and hydrothermal systems from the Variscan Schwarzwald (Germany): The importance of major element composition, sector zoning, and fluid or melt composition. *Chemical Geology*, 344: 73-90. <http://doi.org/10.1016/j.chemgeo.2013.02.025>
- Marschall, H.R. and Jiang, S.Y., 2011. Tourmaline Isotopes: No Element Left Behind. *Elements*, 7(5): 313-319. <http://doi.org/10.2113/gselements.7.5.313>

- McClenaghan, M.B., McCurdy, M., Beckett-Brown, C.E. and Casselman, S., 2020. Indicator mineral signatures of the Casino porphyry Cu-Au-Mo deposit, Yukon. *Geological Survey of Canada, Open File 8711*. <http://doi.org/10.4095/322191>
- McClenaghan, M.B., McCurdy, M., Garrett, R., Beckett-Brown, C.E., Leybourne, M.I., Casselman, S.G. and Pelchat, P., 2021. Heavy mineral and geochemical signatures of porphyry copper mineralization: examples from the Casino porphyry Cu-Au-Mo deposit, Yukon: in Targeted Geoscience Initiative 5: contributions to the understanding and exploration of porphyry deposits; Plouffe (ed.); Schetselaar, E (ed.); Geological Survey of Canada, Bulletin 616, 2021 p. 159-202, <https://doi.org/10.4095/327987>
- McCurdy, M., McClenaghan, M.B. and Garrett, R.G., 2019. The stream sediment geochemical signature of the Casino porphyry Cu-Au-Mo deposit, Yukon Territory: a case study. *Geological Survey of Canada, Open File 8632*. <http://doi.org/10.4095/321381>
- Novak, M., Skoda, R., Filip, J., Macek, I. and Vaculovic, T., 2011. Compositional trends in tourmaline from intragranitic NYF pegmatites of the Trebic pluton, Czech Republic: an electron microprobe, Mossbauer and LA-ICP-MS study. *The Canadian Mineralogist*, 49(1): 359-380. <http://doi.org/10.3749/canmin.49.1.359>
- Palmer, M.R., London, D., Morgan, G.B. and Babb, H.A., 1992. Experimental-Determination of Fractionation of B-11/B-10 between Tourmaline and Aqueous Vapor - a Temperature-Dependent and Pressure-Dependent Isotopic System. *Chemical Geology*, 101(1-2): 123-129. [http://doi.org/10.1016/0009-2541\(92\)90209-N](http://doi.org/10.1016/0009-2541(92)90209-N)

- Plouffe, A., Acosta-Góngora, P., Kjarsgaard, I.M., Petts, D., Ferbey, T. and Venance, K.E., 2021a. Detrital epidote chemistry: detecting the alteration footprint of porphyry copper mineralization in the Quesnel terrane of the Canadian Cordillera, British Columbia: in Targeted Geoscience Initiative 5: contributions to the understanding and exploration of porphyry deposits; Plouffe, (ed.); Schetselaar, E (ed.); Geological Survey of Canada, Bulletin 616, 2021 p. 137-157, <https://doi.org/10.4095/327988>
- Plouffe, A. and Ferbey, T., 2016. Till geochemistry, mineralogy and textural data near four Cu porphyry deposits in British Columbia. *Geological Survey of Canada, Open File 8038, and British Columbia Ministry of Energy and Mines, British Columbia Geological Survey, Geofile 2016-10, 1 .zip file.*: 44. <http://doi.org/10.4095/298805>
- Plouffe, A. and Ferbey, T., 2017. Porphyry Cu indicator minerals in till: A method to discover buried mineralization. In: T. Ferbey, A. Plouffe and A. Hicken (Editors), *Indicator Minerals in Till and Stream Sediments of the Canadian Cordillera*. Geological Association of Canada and the Mineralogical Association of Canada, Topics in Mineral Sciences, Volume 47, Geological Association of Canada, Special Paper 50, pp. 129-159.
- Plouffe, A., Wilton, D.H.C., McNeil, R. and Ferbey, T., 2021b. Automated indicator-mineral analysis of the fine-sand, heavy-mineral concentrate fraction of till: a promising exploration tool for porphyry copper mineralization in Targeted Geoscience Initiative 5: contributions to the understanding and exploration of porphyry deposits; Plouffe, (ed.); Schetselaar, E (ed.); Geological Survey of Canada, Bulletin 616, 2021 p. 203-223, <https://doi.org/10.4095/327991>

- Raczek, I., Stoll, B., Hofmann, A.W. and Peter Jochum, K., 2001. High-Precision Trace Element Data for the USGS Reference Materials BCR-1, BCR-2, BHVO-1, BHVO-2, AGV-1, AGV-2, DTS-1, DTS-2, GSP-1 and GSP-2 by ID-TIMS and MIC-SSMS. *Geostandards and Geoanalytical Research*, 25(1): 77-86. <http://doi.org/10.1111/j.1751-908X.2001.tb00789.x>
- Sciuba, M., Beaudoin, G. and Makvandi, S., 2021. Chemical composition of tourmaline in orogenic gold deposits. *Mineralium Deposita*, 56(3): 537-560. <http://doi.org/10.1007/s00126-020-00981-x>
- Sinclair, W.D. and Richardson, J.M., 1992. Quartz-Tourmaline Orbicules Batholith, in the Seagull Yukon Territory. *Canadian Mineralogist*, 30: 923-935.
- Slack, J.F., 1996. Tourmaline Associations with Hydrothermal Ore Deposits. In: L.M. Anovitz and E.S. Grew (Editors), Boron. Reviews in Mineralogy and Geochemistry. Mineralogical Society of America, Oak Ridge, Tennessee, USA, pp. 559-644. <http://doi.org/10.1515/9781501509223-013>
- Slack, J.F. and Coad, P.R., 1989. Multiple hydrothermal and metamorphic events in the Kidd Creek volcanogenic massive sulphide deposit, Timmins, Ontario: Evidence from tourmalines and chlorites. *Canadian Journal of Earth Sciences*, 26(4): 694-715. <http://doi.org/10.1139/e89-059>
- Slack, J.F. and Trumbull, R.B., 2011. Tourmaline as a Recorder of Ore-Forming Processes. *Elements*, 7(5): 321-326. <http://doi.org/10.2113/gselements.7.5.321>

Slack, J.F.P., M. R.; Stevens, B. P.; Barnes, R. G.; , 1993. Origin and significance of tourmaline-rich rocks in the Broken Hill district, Australia. *Economic Geology*, 88(3): 505-541.

<http://doi.org/10.2113/gsecongeo.88.3.505>

Slack, J.F.R., A.R.; Griffin, W.L.; Win, T. T.; French D. H.; Ryan, C. G., 1999. Trace Elements in Tourmaline from the Kidd Creek Massive Sulfide Deposit and Vicinity, Timmins, Ontario A Proton Microprobe Study in: The Giant Kidd Creek Volcanogenic Massive Sulfide Deposit, Western Abitibi Subprovince, Canada. *Economic Geology Monograph*, Hannington, M.D. and Barrie, C.T. (editors), volume 10: pp. 415-429.

<http://doi.org/10.5382/mono.10.16>

Trumbull, R.B., Garda, G.M., Xavier, R.P., Cavalcanti, J.A.D. and Codeço, M.S., 2018.

Tourmaline in the Passagem de Mariana gold deposit (Brazil) revisited: major-element, trace-element and B-isotope constraints on metallogenesis. *Mineralium Deposita*, 54(3): 395-414. <http://doi.org/10.1007/s00126-018-0819-z>

van Hinsberg, V.J., Henry, D.J. and Dutrow, B.L., 2011a. Tourmaline as a Petrologic Forensic Mineral: A Unique Recorder of Its Geologic Past. *Elements*, 7(5): 327-332.

<http://doi.org/10.2113/gselements.7.5.327>

van Hinsberg, V.J., Henry, D.J. and Marschall, H.R., 2011b. Tourmaline: an ideal indicator of its host environment. *The Canadian Mineralogist*, 49(1): 1-16.

<http://doi.org/10.3749/canmin.49.1.1>

Wilkinson, C.C., Cooke, D.R., Baker, M.J. and Wilkinson, J.J., 2020. Exploration Targeting in Porphyry Cu Systems Using Propylitic Mineral Chemistry: A Case Study of the El

Teniente Deposit, Chile. *Economic Geology*, 115(4): 771-791.

<http://doi.org/10.5382/econgeo.4738>

Wilkinson, J.J., Chang, Z., Cooke, D.R., Baker, M.J., Wilkinson, C.C., Inglis, S., Chen, H. and Bruce Gemmell, J., 2015. The chlorite proximator: A new tool for detecting porphyry ore deposits. *Journal of Geochemical Exploration*, 152: 10-26.

<http://doi.org/10.1016/j.gexplo.2015.01.005>

Xu, L., Bi, X., Hu, R., Tang, Y., Wang, X. and Xu, Y., 2014. LA-ICP-MS mineral chemistry of titanite and the geological implications for exploration of porphyry Cu deposits in the Jinshajiang – Red River alkaline igneous belt, SW China. *Mineralogy and Petrology*, 109(2): 181-200. <http://doi.org/10.1007/s00710-014-0359-x>

Yavuz, F., Iskenderoglu, A. and Jiang, S.Y., 1999. Tourmaline compositions from the Salikvan porphyry Cu-Mo deposit and vicinity, northeastern Turkey. *Canadian Mineralogist*, 37: 1007-1023.

Yavuz, F., Karakaya, N., Yildirim, D.K., Karakaya, M.Ç. and Kumral, M., 2014. A Windows program for calculation and classification of tourmaline-supergroup (IMA-2011).

Computers & Geosciences, 63: 70-87. <http://doi.org/10.1016/j.cageo.2013.10.012>

Zhao, H.-D., Zhao, K.-D., Palmer, M.R. and Jiang, S.-Y., 2019. In-situ elemental and boron isotopic variations of tourmaline from the Sanfang granite, South China: Insights into magmatic-hydrothermal evolution. *Chemical Geology*, 504: 190-204.

<http://doi.org/10.1016/j.chemgeo.2018.11.013>

Chapter 5

5 The missing link between biotite and tourmaline in porphyry systems

5.1 Abstract

At the Casino porphyry Cu-Au-Mo deposit (Yukon Territory-Canada), partial and complete replacements of biotite by tourmaline are observed. Biotite occurs as euhedral, 1-2 mm scale, equant books partially replaced by tourmaline preferentially along planes of cleavage. Atypical internal zonation patterns (zonation that forms irrespective to the *c*-axis) are observed in tourmaline (in both plane-polarized light and backscattered electron imaging) which do not reflect more typical zonation patterns (*i.e.*, oscillatory, sector, or concentric). These features are linear and follow the cleavage direction of the enclosing biotite grains suggesting they are one in the same. Chemical analyses of biotite grains show they are Mg-rich, classifying as phlogopite $(\text{K}_{0.85}\square_{0.08}\text{Ba}_{0.04}\text{Na}_{0.03})_{\Sigma=1}$ $(\text{Mg}_{1.72}\text{Fe}^{2+}_{0.49}\text{Al}_{0.36}\text{Ti}_{0.22}\text{Fe}^{3+}_{0.17})_{\Sigma=2.96}(\text{Si}_{2.81}\text{Al}_{1.11}\text{Fe}^{3+}_{0.08})_{\Sigma=4}(\text{OH}_{1.79}\text{F}_{0.21}\text{Cl}_{0.02})_{\Sigma=2}$ while tourmaline analyses are equally Mg-rich with samples classifying as dravite $(\text{Na}_{0.68}\square_{0.23}\text{Ca}_{0.09}\text{K}_{0.01})_{\Sigma=1.01}(\text{Mg}_{1.71}\text{Fe}_{0.93}\text{Al}_{0.24}\text{Ti}_{0.11})_{\Sigma=3}(\text{Al}_{5.96}\text{Mg}_{0.04})_{\Sigma=6}$ $(\text{Si}_{5.94}\text{Al}_{0.06})_{\Sigma=6}\text{O}_{18}(\text{BO}_3)_3(\text{OH})_3(\text{OH}_{0.98}\text{F}_{0.02})_{\Sigma=1}$. Partially replaced biotite has a *Mg#* of 0.61 and tourmaline, which is texturally replacing that same biotite has a *Mg#* of 0.66. Regions of tourmaline crystals show atypical zonation reflecting and are chemically distinct, reflecting the replaced biotite. The unreacted biotite contains elevated Ti values of 0.22 *apfu avg.* while the tourmaline replacing the biotite contains nearly identical Ti of 0.23 *apfu avg.* Here we present an explanation of the origin of some tourmaline in porphyry systems by the addition of a boron-

bearing fluid to rocks containing earlier formed biotite and plagioclase feldspar. The reaction is summarized here: $\text{K}(\text{Mg,Fe})_3\text{AlSi}_3\text{O}_{10}(\text{OH})_{2(s)} + 4(\text{Na,Ca})\text{Al}_2\text{Si}_2\text{O}_8(s) + 3\text{H}_3\text{BO}_3(\text{aq}) + 5\text{H}^+ \leftrightarrow (\text{Na,Ca})(\text{Mg,Fe})_3\text{Al}_6\text{Si}_6\text{O}_{18}(\text{BO}_3)_3(\text{OH})_{4(s)} + \text{KAl}_3\text{Si}_3\text{O}_{10}(\text{OH})_{2(s)} + 2\text{SiO}_2(s) + 5\text{H}_2\text{O}(l) + 3(\text{Na,Ca}) + 0.5\text{O}_2$. The observations made and the proposed mechanism of replacement are consistent with results from experimental data and provides an important link between biotite and tourmaline in mineralized porphyry systems *via* a simple replacement reaction. This explanation for the formation of atypical zonation in tourmaline is not only important for the biotite-tourmaline relationship in porphyry systems but in other environments as well.

5.2 Introduction

Porphyry deposits are high tonnage, low-grade deposits that contribute significant Cu (>70%) and additional Mo and Au production worldwide (Sillitoe 2010; Arndt *et al.* 2017). Deposits are concentrated in continental arcs and are important indicators of subduction-related processes (Sillitoe 1972; Richards 2003; Sillitoe 2010). Deposits exhibit predictable mineralogical and chemical zonation patterns reflected in their alteration assemblages (Cooke *et al.* 2014). Biotite (Bt) and tourmaline supergroup minerals (TSM) are common accessory phases in mineralized porphyry systems (Sillitoe and Sawkins 1971; Vargas *et al.* 1999; Skewes *et al.* 2003; Frikken *et al.* 2005; Sillitoe 2010; Beckett-Brown *et al.* 2021a, 2021b, 2021c). For example, at the Rio Blanco-Los Bronces district, biotite and/or TSM-bearing breccias contain the bulk of the Cu (chalcopyrite and bornite) mineralization (Skewes *et al.* 2003). Both phases have been identified as important mineralogical components in early-developed breccias within the deeper parts of the porphyry system (Sillitoe 2010), with early (deep) breccias containing Bt whereas later (higher level) ones commonly contain TSM as a cement (Sillitoe 2010). In rare cases, dumortierite (an alkali-deficient borosilicate) can form in the highest portions of a porphyry system (Clark 1995;

Arancibia and Clark 1996). Thus, there appears to be a mineralogical relationship between Bt, TSM, and dumortierite in these systems. Although TSM and dumortierite are the only phases that contain essential boron in relatively high concentrations (between 6 - 11 wt. % B_2O_3), Bt has been documented to contain minor concentrations of B (<100 ppm) (Tonarini *et al.* 2003; Xiang *et al.* 2020). Breccias containing Bt as a cement are slightly paragenetically older and/or form deeper than breccias that contain abundant TSM cement (Skewes *et al.* 2003). There are cases where Bt and TSM are reported to coexist in the matrix of these breccias but no direct evidence for replacement has been observed to date (Skewes *et al.* 2003). It has been suggested that TSM may pseudomorphically replace magmatic Bt and hornblende (Warnaars *et al.* 1985; Skewes *et al.* 2003; Frikken *et al.* 2005) but documenting this replacement of Bt by TSM dominated breccias is challenging due to the fine-grained nature of these minerals (Frikken *et al.* 2005). Equally, there are reports that refute the replacement of Bt by TSM, and state that there is no textural evidence of this replacement and rather their formation is stated to be contemporaneous (Vargas *et al.* 1999).

The purpose of the current study is to investigate the nature of the relationship of Bt and TSM intergrowths in a mineralized porphyry deposit, using the Casino samples, which are unique in that they provide a snapshot of the incomplete Bt-TSM reaction. Three aspects are included in this study: 1) documentation of the relationship between Bt and TSM, 2) interpretation of internal and external textural relationships of these minerals (including morphology, grain size, inclusions, and internal zonation), and 3) integration of the major and minor element variation between coexisting Bt and TSM. The goal of this research is to evaluate the significance of this relationship and to comment on its implications for the evolution of porphyry systems.

5.3 The Casino Deposit

5.3.1 Background Geology

The Casino porphyry Cu-Au-Mo deposit is located ~300 km NW of Whitehorse, Yukon Territory, Canada (Figure 5-1a). It is hosted in a stockwork of late Cretaceous quartz monzonite and includes a number of recognized breccias, all of which belong to the Casino complex (Casselman and Brown 2017). Five principal units are recognized, including the Dawson Range (a phase of the Whitehorse suite) along with four units of the Casino suite. The Casino suite units include the Patton Porphyry, Intrusion Breccia, Explosion Breccia, and Patton Dikes (Casselman and Brown 2017). The bulk of mineralization is hosted in rocks of the Dawson Range, Paton Porphyry, and Breccia rocks (Casselman and Brown 2017). The Dawson Range unit, the main country rocks of the Casino deposit, ranges from biotite-hornblende granodiorite to diorite. The Paton Porphyry is a hypabyssal intrusion containing phenocrysts primarily of plagioclase (An_{47}) with lesser amounts of biotite, hornblende, quartz and opaques (Casselman and Brown 2017).

5.3.2 Sample Material and Mineralogy

Two rock samples containing TSM are investigated (Figure 5-1b), the first (CEBB-012) collected from the periphery of the deposit within the Dawson Range granodiorite which represents a snapshot of the incomplete partial reaction and the second (CEBB-005) from an intrusive breccia close to the core of the deposit that reflects the completed reaction (Figure 5-2).

The first sample (Sample CEBB-012: Figure 5-2a) comes from the periphery of the deposit within the Dawson Range batholith from the diamond drill hole CAS-035, at a depth of 153.92 m. A fresh sample of the Dawson Range is presented for comparison (Figure 5-2b). Sample CEBB-005 is a granodiorite from the phyllic alteration zone, mineralogically it consists of

quartz, plagioclase (An₄₇) feldspars (sericite altered), Bt, and TSM. The TSM occurs throughout the sample as TSM-Py veins and also replacing biotite books and relict feldspar grains (Figure 5-3a-e). The TSM selectively, in some rarer cases completely, replaces primary magmatic Bt exhibiting replacement textures. The replacement of Bt occurs along cleavage planes in association with muscovite, chlorite, and quartz. Minor rutile is also present along cleavage planes in biotite and muscovite and forms inclusions in TSM. Biotite in polished thin section (PTS) under transmitted light (TL) forms euhedral porphyritic books 0.2 x 0.25 mm in size. Grains are pleochroic tan-brown to pale brown and exhibit moderate alteration preferentially along cleavage planes by muscovite, chlorite, ribbons of dolomite, and TSM. Biotite contains abundant inclusions of rutile, texturally occurring along cleavage planes suggesting its exsolution from biotite. Grains of TSM form as sub- to euhedral prismatic grains along the cleavage plane of Bt grains. Grain size is variable but in general grains are 75 x 250 µm. The TSM are pleochroic light brown to brown and pale-green to green when viewed perpendicular to the *c*-axis. Grains are concentrically zoned with darker greenish-brown cores and light blue-green rims. Some TSM grains show minor porosity development. Patchy zones of muscovite (Ms) replacing Bt are noted, typically along cleavage planes of Bt. Its occurrence is most common around the rim of Bt books (Figure 5-3b). Chlorite is unremarkable in its appearance, forming along cleavage planes in Bt as colorless non-pleochroic grains in PPL (Figure 5-3b). In addition to TSM replacing Bt, TSM are also found (less commonly) forming in regions of altered plagioclase feldspars (Figure 5-3e). For the most part these feldspar grains are entirely replaced by white micas, but some less altered grains still exhibit polysynthetic twinning.

The second sample (CEBB-005) is a hydrothermal breccia (Figure 5-2c) from drill hole 93-177 at a depth of 200.33 m. It is a clast-supported breccia with a TSM>Qz cement and minor

disseminated pyrite (~1 modal %). The breccia clasts are of the surrounding quartz monzonite Paton Porphyry wall rock. Most TSM are restricted to the breccia cement, but minor amounts of TSM are also observed replacing the edges of breccia clasts and infill fractures. Regions in the breccia cement dominated by TSM show parallel features, in terms of transmitted light color, and outline a euhedral rectangular shape (Figure 5-4a-c). Here TSM forms as sub- to euhedral prismatic 300 x 50 μ m grains. In PPL grains are weakly colored and are pleochroic from colorless to brownish green. Concentric zoning is present from brownish green cores to lightly colored to colorless rims. There is minor porosity development in the cores of the TSM grains. Muscovite is difficult to identify in PPL but occurs as colorless interstitial grains to quartz and TSM grains. Muscovite forms growing off the grain boundaries of TSM and quartz grains. Rutile is also observed, only in regions that contain TSM. Rutile forms as euhedral, equant grains, ~25 μ m in size and is spatially associated with the linear TSM textures as inclusions in both TSM and quartz. No Bt is observed in this sample.

5.3.3 Chemical Zonation

The chemical zonation observed in TSM from sample one is atypical (Figure 5-5a, Figure 5-6b) in that it forms irrespective to the *c*-axis unlike the more common concentric zoning observed in TSM (Figure 5-5c). The zonation here develops in linear patches perpendicular to the *c*-axis (denoted by the bright BSE zones) and follows the basal cleavage direction of the adjacent Bt grains (Figure 5-5a). There is some minor concentric zoning development, but its occurrence is minor.

Sample CEBB-005 shows compositional variation in the form of concentric zonation in sample two (Figure 5-5c, d). The core exhibits a dark BSEI tone which reflects the low Fe and high Al-Mg concentrations while the intermediate zones are brighter and contain higher Fe values and in

turn lower Mg-Al concentrations. A closer look at the intermediate zone (Figure 5-5c) there exists an additional zonation type which cross-cuts the concentric zonation oriented perpendicular to the *c*-axis. A macro view of TSM from this sample shows linear features denoted by the presence of TSM and their orientation as well as bright BSEI features oriented along the same direction (Figure 5-6a, b).

5.4 Methods: Major and Minor Element Chemistry

Tourmaline, biotite, and muscovite in one polished thin section of each bedrock sample were analyzed at the Ontario Geoscience Laboratories (Sudbury, Ontario) using a Cameca SX-100 electron microprobe equipped with five wavelength dispersive spectrometers. The instrument was operated at 20 kV, 10 nA, and a 5 μm beam raster for biotite, muscovite, and chlorite with an increased beam current for TSM of 20 nA due to their stability under the beam. Calibration standards include albite ($\text{SiK}\alpha$, $\text{AlK}\alpha$, $\text{NaK}\alpha$), orthoclase ($\text{KK}\alpha$), diopside ($\text{MgK}\alpha$, $\text{CaK}\alpha$), tugtapite ($\text{ClK}\alpha$), and synthetics Fe_2O_3 ($\text{FeK}\alpha$), MnTiO_3 ($\text{MnK}\alpha$), SrTiO_3 ($\text{TiK}\alpha$), V_2O_5 ($\text{VK}\alpha$), Cr_2O_3 ($\text{CrK}\alpha$), BaF_2 ($\text{FK}\alpha$), ZnS ($\text{ZnK}\alpha$). Data reduction was carried out using the PAP phi-rho-z correction scheme was applied to all data. All elements were analyzed for 15 s (peak and background) except F (30 s).

Chemical formulae were calculated on the basis of 15 cations using WinTcac (Yavuz *et al.* 2014). Grains of TSM are strongly zoned, as such, analyses of different chemical zones were made oriented both perpendicular and parallel to the *c*-axis to accurately represent the variation of chemistry. Analyses of biotite, muscovite, and chlorite were preferentially acquired in regions oriented perpendicular to the *c*-axis when possible. Biotite and muscovite data were recalculated based on 22 O and calculated H_2O and OH based on $\text{OH} = 4 - (\text{Cl} + \text{F})$. Iron valence were

calculated based on the sum charge contribution, with Fe^{3+} used to balance the sum. Magnesium number ($Mg\#$) were calculated from $\text{Mg}/(\text{Mg}+\text{Fe})$ *apfu* values.

5.5 Results

5.5.1 Biotite

The average major element composition for biotite grains ($n = 10$) from sample one is shown in Table 5-1. The biotite grains are Mg dominant, with the average chemical formula of

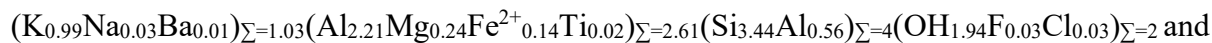


$(\text{Mg}_{1.72}\text{Fe}^{2+}_{0.49}\text{Al}_{0.36}\text{Ti}_{0.22}\text{Fe}^{3+}_{0.17})_{\Sigma=2.96}(\text{Si}_{2.81}\text{Al}_{1.11}\text{Fe}^{3+}_{0.08})_{\Sigma=4}(\text{OH}_{1.77}\text{F}_{0.21}\text{Cl}_{0.02})_{\Sigma=2}$ indicating they are phlogopite. The grains also have elevated Ti values 0.22 *apfu avg.* (range: 0.21-0.23) as well as F values 0.21 *apfu avg.* (range: 0.18-0.27) and a constant $Mg\#$ 0.72 *avg.* (range: 0.69-0.71).

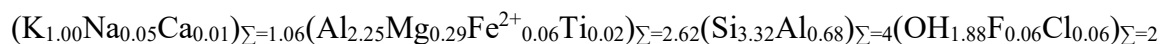
Additionally, grains contain a small proportion (~33%) of total Fe as Fe^{3+} with 0.24 *apfu avg.* (range: 0.18-0.31). Biotite chemistry is comparable (*e.g.*, $Mg\#$ values ~0.69, 0.25 Ti *apfu*, 0.15 F *apfu*) to that observed at other porphyry systems (Jacobs and Parry 1979; Afshooni *et al.* 2013).

5.5.2 Muscovite

The average major element composition for muscovite grains from sample one ($n = 9$) and sample two ($n = 3$) is shown in Table 5-2. The muscovite grains from both samples are phengite-rich with the average chemical formulas of sample 1:



and sample 2:



respectively. The chemistry of the muscovite grains between the two samples is remarkably.

5.5.3 Tourmaline

The TSM major- and minor-element concentrations are more variable than the other minerals analyzed in this study (Table 5-3). Sample one analyses results in the average formula of



$(\text{Si}_{5.94}\text{Al}_{0.06})_{\Sigma=6}\text{O}_{18}(\text{BO}_3)_3(\text{OH})_3(\text{OH}_{0.98}\text{F}_{0.02})_{\Sigma=1}$ corresponding to dravite. Zones showing atypical zonation (*i.e.*, zonation perpendicular to *c*-axis) exhibit a distinguishable chemistry from areas without. Notably, variations (atypical/normal) in Ti (0.23/0.06 *apfu avg.*), Al (5.86/6.47 *apfu avg.*), Fe (1.13/0.73 *apfu avg.*), and *Mg#* (0.61/0.71) differentiate these regions. Sample 2 analyses results in the average formula of



$(\text{Si}_{5.94}\text{Al}_{0.06})_{\Sigma=6}\text{O}_{18}(\text{BO}_3)_3(\text{OH})_3(\text{OH}_{0.96}\text{F}_{0.04})_{\Sigma=1}$ corresponding to dravite. Regions of bright BSE intensity are separated from darker ones, notably variations (bright/darker) in Al (6.20/6.58 *apfu avg.*), Mg (1.88/2.08 *apfu avg.*), Fe (0.88/0.33 *apfu avg.*), and *Mg#* (0.69/0.86) differentiate these regions.

The chemical data shows that based on occupancy of the X-site, the TSM analyzed plots into the alkali-dominant field (*i.e.*, Na dominant). The vacancy content is elevated for the two samples (0.23 and 0.16 respectively), potentially reflecting a lack of available Na. The greatest compositional variation in terms of major and minor element chemistry is observed in the *Y*- and *Z*- crystallographic sites (Figure 5-7a). In terms of *Mg#*, sample one contains a lower average value of 0.66 (range: 0.53-0.84), whereas sample two has a higher average value (0.75) as well as a wider range (0.53-0.97). This higher range is reflected at the individual grain scale (Figure 5-7). Calculated Fe^{2+} and Fe^{3+} contents show a dearth of Fe^{3+} contents with only two analyses

containing any $\text{Fe}^{3+}_{(\text{calc})}$. Concentrations of Ti in TSM are slightly higher in sample one (0.11 *apfu avg.*) than sample two (0.05 *apfu avg.*) (Figure 5-7b). Significantly more rutile is associated with sample two than sample one.

5.6 Discussion

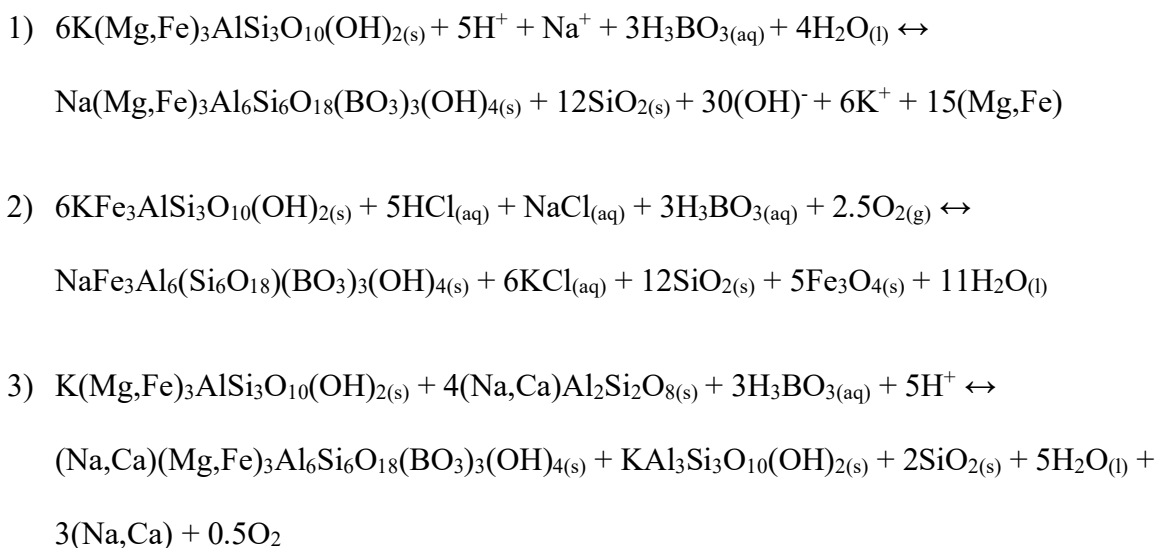
Biotite has been documented to contain minor concentrations of B (<100 ppm), which are not enough to crystallize TSM, and thus an external source of B is required. Experimental investigation demonstrates that an increase in B_2O_3 contents of melts can lead to the replacement of Bt by TSM (Orlando *et al.* 2017; Cheng *et al.* 2019). Orlando *et al.* (2017) used experiments to explain the tourmalinization of a Bt-schist by magmatic fluids. These authors showed that a Bt-rich rock in the presence of H_3BO_3 and a range in fluid compositions (NaCl or H_2O dominant) can result in the formation of TSM at moderate temperatures (500-600 °C, 100-130 MPa). Results showed a positive correlation between decreasing primary Bt modal abundance and increasing TSM produced. The composition of the starting Bt (*Mg#* 0.30) in combination with the associated fluid composition, affected the resulting TSM chemistry. Dravite-rich TSM (*Mg#* 0.77) formed in a salty fluid (20 wt. % NaCl) whereas more schorlitic (Fe-rich) TSM (*Mg#* 0.45) formed in alkali-absent H_2O fluids (Orlando *et al.* 2017). No atypical TSM internal textures were presented. It was also found that the Bt-TSM reaction led to the production of excess Fe producing Fe-oxides (*e.g.*, magnetite). Additionally, albite was produced in the NaCl- H_2O experiment, whereas K-feldspar was produced in the H_2O experiment (Orlando *et al.* 2017). This experimental research was presented to support the formation of TSM at the expense of Bt in the Mt. Calamita Formation, Elba Island, Italy (Orlando *et al.* 2017).

A more recent study that exposed a two-mica granite to B-rich fluids over a range of T (600 and 700 °C) also showed that TSM was formed (Cheng *et al.* 2019). Embayed shapes on plagioclase grains suggest it was a reactant in the TSM producing reaction. Minimal to no Bt remained in the experiment products, but when observed it showed reaction textures and was strongly decomposed (Cheng *et al.* 2019). The experiment produced schorl-rich TSM, this is likely dependent on the composition of the primary Bt which was annite (Fe-rich). The composition of the starting Bt had a $Mg\#$ of 0.27, similar to the resulting 0.34 in the TSM produced through the reaction. Results from the experiments of Orlando *et al.* (2017) and Cheng *et al.* (2021) show a trend from Bt in the reactants with lower $Mg\#$ and trends to higher $Mg\#$ in the resulting TSM reflecting an increase in Mg and a decrease in Fe concentrations.

The conversion of Bt to TSM, in the presence of excess boron, is also supported by the experiments of van Hinsberg (2011), specifically designed to investigate trace-element partitioning. As opposed to the previous experiments discussed, van Hinsberg (2011) used magmatic biotite and pegmatite-derived TSM in the mass ratio of 2:98 and subjected that to 800 °C and 7.5 kbar for 2 hours. One important outcome of that research was the observation of an absence of Bt in the product suggesting Bt was consumed in the TSM forming reaction as well as the production of Fe-rich spinels. The $Mg\#$ of the starting Bt was 0.79 (*avg.*) and that of the initial TSM was 0.37. Interestingly, the $Mg\#$ of the secondary TSM was found to be 0.63, distinctly different from that of the primary TSM. The Al content was also drastically different from the starting TSM to the newly formed TSM with values of 4.94 and 5.96 *apfu* respectively. No noteworthy internal TSM textures were observed.

The potential for the conversion of Bt to TSM has thus been demonstrated experimentally, but to date, few have recognized this phenomenon in nature. One example of this has been presented by

London (2016). The author presents a BSE image of Bt and TSM and suggests that TSM growth is at the expense of Bt, although no mechanism by which the reaction may occur has been proposed. Nabelek (2021) presented tourmalinite bound quartz veins whereby TSM has almost completely replaced minerals in the host schist (including biotite, muscovite, and plagioclase). Specifically, the TSM *Mg#* (~0.5) is fairly consistent and higher than the precursor Bt at 0.37. Mass-balance presented by the authors suggested the metasomatic fluid introduced $B(OH)_3$ and H^+ while removing K^+ , SiO_2 , and some Fe^{2+} during the tourmalinization process (Nabelek 2021). The conversion of Bt to TSM in the presence of a boron-bearing fluid is clear based on the experiments and natural examples presented above. Thus, we can consider some reactions for this conversion based on experiments and the observations of natural samples presented here.



Reaction (1) proposed from Orlando *et al.* (2017) suggesting the reaction of 6 moles of biotite in the presence of a boron fluid produces 1 mole of TSM and 12 moles of quartz. Reaction (2) from Frikken *et al.* (2005) proposed a reaction of biotite (annite) to TSM (schorl) to constrain the lower limit of f_{O_2} for breccias in the Rio Blanco-Los Bronces region. This reaction converts 6 moles of biotite in the presence of boron bearing salty fluid, which produces 1 mole of TSM, 12

moles of quartz, and 5 moles of magnetite. Reactions 1 and 2 are similar in that they produce large volumes of excess Fe and/or Mg which is not observed in the samples from this study. Additionally, the textural evidence presented in this study (discussed further below) does not support the conversion of 6 moles of Bt to 1 mole of TSM. Based on the textural observations and the associated mineralogy observed in the samples examined we propose an alternative reaction. Reaction (3) is the conversion of 1 mole of Bt to 1 mole of TSM in the presence of 4 moles of plagioclase feldspar while also producing 1 mole of muscovite and 2 moles of quartz. This simple 1:1 conversion more elegantly explains the atypical zonation features presented here. The atypical (zoning irrespective of *c*-axis orientation) internal chemical zonation patterns (*i.e.*, not concentric, oscillatory, or sector or a combination thereof) of TSM are not understood. Textures such as Fig. 2b in Baksheev *et al.* (2010) show atypical TSM zoning, where the authors suggest that later aggregates of TSM enclose earlier grains to form unified crystals, possibly suggesting the replacement of an earlier phase such as Bt. A natural example from London (2016; Fig 5b) shows two generations of TSM, whereby the second generation of TSM overgrows a grain of Bt while still reflecting some of the cleavage traces, now reflected as chemical zonation within the TSM. Further evidence supporting TSM replacing pre-existing mica foliation that is now reflected as chemical zonation in the core of a TSM grain can be found in van Hinsberg *et al.* (2017; Fig. S-2). Similar mica replacement textures can also be observed under PPL, with mica-shaped features (denoted by color difference) enclosed within a larger TSM crystals (Spránitz *et al.* 2018; their Fig. 4b). Results from sample one of this current study show similar complicated internal zonation patterns (Figure 5-5a, b), which do not reflect more typical zonation patterns (*i.e.*, oscillatory, sector, *etc.*). These zonation patterns can be observed as color changes in PPL (Figure 5-3c) but also in BSEI (Figure 5-5a, b). These zoning features

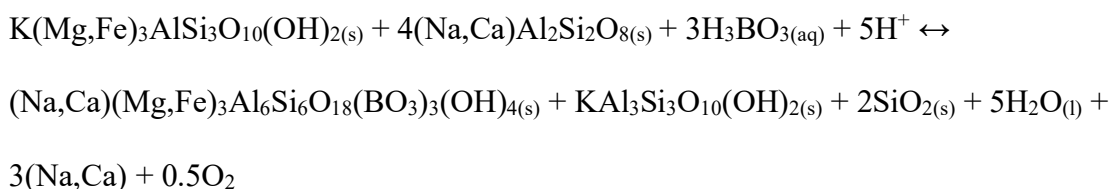
are linear and follow the cleavage direction of the enclosing/relic Bt grains suggesting they are one in the same. Chemically, these atypical zonation features are differentiated by their chemistry, most notably the difference in Ti values from 0.23 in the atypical zones and 0.06 *apfu* *avg.* in regions without zonation. Titanium is generally incorporated into Bt at higher temperatures and the subsequent TSM forming from a reaction with such Bt would also contain elevated concentrations of Ti. There also exists an abundance of rutile inclusions along cleavage planes of Bt and within the TSM replacing it. A closer examination of Figure 5-5c, 5d, in sample two shows an absence of the same features presented above, there does exist bright zones within TSM grains that define parallel zones. Rutile, although not part of the reaction, is commonly observed alongside the Bt-TSM relationship from sample one (Figure 5-5a, b). Of interest, in sample two, rutile is only observed in regions containing TSM exhibiting the linear zonation features outlined above (Figure 5-6a) supporting biotite as a precursor phase. In addition to similar zonation features and TSM chemistry between samples, the muscovite chemistry is remarkably similar associated with TSM suggesting a similar genesis.

Biotite in the Casino deposit (Selby and Nesbitt 2000) is enriched in Mg, Al, Si, F, and Cl and contains lower Ti, Ba, and Mn concentrations compared to least altered, Bt observed outside of the deposit (Selby and Nesbitt 2000). The initial *avg.* Mg# for magmatic Bt grains in the Dawson Range is 0.45 (Selby and Nesbitt 2000). The Bt presented in this study is comparable to that previously examined at Casino. Partially replaced Bt has a Mg# of 0.72 and coexisting TSM that replaces the Bt has a Mg# of 0.66. The elevated vacancy content of sample one (0.23 *apfu*) draws attention in that it suggests the fluid was depleted or lacking sufficient Na to fill the X-site. Similar results were observed during the experiments of Orlando *et al.* (2017) whereby the runs without a salty fluid had on average lower Na and in turn higher vacancy values.

In porphyry deposits, breccias with a matrix dominated by Bt are generally older and/or deeper than breccias with abundant TSM (Sillitoe 2010). Specifically, there exists a mineralogical transition from 1) Bt dominated matrix to, 2) TSM dominated (Figure 5-8). Given the observations and data from this current study, the implications are that the transition from early Bt breccias to TSM breccias could simply be the lag time for B-rich fluids to be concentrated from crystal fractionation. Once a fluid becomes saturated in boron, it can react with Bt in the presence of feldspars to produce TSM. Additionally, this reaction can help explain some of the issues surrounding a hydrothermal fluid carrying high concentrations of Fe, Mg, and Al required to form large volumes of TSM as observed in some deposits (*e.g.*, Rio Blanco-Los Bronces district).

5.7 Conclusions

In mineralized porphyry deposits, Bt and TSM are shown to have an intimate relationship whereby early magmatic or hydrothermal Bt has been partially or completely converted to TSM. This process is simplified by the equation:



Two samples from this investigation illustrate this process, either partially (sample one) or completely (sample two). Textural observations of co-existing Bt and TSM are the most compelling evidence for this replacement reaction highlighted by the internal textures of TSM from sample one. Internal textures of TSM show linear zonation features parallel to the basal cleavage of the adjacent Bt grain it is replacing. This reaction is supported by experimental

observations (Orlando *et al.* 2017; Cheng *et al.* 2019). The $Mg\#$ values of coexisting Bt-TSM are similar with Bt values of 0.72 and TSM values of 0.66. Zones showing atypical zonation (*i.e.*, zonation perpendicular to c -axis) exhibit a distinguishable chemistry from areas without. Notably, variations (atypical/normal) in Ti (0.23/0.06 *apfu avg.*), Al (5.86/6.47 *apfu avg.*), Fe (1.13/0.73 *apfu avg.*), and $Mg\#$ (0.61/0.71) differentiate these regions, with atypical regions exhibiting chemical variations similar to the enclosing adjacent Bt.

This explanation for the formation of atypical zonation in TSM is not only important for the Bt-TSM relationship in porphyry systems but other environments as well. Whereby we present an example of the incomplete reaction supporting the notion that TSM can replace a pre-existing phase while retaining some chemical and morphological remnants of the primary phase.

Finally, the identification of this relationship has implications for the understanding of Bt and TSM in mineralized porphyry systems. In breccias specifically, there exists a mineralogical transition from Bt dominated matrix to TSM dominated. The reaction of converting Bt in the presence of feldspars and a boron bearing fluid producing TSM, muscovite, and quartz could explain the relationship between Bt and TSM in these systems. It could also explain the lack of TSM in some porphyry systems whereby they did not contain sufficient Bt (or other mafic minerals) to crystalize TSM in the presence of a boron-bearing fluid.

Figure 5-1: Sample locations.

a) Location of the Casino deposit (Yukon Territory, Canada), and the regional bedrock geology modified after McClenaghan *et al.* (2021). b) Casino deposit bedrock map after Casselman and Brown (2017) showing the location of the investigated samples.

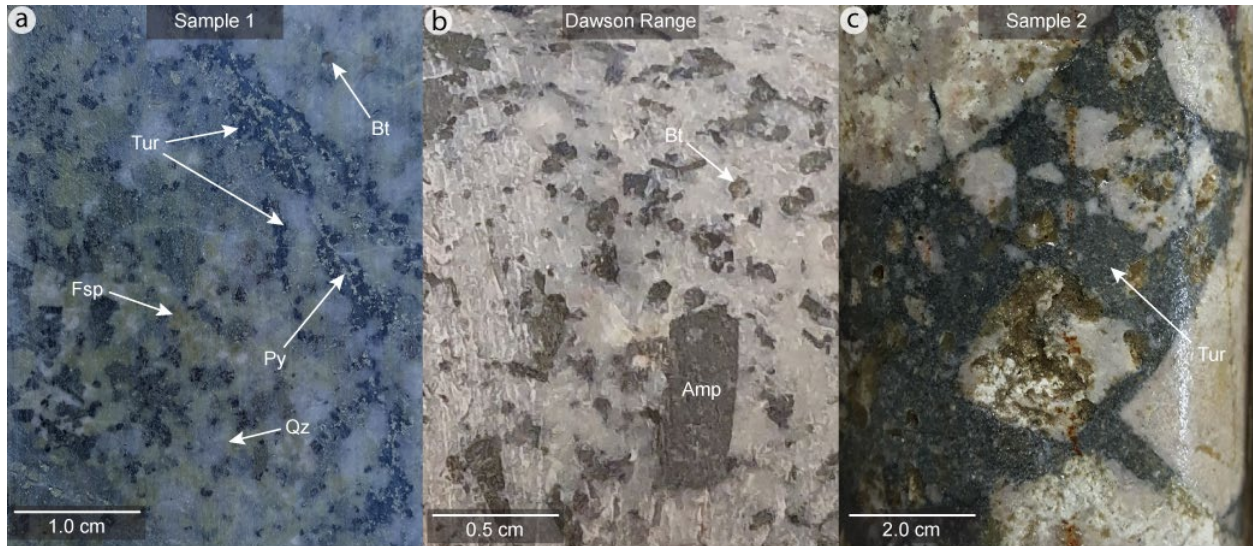


Figure 5-2: Hand sample photos.

Hand sample photographs. a) Sample 1 showing the relationships between the major mineral phases tourmaline (Tur), biotite (Bt), and pyrite (Py). The white mineral is quartz (Qz) and the yellowish phase is sericite altered feldspars (Fsp). b) Dawson Range granodiorite with porphyritic biotite (Bt) and amphibole (Amp), which is the unaltered equivalent of sample 1. c) Sample 2 consisting of a tourmaline-quartz cemented breccia.

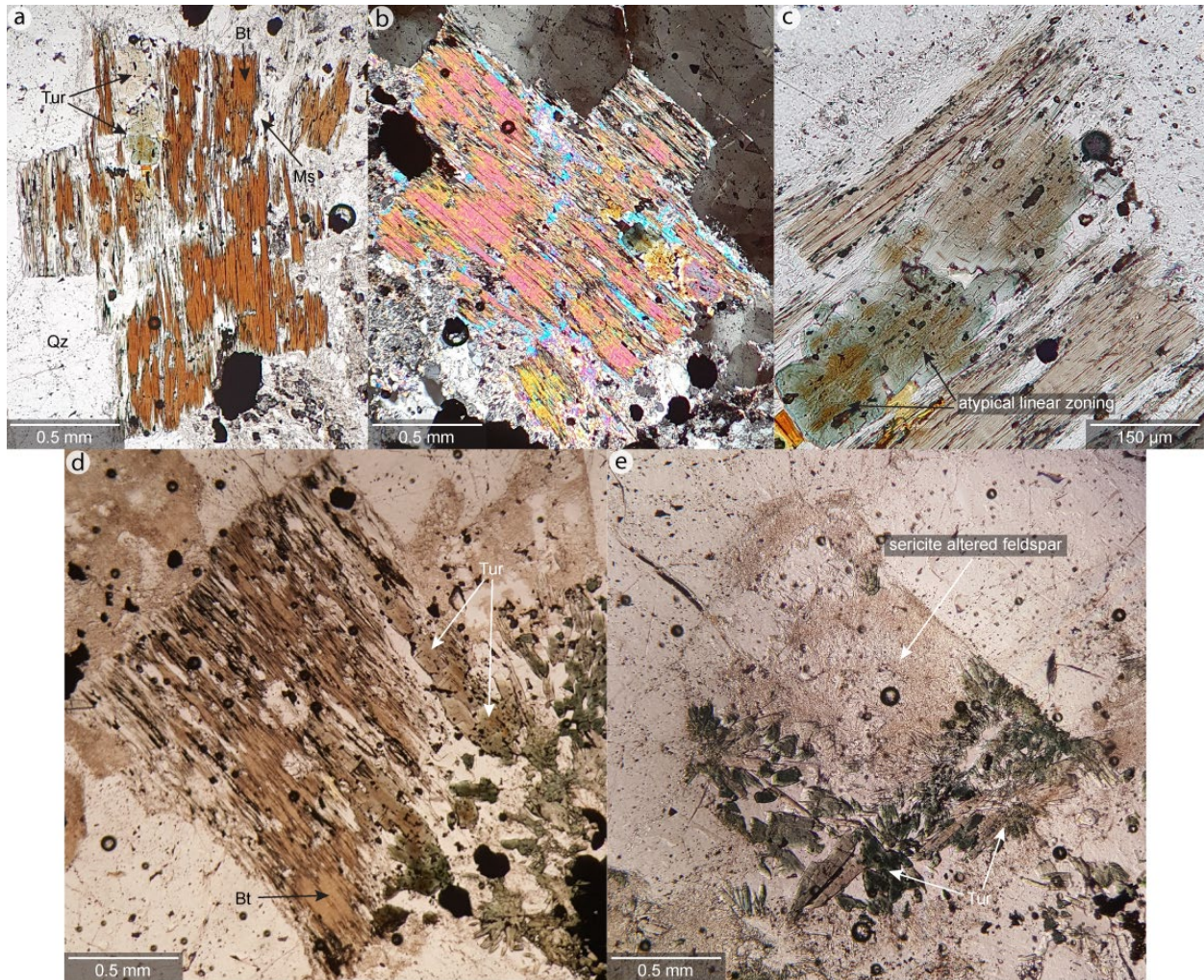


Figure 5-3: Photomicrographs of biotite-tourmaline textures.

Transmitted light photomicrographs from sample 1. a) image showing tourmaline (Tur) replacing biotite (Bt) along cleavage planes. b) same as (a) except in cross polarized light highlighting the presence of muscovite (Ms) denoted by the 2° blue colors. c) a zoomed in section of (a) showing the intimate relationship between biotite and tourmaline. Arrows denote the color zonation which is atypical for tourmaline and follows the basal cleavage direction of the surrounding biotite. d) an additional example showing tourmaline replacing biotite along planes of cleavage. e) a less common example of tourmaline infilling or replacing primary feldspar crystals which are now partially to entirely altered to sericite.

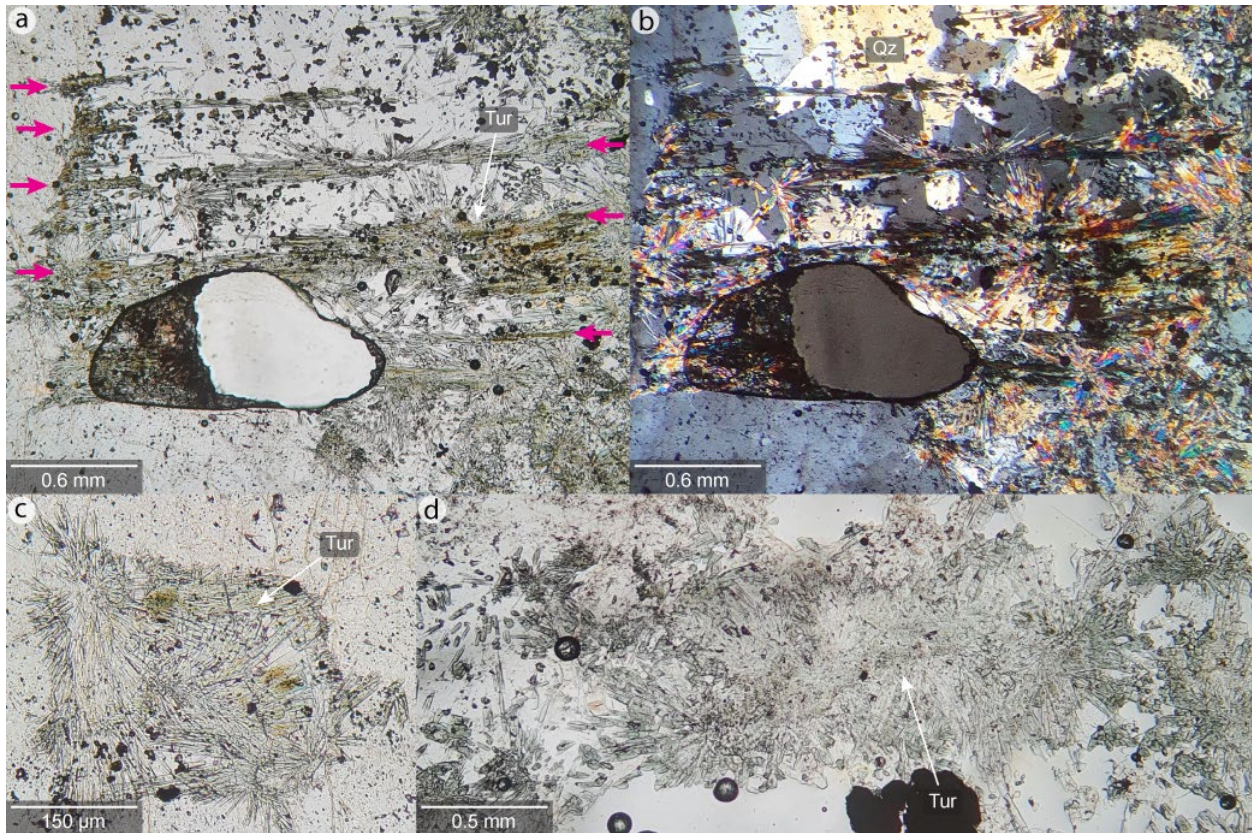


Figure 5-4: Photomicrographs of tourmaline forming after biotite.

Transmitted light photomicrographs from sample 2. a) Image of a cluster of tourmaline (Tur) grains forming a rectangular outline in quartz (Qz). Pink arrows denote linear features of tourmaline grains as well as brown color zonation. b) same as (a) except in cross polarized light highlighting the sub to euhedral quartz grains. c) and d) two additional examples of tourmaline (Tur) aggregates showing equant to rectangular outlines.

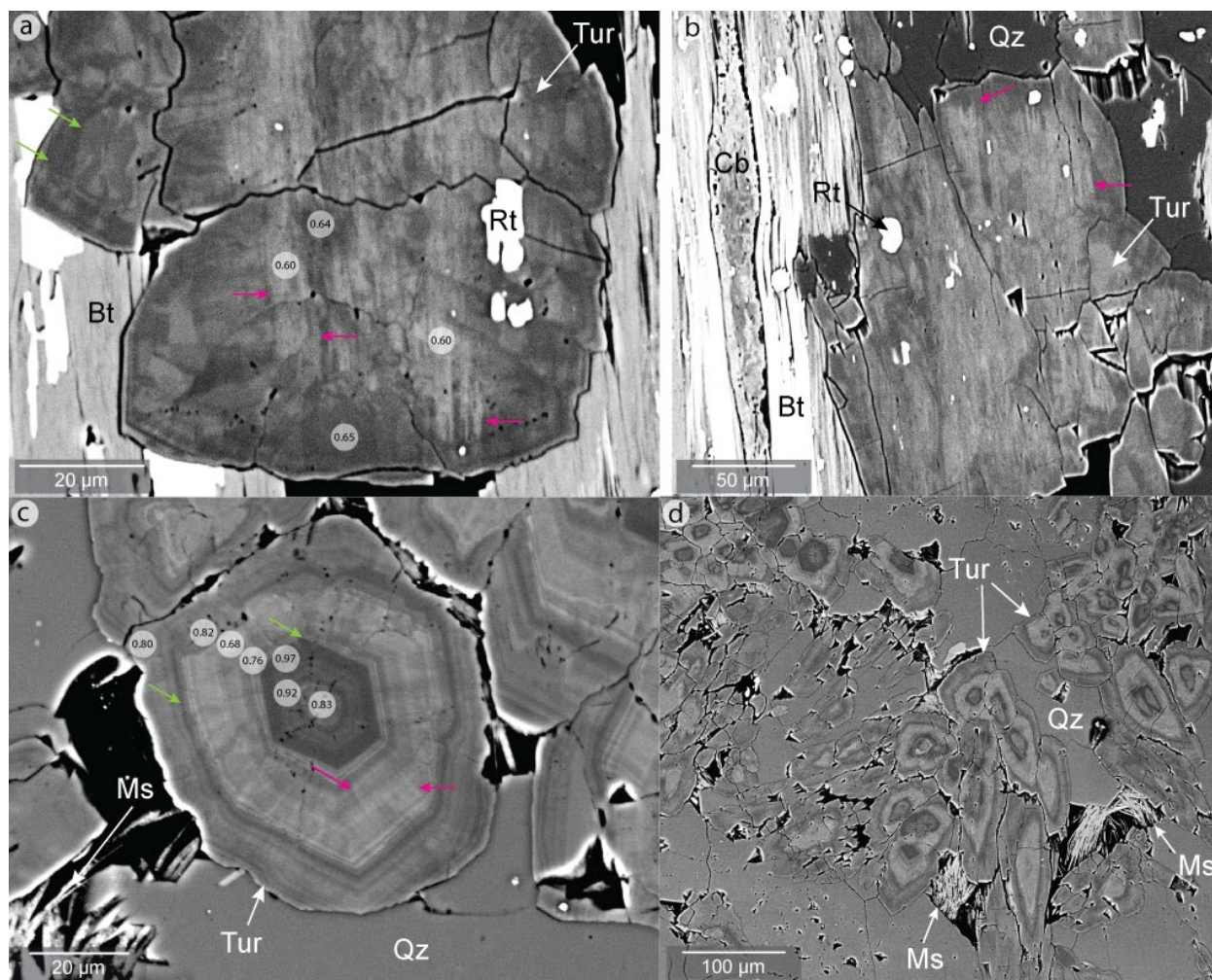


Figure 5-5: Backscattered electron images of biotite and tourmaline

Backscattered electron images (BSEI) of biotite and tourmaline. The contrast of (a) and (b) images are increased to draw attention to the internal features of tourmaline. Sample 1 a) BSEI of tourmaline (Tur) with inclusions of rutile (Rt) surrounded by biotite (Bt). Values in the grey circles represent $Mg\#$ values. Pink arrows indicate the atypical zonation features within tourmaline that are oriented parallel to the enclosing biotite. Green arrows denote subtle concentric zonation features. b) BSEI of tourmaline (Tur) with abundant inclusions of rutile (Rt) surrounded by biotite (Bt) and minor carbonate (Cb). Pink arrows indicate the atypical zonation features oriented parallel to the adjacent biotite. Sample 2 c) concentric zoned tourmaline grain

overlain by $Mg\#$ values. Grains are typically associated with muscovite (Ms). Pink arrows denote atypical zonation which is oriented perpendicular and radial to the c -axis. Green arrows point to the concentric zonation. d) Clusters of tourmaline grains associated with muscovite (Ms) and quartz (Qz).

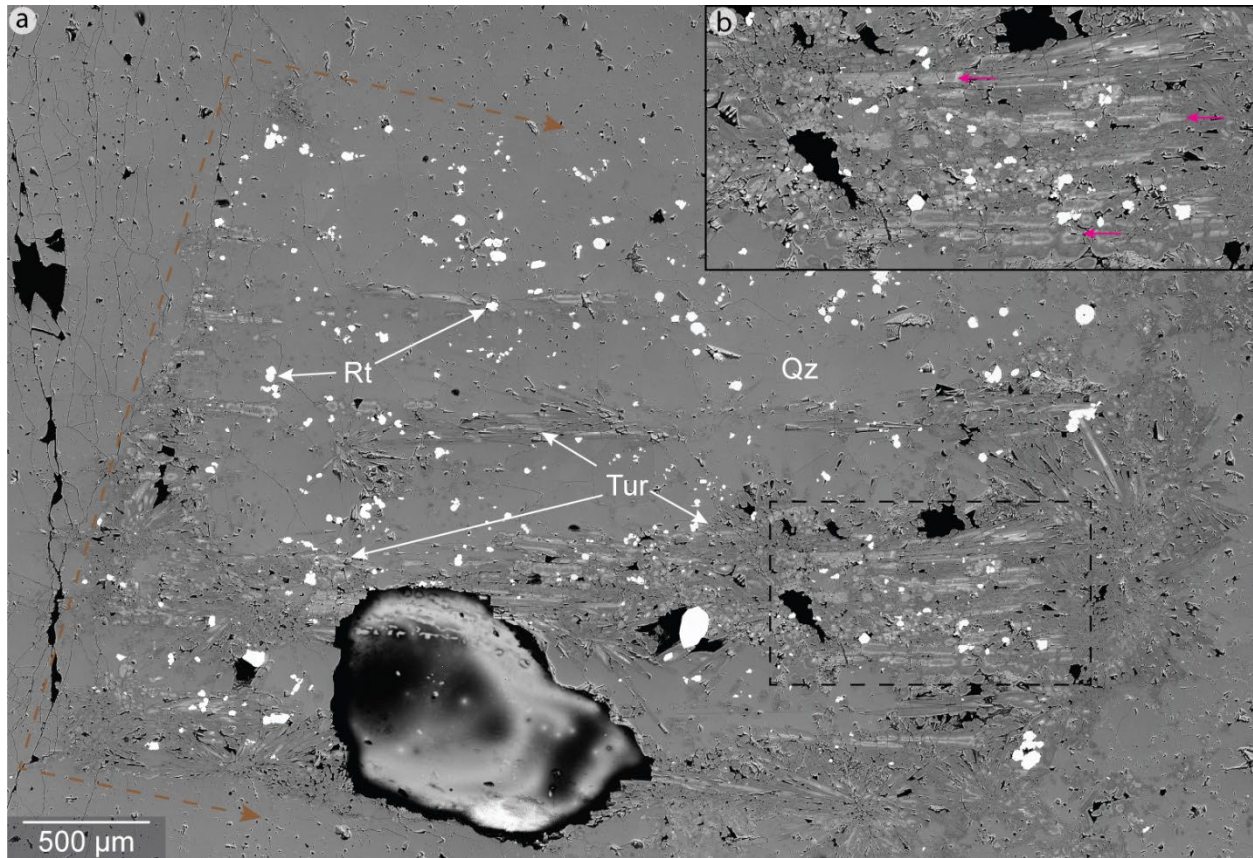


Figure 5-6: Backscatter image montage showing tourmaline that has replaced biotite
 BSEI montage of 100 images. a) aggregate of tourmaline (Tur) grains forming a rectangular outline denoted by the brown dashed line. Note the abundant inclusions of rutile (Rt) which are restricted to this rectangular region. Within the rectangular shape, tourmaline grains form linear features across the image. b) enlarged section from the dashed black box highlighting some of the linear features. In addition to the linear features, the tourmaline grains in these regions are also chemically zoned showing a more intense BSE response in parallel zones.

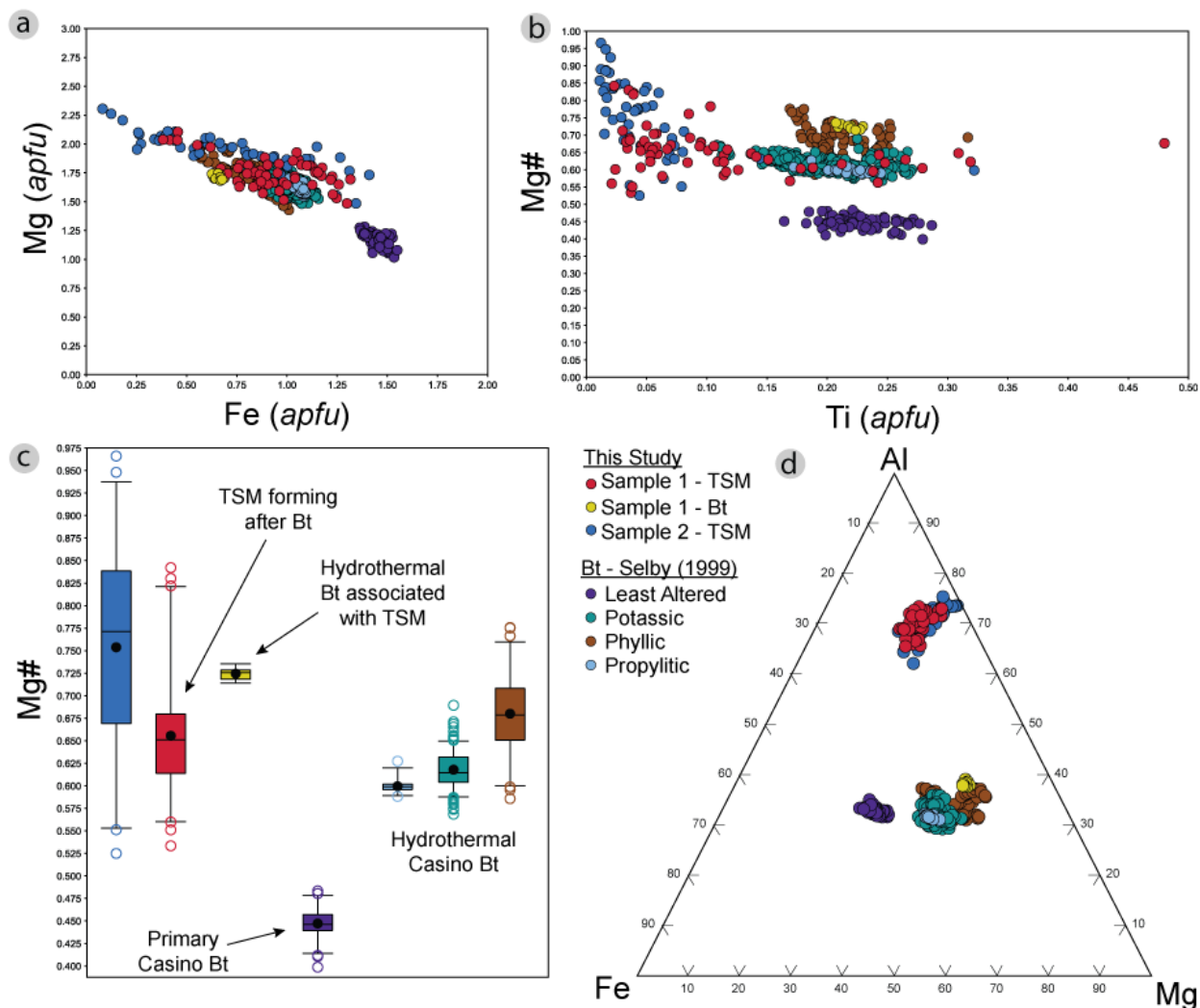


Figure 5-7: Major and minor element chemistry for biotite and tourmaline analyses

Major and minor element chemistry for biotite and tourmaline analyses. Additional biotite chemistry was compiled from Selby (1999). a) a binary plot of Mg vs. Fe (*apfu*) showing the trend from magmatic to hydrothermal biotite and the similarity in tourmaline chemistry. b) a binary plot of $Mg\#$ ($Mg/Mg+Fe$) vs. Ti (*apfu*) showing the Ti-bearing nature of biotite grains in comparison to the tourmaline grains. c) percentile box plots of $Mg\#$ ($Mg/Mg+Fe$) for biotite and tourmaline. The central box is the middle 50% of data from Q1 to Q3, an outlier (circle) represents analysis in the top or bottom 5% of the data. This shows the variation from magmatic biotite which is Fe-rich to hydrothermal biotite which transitions to Mg-rich. The tourmaline

forming in association with the hydrothermal biotite has similar but slightly lower $Mg\#$ values. Tourmaline from sample 2 has a higher average $Mg\#$ and more closely reflects the values from the hydrothermal biotite. d) Ternary diagram of Mg-Fe-Al values for biotite and tourmaline showing the major element variations that exist. Tourmaline samples follow the oxy-dravite – povondraite trend (not shown).

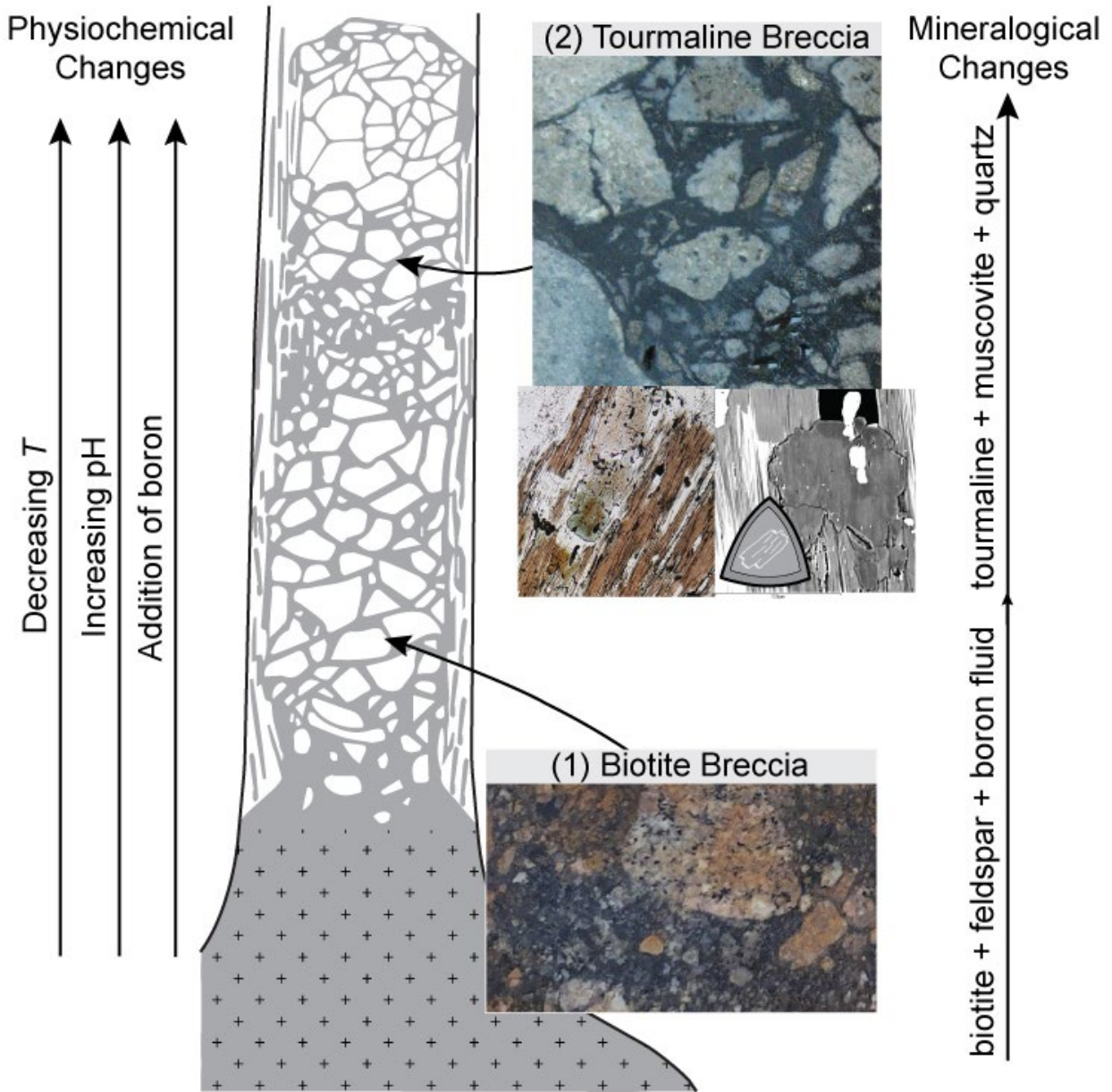


Figure 5-8: Idealized diagram of biotite-tourmaline transition

Idealized diagram showing the mineralogical transition from 1) Bt dominated matrix to, 2) TSM dominated.

5.9 Tables

Table 5-1: Major and minor element chemistry for biotite grains from CEBB-012

Sample	Avg	Min	Max	012S2P6	012S2P26	012S2P27	012S2P31	012S2P44	012S2P47	012S4P1	012S4P2	012S6P7	012S6P9
SiO ₂	37.280	36.629	37.718	37.415	36.988	36.629	37.469	37.395	37.718	37.304	37.709	37.119	37.054
TiO ₂	3.853	3.668	4.116	3.895	3.890	3.675	3.668	3.876	4.116	4.028	3.955	3.719	3.711
Al ₂ O ₃	16.463	16.288	16.871	16.288	16.871	16.454	16.301	16.371	16.552	16.361	16.309	16.519	16.606
Cr ₂ O ₃	0.010	0.000	0.032	0.000	0.012	0.032	0.006	0.004	0.000	0.023	0.011	0.007	0.005
FeO ₁	11.709	11.219	12.078	11.708	11.710	11.219	11.722	11.764	11.695	11.871	11.648	12.078	11.676
MnO	0.049	0.003	0.080	0.077	0.015	0.074	0.003	0.040	0.080	0.078	0.059	0.012	0.055
MgO	14.844	14.525	15.192	14.990	14.525	14.680	15.063	15.192	14.771	14.607	14.827	14.674	15.106
CaO	0.025	0.005	0.067	0.067	0.017	0.010	0.052	0.036	0.005	0.014	0.020	0.017	0.007
BaO	1.214	0.870	1.506	1.148	1.363	1.506	1.053	0.870	1.391	1.320	0.991	1.477	1.024
Na ₂ O	0.190	0.168	0.215	0.197	0.215	0.207	0.180	0.182	0.193	0.176	0.193	0.184	0.168
K ₂ O	9.338	9.155	9.525	9.368	9.279	9.357	9.211	9.389	9.445	9.252	9.525	9.155	9.397
F	0.643	0.511	0.861	0.677	0.572	0.841	0.620	0.603	0.552	0.516	0.861	0.676	0.511
Cl	0.152	0.112	0.194	0.132	0.194	0.144	0.183	0.155	0.160	0.128	0.112	0.188	0.124
H ₂ O	4.152	3.229	5.072	4.005	4.253	5.072	4.354	4.050	3.229	4.246	3.746	4.056	4.508
Total				99.999	99.998	100.000	99.999	99.999	99.990	99.999	100.000	100.001	100.002
-O=F+Cl				0.315	0.285	0.387	0.302	0.289	0.269	0.246	0.388	0.327	0.243
Fe ₂ O ₃ *	4.311	3.104	5.400	4.055	4.759	4.211	4.632	3.887	4.728	4.513	3.104	5.400	3.825
FeO*	7.830	7.219	8.855	8.059	7.427	7.430	7.554	8.267	7.440	7.810	8.855	7.219	8.234

APFU	Avg	Min	Max	012S2P6	012S2P26	012S2P27	012S2P31	012S2P44	012S2P47	012S4P1	012S4P2	012S6P7	012S6P9
²⁸ Si	2.809	2.792	2.832	2.812	2.795	2.792	2.820	2.811	2.821	2.811	2.832	2.800	2.792
²⁷ Al	1.106	1.069	1.138	1.120	1.103	1.125	1.069	1.106	1.092	1.110	1.113	1.080	1.138
⁵⁴ Fe ³⁺	0.086	0.055	0.121	0.068	0.102	0.084	0.111	0.083	0.087	0.080	0.055	0.121	0.070
sum				4.000	4.000	4.000	4.000	4.000	4.000	4.000	4.000	4.000	4.000
²⁷ Al	0.356	0.323	0.399	0.323	0.399	0.354	0.377	0.344	0.367	0.343	0.331	0.389	0.337
²⁴ Mg	1.715	1.683	1.745	1.712	1.702	1.724	1.741	1.745	1.700	1.683	1.692	1.713	1.736
⁵⁶ Fe ²⁺	0.493	0.455	0.556	0.507	0.469	0.474	0.475	0.520	0.465	0.492	0.556	0.455	0.519
⁵⁶ Fe ³⁺	0.159	0.121	0.186	0.162	0.169	0.158	0.151	0.137	0.179	0.176	0.121	0.186	0.147
⁴⁸ Ti	0.217	0.207	0.230	0.219	0.219	0.211	0.207	0.217	0.230	0.227	0.223	0.210	0.209
⁵² Cr	0.001	0.000	0.002	0.000	0.001	0.002	0.000	0.000	0.000	0.001	0.001	0.000	0.000
⁵⁵ Mn	0.003	0.000	0.005	0.005	0.001	0.005	0.000	0.003	0.005	0.005	0.004	0.001	0.004
sum				2.927	2.960	2.927	2.953	2.966	2.947	2.928	2.928	2.954	2.951
¹³ Vac	0.056	0.034	0.073	0.073	0.040	0.073	0.047	0.034	0.053	0.072	0.072	0.046	0.049
K	0.854	0.828	0.879	0.866	0.837	0.867	0.838	0.858	0.851	0.854	0.879	0.828	0.867
Na	0.028	0.025	0.031	0.029	0.031	0.031	0.026	0.027	0.028	0.026	0.028	0.027	0.025
Ba	0.036	0.026	0.045	0.034	0.040	0.045	0.031	0.026	0.041	0.039	0.029	0.044	0.030
Ca	0.002	0.000	0.005	0.005	0.001	0.001	0.004	0.003	0.000	0.001	0.002	0.001	0.001
sum				0.934	0.910	0.943	0.899	0.913	0.920	0.919	0.938	0.900	0.922
Vac	0.080	0.057	0.101	0.066	0.090	0.057	0.101	0.087	0.080	0.081	0.062	0.100	0.078
¹⁹ F	0.214	0.176	0.270	0.206	0.217	0.270	0.212	0.201	0.199	0.178	0.250	0.236	0.176
³⁵ Cl	0.019	0.014	0.025	0.017	0.025	0.019	0.023	0.020	0.020	0.016	0.014	0.024	0.016
¹⁷ OH	1.349	1.298	1.407	1.325	1.363	1.329	1.366	1.362	1.337	1.350	1.298	1.358	1.407
¹⁷ O ₂ -	0.417	0.382	0.455	0.452	0.396	0.383	0.399	0.418	0.445	0.455	0.438	0.382	0.401
Mg#	0.699	0.692	0.707	0.699	0.697	0.707	0.702	0.702	0.699	0.692	0.698	0.692	0.702

Table 5-2: Major and minor element chemistry for muscovite grains

Spot Point Quality	Sample 1										Sample 2							
	S2P7	S2P8	S2P22	S2P46	S2P48	S3P2	S3P3	S3P10	S6P6		S7P29	S7P30	S7P31					
	Good	Good	Mod	Mod	Good	Mod	Mod	Mod	Good	Avg	Min	Max	Poor	Poor	Poor	Avg	Min	Max
SiO ₂	46.419	48.504	46.781	47.618	45.942	45.879	45.480	47.372	47.739	46.859	45.480	48.504	44.185	42.320	41.935	42.813	41.935	44.185
TiO ₂	0.491	0.341	0.472	0.502	0.481	0.399	0.506	0.346	0.381	0.435	0.341	0.506	0.331	0.229	0.358	0.306	0.229	0.358
Al ₂ O ₃	31.936	31.101	32.176	30.886	31.830	32.426	31.849	32.403	32.130	31.860	30.886	32.426	33.277	31.659	31.166	32.034	31.166	33.277
Cr ₂ O ₃	0.006	0.012	0.031	0.000	0.000	0.016	0.013	0.026	0.015	0.013	0.000	0.031	0.025	0.057	0.008	0.030	0.008	0.057
FeO	2.142	2.290	2.495	2.787	2.781	1.622	2.342	1.682	2.164	2.256	1.622	2.787	0.719	0.951	0.938	0.869	0.719	0.951
MnO	0.000	0.009	0.028	0.025	0.046	0.000	0.000	0.007	0.000	0.013	0.000	0.046	0.017	0.038	0.001	0.019	0.001	0.038
MgO	1.998	2.853	1.932	3.859	2.157	1.491	1.812	1.854	1.973	2.214	1.491	3.859	2.323	2.280	2.800	2.468	2.280	2.800
CaO	0.011	0.018	0.004	0.025	0.001	0.022	0.023	0.065	0.002	0.019	0.001	0.065	0.089	0.171	0.245	0.168	0.089	0.245
BaO	0.294	0.306	0.293	0.175	0.341	0.428	0.389	0.387	0.349	0.329	0.175	0.428	0.059	0.125	0.178	0.121	0.059	0.178
Na ₂ O	0.262	0.206	0.280	0.176	0.272	0.242	0.244	0.254	0.173	0.234	0.173	0.280	0.347	0.329	0.281	0.319	0.281	0.347
K ₂ O	10.698	10.167	10.698	9.778	10.831	10.518	10.748	10.871	10.733	10.560	9.778	10.871	10.348	10.142	9.751	10.080	9.751	10.348
F	0.129	0.147	0.241	0.211	0.013	0.115	0.095	0.202	0.115	0.141	0.013	0.241	0.228	0.200	0.286	0.238	0.200	0.286
Cl	0.006	0.008	0.017	0.007	0.014	0.003	0.010	0.004	0.026	0.011	0.003	0.026	0.066	0.073	0.068	0.069	0.066	0.073
H ₂ O	5.551	3.985	4.472	3.855	5.281	6.794	6.414	4.489	4.130	4.997	3.855	6.794	7.951	11.378	11.895	10.408	7.951	11.895
Total	99.997	100.001	100.002	99.992	100.000	99.995	99.994	99.999	99.996				99.965	100.002	100.001			
<i>APFU</i>	S2P7	S2P8	S2P22	S2P46	S2P48	S3P2	S3P3	S3P10	S6P6	Avg	Min	Max	S7P29	S7P30	S7P31	Avg	Min	Max
Al(tot)	2.784	2.654	2.778	2.639	2.782	2.856	2.813	2.786	2.754	2.761	2.639	2.856	2.955	2.933	2.903	2.931	2.903	2.955
Si(t)	3.434	3.511	3.427	3.452	3.407	3.428	3.408	3.456	3.472	3.444	3.407	3.511	3.329	3.327	3.315	3.324	3.315	3.329
Al(t)	0.566	0.489	0.573	0.548	0.593	0.572	0.592	0.544	0.528	0.556	0.489	0.593	0.671	0.673	0.685	0.676	0.671	0.685
Sum T	4.000	4.000	4.000	4.000	4.000	4.000	4.000	4.000	4.000				4.000	4.000	4.000			
Al	2.218	2.165	2.206	2.091	2.190	2.284	2.221	2.242	2.227	2.205	2.091	2.284	2.284	2.260	2.218	2.254	2.218	2.284
Ti	0.027	0.019	0.026	0.027	0.027	0.022	0.029	0.019	0.021	0.024	0.019	0.029	0.019	0.014	0.021	0.018	0.014	0.021
Cr	0.000	0.001	0.002	0.000	0.000	0.001	0.001	0.001	0.001	0.001	0.000	0.002	0.001	0.004	0.000	0.002	0.000	0.004
Fe2+	0.133	0.139	0.153	0.169	0.172	0.101	0.147	0.103	0.132	0.139	0.101	0.172	0.045	0.063	0.062	0.057	0.045	0.063
Mn	0.000	0.001	0.002	0.002	0.003	0.000	0.000	0.000	0.000	0.001	0.000	0.003	0.001	0.003	0.000	0.001	0.000	0.003
Mg	0.220	0.308	0.211	0.417	0.238	0.166	0.202	0.202	0.214	0.242	0.166	0.417	0.261	0.267	0.330	0.286	0.261	0.330
Sum Y	2.598	2.631	2.599	2.705	2.630	2.574	2.600	2.567	2.594				2.611	2.610	2.632			
Ba	0.009	0.009	0.008	0.005	0.010	0.013	0.011	0.011	0.010	0.009	0.005	0.013	0.002	0.004	0.006	0.004	0.002	0.006
Ca	0.001	0.001	0.000	0.002	0.000	0.002	0.002	0.005	0.000	0.001	0.000	0.005	0.007	0.014	0.021	0.014	0.007	0.021
Na	0.038	0.029	0.040	0.025	0.039	0.035	0.035	0.036	0.024	0.033	0.024	0.040	0.051	0.050	0.043	0.048	0.043	0.051
K	1.010	0.939	1.000	0.904	1.025	1.003	1.028	1.012	0.996	0.991	0.904	1.028	0.995	1.017	0.983	0.998	0.983	1.017
Sum X	1.057	0.978	1.048	0.936	1.074	1.052	1.076	1.064	1.030				1.054	1.086	1.053			
Cl	0.030	0.034	0.056	0.048	0.003	0.027	0.023	0.047	0.026	0.033	0.003	0.056	0.054	0.050	0.071	0.059	0.050	0.071
F	0.030	0.034	0.056	0.048	0.003	0.027	0.023	0.047	0.026	0.033	0.003	0.056	0.054	0.050	0.071	0.059	0.050	0.071
OH	1.940	1.933	1.888	1.903	1.994	1.946	1.955	1.907	1.947	1.935	1.888	1.994	1.891	1.901	1.857	1.883	1.857	1.901

Table 5-3: Summary of the major and minor element chemistry of tourmaline

	CEBB-012			CEBB-005		
	Avg (<i>n</i> =62)	Min	Max	Avg (<i>n</i> =48)	Min	Max
SiO ₂	35.991	35.021	37.035	35.238	33.230	36.280
TiO ₂	0.883	0.092	2.542	0.384	0.092	2.524
Al ₂ O ₃	32.207	29.133	34.594	32.953	25.854	35.798
V ₂ O ₃						
Cr ₂ O ₃	0.012	<LOD	0.031	0.015	<LOD	0.046
FeO	6.724	2.833	9.420	4.933	0.604	11.395
MnO	0.008	<LOD	0.047	0.010	<LOD	0.080
ZnO	0.001	<LOD	0.041	0.001	<LOD	0.041
MgO	7.102	5.982	8.669	8.045	5.943	9.686
CaO	0.512	0.288	0.978	0.409	0.015	1.013
Na ₂ O	2.112	1.910	2.279	2.404	1.801	2.837
K ₂ O	0.034	0.010	0.065	0.028	0.011	0.089
F	0.050	<LOD	0.150	0.083	<LOD	0.326
Cl	0.001	<LOD	0.033	0.006	<LOD	0.025
B ₂ O ₃ *	10.534			10.632		
H ₂ O*	3.403			3.481		
O=F	0.021			0.035		
O=Cl	0.002			0.001		
Total	99.653			99.859		
<i>apfu</i>						
^T Si	5.94	5.728	6.044	5.955	5.806	6.133
^T B	0.00	0.000	0.009	0.000	0.000	0.010
^T Al	0.06	0.000	0.272	0.052	0.000	0.194
^Z Al	5.96	5.688	6.000	5.963	5.158	6.000
^Z Mg	0.04	0.000	0.287	0.025	0.000	0.467
^Y Al	0.24	0.000	0.562	0.330	0.000	0.748
^Y Ti	0.10	0.021	0.480	0.048	0.011	0.322
^Y V	0.01	0.000	0.021	0.001	0.000	0.034
^Y Cr	0.00	0.000	0.004	0.002	0.000	0.006
^Y Fe ²⁺	0.93	0.382	1.316	0.671	0.081	1.410
^Y Mn ²⁺	0.00	0.000	0.007	0.001	0.000	0.011
^Y Mg	1.71	1.439	2.105	1.934	1.416	2.305
^Y Zn	0.00	0.000	0.005	0.001	0.000	0.005
^X Ca	0.09	0.051	0.172	0.007	0.003	0.176
^X Na	0.68	0.599	0.732	0.762	0.567	0.905
^X K	0.01	0.002	0.013	0.006	0.002	0.018
^X □	0.23	0.158	0.316	0.160	0.038	0.415
^V OH	3.00	3.000	3.000	3.000	3.000	3.000
^W OH	0.75	0.675	0.806	0.796	0.562	0.953
^W F	0.03	0.000	0.077	0.043	0.000	0.171
^W Cl	0.00	0.000	0.009	0.002	0.000	0.007
^W O	0.23	0.158	0.306	0.160	0.038	0.415
Mg#	0.66	0.533	0.842	0.754	0.525	0.966

apfu: calculated based on 15 *Y+Z+T* cations. Boron was assumed to be stoichiometric (3) in the trigonal site.

5.10 References

- Afshooni, S.Z., Mirnejad, H., Esmacily, D. and Haroni, H.A., 2013. Mineral chemistry of hydrothermal biotite from the Kahang porphyry copper deposit (NE Isfahan), Central Province of Iran. *Ore Geology Reviews*, 54: 214-232.
<http://doi.org/10.1016/j.oregeorev.2013.04.004>
- Arancibia, O.N. and Clark, A.H., 1996. Early magnetite-amphibole-plagioclase alteration-mineralization in the Island Copper porphyry copper-gold-molybdenum deposit, British Columbia. *Economic Geology*, 91(2): 402-438.
<http://doi.org/10.2113/gsecongeo.91.2.402>
- Arndt, N.T., Fontboté, L., Hedenquist, J.W., Kesler, S.E., Thompson, J.F.H. and Wood, D.G., 2017. Future Global Mineral Resources. *Geochemical Perspectives*: 1-171.
<http://doi.org/10.7185/geochempersp.6.1>
- Baksheev, I.A., Chitalin, A.F., Yapaskurt, V.O., Vigasina, M.F., Bryzgalov, I.A. and Ustinov, V.I., 2010. Tourmaline in the Vetka porphyry copper-molybdenum deposit of the Chukchi Peninsula of Russia. *Moscow University Geology Bulletin*, 65(1): 27-38.
<http://doi.org/10.3103/s0145875210010035>
- Casselmann, S.C. and Brown, H., 2017. Casino porphyry copper-gold-molybdenum deposit, central Yukon (Yukon MINFILE 115J028); in Yukon Exploration and Geology Overview 2016, (ed.) K.W. MacFarlane; Yukon Geological Survey, p. 61–74, plus digital appendices.
- Cheng, L., Zhang, C., Liu, X., Yang, X., Zhou, Y., Horn, I., Weyer, S. and Holtz, F., 2021. Significant boron isotopic fractionation in the magmatic evolution of Himalayan

- leucogranite recorded in multiple generations of tourmaline. *Chemical Geology*, 571. <http://doi.org/10.1016/j.chemgeo.2021.120194>
- Cheng, L., Zhang, C., Yang, X., Qi, D., Zhou, Y. and Holtz, F., 2019. Experimental investigation of reactions between two-mica granite and boron-rich fluids: Implications for the formation of tourmaline granite. *Science China Earth Sciences*, 62, 1630-1644. <http://doi.org/10.1007/s11430-019-9442-y>
- Clark, A.H., 1995. Are outsize porphyry copper deposits either anatomically or environmentally distinctive?, Giant Ore Deposits. Society of Economic Geologists, Littleton CO, USA, pp. 213-284. <http://doi.org/10.5382/sp.02.06>
- Cooke, D.R., Hollings, P., Wilkinson, J.J. and Tosdal, R.M., 2014. 13.14 - Geochemistry of Porphyry Deposits, In: Heinrich D. Holland, Karl K. Turekian (Editors), *Treatise on Geochemistry*, pp. 357-381. <http://doi.org/10.1016/b978-0-08-095975-7.01116-5>
- Frikken, P.H., Cooke, D.R., Walshe, J.L., Archibald, D., Skarmeta, J., Serrano, L. and Vargas, R., 2005. Mineralogical and isotopic zonation in the Sur-Sur tourmaline breccia, Río Blanco-Los Bronces Cu-Mo deposit, Chile: Implications for ore genesis. *Economic Geology*, 100(5): 935-961. <http://doi.org/10.2113/gsecongeo.100.5>
- Jacobs, D.C. and Parry, W.T., 1979. Geochemistry of Biotite in the Santa Rita Porphyry Copper Deposit, New Mexico. *Economic Geology*, 74: 860-887.
- London, D., 2016. Reading Pegmatites—Part 2: What Tourmaline Says. *Rocks & Minerals*, 91(2): 132-149. <http://doi.org/10.1080/00357529.2016.1113464>

- McClenaghan, M.B., McCurdy, M., Garrett, R., Beckett-Brown, C.E., Leybourne, M.I., Casselman, S.G. and Pelchat, P., 2021. Heavy mineral and geochemical signatures of porphyry copper mineralization: examples from the Casino porphyry Cu-Au-Mo deposit, Yukon: in Targeted Geoscience Initiative 5: contributions to the understanding and exploration of porphyry deposits; Plouffe (ed.); Schetselaar, E (ed.); Geological Survey of Canada, Bulletin 616, 2021 p. 159-202, <https://doi.org/10.4095/327987>
- Nabelek, P.I., 2021. Formation of metasomatic tourmalinites in reduced schists during the Black Hills Orogeny, South Dakota. *American Mineralogist*, 106(2): 282-289. <http://doi.org/10.2138/am-2020-7405>
- Orlando, A., Ruggieri, G., Chiarantini, L., Montegrossi, G. and Rimondi, V., 2017. Experimental Investigation of Biotite-Rich Schist Reacting with B-Bearing Fluids at Upper Crustal Conditions and Correlated Tourmaline Formation. *Minerals*, 7(9), 155. <http://doi.org/10.3390/min7090155>
- Richards, J.P., 2003. Tectono-Magmatic Precursors for Porphyry Cu-(Mo-Au) Deposit Formation. *Economic Geology*, 98.
- Selby, D., 1999. Fluid characteristics and evolution in porphyry Cu and Mo systems, Yukon and British Columbia, University of Alberta.
- Selby, D. and Nesbitt, B.E., 2000. Chemical composition of biotite from the casino porphyry Cu-Au-Mo mineralization, Yukon, Canada: Evaluation of magmatic and hydrothermal fluid chemistry. *Chemical Geology*, 171: 77-93.
- Sillitoe, R.H., 1972. A plate tectonic model for the origin of porphyry copper deposits. *Economic Geology*, 67: 184-197.

Sillitoe, R.H., 2010. Porphyry copper systems. *Economic Geology*, 105(1): 3-41.

<http://doi.org/0.2113/gsecongeo.105.1.3>

Sillitoe, R.H. and Sawkins, F.J., 1971. Geologic, mineralogic and fluid inclusion studies relating to the origin of copper-bearing tourmaline breccia pipes, Chile. *Economic Geology*, 66(7): 1028-1041. <http://doi.org/10.2113/gsecongeo.66.7.1028>

Skewes, M.A., Holmgren, C. and Stern, C.R., 2003. The Donoso copper-rich, tourmaline-bearing breccia pipe in central Chile: petrologic, fluid inclusion and stable isotope evidence for an origin from magmatic fluids. *Mineralium Deposita*, 38(1): 2-21.

<http://doi.org/10.1007/s00126-002-0264-9>

Spránitz, T., Józsa, S., Kovács, Z., Váczi, B. and Török, K., 2018. Magmatic and metamorphic evolution of tourmaline-rich rocks of the Sopron area, Eastern Alps. *Journal of Geosciences*: 175-191. <http://doi.org/10.3190/jgeosci.263>

Tonarini, S., Forte, C., Petrini, R. and Ferrara, G., 2003. Melt/biotite 11B/10B isotopic fractionation and the boron local environment in the structure of volcanic glasses.

Geochimica et Cosmochimica Acta, 67(10): 1863-1873. [http://doi.org/10.1016/s0016-7037\(02\)00987-0](http://doi.org/10.1016/s0016-7037(02)00987-0)

van Hinsberg, V.J., 2011. Preliminary experimental data on trace-element partitioning between tourmaline and silicate melt. *The Canadian Mineralogist*, 49(1): 153-163.

<http://doi.org/10.3749/canmin.49.1.153>

van Hinsberg, V.J., Franz, G. and Wood, B.J., 2017. Determining subduction-zone fluid composition using a tourmaline mineral probe. *Geochemical Perspectives Letters*: 160-169. <http://doi.org/10.7185/geochemlet.1719>

- Vargas, R., Gustafson, L.B., Vukasovic, M., Tidy F, E. and Skewes, M.A., 1999. Ore Breccias in the Rio Blanco-Los Bronces Porphyry Copper Deposit, Chile. In: B.J. Skinner (Editor), *Geology and Ore Deposits of the Central Andes, Colorado*.
- Warnaars, F.W., Holmgren, C. and Barassi, S., 1985. Porphyry Copper and Tourmaline Breccias at Los-Bronces-Rio-Blanco, Chile. *Economic Geology*, 80(6): 1544-1565.
<http://doi.org/10.2113/gsecongeo.80.6.1544>
- Xiang, L., Wang, R., Romer, R.L., Che, X., Hu, H., Xie, L. and Tian, E., 2020. Neoproterozoic Nb-Ta-W-Sn bearing tourmaline leucogranite in the western part of Jiangnan Orogen: Implications for episodic mineralization in South China. *Lithos*, 360-361.
<http://doi.org/10.1016/j.lithos.2020.105450>
- Yavuz, F., Karakaya, N., Yildirim, D.K., Karakaya, M.Ç. and Kumral, M., 2014. A Windows program for calculation and classification of tourmaline-supergroup (IMA-2011). *Computers & Geosciences*, 63: 70-87. <http://doi.org/10.1016/j.cageo.2013.10.012>